Regional-scale controls on rockfall occurrence

JESSICA BENJAMIN

Jessica Benjamin

Regional-scale controls on rockfall occurrence

Thesis submitted in partial fulfilment for the degree of Doctor of Philosophy

Department of Geography
Durham University

2018

Declaration

I confirm that no part of the material presented in this thesis has previously been submitted for a degree in this or any other university. In all cases the words of others, where relevant, have been fully acknowledged.

Jessica Benjamin
Durham University
May 2018

Cover image: Orthophoto of the sea cliffs at Old Nab, North Yorkshire (April 2016).

Abstract

Rockfalls exert a first-order control on the rate of rock wall retreat on mountain slopes and on coastal rock cliffs. Their occurrence is conditioned by a combination of intrinsic (resisting) and extrinsic (driving) processes, yet determining the exact effects of these processes on rockfall activity and the resulting cliff erosion remains difficult. Although rockfall activity has been monitored extensively in a variety of settings, high-resolution observations of rockfall occurrence on a regional scale are scarce. This is partly owing to difficulties in adequately quantifying the full range of possible rockfall volumes with sufficient accuracy and completeness, and at a scale that exceeds the influence of localised controls on rockfalls. This lack of insight restricts our ability to abstract patterns, to identify long-term changes in behaviour, and to assess how rock slopes respond to changes in both structural and environmental conditions, without resorting to a space-for-time substitution.

This thesis develops a workflow, from novel data collection to analysis, which is tailored to monitoring rockfall activity and the resulting cliff retreat continuously (in space), in 3D, and over large spatial scales ($> 10^4$ m). The approach is tested by analysing rockfall activity and the resulting erosion recorded along 20.5 km of near-vertical coastal cliffs, in what is considered as the first multi-temporal detection of rockfalls at a regional-scale and in full 3D. The resulting data are then used to derive a quantitative appraisal of along-coast variations in the geometric properties of exposed discontinuity surfaces, to assess the extent to which these drive patterns in the size and shape of the rockfalls observed. High-resolution field monitoring is then undertaken along a subsection of the coastline ($> 10^2$ m), where cliff lithology and structure are approximately uniform, in order to quantify spatial variations in wave loading characteristics and to relate these to local morphological conditions, which can act as a proxy for wave loading characteristics.

The resulting rockfall inventory is analysed to identify the characteristics of rock slope change that only become apparent when assessed at this scale, placing bounds on data previously collected more locally ($< 10^2$ m). The data show that spatial consistencies in the distribution of rockfall shape and volume through time approximately follow the geological setting of the coastline, but that variations in the strength of these consistencies are likely to be conditioned by differences in local processes and morphological controls between sites. These results are used to examine the relationships between key metrics of erosion, structural, and morphological controls, which ultimately permits the identification of areas where patterns of erosion are dominated by either intrinsic or extrinsic processes, or a mixture of both. Uniquely, the methodologies and data presented here mark a step-change in our ability to understand the competing effects of different processes in determining the magnitude and frequency of rockfall activity, and the resulting cliff erosion. The findings of this research hold considerable implications for our understanding of rockfalls, and for monitoring, modelling, and managing actively failing rock slopes.

Acknowledgments

The past three and a half years have brought as many hurdles as opportunities, throughout which my friends, family, and colleagues have been there to support and guide me. I can no longer remember when exactly it was that I first put pen to paper (or hand to keyboard), but it is with great pride and pleasure that I present this as my doctoral thesis.

Firstly, I would like to thank my supervisors Nick Rosser and Matt Brain for their time, support, and enthusiasm over the past three and a half years. Words cannot express how incredibly grateful I am to them both for giving me this opportunity, for being so generous with their time, and for their confidence in my capabilities. Their invaluable knowledge and dedication to producing only the highest quality research have tested my abilities in the best possible way, and I hope I have been able to deliver. Additionally, this work would not have been possible without funding from ICL Fertilizers UK (Ltd), who continue to support the monitoring undertaken along the North Yorkshire coast. This funding has allowed me to pursue a number of incredible opportunities over the course of my PhD, including travelling internationally to present at conferences and attending the LARAM Landslide School.

My thanks are also due to Leine Starka and Chris Cox from 3D Laser Mapping Ltd, who took time out of a busy schedule to spend several days working with me at the beginning of my PhD. During this time, both Leine and Chris taught me how to process raw airborne LiDAR data and, later, they were instrumental in the commissioning and capture of numerous airborne LiDAR surveys of the North Yorkshire coast. These datasets were central to this work, and I am grateful for their input in this process. I would also like to express my gratitude to Stephen Lishman and his colleagues in the Mechanical Engineering Services Workshop (Department of Physics). Stephen took my designs for a waterproof casing for some monitoring instruments and manufactured them flawlessly, despite being given an unrealistically tight deadline to do so. I would also like to express my gratitude to Jonathan Rasmussen from Airfotos for giving up his weekend to capture a wonderful dataset of oblique and vertical imagery of the coastline - in *exactly* the right conditions!

I extend sincere thanks to Simon Varley for coming to Staithes with me to collect my ground motion data, month after month, and often at unsociable hours. Simon was always incredibly good-humoured, even when fieldwork really was not going to plan, and provided great company on many a trip to Dotty's. In addition, my thanks are also due to Emma Vann Jones, Saskia de Vilder, Zuzanna Swirad, Heather Bell, Siobhan Whadcoat, Sam Waugh, Dave Hodgson, Neil Tunstall, and Chris Longley for their help in collecting the ground control data for the airborne LiDAR surveys that were central to this work. Collecting this data all too often required sitting alone on a cliff top, for many hours, while babysitting a GPS (a side note: they are not great company). I am well aware of how tedious this was, and remain indebted to everyone who offered me their full support to make these surveys happen.

My thanks also go to the community in the Department of Geography. It has been a privilege to be a part of such an intelligent, talented, and fun group of people over the course of my PhD. I have made many friends in the Department, many of whom will be friends for life, and seeing their own successes has been a source of inspiration for me when times were tough. Thanks in particular go to Hannah, Matt, Jess, Will, and Sophie for being great friends.

Last but not least, thanks to my family and to Jack. To Mum, Dad, and Helen; thank you, not only for your patience, but also for keeping a veritable clowder of cats to greet me on every visit home. Jack, you have always been a huge source of encouragement for me, and your successes are something I truly aspire to. Thank you for tolerating me whenever I get 'hangry', but most importantly thank you for helping me out time and time again with MATLAB problems, for grounding me, and for always having faith in me.

To anyone else who played a part in my postgraduate journey, whether it was through academic support, collaboration on research, or friendship, thank you for your invaluable input.

Contents

List of Figures

Chapter 1 – Introduction

Chapter 2 – Study site

Chapter 3 – Quantifying regional variations in rockfall activity along coastal cliffs

Chapter 4 – Evaluating structural controls on variations in rockfall activity

Chapter 5 – Coastal cliff ground motions and response to wave loading

Chapter 6 – Discussion

List of Tables

Chapter 2 – Study site

Chapter 3 – Quantifying regional variations in rockfall activity along coastal cliffs

Chapter 4 – Evaluating structural controls on variations in rockfall activity

Chapter 5 – Coastal cliff ground motions and response to wave loading

This page is intentionally left blank

Chapter 1

Introduction

The mechanical properties and stress state of a rock mass play a fundamental role in landscape evolution by influencing surface morphology and moderating the efficiency of erosive processes (Clarke and Burbank, 2011; Koons *et al.*, 2012). At the hillslope scale, intact rock strength and the density, orientation, and spatial distribution of discontinuities combine to control rock mass strength (Douglas *et al.*, 1991; Coe and Harp, 2007; Stead and Wolter, 2015). These physical characteristics, which are intrinsic (and elsewhere termed 'resisting') to the rock mass, are often conceptualised as resisting or inhibiting rock slope failure (Gunzberger *et al.*, 2005; Gischig *et al.*, 2016) and are constantly in transition as extrinsic (erosional, or 'driving') processes act upon the rock. These processes include thermal stresses (Collins and Stock, 2016), (chemical) weathering (Viles, 2013), seismic loading (Parker *et al.*, 2015), and, on coastal cliffs, wave impacting (Lim *et al.*, 2011). However, determining the relative importance of intrinsic versus extrinsic controls on mass wasting processes, and the resulting erosion that they accumulate, remains difficult, particularly across different spatial and temporal scales. Although mass wasting processes have been monitored extensively in a variety of settings, high-resolution observations of rock slope erosion on a regional scale ($> 10^4$ m) are scarce. This is primarily due to difficulties in capturing data in a way that ensures a volumetrically complete inventory, and at length scales over which both resisting and driving stresses may vary. This restricts our ability to assess how rock slopes respond to changes in structural and environmental conditions, both at present and in the future.

This thesis seeks to address these challenges by attempting to relate regional-scale variations in cliff erosion, primarily via rockfalls, to a set of well-constrained controls. The aim of this research is to provide a unique understanding of why rockfalls occur where they do, and to establish the relative importance of resisting (intrinsic) and driving (extrinsic) forces on erosion. This requires the ability to make a step-change in our understanding of changes in rock slope morphology, shifting the focus towards the regional scale (10^3 – 10^4 m) while retaining the high

resolution and precision of existing terrestrial monitoring practices ($< 10^{-2}$ m) and allowing variability in drivers to be considered at scales previously not possible. Addressing this issue requires the development of novel workflows, from data collection to analysis, and a site that enables the effects of these controls to be isolated. The approaches developed in this thesis are applied to the coastal cliffs of North Yorkshire, UK. The physiographic setting of these cliffs, where rock type, precipitation regime, and weathering environment are approximately consistent along their length, enables an assessment of variations in rock mass structure and the assailing forces of waves that drive rockfall, all within *ca.* 24 km of coastline.

1.1 Rationale

Rockfalls exert a first-order control on the rate of rock wall retreat on mountain slopes and on rock cliffs (Moore *et al.*, 2009). They are a frequent process initiated when rock blocks become detached from a rock mass under the influence of gravity (Selby, 1982). Their volumes typically range from *ca.* $10^{-2} - 10^{2}$ m^3, but in some cases they have been known to reach 10^{5} m^3 (for example, Wieczorek *et al.*, 1998; Stock *et al.*, 2012a). Rockfall activity is also a chronic hazard (Evans and Hungr, 1993; Guzzetti *et al.*, 2003; Wieczorek *et al.*, 2008), often posing significant risks to transportation corridors (Guzzetti *et al.*, 2004; Katz *et al.*, 2011; Blais-Stevens *et al.*, 2012; Michoud *et al.*, 2012; Ansari *et al.*, 2014), pipelines (Blais-Stevens *et al.*, 2010; Couture *et al.*, 2010), and to areas beneath (sea) cliffs (Dewez *et al.*, 2013; Marques *et al.*, 2013). Rockfall activity has been monitored extensively in these settings, and in some cases this monitoring has been used to provide hazard and risk forecasting (Collins and Stock, 2012; Stock *et al.*, 2012a; Royán *et al.*, 2013).

Rock slope evolution is not uniquely governed by large, infrequent events, but it instead reflects a continuum of change where failures can also be small in magnitude and variable in frequency over large areas (Lim *et al.*, 2010). While the smallest events have been observed to occur at high frequencies, often resulting in near-continuous mass wasting and therefore representing a chronic hazard in some areas, the scars and debris of catastrophic events tend to reside in the landscape for longer, controlling long-term rates of landform and landscape evolution (Hovius and Stark, 2006). However, much of the existing research undertaken has made use of datasets covering relatively short extents (cliffs *ca.* $10^{1} - 10^{2}$ m in width), often defined by monitoring instrument capabilities and logistics rather than by any scientific rationale. The consequences of this are that (1) data captured at a single site are likely to reflect and potentially be dominated by site-specific conditions, and therefore remain difficult to extrapolate, (2) the effects of gradual, long wavelength ($> 10^{2}$ m) changes in resisting versus driving stresses cannot be observed at a local scale, and (3) establishing a direct cause-effect relationship from the high levels of inherent noise in rockfall observations remains challenging. To address these challenges, an idealised study might consider variations in the occurrence of and controls upon rockfalls

observed along a valley (for example, Strunden *et al.*, 2015), on a coastline that changes in aspect (for example, Matsumoto *et al.*, 2017), or across a climatic gradient (for example, Dietze *et al.*, 2017). There is a similar need for this knowledge in an applied context; for example, in assessing rockfall risk to transportation corridors, which requires an extensive but detailed approach (for example, Lato *et al.*, 2009a).

The following discussion reviews the challenges associated with monitoring regional-scale variations in rockfall activity and the resulting cliff erosion (*Section 1.1.1*), with particular emphasis on the processes occurring at coastal cliffs (*Section 1.1.2*). The current state of knowledge on the implications of these processes for the spatio-temporal distribution of rockfalls is also outlined (*Section 1.1.3*). The discussion explores the context and justification for understanding what drives regional-scale variations in rockfall activity, and is used to define the research aim, questions, and objectives identified in *Section 1.2*. The thesis structure is then outlined in *Section 1.3*.

1.1.1 Monitoring regional-scale variations in rockfall activity

Initial methods used to measure rates of rock wall retreat and rockfall supply include acoustic observations and subsequent estimations of rockfall size (Gardner, 1970, 1980), painted rock walls (Matsuoka, 1990; Matsuoka and Sakai, 1999), and rockfall nets (Krautblatter, 2003; for a comprehensive review, see Krautblatter and Dikau, 2007). Recently, significant advances in our ability to detect changes to rock slopes and to quantify the resultant retreat have come from the use of ground-based LiDAR and Structure-from-Motion photogrammetry (Metternicht *et al.*, 2005). These techniques have become increasingly widespread owing to their ability to rapidly acquire dense point clouds that can be used to derive 3D slope geometry on vertical rock walls (for example, Rosser *et al.*, 2005a; Abellán *et al.*, 2009; Royán *et al.*, 2013). However, monitoring rockfall activity at length scales over which both resisting (for example, rock mass strength and structure) and driving (erosional) factors also vary requires upscaling from the ground-based monitoring campaigns typically undertaken on a single rock slope to extents $> 10^3$ m.

Upscaling detailed monitoring of rock slopes is difficult, both in terms of capturing and processing data, as the topographic complexity of the area monitored inevitably increases with scale. This can mean moving from a single, near-planar rock face to a more complex series of hillslopes with variable lithology, geometry, and structure. Upscaling is, therefore, very rarely a case of applying local approaches more extensively. Similarly, increasing the likelihood of capturing a large event by prolonging the period of monitoring can be prohibitively costly, and, where monitoring intervals do increase, the data captured are inevitably subject to rockfall coalescence and superimposition, which decreases the likelihood of detecting small events (Williams *et al.*, 2018). Whether or not ergodic reasoning (space-for-time substitution) can be applied also remains to be tested. This has implications for our understanding of rock slope failure. A fundamental

uncertainty, for example, is whether monitoring 1.0 km^2 of cliff face over 1 year would generate a rockfall inventory that is statistically comparable to that captured from 0.1 km^2 over 10 years, from a set of apparently uniform cliffs. This is unlikely where the timescales of path-dependent behaviour in rockfall evolution, via brittle fracture growth (Kemeny, 2003) and progressive failure (Stock *et al.*, 2012b), and over longer time scales via changes to slope-profile form and/or post-glacial or post-incision relaxation (Cordes *et al.*, 2013; Messenzehl *et al.*, 2017), are commensurate with or exceed those of most monitoring campaigns.

As with many other natural hazards, inventories of rockfall activity have revealed that event volumes adhere to power law magnitude-frequency relations that hold over several orders of magnitude (Malamud *et al.*, 2004; Guthrie and Evans, 2007). A considerable body of research has been published on magnitude-frequency distributions and their application to quantifying the cumulative yield of rockfalls on montane, alpine, and arctic rock walls (Dussauge-Peisser *et al.*, 2002; Malamud *et al.*, 2004; Santana *et al.*, 2012; Messenzehl and Dikau, 2017), along transport corridors (Bunce *et al.*, 1997; Hungr *et al.*, 1999; van Veen *et al.*, 2017), and on sea cliffs (Dong and Guzzetti, 2005; Teixeira, 2006; Rosser *et al.*, 2007; Marques, 2008; Lim *et al.*, 2010; Young *et al.*, 2011; Barlow *et al.*, 2012; Rohmer and Dewez, 2013; Kuhn and Prüfer, 2014; Williams *et al.*, 2018). One empirical/statistical approach to compensate for the difficulty in capturing regional-scale observations is to use the power law behaviour in rockfall magnitude and frequency to upscale, in both time and space, and model future rockfalls and hence cliff erosion, assuming that what is monitored at a small scale is more widely representative (Lim *et al.*, 2010). These approaches have inherent assumptions and limitations that restrict their application, including (1) that they rely on extrapolating a non-biased, assumed complete portion of an inventory to predict both larger and smaller volume frequencies, (2) the need to apply power laws within limits, in order to avoid generating biased scaling coefficients (Barlow *et al.*, 2012), (3) the implicit assumption that a single underlying mechanism, and hence a single form of power law behaviour, transcends all scales of events under investigation (Brunetti *et al.*, 2009), and that extrinsic controls are essentially constant, and (4) that all rockfalls in an inventory are statistically independent of one another, although it is known that rockfalls exhibit some degree of spatial and/or temporal path-dependency (Rohmer and Dewez, 2015). Fundamentally, this approach loses any site specificity, generating only broad rockfall magnitude probabilities rather than an estimation of what could or will happen at an individual location.

An increasingly viable alternative, enabled by rapid advances in (mobile) 3D data capture on near-vertical surfaces, is to monitor rockfalls over a larger area while retaining a high spatial resolution (Lato *et al.*, 2009a). To achieve this, some airborne LiDAR systems have the capability to collect data from oblique as well as vertical view angles, permitting the capture of point cloud data both on near-vertical surfaces and over much larger extents. However, the volume and quality of data that can be collected using airborne LiDAR present their own unique challenges. Such

data require methods that are able to retain the 3D character of the data while also being able to measure rockfall volumes that can span over $6 - 7$ orders of magnitude, and over spatial extents that can exceed *ca.* 10^6 m^2. These settings could include, but are not limited to, a length of coastline, cut slopes along a transport corridor, or a full valley-side escarpment. However, at present there exists no workflow optimised for detecting wide-area rock slope adjustment while retaining point cloud data in their original 3D form. The ability to monitor at length scales over which both resisting and driving controls on rockfall activity may also vary is therefore crucial to further our understanding of rock slope behaviour.

1.1.2 Coastal cliffs under wave loading

Along hard rock cliffs, which are the focus of this thesis and front over three-quarters of the world's coastlines (Bird, 2000), rising global sea-level in conjunction with projected changes in winds, tides, precipitation, storm events, and wave climate has been projected to accelerate coastal cliff retreat and threaten populations (IPCC, 2013). The result is a pressing need to understand and model the erosional response of hard rock coastlines to these processes (Trenhaile, 2011). While there has been a growing interest in hard rock coasts over the past decade, much of the recent research has used case-specific approaches that infer a wider morphological model of the evolution of cliff and platform systems from only a limited selection of sites (Kennedy *et al.*, 2017). These methodological shortcomings, as well as those detailed above, have limited the development of predictive models that can be used for assessing the evolution of coastal rock slopes under a changing climate (Castedo *et al.*, 2012), with many models remaining limited to a stochastic representation of cliff behaviour. These are often based on assumptions regarding the magnitude and frequency of rockfalls in a probabilistic framework (for example, Lee *et al.*, 2001; Hall *et al.*, 2002; Williams *et al.*, 2004; Drake and Phipps, 2007; Walkden and Hall, 2005, 2011), with limited reference to the role and interplay between intrinsic and extrinsic controls on change. In the context of this thesis, rocky coastlines offer the ideal physiography for investigating the relative importance of these controls on rockfall occurrence: many coastlines, such as that studied here, are actively eroding, with aggressive weathering and marine conditions combining to drive high rates of erosion via rockfall. Periodic straining of the rock mass by wave loading often varies considerably along shore due to variable coastal geometry and bathymetry: this variability in wave loading, combined with varying lithology and structure, should permit the constraint of the nature of rockfall occurrence beyond that observed on a single slope. The following discussion explores why these sites are ideal for exploring the underlying aims of this thesis, and why insights gained from studying coastal cliffs may hold implications for (non-coastal) rock slopes more widely.

One means of examining marine controls on coastal erosion is to examine the ground motions generated by ocean waves. Recent research has demonstrated that coastal cliff ground motions are reliable proxies for a number of environmental drivers that influence wave energy

delivery to the cliff face, including coastal geometry and foreshore bathymetry (Young *et al.*, 2011, 2012, 2013, 2016; Dickson and Pentney, 2012; Norman *et al.*, 2013; Earlie *et al.*, 2015; Vann Jones *et al.*, 2015). These measurements of coastal cliff ground motion can be used to inform investigations into incremental damage and, therefore, cliff erosion (Adams *et al.*, 2002, 2005; Brain *et al.*, 2014). Along coastal cliffs, the repeated loading and unloading cycles delivered to the cliff face by wave activity involve variations in the magnitude of the dynamic stresses, their amplitude relative to baseline stress conditions, and their orientation relative to existing fracture sets and ground surface topography (Zhang and Sanderson, 2001). Critical stressing of a rock mass can be achieved under cyclic loading, provided that the applied stress amplitude is sufficiently high relative to the ultimate intact failure stress (Attewell and Farmer, 1973). When considering progressive failure, smaller, more iterative events relative to this baseline stress are important. A number of studies have investigated brittle fracture initiation and coalescence in rock samples subjected to regular patterns or sequences of cyclic loading and random patterns of loading. It is well known that load interaction and sequencing effects can have a significant influence on the fatigue crack growth rate and, consequently, fatigue life (Skorupa, 1999). Experimental results from random amplitude cyclic testing of steel bridge piers attest to this effect, showing that a sudden increase or decrease in displacement amplitude can result in a rapid increase in cumulative damage (Ge and Kang, 2014). This effect has also been observed in cliff-top microseismic datasets, where periods of relatively low amplitude microseismic ground motion are often interrupted by periods of greater displacement during energetic storm events (Adams *et al.,* 2005; Brain *et al.*, 2014). During these events, higher amplitude displacements are thought to cause more damage to the rock mass, extending microcracks beyond conditions achievable by low amplitude background displacements.

The cumulative effect of this (micro)seismicity has been suggested to play a crucial role in reducing rock slope stability by allowing macro-scale rock fracture to occur at values that are considerably less than the peak strength of intact rocks (Stead and Wolter, 2015). Evidence of this effect can be seen in the field, where some rock slopes remain intact during large seismic events despite experiencing a similar stress state to those that collapse, implying that the rock mass must accrue a sufficient amount of damage to instigate final collapse (Parker *et al.*, 2013). If this is the case, then cyclic fatigue of coastal cliffs via wave impacting could hold important implications for the timing and spatial distribution of coastal change (Brain *et al.*, 2014), and for how iterative damage accumulation influences landscape evolution more generally. However, the relative importance of the various components of cyclic loading (magnitude, frequency, and direction) in preparing rock slopes for failure is difficult to constrain, particularly in coastal landscapes, which are inherently noisy and subject to a wide range of conditions. This is, in part, due to the complexity of factors that control the dynamic response of potentially unstable rock slopes. However, there is also a lack of instrumental observations of slope-specific ground motion,

which can be useful in providing a constraint on laboratory testing and slope dynamic behaviour modelling. Although short-term seismic monitoring has been attempted on some unstable rock slopes, these experiments have encountered difficulties in recording enough events with sufficiently differentiated properties for inferring general characteristics of rock slope behaviour under seismic shaking (Gaudio and Wasowski, 2011).

1.1.3 Spatio-temporal distribution of rockfalls

Rock slope stability is controlled by the mechanical properties and stress state of the rock mass as well as the effectiveness of environmental forcing (Moore *et al.*, 2009). On rock slopes, numerical modelling suggests that critical levels of stress propagate along a spatially concentrated failure surface that is relatively close to the rock face, and that shear stresses along this surface reduce significantly with depth from the fracture surface (Wolters and Müller, 2008; Styles *et al.*, 2011). A similar effect can be observed along major tectonic faults (Mitchell and Faulkner, 2008). Brain *et al.* (2014) suggest that this spatial pattern of *in situ* stresses results in a strong spatial pattern in the effectiveness of (micro)seismic ground motions in propagating and connecting microcrack populations. On coastlines, the opportunity for cyclic loading to cause damage and weakening through propagation and coalescence of microcracks is likely to be spatially and temporally restricted. However, determining the exact effects of these motions on rockfall activity and the resulting cliff erosion remains difficult.

High-resolution monitoring of progressive collapses has given a considerable insight into the rates and patterns of failure propagation on rock slopes. Stock *et al.* (2012b) considered a sequence of 14 progressive rockfall events that occurred over 15 months, highlighting the importance of stress redistribution from preceding rockfalls in conditioning subsequent instability in adjoining areas over time. Similarly, Rohmer and Dewez (2015) applied spatial statistics to several thousand rockfall scars, inferring that progressive incremental failure is manifest as small rockfall events (10^{-3} – 10^{-2} m^3) that aggregate in clusters across the cliff face. On coastal cliffs, the propagation of rockfalls has been observed to facilitate the transmission of marine loading up the cliff face over time (Rosser *et al.*, 2013). These observations are supported by numerical modelling of the response of the rock mass to marine loading, which confirms the role of upward migration of shear strain through the cliff in inducing tensile failure and crack growth at the cliff top (Styles *et al.*, 2011). The connectivity between events attests to the importance of stress redistribution following previous rockfalls in promoting damage accumulation and, eventually, further rock slope failure (Amitrano, 2006). However, the response of rock slopes to different preparatory and triggering conditions remains poorly understood (Krautblatter *et al.*, 2012). If rock slope evolution is driven by progressive failure, which is the product of iterative and then runaway microcracking, progressive damaging of the rock mass could explain the poor correlations between rockfall activity and energetic environmental conditions (Vann Jones *et al.*, 2015).

1.2 Research aim, questions, and objectives

The aim of this research is to use high-resolution field monitoring techniques, deployed at regional scales ($> 10^4$ m), in order *to understand how regional-scale variations in cliff structure and wave loading interact to condition variations in rockfall activity.* A series of research questions has been designed in order to achieve this aim:

RQ1. *How do rockfalls and the resulting cliff erosion vary over regional scales?*

RQ2. *To what extent does rock slope structure drive spatial variations in rockfall activity?*

RQ3. *Do spatial variations in cliff erosion reflect variations in wave loading conditions?*

RQ4. *What is the relative importance of cliff structure and wave loading in determining rates of erosion, and is there an optimal scenario of conditions that drives high rates of erosion?*

An outline of the theoretical framework for this research is presented in Figure 1.01. A number of requirements must be fulfilled in order to address the above research questions, and these requirements are addressed in the following research objectives:

RO1. To identify a field site where both structure and wave loading vary, and rockfalls are frequent (*Chapter 2*).

RO2. To develop a workflow for detecting and characterising rockfalls across multiple scales (*Chapter 3*).

RO3. To use this workflow to produce a quantitative estimate of multi-temporal, regional-scale variations in rockfall magnitude, frequency, and the resulting cliff erosion, taking into account patterns in both cliff profile- and plan-form (*Chapter 3*).

RO4. To derive a quantitative appraisal of spatial variations in the geometric properties of exposed discontinuity surfaces, and to assess the extent to which these drive patterns in the size and shape of rockfalls (*Chapter 4*).

RO5. To use high-resolution field monitoring in order to quantify local (10^1 – 10^2 m) variations in wave loading characteristics at a representative site, and to relate these variations to morphological and environmental conditions (*Chapter 5*).

RO6. To establish the relative importance of intrinsic versus extrinsic controls on coastal cliff change behaviour by synthesising the findings of this thesis (*Chapter 6*).

1.3 Thesis structure

The methodological focus of this thesis is to develop novel workflows for undertaking regional-scale ($> 10^4$ m) assessments of rockfall activity at previously unprecedented resolutions (10^{-1} m). Uniquely, this thesis seeks to relate rockfall activity to along-coast variations in structural and morphological controls, upscaling previous work undertaken at the local scale (10^1 – 10^2 m)

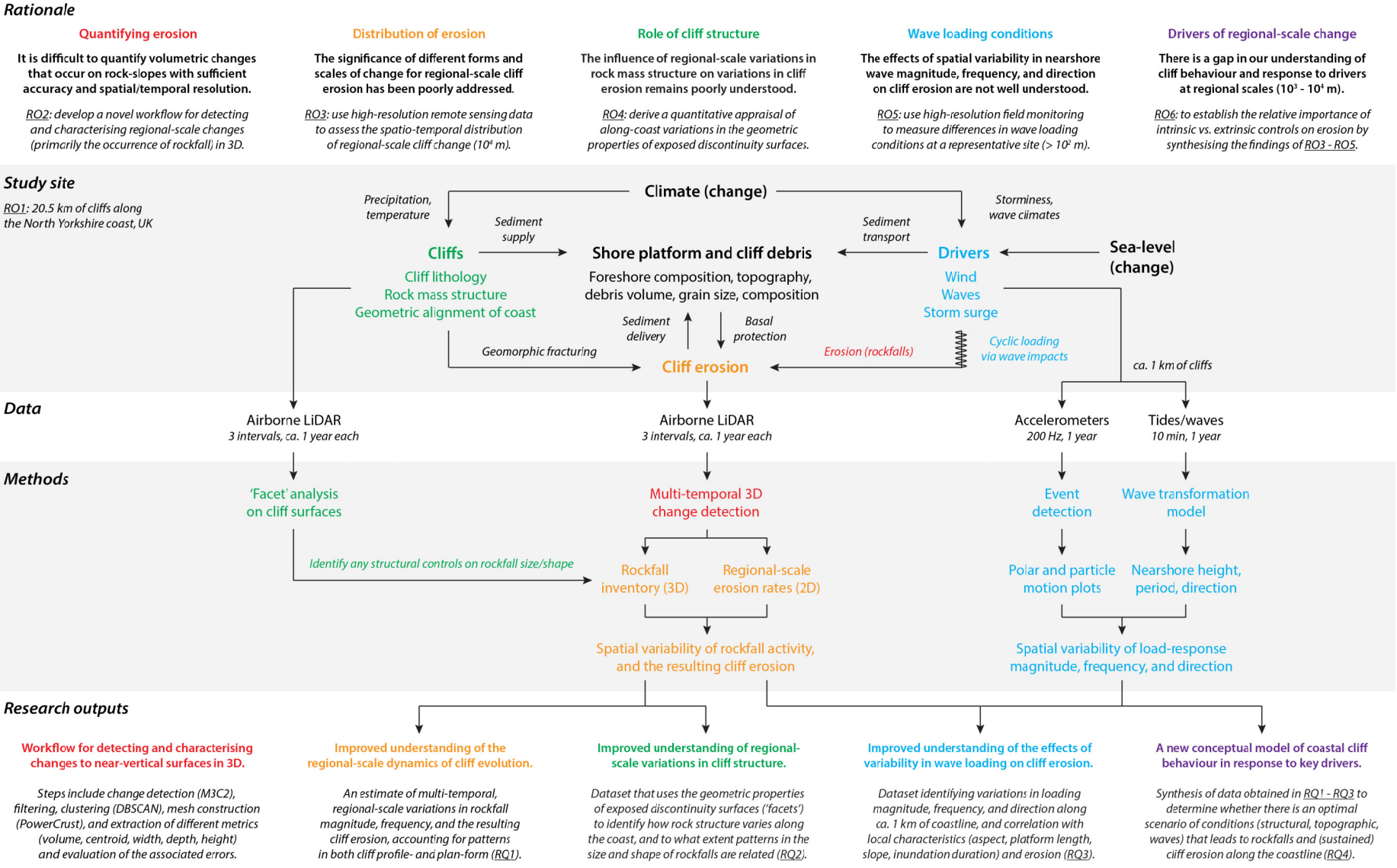
Rationale
Quantifying erosion
It is difficult to quantify volumetric changes that occur on rock-slopes with sufficient accuracy and spatial/temporal resolution.
RO2: develop a novel workflow for detecting and characterising regional-scale changes (primarily the occurrence of rockfall) in 3D.
Distribution of erosion
The significance of different forms and scales of change for regional-scale cliff erosion has been poorly addressed.
RO3: use high-resolution remote sensing data to assess the spatio-temporal distribution of regional-scale cliff change (10⁴ m).
Role of cliff structure
The influence of regional-scale variations in rock mass structure on variations in cliff erosion remains poorly understood.
RO4: derive a quantitative appraisal of along-coast variations in the geometric properties of exposed discontinuity surfaces.
Wave loading conditions
The effects of spatial variability in nearshore wave magnitude, frequency, and direction on cliff erosion are not well understood.
RO5: use high-resolution field monitoring to measure differences in wave loading conditions at a representative site (> 10² m).
Drivers of regional-scale change
There is a gap in our understanding of cliff behaviour and response to drivers at regional scales (10³ - 10⁴ m).
RO6: to establish the relative importance of intrinsic vs. extrinsic controls on erosion by synthesising the findings of RO3 - RO5.
Study site
RO1: 20.5 km of cliffs along the North Yorkshire coast, UK
Climate (change)
Precipitation, temperature
Storminess, wave climates
Sediment supply
Sediment transport
Cliffs
Cliff lithology
Rock mass structure
Geometric alignment of coast
Shore platform and cliff debris
Foreshore composition, topography, debris volume, grain size, composition
Drivers
Wind
Waves
Storm surge
Sea-level (change)
Sediment delivery
Basal protection
Geomorphic fracturing
Cliff erosion
Erosion (rockfalls)
Cyclic loading via wave impacts
ca. 1 km of cliffs
Data
Airborne LiDAR
3 intervals, ca. 1 year each
Airborne LiDAR
3 intervals, ca. 1 year each
Accelerometers
200 Hz, 1 year
Tides/waves
10 min, 1 year
Methods
'Facet' analysis on cliff surfaces
Multi-temporal 3D change detection
Event detection
Wave transformation model
Identify any structural controls on rockfall size/shape
Rockfall inventory (3D)
Regional-scale erosion rates (2D)
Polar and particle motion plots
Nearshore height, period, direction
Spatial variability of rockfall activity, and the resulting cliff erosion
Spatial variability of load-response magnitude, frequency, and direction
Research outputs
Workflow for detecting and characterising changes to near-vertical surfaces in 3D.
Steps include change detection (M3C2), filtering, clustering (DBSCAN), mesh construction (PowerCrust), and extraction of different metrics (volume, centroid, width, depth, height) and evaluation of the associated errors.
Improved understanding of the regional-scale dynamics of cliff evolution.
An estimate of multi-temporal, regional-scale variations in rockfall magnitude, frequency, and the resulting cliff erosion, accounting for patterns in both cliff profile- and plan-form (RQ1).
Improved understanding of regional-scale variations in cliff structure.
Dataset that uses the geometric properties of exposed discontinuity surfaces ('facets') to identify how rock structure varies along the coast, and to what extent patterns in the size and shape of rockfalls are related (RQ2).
Improved understanding of the effects of variability in wave loading on cliff erosion.
Dataset identifying variations in loading magnitude, frequency, and direction along ca. 1 km of coastline, and correlation with local characteristics (aspect, platform length, slope, inundation duration) and erosion (RQ3).
A new conceptual model of coastal cliff behaviour in response to key drivers.
Synthesis of data obtained in RQ1 - RQ3 to determine whether there is an optimal scenario of conditions (structural, topographic, waves) that leads to rockfalls and (sustained) cliff erosion along the coastline (RQ4).

Figure 1.01 *Overleaf. An outline of the theoretical framework for this research with respect to the research questions and objectives (Section 1.2).*

and therefore marking a step-change in our understanding of (the drivers of) changes in rock slope morphology. The thesis comprises six chapters following the Introduction. Each of the results chapters (*Chapters 3*, *4*, and *5*) are presented in a self-contained style with an introduction and brief review of the relevant literature, description of the methods used, and presentation of results.

Chapter 2 provides an overview of the field site, which comprises *ca.* 20.5 km of coastal rock cliffs in North Yorkshire, UK. The overview describes the stratigraphic succession of the surrounding Cleveland Basin, before discussing the prevailing environmental conditions, including climate, wave climate, and tidal regime. The history of monitoring in the area is outlined, with particular emphasis on recent research into rockfall activity between Boulby and Staithes. This area constitutes an important case study in *Chapter 5*.

Chapter 3 presents a novel workflow for detecting and characterising multi-scale changes in rock slope morphology via rockfalls in 3D. The work presented in this chapter draws on high-density point clouds derived from uniquely high-resolution, multi-temporal airborne LiDAR surveys to monitor regional-scale variations in rockfall activity along the North Yorkshire coast. Using the resulting inventory of rockfall activity, this chapter explores regional-scale variations in rockfall magnitude, frequency, and the resulting erosion along the North Yorkshire coast.

Chapter 4 presents the methods used to derive a detailed, quantitative appraisal of regional-scale variations in rock mass structure. This involves using the point clouds obtained in *Chapter 3* to derive the geometric properties of exposed discontinuity surfaces ('facets'), which are used in this study as a proxy for rock mass structure. The analyses presented in this chapter explore how rock mass structure varies, here along the coastline, and to what extent patterns in the size and shape of rockfalls are related to the differences in rock mass structure identified.

Chapter 5 presents the results of a yearlong monitoring campaign, which aimed to identify relative variations in the ground motion response to wave impacting along a *ca.* 900 m stretch of cliffs. The findings constitute some of the first concurrent observations of along shore variations in wave impact-driven ground motions on coastal cliffs. The chapter explores how wave loading characteristics vary along the coastline, how these are related to morphological controls, and the implications of these for driving spatial variations in erosion, which were quantified in *Chapter 3*.

Chapter 6 synthesises the results presented in *Chapters 3*, *4*, and *5*, in the development of a new, semi-empirical analysis of coastal cliff change behaviour. The implications of these results for monitoring rockfall activity, and for understanding its drivers on (coastal) cliffs, are discussed.

Chapter 7 summarises the major findings of this work in relation to the research questions outlined in *Section 1.2*. The chapter concludes with a discussion of directions for future research based on the findings of this study.

Chapter 2

Study site

The discussion presented in *Chapter 1* demonstrates the importance of monitoring at length scales over which both intrinsic (rock mass strength and structure) and extrinsic (erosional) processes on rockfall activity may vary. A regional-scale field site that is suited to addressing some of the complexities discussed is presented in this chapter, where (1) there are long wavelength ($> 10^3$ m) changes in lithology and structure, (2) the cliffs are exposed to a range of wave loading (erosional) conditions, and (3) there is a high rate of rockfall activity. The latter allows an investigation into the influence of (1) and (2) on rock slope failure. This chapter introduces the study site (*Section 2.1*) and provides an overview of the statigraphic succession of the surrounding Cleveland Basin. The implications of the regional geology for the evolution of coastal cliffs in the area are then discussed, in addition to the prevailing environmental conditions, including climate, wave climate, and tidal regime. The history of research in this area is outlined with particular emphasis on recent monitoring of rockfall activity between Boulby and Staithes (*Section 2.2*). This constitutes an important case study later in this research, with the directions of this research summarised in *Section 2.3*.

2.1 Regional setting

The highest coastal rock slopes in England, and some of the highest in the UK, are found along the North Yorkshire coast (Figure 2.01). The cliffs reach heights of over 150 m and are cut into near-horizontally interbedded Lower Jurassic mudstones, shales, siltstones, limestones, and sandstones, which are often capped by silty glacial tills (Rawson and Wright, 2000). The cliff surfaces are weathered, with dilated joints and face-parallel fractures (Rosser *et al.*, 2013). Much of the coastline is fringed by a gently sloping (*ca.* 2°) foreshore platform that extends up to 300 m seaward of the cliff toe. This is partially exposed at low tide, and fully exposed when high atmospheric pressure systems coincide with the lowest astronomical tides and calm conditions.

The cliffs have been extensively monitored, providing a baseline dataset on erosion rates, rockfall inventories, nearshore wave conditions, and patterns of energy delivery along the coastline (Agar, 1960; Robinson, 1974; Lim *et al.*, 2005, 2010; Rosser *et al.*, 2005a, 2005b, 2013; Lim, 2006; Barlow *et al.*, 2012; Norman, 2012; Norman *et al.*, 2013; Brain *et al.*, 2014; Vann Jones *et al.*, 2015).

2.1.1 Location and geology

The Jurassic and Cretaceous rocks that were deposited in the Cleveland Basin and on the adjacent northern margin of the East Midlands Shelf can be seen in a series of exposures along the North Yorkshire coast (Rawson and Wright, 2000). Along much of the coastline, Quaternary drift deposits of boulder clays (tills) overlie Jurassic deposits of interbedded mudstones, shales,

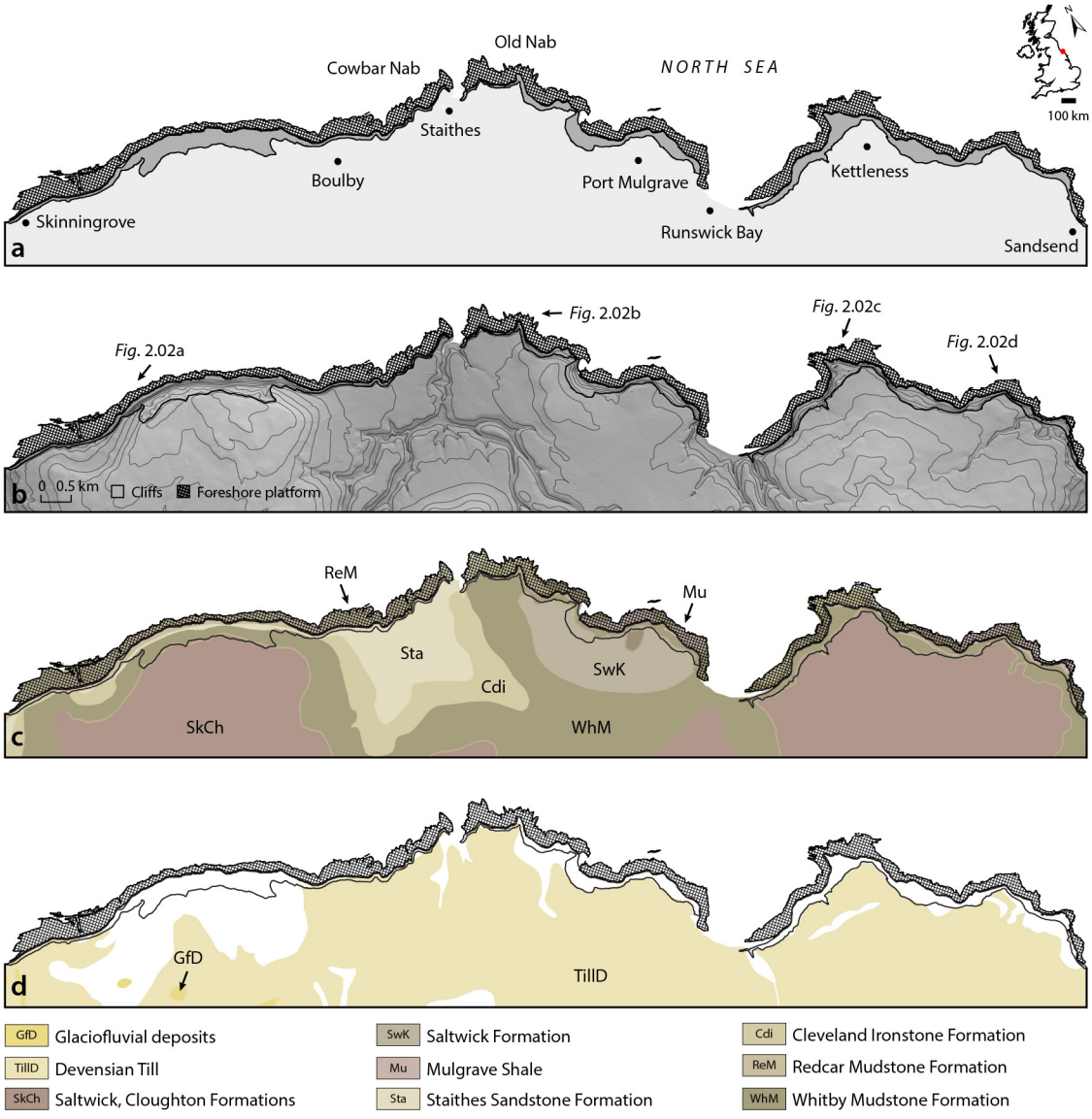

Figure 2.01 *(a) Map of the North Yorkshire coast. The total length of cliff face monitored is approximately 20.5 km, (b) topographical map, with contours at 20 m intervals, (c) bedrock geology, and (d) superficial geology. Maps produced using shapefiles from the Ordnance Survey © Crown Copyright and Database Right 2017. Ordnance Survey (Digimap Licence).*

siltstones, limestones, and sandstones (Figure 2.02). The tills, which were deposited following the last (Devensian) glaciation, form composite sheets containing erratic pebbles and boulders derived from sources as distant as the Lake District (north west England), Scotland, and Scandinavia, in addition to some local materials (Rawson and Wright, 2000). During the Middle Jurassic, sedimentation in the Cleveland Basin was characterised by marine transgressions that advanced in a north-westerly direction due to tilting of the Mid North Sea High in response to doming (Powell, 2010). Basin uplift accompanied by gentle folding in the late Toarcian to the early Aalenian removed much of the late Toarcian succession, such that the Dogger Formation now rests unconformably on beds as low as the Alum Shales over much of the basin (Figure 2.03; Hemingway, 1974). The Jurassic sequences along the North Yorkshire coast therefore rise and fall, producing a coastline characterised by crenulous coves and headlands formed of solid outcrops separated by embayments, such as Runswick Bay, which are formed where the glacial tills outcrop at sea level. In places, these headlands rise up to form cliffs exceeding 150 m, such as the cliffs at Boulby, while embayments are characterised by sandy beaches backed by low cliffs (< 10 m). Given the alongshore variability in the exposed stratigraphy, photographs are provided alongside all of the site-specific analyses presented in *Chapters 3 – 5*.

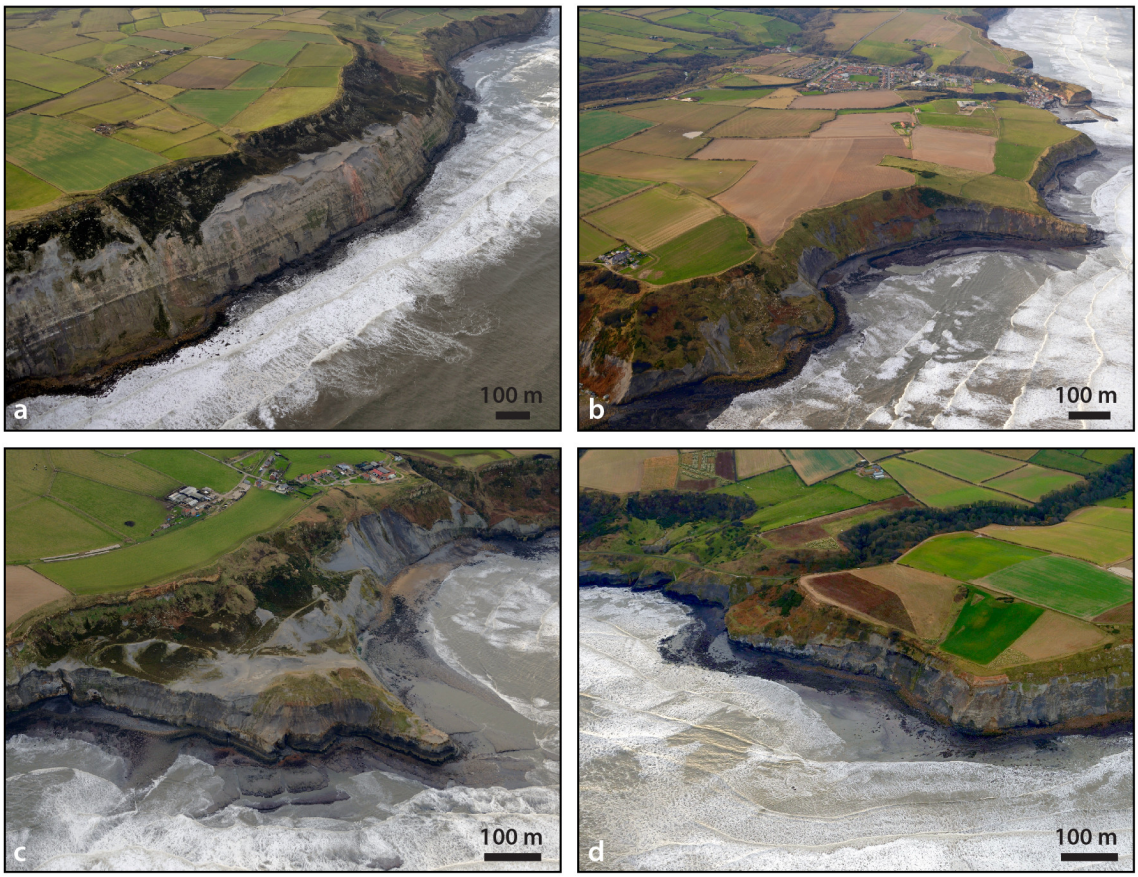

Figure 2.02 *Aerial photos of four sites along the North Yorkshire coast, including the cliffs at (a) Boulby, (b) Old Nab (foreground) and Staithes (background), (c) Kettleness, and (d) Sandsend. Locations are shown in Figure 2.01b. The height of these cliffs above the foreshore platform varies between 20 m (Sandsend) and 150 m (Boulby).*

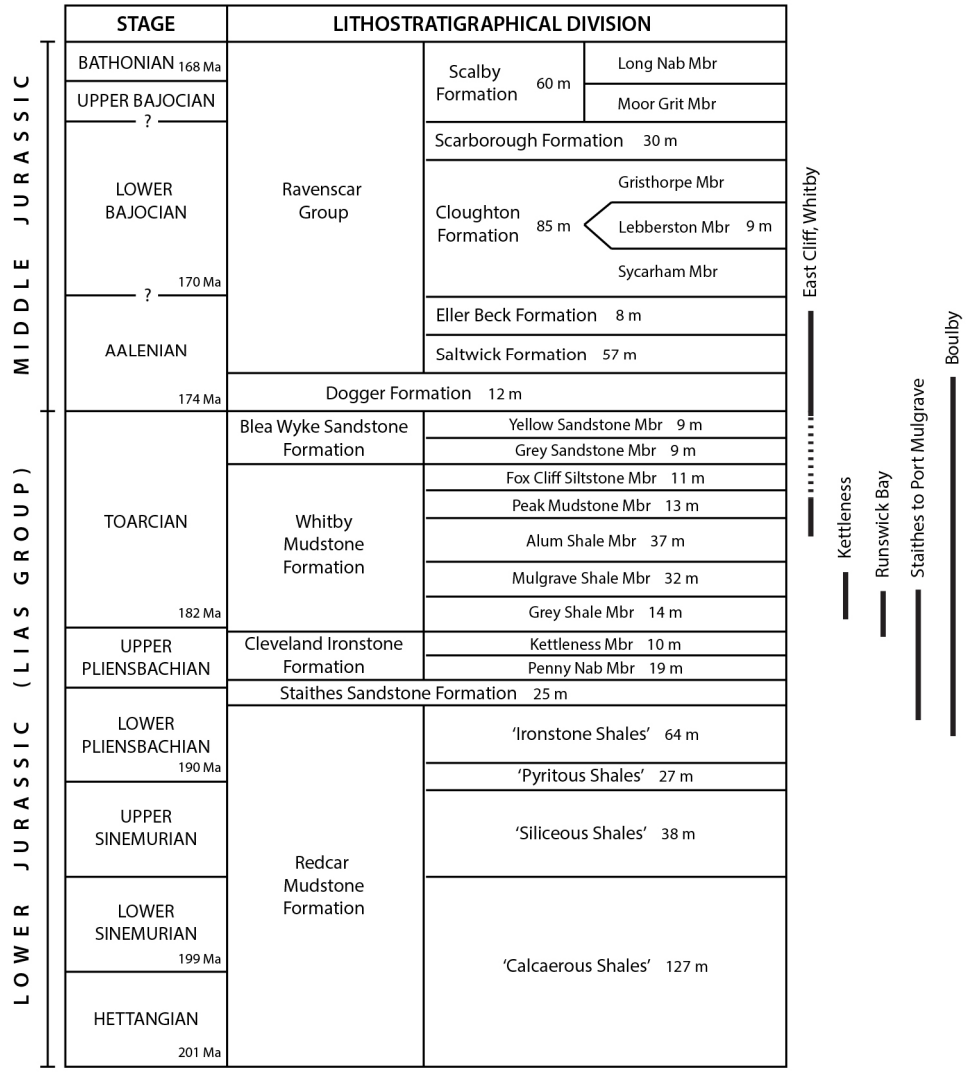

Figure 2.03 *Subdivision of the Lower Jurassic (Hettangian-Toarcian) and Middle Jurassic (Aalenian-Bathonian) sequences in the Cleveland Basin, with approximate stratigraphical ranges indicated for sites named in Figure 2.01, as well as East Cliff, Whitby. Adapted from Rawson and Wright (2000, p. 4).*

2.1.2 Wave climate and tidal regime

The North Yorkshire coast is macro-tidal, experiencing two daily tides that cycle between spring and neap highs over a range of *ca.* 6 m (Figure 2.04a). The bases of the cliffs are often submerged during high spring tides, in places up to a depth of 3 m. When high spring tides coincide with storm events and high swells, the vertical reach of the tide can exceed 4.3 m (Rosser *et al.*, 2013). Over the monitoring period of this study (August 2014 – September 2017), the maximum wave height recorded by the Datawell Directional WaveRider (Mk III) buoy, located 5 km east of Sandsend, was 10.8 m in the winter storms of November 2016 (Figure 2.04b). Wave fetch at the site is limited in most directions by the boundary coasts of the North Sea. Winds from the north and northeast have the longest fetch, *ca.* 860 km, and often result in the largest waves, although their impact is dependent upon local factors, including cliff aspect and bathymetry (Trenhaile, 2002). The wave climate is dominated by mixed wind and swell wave conditions, which can be

inferred from their statistical properties, including significant wave height and peak wave period (Figure 2.04c). Significant wave height represents the mean height of the highest third of waves, from trough to crest, while peak wave period represents the wave period associated with the peak of the wave energy spectrum. Wave regimes that are dominated by wind waves tend to have shorter peak wave periods, and regimes dominated by swell tend to have longer wave periods (Schwartz, 2005). The wave buoy recorded a mean peak wave period of *ca.* 4.8 s between August 2014 and September 2017 (Figure 2.04c). Over this period, conditions varied from low-energy pure swell, mixed swell-sea, to strongly wind-forced conditions. This macro-tidal, storm-dominated setting generates highly variable conditions at the cliff face, both over a single semi-diurnal tidal cycle and between seasons. Trends toward higher storm surge levels have recently been reported for the North Sea (Woth *et al.*, 2006; Vousdoukas *et al.*, 2016), renewing the need to understand the links between wave impacting, regional geology, and cliff erosion.

2.1.3 Climate

The marine climate of the North Sea is dominated by pronounced seasonal variations in wind velocities and directions, much of which is associated with pressure anomalies that arise from the North Atlantic Oscillation (NAO; Woolf *et al.*, 2002). The winter months (December – February) are characteristically colder and marginally wetter than the summer months (June – August), with daily mean minimum air temperatures of 3.2°C experienced in January, based on records taken at the Whitby weather station located 15 km south east of Sandsend (Figure 2.04d). Air temperatures are partially moderated by the coastal setting, seldom yielding conditions below freezing for more than several hours at a time. The climate of the North Yorkshire coast is generally drier than most of the UK, with an average annual rainfall over the monitoring period of 513 mm and mean monthly precipitation peaking at 79 mm in January (Figure 2.04e). Cliff aspect ranges from *ca.* 290° to *ca.* 120°, exposing the coastline to easterly and northerly North Sea storm wave events while sheltering the cliffs from prevailing south-westerly weather systems. As a result, wave conditions are such that the cliffs are constantly exposed to highly variable loading conditions. The effect of winter storms on cliff erosion is expressed in seasonal signals of heightened rockfall activity, particularly in temperate regions such as the North Yorkshire coast (Lim, 2014). Daily average wind speeds have been recorded at over 38 km h^{-1} during the winter months, with gusts of up to 85 km h^{-1} recorded during Storm Frank on 30th December 2015 (Figure 2.04f). A total of 14 named stormed events, active between November and March, occurred during the monitoring period. These events have been named since 2015 by the UK Met Office in order to highlight their potential severity.

In summary, the energy available for delivery to coastal cliffs is highly moderated by the combined effects of waves, wind, and rainfall. The impact of these processes on patterns of erosion observed at sites along the North Yorkshire coast is therefore reviewed in *Section 2.2.*

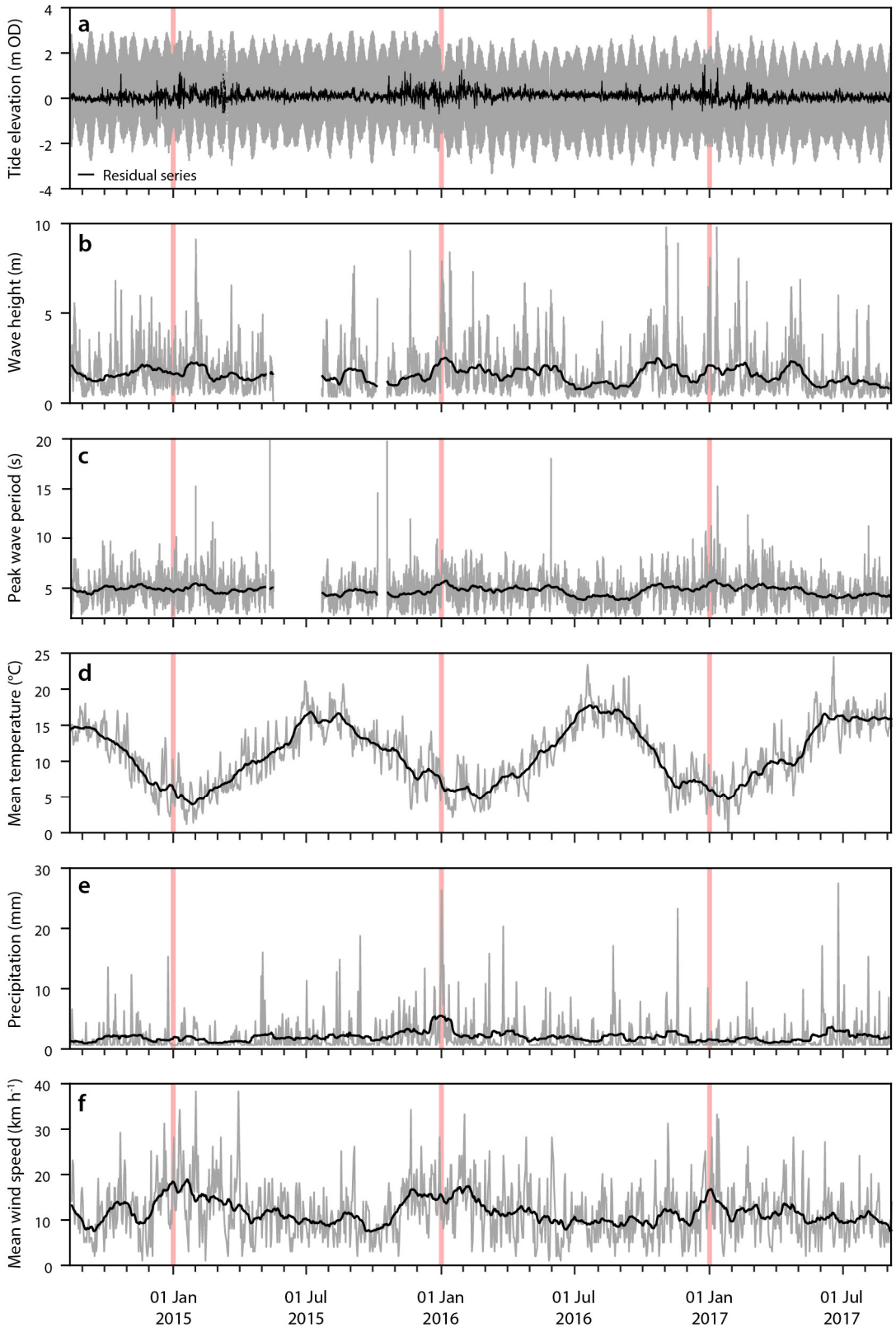

Figure 2.04 *Environmental conditions over the monitoring period (August 2014 – September 2017). (a) Tide elevations and residuals from Whitby tide gauge data, (b) wave heights measured at a wave buoy ca. 1.5 km offshore from Whitby, (c) peak wave period, (d) mean temperature measured at Whitby, (e) precipitation accumulation measured at Whitby, (f) mean wind speed measured at Whitby. In subplots (b – f), data presented are raw (grey) and smoothed using a 30-day moving average (black). Red bands denote the start of each calendar year. White bands denote missing data.*

2.2 Geomorphology and erosional processes

The North Yorkshire coast is shaped by an inheritance of marine, subaerial, and anthropogenic (mining exploitation and management intervention) processes, leading to complex patterns of morphological change as the coastline adjusts and retreats (Lim, 2014). The rate of cliff erosion at Staithes (Figure 2.01a) has been estimated at *ca.* 0.05 m yr^{-1} over the last century, based on the analysis of historic maps and photographs (Agar, 1960). This has been derived from a calculated retreat rate of *ca.* 0.04 m yr^{-1} for headlands and *ca.* 0.07 m yr^{-1} for embayments. However, when considered at this scale and monitoring interval, this rate falls well beneath the minimum achievable mapping precision at any given point. Measurements of coastal erosion using historic map data neglect processes of undercutting and small scale, iterative failures of localised sections of the cliff face, instead focussing on the overall recession of the cliff top or toe (see Lim *et al.*, 2005 and Rosser *et al.*, 2005a). The practical implications of this are that erosion rates determined using these approaches are associated with very high levels of uncertainty.

In recent years, the use of terrestrial LiDAR has become increasingly widespread owing to its ability to rapidly acquire dense 3D point clouds that can be used to derive 3D slope geometry on steep to vertical rock faces (Jaboyedoff *et al.*, 2012; Royán *et al.*, 2013; Abellán *et al.*, 2014). An overview of change detection using laser scanning technologies, with particular reference to monitoring slope deformation and rockfalls, is given in *Section 3.1.* The cliffs at Whitby (*ca.* 5 km southeast of Sandsend and outside of the area monitored in this research) and between Staithes and Boulby have been extensively monitored using terrestrial LiDAR in the past; these sites are shown in Figure 2.05, with corresponding rates of erosion provided in Table 2.01.

Although the behaviour of hard rock cliffs, both in terms of rockfalls that occur on the rock face and the resultant step-back retreat, is often described as episodic, monitoring at Whitby and at Staithes has revealed that smaller and more iterative changes occur at higher frequencies (Rosser *et al.*, 2005a, 2005b). An inventory of over 100,000 individual changes on these cliffs (sites A, B, D – F) over a 20-month period demonstrated that failure activity occurs over a range of scales, with the volume of individual changes ranging from *ca.* 1.25×10^{-4} m^3 to over 2.50×10^3 m^3 (Lim *et al.*, 2010). Multiple failure mechanisms, including constant spalling of material, overhang collapse, fragmentation, and large-scale, coherent rockfalls were observed and related to differences in lithology across the rock face and between sites. Monitoring at the same sites (A – G) over a seven-year period revealed that erosion rates in the inundated zone of the cliff broadly outpace those of the cliff above, yet there is no evidence of longer-term profile form change (Rosser *et al.*, 2013). Failure scars were observed to evolve through time, progressing upwards and also laterally (confined by lithology). The absence of notching in these areas indicates that abrasion by wave impacting appears not to be a dominant process in driving rock slope failure in this setting. Instead, both fracturing of rock bridges and discontinuity-controlled failure have been inferred from scar morphology (Rosser *et al.*, 2013). These are discussed further in *Section 2.2.1.*

2.2.1 Evidence for the influence of lithology and structure

The strata exposed at sites A – G, in particular the shales of the Lias Group, are friable and can be subject to considerable rates of erosion dependent upon local characteristics, such as cliff aspect and the presence of the foreshore platform. A range of rock strengths, bedding patterns, and jointing mean that the exposed sections at these sites are variable, comprising a mixture of smooth and irregular, blocky surfaces. Triaxial testing of samples taken from the cliffs at Staithes revealed a peak in resistance at the mudstone base (uniaxial compressive strength, σ_{ucs} = 41.54 MPa), which is overlain by weakened shale (σ_{ucs} = 16.69 MPa) and by more competent siltstone (σ_{ucs} = 30.20 MPa) and sandstone (σ_{ucs} = 34.21 MPa) above (Lim *et al.*, 2010). Failures in the till capping the cliffs often stain the cliffs red-brown and concentrate the flow of water over the rock face, with recent failures on the cliff face leaving clean, easily distinguishable scars (Lim, 2006). Where this occurs, the cliffs have a steep lower section and a shallow upper profile. Failures in the till have also been observed to dislodge other rock material from the underlying strata.

Patterns of retreat broadly reflect the exposed area of each rock type, with shales eroding iteratively through many small-scale losses, while mudstones and sandstones erode to greater depths, yielding larger, more coherent block failures (Lim *et al.*, 2010). Similar patterns occur at Whitby, where low rates of detachment are observed from the comparatively strong, widely jointed sandstone bands, and the weaker shales show consistently increased levels of activity (Rosser *et al.*, 2005a). Although there is little evidence of a wave-cut notch at the base of these cliffs, either because they are too short-lived or because they never form, the majority of change is known to occur in the mudstone at the cliff base, indicating that the overlying strata quickly adjust to changes in the stress environment brought about by erosion at the cliff toe (Barlow *et al.*, 2012).

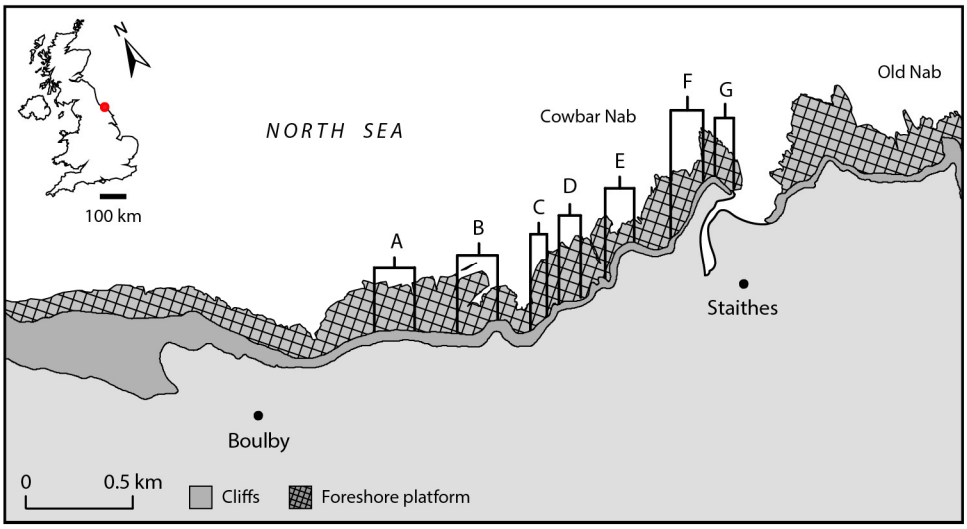

Figure 2.05 *Previously monitored sites in the Boulby/Staithes area, North Yorkshire. Details of monitoring periods, the associated rates of erosion, and references are included in Table 2.01. Map produced using shapefiles from the Ordnance Survey © Crown Copyright and Database Right 2017. Ordnance Survey (Digimap Licence).*

Analysis of the shape of rockfall scars at Boulby (site A) suggests a structural control on rockfall geometry, with failures tending to cluster around single or multiple joint sets (Rosser *et al.*, 2005b; de Vilder *et al.*, 2017). The shales and siltstones are fissile deposits that abrade, yielding small, slab-like failures. The more widely jointed limestone and sandstones tend to produce elongated failures, which is likely explained by shallow bedding depths and wide joint spacing. Mudstones in particular tend towards blocky shapes, representing failures deeper into the rock face (Rosser *et al.*, 2005b). Block shape also appears to vary up the cliff, indicating a potential transition from marine-controlled processes at the toe to weathering and rock mass collapse further up the cliff. Failure of convex features, such as overhangs, occurs as a function of localised stress concentration, removing support from the material above.

At each of the sites, rockfalls are observed to evolve through time, propagating both upwards and laterally (Rosser *et al.*, 2013). This occurs only where it is kinematically permissible, and is moderated by the local lithology, rock mass structure, and subaerial processes (Rosser *et al.*, 2013). At some elevations, exposures of massively jointed, fine-grained sandstones inhibit failure propagation, reflecting previously observed structural controls on rockfall magnitude-frequency scaling (Barlow *et al.*, 2012). Where large-scale failure of the cliff face has occurred (site D, for example, underwent a > 2,400 m^3 failure in January 2005), deeper seated and/or cantilever failure is thought to have been driven by locally high toe incision during high astronomical tides.

Table 2.01 *Erosion rates derived from terrestrial monitoring of rockfalls at the sites shown in Figure 2.05.*

Site	*Erosion rate*	*Monitoring period*	*Reference*
	m yr^{-1}	*mm/yyyy – mm/yyyy*	-
A	0.009	10/2003 – 04/2005	Lim (2006); Lim *et al.* (2010)
	0.004	09/2003 – 09/2010	Rosser *et al.* (2013)
	0.024	07/2008 – 06/2010	Vann Jones *et al.* (2015)
B	0.079	10/2003 – 04/2005	Lim (2006); Lim *et al.* (2010)
	0.052	09/2003 – 09/2010	Rosser *et al.* (2013)
C	0.009	09/2003 – 09/2010	Rosser *et al.* (2013)
D	0.073	10/2003 – 04/2005	Lim (2006); Lim *et al.* (2010)
	0.079	09/2003 – 09/2010	Rosser *et al.* (2013)
E	0.068	10/2003 – 04/2005	Lim (2006); Lim *et al.* (2010)
	0.007	09/2003 – 09/2010	Rosser *et al.* (2013)
F	0.128	10/2003 – 04/2005	Lim (2006); Lim *et al.* (2010)
	0.024	09/2003 – 09/2010	Rosser *et al.* (2013)
G	0.011	09/2003 – 09/2010	Rosser *et al.* (2013)

2.2.2 Evidence for environmental drivers

Quantification of marine and atmospheric energy delivery to the coastal cliffs at Boulby (site A) has been undertaken using microseismic monitoring, which draws on different frequency bands of ground motion as proxies for wind and wave conditions (Lim *et al.*, 2011; Norman, 2012; Norman *et al.*, 2013; Brain *et al.*, 2014; Vann Jones *et al.*, 2015). Monitoring has shown that energy delivery to the cliffs is highly variable over time, and is strongly conditioned by tide height and foreshore microtopography (Lim *et al.*, 2011). Peak energy transfer occurs during the largest storm events, where bottom frictions and water depths are sufficient to maintain constant wave impacting, and therefore energy delivery, at the cliff (Norman, 2012; Norman *et al.*, 2013). The variability observed in certain frequency bands of a two-year microseismic dataset obtained from the cliffs at Boulby shows moderate, statistically significant correlations ($r^2 < 0.6$, $p < 0.001$) with rockfall activity observed across the whole cliff face, rather than solely within the inundated wet zone (Vann Jones *et al.*, 2015). This indicates that the marine influence on erosion extends above and beyond the inundated area of the cliff. Ground motions generated by wind and wave processes are therefore thought to play a role in the final release of rockfalls from the upper parts of the cliff face, which were previously considered to be disconnected from marine processes occurring at the cliff toe (Rosser *et al.*, 2005a). Moderate correlations may be partially explained by the strong geological controls on rockfall occurrence (*Section 2.2.1*), although analysis undertaken over monitoring intervals of 4 – 8 weeks fails to differentiate between the observed failures occurring as a near-immediate or a lagged response to forcing.

In addition to acting as proxies for environmental forcing, microseismic ground motions are hypothesised to play a direct role in fracturing rock via cyclic loading and subcritical crack growth. A 32-day microseismic dataset obtained from the cliff top at site A demonstrated that periods of relatively low amplitude microseismic ground motion are often interrupted by periods of greater displacement during energetic storm events (Brain *et al.*, 2014). Ground motions with a sustained cliff-normal component were also observed during these events. Brain *et al.* (2014) suggested that changes in loading direction beyond those that are commonly experienced could lead to a change in the micro-scale stress field and therefore the crack tip separation mode, extending microcracks beyond conditions achievable by low amplitude background displacements. As a result, the opportunity for microseismic loading to cause damage and weakening through propagation and coalescence of microcracks is likely to be spatially and temporally restricted. However, determining the exact effects of these motions on damage accumulation as a trigger for rockfall remains difficult.

Between Staithes and Boulby, the propagation of rockfalls has been observed to facilitate the transmission of marine loading up the cliff face over time (*Section 2.2.1*; Lim *et al.*, 2010; Rosser *et al.*, 2013; Vann Jones *et al.*, 2015). However, the response of rock slopes to different promoting and triggering conditions remains poorly understood. If rock slope evolution is driven

by progressive failure, which is the product of iterative and then runaway microcracking that is independent of external loading, progressive damaging of the rock mass could explain the poor correlations between rockfall activity and energetic environmental conditions thus far.

2.3 Summary

The discussion presented in *Chapter 1* demonstrated the importance of being able to upscale existing monitoring of rockfall activity, in order to account for the influence of variations in intrinsic (here, rock mass strength and structure) and extrinsic (here, erosion induced by wave loading) controls. This in turn may provide an understanding of how these controls interact to condition patterns of rockfall occurrence. In this chapter, a field site has been identified that constitutes a suitable analogue for a range of wave loading conditions, and where the relationships between wave loading, rock mass structure, and rockfall occurrence can be investigated. In this context, the North Yorkshire coast is suitable for a number of reasons, including:

1. The cliffs fall inside one of three distinct precipitation sub-regions in North Yorkshire, which are defined using at least 10 years of precipitation observations from 150 sites (Fowler *et al.*, 2000, 2005), such that the effect of weather on rockfall occurrence is effectively held constant along their length;
2. Periodic straining of the rock mass by wave loading varies considerably along the coastline due to variable coastal geometry and bathymetry. This variability can occur over short ($< 10^2$ m) and longer ($> 10^3$ m) length scales;
3. This variability in wave loading, combined with varying lithology and structure (predominantly over length scales of $> 10^3$ m), permits the constraint of the nature of rockfall occurrence beyond that observed on a single slope, which is often the maximum that is achievable due to limitations in data capture.

In order to do this, *Chapter 3* focuses on developing a workflow for detecting and characterising regional-scale changes to rock slope morphology in 3D, and uses this workflow to explore regional-scale variations in rockfall magnitude, frequency, and erosion along the North Yorkshire coast.

This page is intentionally left blank

Chapter 3

Quantifying regional variations in rockfall activity along coastal cliffs

A paper published using some of the material from this chapter (Benjamin et al., 2016) is presented in Appendix A, and is referred to in text.

The ability to precisely quantify and understand rockfall behaviour on a regional scale is critical for a number of reasons (*Chapter 1*), including (1) that rockfalls are an important factor in defining rates of rock wall retreat in sea cliff and high-mountain geosystems, (2) that monitoring at this scale overcomes site-specific conditions, allowing a full assessment of the emergent characteristics of rock slope failure and the associated drivers, and therefore (3) for successfully modelling the present and future dynamics of failing rock slopes. This chapter therefore uses high-density point clouds derived from airborne LiDAR to monitor rockfalls along the North Yorkshire coast. Building on existing monitoring data presented in *Chapter 2*, this research upscales previous work undertaken using terrestrial LiDAR and shifts the focus towards understanding changes in rock slope morphology at the regional scale. Quantifying the magnitude of these changes has previously proven problematic, with a range of approaches currently adopted to measure the retreat, area, or volume of changes to rock slopes. The following discussion reviews a number of these approaches (*Section 3.1*), before proposing a workflow for detecting and characterising regional-scale changes to rock slope morphology (*Section 3.2.*). This method is used to detect rockfalls along *ca.* 20.5 km of coastal cliffs over three approximately equal monitoring intervals between August 2014 and March 2017. Using the resulting inventory of rockfall activity, *Section 3.3* explores regional-scale variations in rockfall magnitude, frequency, and erosion along the North Yorkshire coast (*RQ1*). These findings are summarised in *Section 3.4*.

3.1 Change detection using laser scanning

The most significant advances in our ability to detect rock slope deformation and to quantify change across a range of spatial and temporal scales have come from the application of terrestrial, airborne, and/or spaceborne remote sensing (Metternicht *et al.*, 2005). Among these, the use of terrestrial LiDAR has become increasingly widespread. Sequential surveys can be used to monitor displacements and detachments on cliffs, providing a more accurate representation of the distribution of types and rates of cliff change than 2D measurements of cliff top recession (Lee and Clark, 2002) or measurements of rockfall volume flux derived from sediment traps (Krautblatter and Dikau, 2007).

Quantification of volumetric change between LiDAR surveys, in a manner that permits individual rockfalls to be considered, is commonly achieved by rasterising successive point clouds and differencing the resultant Digital Elevation Models (DEMs, Figure 3.01). This technique has been used to monitor rock slope deformation (Bauer *et al.*, 2005) and precursors to slope failure (Abellán *et al.*, 2009); debris flows (Scheidl *et al.*, 2008; McCoy *et al.*, 2010; Schürch *et al.*, 2011; Blasone *et al.*, 2014); landslide dynamics (Corsini *et al.*, 2009; Burns *et al.*, 2010; Kasperski *et al.*, 2010); rock glaciers (Avian and Kellerer-Pirklbauer, 2009); and slope failures in rapidly eroding soft rock sea cliffs (Kidner *et al.*, 2004; Xhardé *et al.*, 2006; Kuhn and Prüfer, 2014; Young, 2015). Quantifying change using this technique is simple and fast, and permits the explicit calculation of uncertainties related to point cloud quality, co-registration, and surface roughness.

Differencing two DEMs derives a 1D measurement of change in the z direction only, typically aligned towards the sensor (Avian and Kellerer-Pirklbauer, 2009). A number of techniques have therefore been developed to compute a displacement field based on the identification of corresponding elements within two DEMs. These techniques are based on a set of image-based cross-correlation techniques and have been used to monitor glacier movements (Abdalati and Krabill, 1999; Schwalbe *et al.*, 2008); mudslides (Travelletti *et al.*, 2008); landslides (Aryal *et al.*, 2012; Feng *et al.*, 2012; Ghuffar *et al.*, 2013); and post-seismic ground displacements (Ayoub *et al.*, 2009; Borsa and Minster, 2012). The use of cross-correlation functions exploits the high point densities acquired by laser scanners, although the quality of these techniques is limited in the presence of vegetation and minimally textured surfaces. Object-oriented methods expand on these techniques and quantify deformation by separating measured displacements into rotational and translational components, using either manual or semi-automatic methods (Monserrat and Crosetto, 2008; Oppikofer *et al.*, 2008, 2009; Travelletti *et al.*, 2008; Carrea *et al.*, 2012). These approaches consist of the manual identification and tracking of features common to both point clouds in order to calculate a series of displacement vectors and velocities, yielding precise information (10^{-2} m) on small-scale deformations on slope surfaces (Oppikofer *et al.*, 2008, 2009; Carrea *et al.*, 2012). However, the accuracy of these methods strongly depends upon the identification of consistent point pairs between scans and the deformation patterns of the tracked

objects. Given that the point pairs are often identified manually, object-oriented methods can represent a fastidious processing task for very large datasets (Travelletti *et al.*, 2014).

The gridding of data during DEM creation requires a fixed cell width to be selected, which is ultimately defined by the maximum point spacing and therefore acts to average out smaller scale features. Rasterising rough surfaces also generates patterns of occlusion that are view-dependent and convolute volume estimation. Deviation away from the normal viewing angle (0°) can have a profound influence on the magnitude of change detected. The case in Figure 3.01 illustrates the influence of viewing angle on the amount of occlusion generated by roughness and pre-/post-failure micro-topography across the rockfall surface, and the consequences of this for volume estimation. Where rock slopes have more a complex, non-planar aspect, this type of

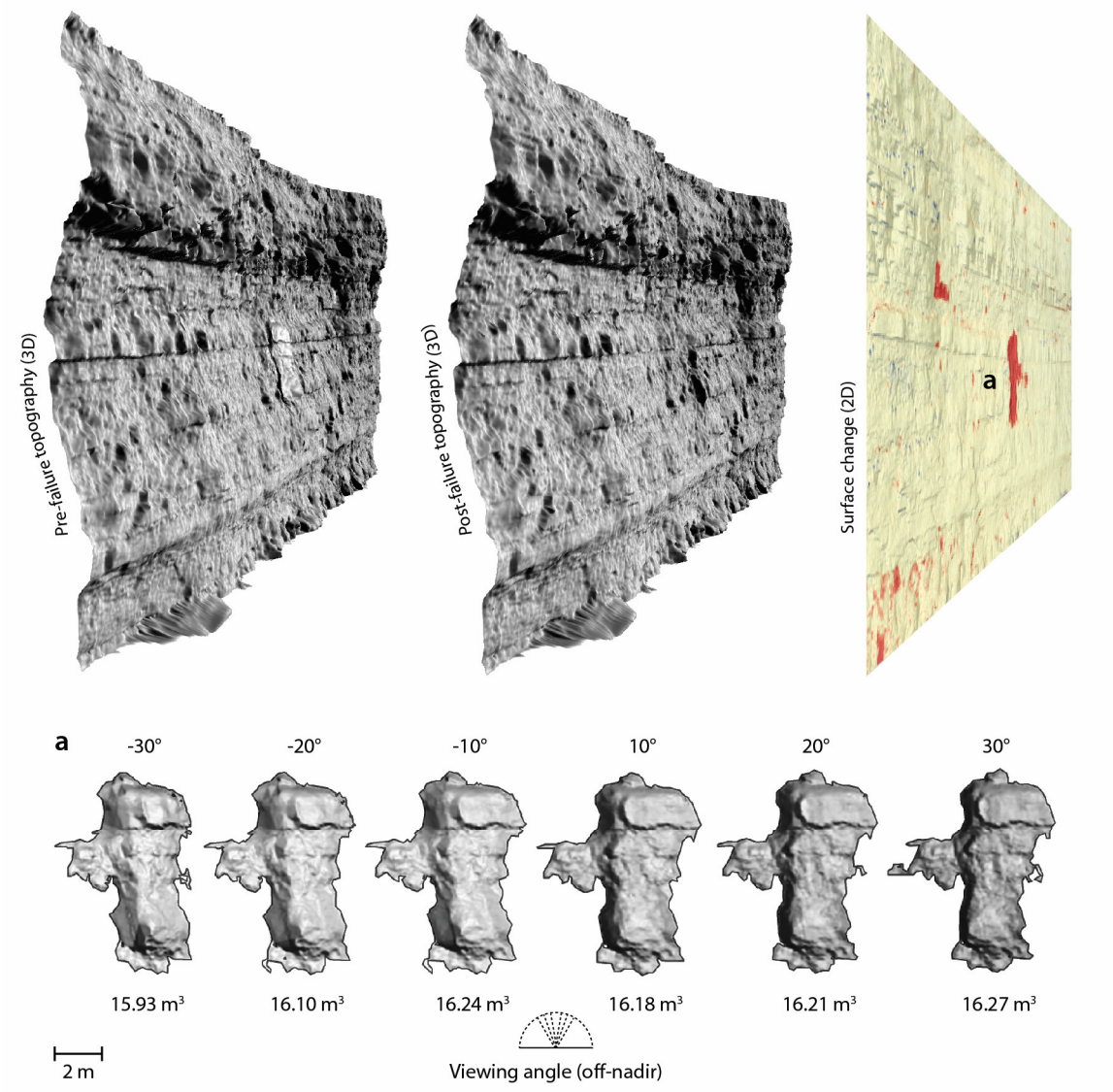

Figure 3.01 *Differencing technique using DEMs derived from 3D point clouds. Here, the rockfall (a) is shown on the plot of 2D surface change and is used to illustrate the influence of viewing angle on the magnitude of change detected. The rockfall (volume = 16.20 m³) was recorded at Staithes, North Yorkshire (UK) over a 10-month monitoring period between August 2014 and June 2015. Note that the 2D volume quoted here differs to 3D volumes quoted later, for reasons explained in Section 3.1 (p. 27).*

approach requires the scan data to be rasterised and differenced in separate sections in order to maintain a cliff-normal viewing angle. Given that there is no coherent relationship between the estimated volume and view-angle, the degree of under- or over-estimation of change cannot necessarily be compensated for if the view-angle from the sensor to the slope is known. Reducing 3D point cloud data to a pseudo-3D surface in this manner therefore hinders accurate quantification of rock wall adjustment and retreat (Abellán *et al.*, 2014). This has the effect of losing detail and the true 3D character of the data, with the development of new algorithms for 3D deformation tracking and change detection therefore representing a priority for monitoring rock slope dynamics (Carrea *et al.*, 2012).

A number of 3D methods have been developed to measure the distance between two successive point clouds (Girardeau-Montaut *et al.*, 2005). These techniques include cloud-to-mesh (C2M) and cloud-to-cloud (C2C) comparison methods. C2M methods create a surface model from the reference point cloud via meshing or triangulation and measure the distance between this and subsequently gathered point clouds (Abellán *et al.*, 2009, 2010; Olsen *et al.*, 2010). Such methods have been successfully used to investigate cases of structural or surface deformation, including monitoring of a large dam (Alba *et al.*, 2006); detecting land surface changes in the Grand Canyon, Arizona (Collins *et al.*, 2012); and quantifying erosion in the coastal bluffs of the Le Sueur River, southern Minnesota (Day *et al.*, 2013). To accurately determine volumetric change, triangulated surfaces must be free of topological holes and intersecting triangles. To do this, the vector perpendicular to the surface at the centroid of each triangle, known as the surface normal, must be calculated. The surface normal for each triangle is calculated using the orientation of its three edges, and must also point towards the same side of the mesh. The majority of surface reconstruction techniques have been developed and tested using regular shapes and denoised point clouds (Lim and Haron, 2014), meaning that they are difficult to employ on rough, complex surfaces defined by marked topographic variability (Olsen *et al.*, 2015).

C2C techniques instead estimate surface changes directly from the distance between point neighbours in successive point clouds, eliminating the need for mesh construction and the smoothing of any noisy data (Lague *et al.*, 2013). These distances can be measured automatically using the Hausdorff metric, which computes the unsigned distance for each point in the reference cloud to its nearest neighbour in the second cloud. Where point clouds are sparse, they can be improved by using a local model of the reference surface obtained by a quadratic height function, a least square fit, or a Delaunay triangulation of the closest point neighbours (Gruen and Akca, 2005). These provide a better approximation of the true position of the surface and are better able to deal with outliers and variations in surface roughness. These techniques have recently been extended by the Multiscale Model-to-Model Cloud Comparison (M3C2) approach, the principles of which are illustrated in Figure 3.02 (Lague *et al.*, 2013). More widely, M3C2 has been used to monitor lava lakes (Smets *et al.*, 2016), patterns of erosion in bedrock gorges (Beer *et al.*, 2017;

Cook, 2017), landslides (Stumpf *et al.*, 2015), cliff erosion (Warrick *et al.*, 2017), the evolution of Antarctic moraine complexes (Westoby *et al.*, 2016), and glacier surface topography (Midgley and Tonkin, 2017). For each point, M3C2 estimates the surface normal and measures the signed mean surface change along the normal direction, with the explicit calculation of a spatially variable confidence interval (SVCI). M3C2 incorporates a local measure of cloud roughness and point density for estimating the SVCI, which can be used to test the statistical significance of any measured changes (Barnhart and Crosby, 2013; Earlie *et al.*, 2013; Stumpf *et al.*, 2015). The measured surface change is then projected back onto either the pre- or post-event point cloud.

The volume and quality of data that can be collected using laser scanning technologies is unprecedented and presents its own unique challenges for regional-scale research, including questions regarding how data scales from the local to regional level, where data may increase in size from 10^6 to 10^9 points. Many approaches resort to gridding the data in order to reduce processing time and complexity (Leyland *et al.*, 2017). However, localised tests examining the relative benefits of 2D and 3D methods of change detection show that the total erosion estimated by differencing DEMs of a rock slope can exceed that obtained by volumetric meshing by over 25% (Benjamin *et al.*, 2016; *Appendix A*, *p.* 171). This is attributed to the fact that 2D and 3D approaches behave differently when considering small depth changes on the periphery of a rockfall (Williams *et al.*, 2018). Assuming a similar performance, these results suggest that existing inventories may considerably overestimate rockfall volumes, reaffirming the need to develop new ways of processing and analysing point cloud data for monitoring regional-scale rock slope dynamics.

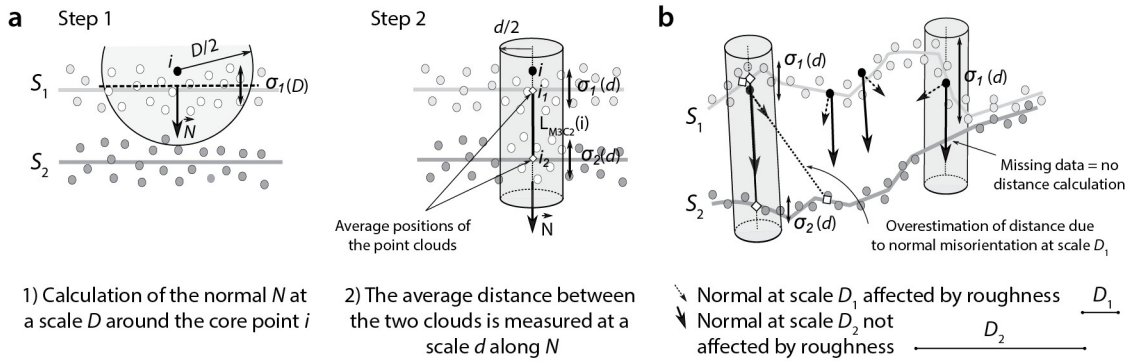

Figure 3.02 *Principles of the M3C2 technique. In the first step (a), the surface normal at each point in the reference cloud (S_1) is estimated by considering all points in a neighbourhood of radius D/2, where D is the user-defined normal diameter. The distance at each point is then calculated as the mean distance between all points in a neighbourhood of the size d/2, where d is the user-defined projection scale. These neighbourhoods are denoted i_1 and i_2. When used on complex topography (b), normals can be estimated at a scale too small with respect to the surface roughness characteristics (D_1), meaning that their orientation varies strongly. A larger scale (D_2) yields more uniform normal orientations. Diagram adapted from Figure 3 in Lague et al. (2013, p. 14).*

3.2 Measuring regional-scale variations in rockfall activity

The most commonly used methods for calculating rockfall volume involve differencing high resolution DEMs (Santana *et al.*, 2012) or meshes (Rabatel *et al.*, 2008; Zimmer *et al.*, 2012; Stock *et al.*, 2013). While these methods can be useful for estimating the volume of a single rockfall, they prove time consuming when considering large rockfall inventories covering wide areas. Integrating the mean distance between two point clouds as calculated by a C2C comparison can also be problematic due to local changes in surface roughness and normal direction (Earlie *et al.*, 2013), which may lead to considerable under- or over-estimation of the calculated volume. To address these difficulties, a workflow for detecting and characterising regional-scale change in 3D is proposed in Figure 3.03. In this workflow, M3C2 is used to detect change between two scans and to project the measured changes onto both the pre- and post-event point clouds. The point cloud is then filtered to remove areas of deposition and insignificant change, as defined by the SVCI. At this stage, a threshold for detectable change can be defined by the user, if necessary. Each individual rockfall event is classified using the data clustering algorithm DBSCAN (Ester *et al.*, 1996), and the PowerCrust algorithm is then used to construct a watertight triangular surface mesh for each rockfall (Amenta *et al.*, 2001). The volume, volumetric error, and centroid of each mesh is then derived, and other properties including the surface area, width, depth, and height of the observed rockfalls are also calculated.

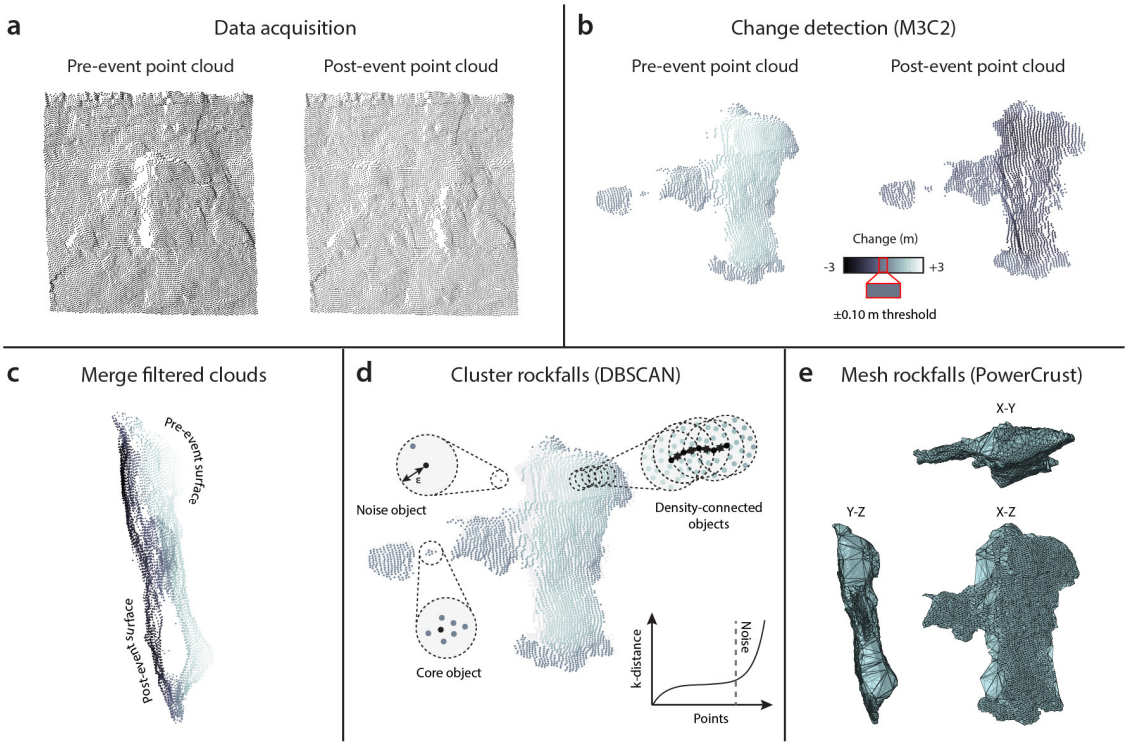

Figure 3.03 *Workflow for detecting and characterising regional-scale change in 3D. The changes between two scans in (a) are detected using M3C2 (b) and projected onto both the pre- and post-event point clouds. The clouds are filtered and merged in (c) and rockfalls are clustered using DBSCAN (d). The clustered points are then meshed using the PowerCrust algorithm in (e).*

3.2.1 Data acquisition

Four surveys of the North Yorkshire coast (*Chapter 2*) were captured at approximately equal intervals using a mobile mapping system installed on a twin engine EuroCopter AS355 F1 helicopter. The system comprises a RIEGL VQ-450 or VUX-1 laser scanner coupled with an IGI AeroControl III navigation system, which combines a GPS receiver with an Inertial Measurement Unit (IMU-IIe) in order to measure the position and attitude (pitch, roll, and yaw) of the helicopter. The scanner uses a high pulse repetition rate (up to 550 kHz) near-infrared laser and a rotating mirror to return a swath of range estimates beneath the flight path (RIEGL, 2014). During the surveys, the mapping system was housed in a protective pod on the front of the helicopter, providing a 180° downward- and sideways-looking field-of-view. This enabled both the terrain surface and near-vertical cliff faces to be scanned simultaneously. An example of the data collected is shown in Figure 3.04[1]. A number of overlapping flight lines were flown in each survey to increase point density, and variations in the attitude of the aircraft gave multiple views of the same area of the cliff face, minimising any occlusions due to surface roughness. In addition, a downward-looking 36.3 MP Nikon D-800 camera with a 24 mm lens captured optical imagery. The system was deployed at an average flying height of *ca.* 100 m above the foreshore, providing a spatial resolution of *ca.* 0.01 m for the optical imagery (Figure 3.05b). Leica 1200 GPS receivers recorded ground control data at one sample per second. The GPS antennas were mounted on tripods placed over targets in 12 locations (Figure 3.05a). A summary of the data collected is presented in Table 3.01 and ground control data are provided in *Appendix B (p. 181)*.

Table 3.01 *Summary of the raw airborne LiDAR data collected. Vertical RMSE are quoted as the average difference between the laser z and each of the ground control z (see Appendix B, p. 181).*

Date	*Number of points*	*Average point density*	*Vertical RMSE*
	-	*points m^{-2}*	*m*
15/08/2014	381,649,773	30 – 50	± 0.025
04/06/2015	422,283,194	40 – 60	± 0.053
08/04/2016	476,025,155	50 – 70	± 0.032
29/03/2017	555,389,153	60 – 80	± 0.010

3.2.2 Point cloud processing

Point cloud data were assigned to a global coordinate system by 3D Laser Mapping Ltd and provided as .las files containing the *x, y,* and *z* coordinates for each point, as well as RGB values (derived from orthophotos) and 16-bit intensity information. The point clouds were clipped in plan-view to retain the extent of the vertical cliff faces, which were mapped using a 0.25 m

[1] *Flythroughs can be viewed at: https://www.youtube.com/channel/UCKXC7KN_eL8N_ciKB5a281q*

a
b
160 m
120 m
0 m
c
Brighter
Intensity
Darker
NORTH SEA
100 km
Old Nab
Cowbar Nab
A
B
Staithes
Boulby
0
0.5 km
Cliffs
Foreshore platform

Figure 3.04 *Overleaf. Mosaicked orthophotos (a) and a point cloud (b,c) of the cliffs between Cowbar and Boulby. Inset: map of the surrounding area, including sites previously monitored (Section 2.2).*

raster of the LiDAR point cloud derived from the first survey and coloured by RGB value. The data were divided into 38 blocks to increase processing efficiency, with each block 500 m in width. To minimise the error between surveys, the data were re-aligned block-by-block for each monitoring period using an iterative closest point alignment, with a maximum permissible registration error of 0.10 m. The cliffs and their corresponding blocks are shown in Figure 3.05c.

Airborne LiDAR data are routinely classified using point filters designed to separate bare-earth from vegetation, such as the adaptive Triangular Irregular Network (TIN) method developed by Axelsson (2000). This is required to ensure that only rockfalls are included in the subsequent analysis. The algorithm creates and iteratively densifies a TIN from a sparse distribution of seed points. Seed points are local low points, which are initially classified as ground points. The algorithm assumes that the triangles in the TIN initially created from the seed points are mostly below ground level, since their vertices are the lowest points in a localised area. In each iteration, a point is added to the TIN if the point meets certain criteria in relation to its bounding triangle. These criteria are that the angle the point makes to the triangle must be below a defined threshold

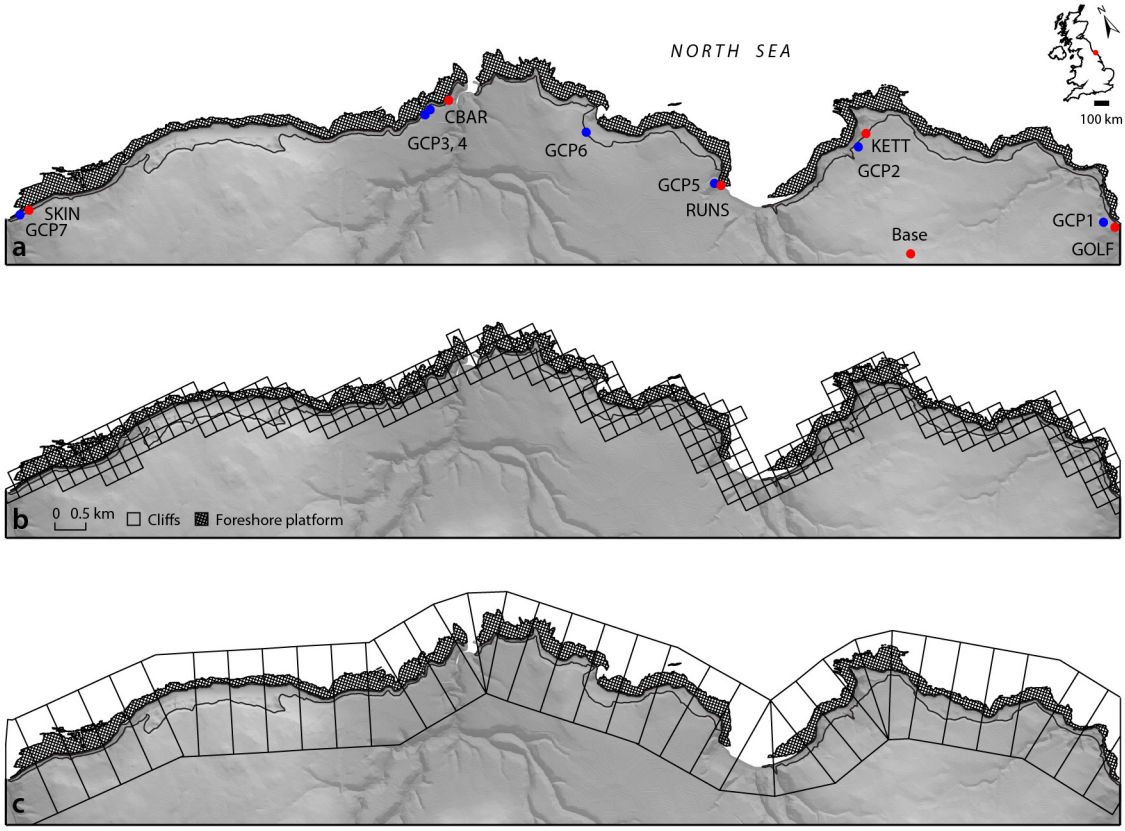

Figure 3.05 *Map showing the ground control points used in the four airborne LiDAR surveys undertaken (see Appendix B, p. 181). Red points denote sites that were repeated in all four surveys, while blue points denote those that were used in the first survey only. The data was divided into 38 blocks for processing and merged for analysis. Orthophoto tiles cover the full extent of the surveyed area.*

(the 'iteration angle'), and that the point must be within a minimum distance of the nearest triangle node (the 'iteration distance'). Many existing filters operate under similar assumptions, and can therefore fail when classifying steep terrain, particularly cliff edges and overhangs (Sithole and Vosselman, 2004). This is illustrated in Figure 3.06. Increasing the iteration angle and distance can partially overcome this problem, but doing so acts to include vegetation and other objects into the ground model. Although Riquelme *et al.* (2014) present a solution, which involves rotating the point cloud such that the cliff surface is upward facing and therefore capable of being successfully classified, this is unfeasible for large datasets where cliffs vary considerably in aspect.

The point cloud data for each of the surveys were classified using RGB information taken from 11 training sets of exposed rock and vegetated surfaces along the coastline. The training data for the cliff surfaces comprised the Lower-Middle Jurassic strata, tills, and overhangs that caused shadow in the orthophotos. Above the cliffs, vegetation occurs predominantly as grasses and shrubs growing in the glacial till. Training sets included different types of vegetation, as well as patches of vegetation under different light conditions, in order to capture the associated differences in colour. The final training sets were plotted in RGB colour space to ensure no overlapping between each set. The data were classified into exposed rock and vegetated points using a macro routine informed by the training data. Isolated 'air' points (for example, birds) were then classified by finding the median and standard deviation of the elevation of all the neighbouring points within a radius of 5 m. A point was considered as an air point if its elevation exceeded the standard deviation multiplied by a given factor (default = 5) above the median elevation, in order to account for changes in surface roughness. The results of the classification were manually checked and corrected, as warping of the orthophotos on the steepest surfaces yielded inaccurate results in some areas. Field photos were used to verify the results, where possible. The relative benefits of this technique over the adaptive TIN method are illustrated in Figure 3.06. All vegetated surfaces were filtered out prior to change detection.

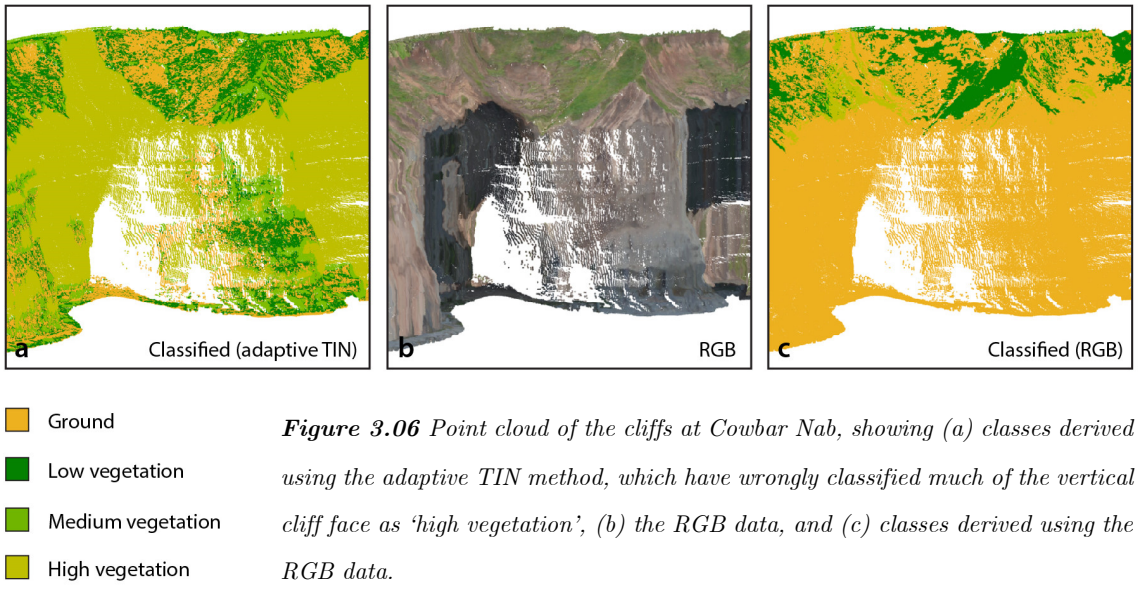

Figure 3.06 *Point cloud of the cliffs at Cowbar Nab, showing (a) classes derived using the adaptive TIN method, which have wrongly classified much of the vertical cliff face as 'high vegetation', (b) the RGB data, and (c) classes derived using the RGB data.*

3.2.3 Change detection analysis

The four monitoring periods were defined using the airborne LiDAR data collected between 2014 – 2015, 2015 – 2016, 2016 – 2017 and 2014 – 2017 (Table 3.01). For each monitoring period, change was estimated between the point clouds block-by-block using the M3C2 algorithm (Lague *et al.*, 2013). As illustrated in *Section 3.1*, the algorithm was implemented in two stages, (1) the estimation of 3D surface normals using the normal diameter, D, and (2) quantification of the mean distance between the two point clouds along the normal vector using the projection scale, d. This step includes the explicit calculation of the SVCI, which can be used to test the statistical significance of any measured changes.

Change detections on four different types of surface were undertaken to demonstrate how the measured change differs between surfaces of varying roughness, and with variations in normal diameter and projection scale (Figure 3.07). For this purpose, surface roughness is defined as the standard deviation of local surface elevations (σ). Vegetated surfaces are shown for completeness, but were filtered out prior to change detection on the cliffs themselves (*Section 3.2.2*). A trial-and-error approach was used to estimate the normal diameter, D. Surface normals must be estimated at a scale that is small enough to capture medium-to-large scale changes in surface orientation, such as changes in cliff aspect, but large enough to avoid fluctuation of the resulting normals due to small scale changes in roughness, such as small cobbles or overhangs. A normal diameter, D, of 2 m was selected as a compromise (Figure 3.07a). Smaller projection scales ($d <$ 1 m) sample too few points from each point cloud and exaggerate change, while larger projection scales ($d >$ 3 m) cause smearing and average out many of the largest changes recorded. This effect is most pronounced on blocky and vegetated surfaces (Figure 3.07b). The diameter of the projection scale, d, was therefore specified as 1 m. This ensured that the number of points sampled in each cloud was ≥ 30, following Lague *et al.* (2013), while minimising the effect of averaging.

Cloud-to-cloud distances were projected onto the pre- and post-event point clouds, and both were filtered to remove any areas of deposition and insignificant change, as defined by the SVCI. This is also known as the level of detection (LoD) threshold for a 95% confidence interval:

$$LoD_{95} = \pm 1.96\left(\frac{\sigma_1(d)^2}{n_1} + \frac{\sigma_2(d)^2}{n_2} + reg\right) \quad [3.1]$$

where reg is the user-defined registration error, which is substituted for the alignment error for point clouds n_1 and n_2 (*ca.* 0.10 m) of surface roughness σ_1 and σ_2. Given the uniformity of the point distribution across the datasets, this error is assumed to be isotropic and spatially uniform. However, the LoD selected represents the maximum of all blocks in the dataset, in order to minimise the likelihood of capturing noise. Having isolated the areas of erosion, the pre- and post-event point clouds were merged for each block and for each monitoring period.

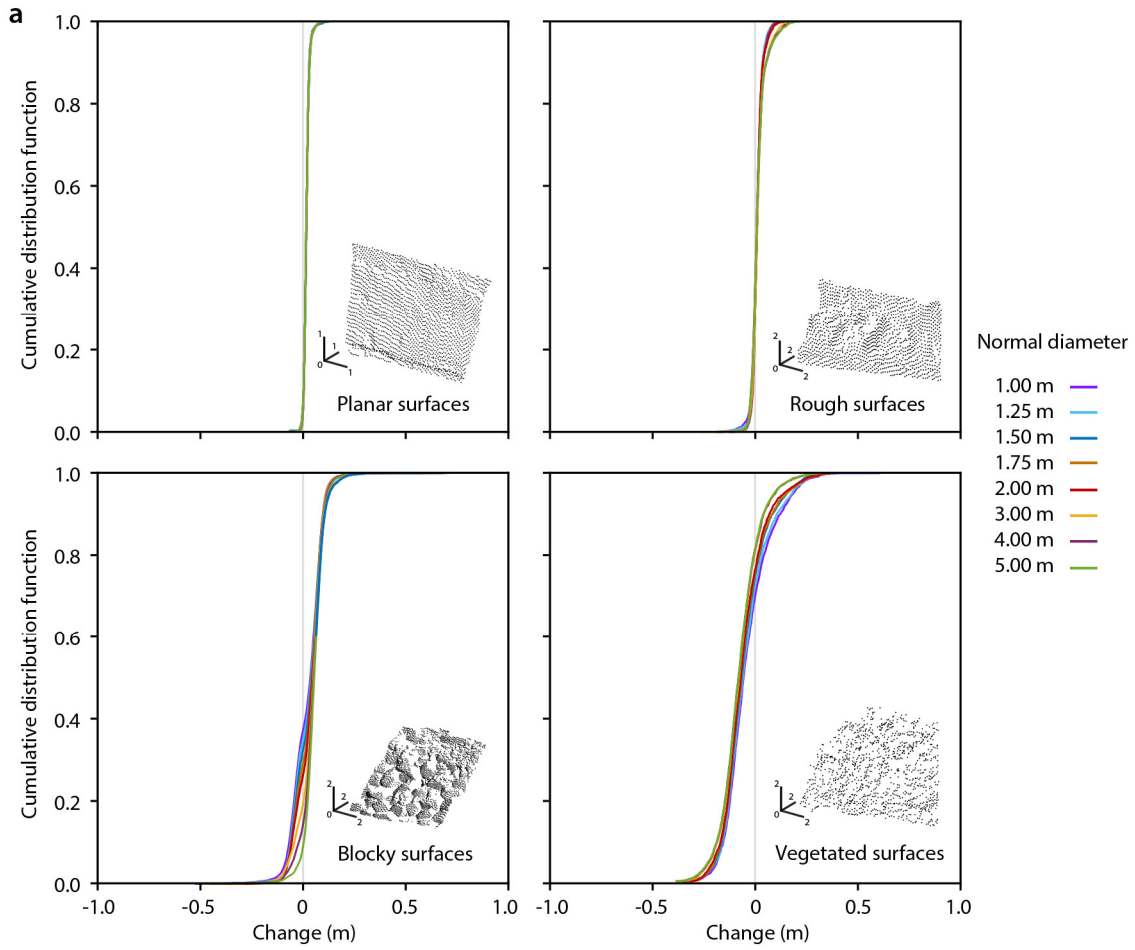
a
Cumulative distribution function
Planar surfaces
Rough surfaces
Blocky surfaces
Vegetated surfaces
Change (m)
Normal diameter
1.00 m
1.25 m
1.50 m
1.75 m
2.00 m
3.00 m
4.00 m
5.00 m

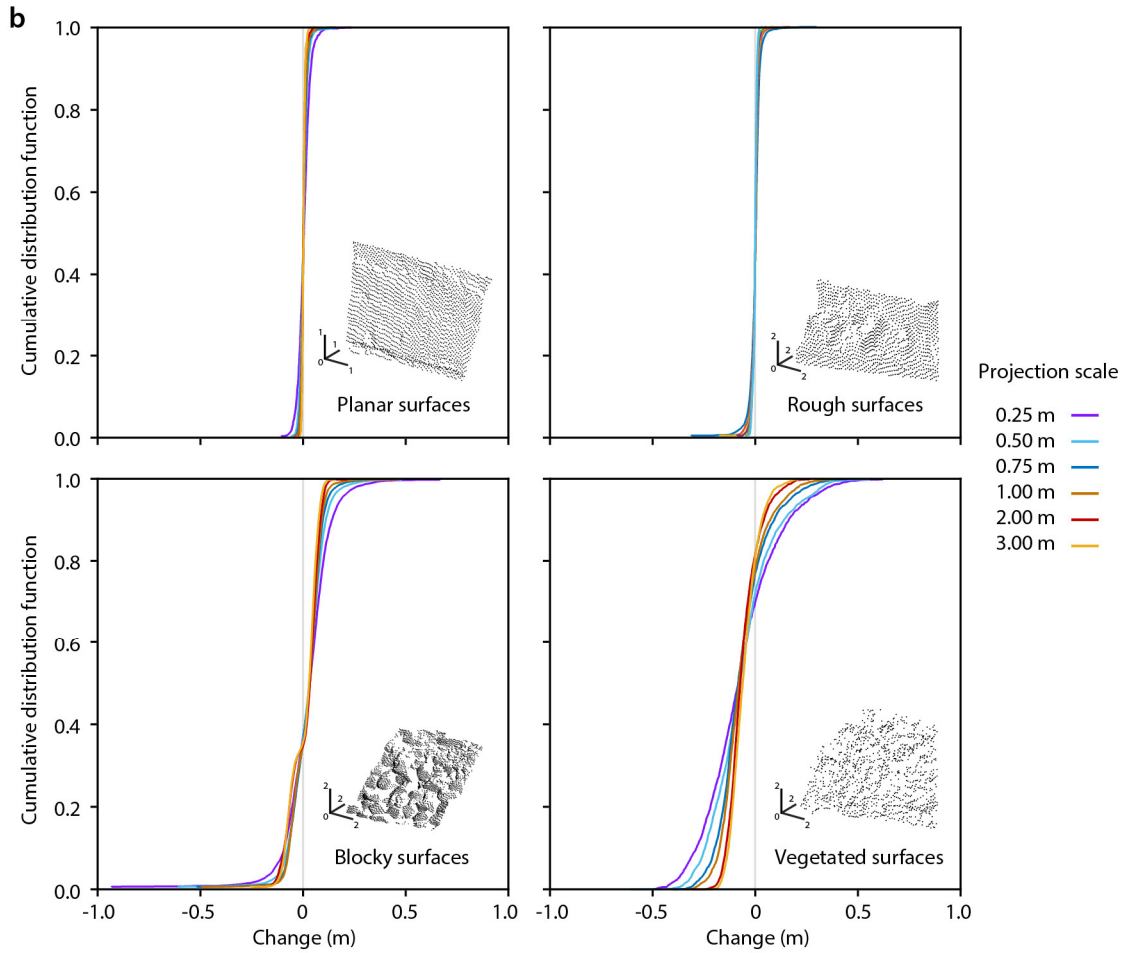
b
Cumulative distribution function
Planar surfaces
Rough surfaces
Blocky surfaces
Vegetated surfaces
Change (m)
Projection scale
0.25 m
0.50 m
0.75 m
1.00 m
2.00 m
3.00 m

Figure 3.07 *Overleaf. Cumulative distribution functions of the change measured across surfaces of varying roughness. The surfaces were sampled from two LiDAR surveys taken on the North Yorkshire coast in August 2014 and June 2015. Given that no rockfalls were observed, the plots demonstrate how change differs with variations in (a) the normal diameter, D, and (b) projection scale, d, used in the M3C2 algorithm.*

3.2.4 Rockfall detection and clustering

The points belonging to each individual rockfall event were grouped using the clustering algorithm DBSCAN (Density-Based Spatial Clustering of Applications with Noise), developed by Ester *et al.* (1996). Contiguous points of change are assumed to belong to a single event, although the influence of rockfall scar coalescence through time is also recognised in later analysis (Williams *et al.*, 2018). The principles of the DBSCAN technique are illustrated using three rockfall events recorded at Staithes (Figure 3.08). DBSCAN is the most commonly used single-scan clustering technique and defines clusters based on the local density of points. The algorithm requires two inputs: the minimum number of points (*MinPts*) within a maximum radius (ε) from each randomly chosen point (p) in the dataset. DBSCAN defines a neighbourhood of points, $N\varepsilon$, which falls within the circle of radius ε around a point, p. *MinPts* is defined as the minimum number of neighbours of point p to consider p as a core object. If $N\varepsilon$ contains more than *MinPts*, the algorithm creates a new cluster with p as the core point, and iteratively collects directly density-reachable points from p. The process terminates when no new points can be added to any cluster. If each point in the cluster is plotted against the distance to its k^{th} nearest neighbour, the threshold point p in the *k-distance* graph can be used to define $\varepsilon = k^{th}\ dist(p)$, where $MinPts = k$. All points with a higher *k-dist* value are considered as noise (Ester *et al.*, 1996). For databases where each point only occurs once, Sander *et al.* (1998) proposed that *MinPts* is equal to twice the number of dimensions of data.

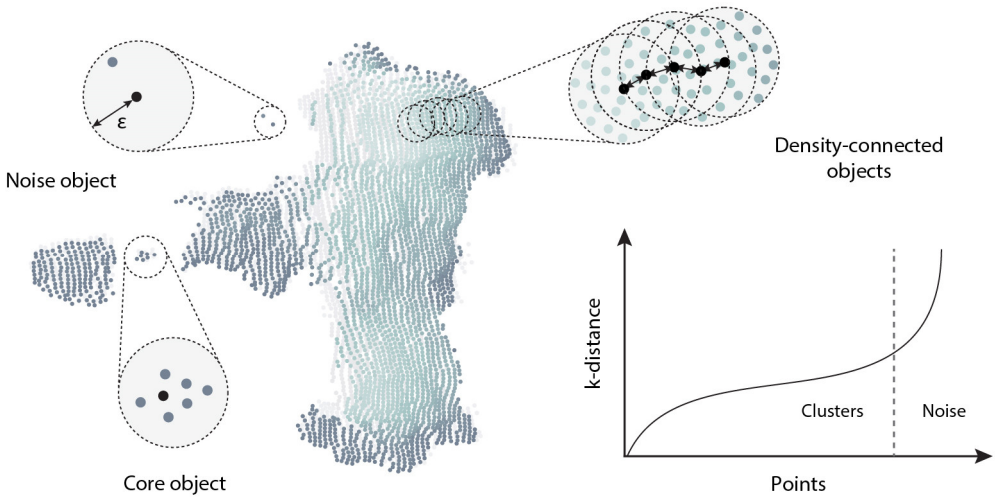

Figure 3.08 *Principles of the DBSCAN technique illustrated using three rockfall events recorded at Staithes over a 10 month monitoring period between August 2014 and June 2015. Inset: sorted 6^{th}-distance graph for the rockfall points, where the point of inflection is used to define the value of ε.*

After merging the filtered pre- and post-event rockfall inventories, each block of points was run sequentially using a parallel DBSCAN algorithm (PDSDBSCAN-S) developed by Patwary *et al.* (2012) for shared memory computation. Parallelisation of the algorithm achieves considerable speedups when compared to traditional approaches, and is therefore optimised for large volumes ($> 10^7$ points) of high-dimensional data. *MinPts* was set to 6 (2 × the number of dimensions) and ε was determined by plotting the 6^{th}-distance graph for the rockfalls in each block and averaging the distance at the point of inflection, p, for all blocks ($\varepsilon = 0.45$ m). The results for each block were manually verified, and any noise objects were filtered out of the dataset. For each monitoring period, this yielded 38 files containing the *x, y*, and *z* coordinates of each rockfall point and a unique class identifier, which is used as the rockfall ID.

3.2.5 Meshing and volumetric characterisation

The use of triangulated surfaces for surface reconstruction and the volumetric characterisation of objects is well-established, and attempts to quantify rockfall volume and shape have been made using the alpha shapes method on a site-specific scale (Guerin *et al.*, 2014; Carrea *et al.*, 2015; van Veen *et al.*, 2017). These are often subject to considerable post-processing in order to ensure a watertight mesh and fail to provide error estimates for the calculated volumes. Here, the PowerCrust algorithm was used to construct a watertight triangular surface mesh for each rockfall (Amenta *et al.*, 2001). This algorithm is depicted in 2D for simplicity (Figure 3.09). For a given group of points, S, the PowerCrust algorithm is able to extract a simplified skeletal shape, or the medial axis, which is then used to produce a surface representation of the points. The medial axis transform (MAT) represents a solid by the set of maximal balls completely contained in its interior (Figure 3.09a). The MAT is approximated by a subset of Voronoi vertices of S, called poles, which lie near the medial axis (Figure 3.09b). The balls surrounding the poles are known as polar balls (Figure 3.09c), the radius of which determines the weighting of each pole. An inverse transform is approximated by using a power diagram of the weighted poles. This acts like a weighted Voronoi diagram by dividing space into polyhedral cells (Figure 3.09d). These are then divided into interior and exterior faces, where the boundary of separation of these subsets forms the output surface, or PowerCrust (Figure 3.09e). The PowerCrust is therefore a watertight boundary of the 3D solid described by the approximate MAT (or power shape), and eliminates the need for the polygonalisation, hole-filling, or manifold extraction post-processing steps required in other surface reconstruction algorithms (Berger *et al.*, 2014; Lim and Haron, 2014).

The MATLAB® implementation of the PowerCrust algorithm was used on an event-by-event basis to construct a watertight triangular surface mesh for each rockfall (Sanche, 2016). The algorithm uses each set of rockfall points and a tolerance, defined between 0 and 1, as inputs. The tolerance is used to determine the inner and outer poles of the power diagram, which defines the boundary of the power crust (Figure 3.09d). In the majority of cases, a higher tolerance yields a

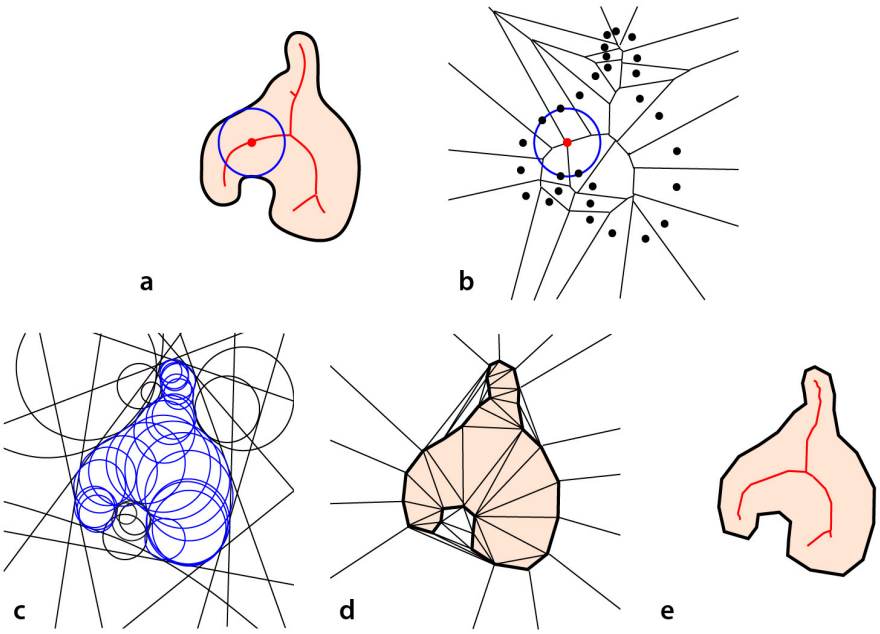

Figure 3.09 *Principles of the PowerCrust algorithm, where (a) shows an object with its medial axis, with one maximal interior ball, (b) the Voronoi diagram of S, with the Voronoi ball surrounding one pole, (c) the inner and outer balls, (d) the power diagram cells of the poles, labelled inner and outer, and (e) the power crust and power shape of the solid. Diagram adapted from Amenta et al. (2001).*

more robust fit, although this varies from mesh to mesh. To ensure the most robust fit in every case, each rockfall was meshed at nine different tolerances and the mesh closest to the average volume of the nine resulting meshes was chosen. The lower and upper bounds of the calculated rockfall volumes, interpreted here as the minimum and maximum rockfall volume, were then determined for each rockfall by using the smallest and largest possible meshes. An example of the outcome of this process is shown in Figure 3.10. It should be noted that the error in volume estimates is conditioned by the number of meshing configurations available for each set of points: if there is only one meshing configuration for a set of points, the error is reported as ± 0.00 m^3.

The volume and centre of mass of each rockfall mesh was calculated using the divergence theorem, a process that is described in detail in *Appendix C* (*p.* 183) and is summarised here. All rigid bodies, and therefore their parameters, can be expressed in terms of 3D moments (Semechko, 2014). Closed-form expressions for the 3D moments of objects represented by triangular surface meshes can be derived and used to calculate volume, V, which is equal to the zeroth moment:

$$V = m_{0,0,0} \qquad [3.2]$$

and the position of the centre of mass:

$$\bar{x} = \frac{m_{1,0,0}}{m_{0,0,0}} \qquad \bar{y} = \frac{m_{0,1,0}}{m_{0,0,0}} \qquad \bar{z} = \frac{m_{0,0,1}}{m_{0,0,0}} \qquad [3.3]$$

which is equal to the value of the first moments of x, y, and z, divided by volume. The surface area, width, depth, and height of each rockfall mesh were also calculated for each rockfall. For each monitoring period, this yielded a database of rockfalls spanning the length of the North Yorkshire coastline between Skinningrove and Sandsend (*ca.* 20.5 km of cliffs). The properties recorded in the rockfall databases are listed in Table 3.02 and will be used in this chapter to consider spatial variations in rockfall activity and the resulting erosion, and in *Chapter 4* to consider the structural control on rockfalls.

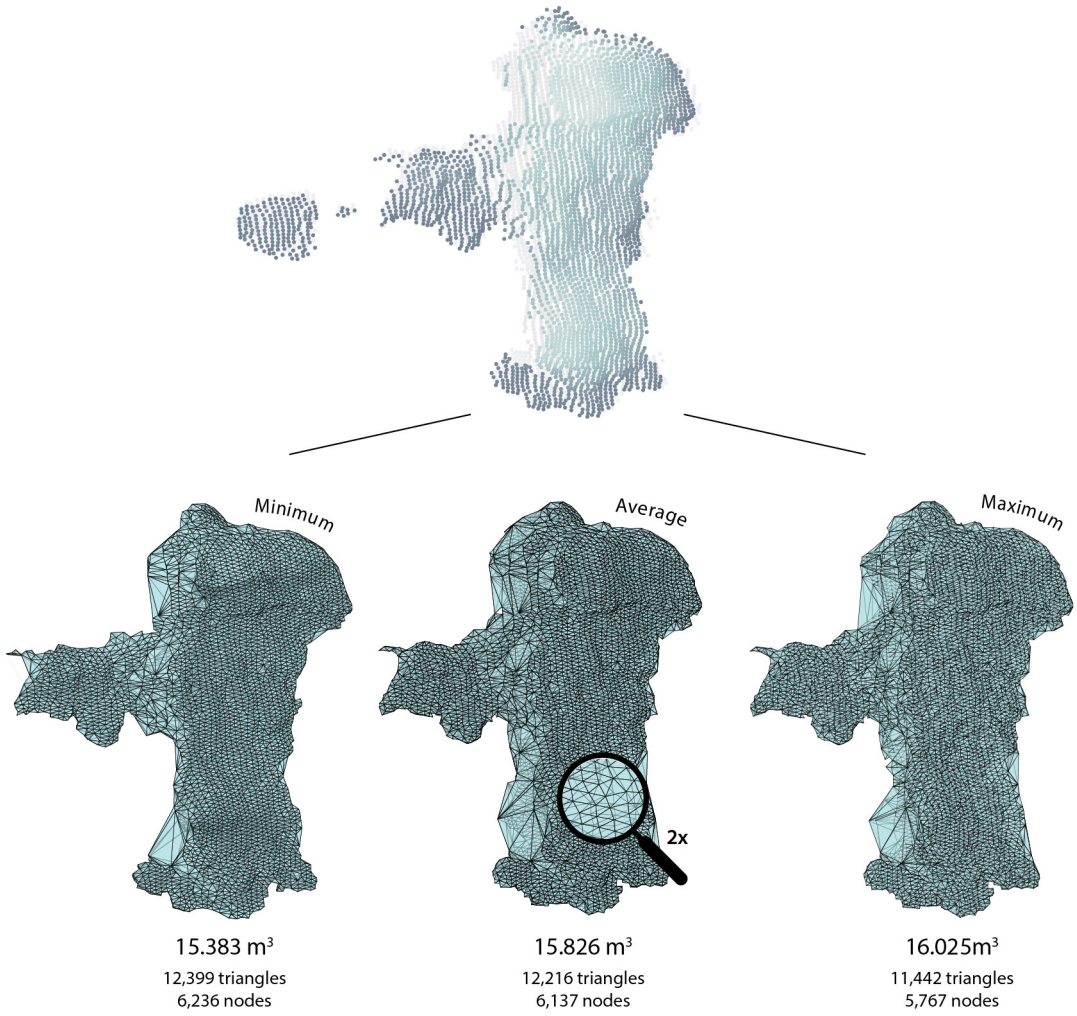

Figure 3.10 *Three 3D triangular surface meshes generated using the PowerCrust algorithm. The minimum, average, and maximum possible mesh sizes for the given rockfall are shown.*

Table 3.02 *Summary of the properties recorded for each rockfall in the inventory.*

Rockfall mesh	*Centre of mass*			*Axis length*			*Surface area*			*Volume*		
	-			*m*			m^2			m^3		
Nodes, triangles	x	y	z	a	b	c	Min	Mean	Max	Min	Mean	Max

3.2.6 Negative power law estimation

It is well-established that rockfall magnitude-frequency distributions exhibit a negative power law scaling that can be modelled using:

$$f(V_R) = sV_R^{-\beta}, \quad [3.4]$$

where $f(V_R)$ is the frequency density of a rockfall of magnitude V_R, and s and β are empirical constants (Malamud *et al.*, 2004). These provide an indication of the level of activity and relative size distribution in an inventory, respectively. Power law scaling relationships were therefore fitted to each rockfall inventory, in order to assess both along-coast and up-cliff variations in the magnitude and frequency of rockfall activity. For each inventory, rockfall magnitude-frequency was plotted on logarithmic axes using logarithmically binned data. Frequency densities were calculated for events of differing magnitudes using the formula provided by Malamud *et al.* (2004):

$$f(V_R) = \frac{\delta N_R}{\delta V_R}, \quad [3.5]$$

where δN_R is the number of rockfalls with volumes that fall within the range of δV_R, and δV_R is the associated bin width. Parameter estimation was undertaken using least squares regression on the logarithmically transformed data (Goldstein *et al.*, 2004). This is in keeping with previous research undertaken along the coastline and ensures full comparability with other findings. Due to the high rate of rockfall along the cliffs (Lim *et al.*, 2005, 2010; Rosser *et al.*, 2005a, 2005b, 2007, 2013; Barlow *et al.*, 2012; de Vilder *et al.*, 2017), the effect of superimposition and coalescence of rockfall scars on the form of the magnitude-frequency distribution is also assessed by comparing the scaling coefficients s and β derived from annual inventories to those of a change detection between the first and last survey only.

3.2.7 Spatial variations in power law scaling parameters

Although the length of time over which rockfall frequency estimates are made is known to exert a profound influence on β (Barlow *et al.*, 2012; Williams *et al.*, 2018), the length scale, L, over which a single power law can be applied remains poorly constrained. Many previously reported observations do not indicate whether power laws derived on a site-specific basis ($L < 10^2$ m) can adequately explain behaviour over larger spatial scales ($L > 10^3$ m). Given the emerging need to address this scale of investigation (Kennedy *et al.*, 2017), the effect of using a variable length scale to calculate β was considered. The size of the longest rockfall axis, 100 m (see inset, Figure 3.11a), was used to determine the minimum window size, L, which also approximates a common scale of site-specific monitoring (for example, Lim *et al.*, 2010). L was

increased in 100 m increments to a maximum window length $L_{max} = 24$ km, which is equal to the length of coastline monitored. For each value of L, β was estimated using a sliding window of length L, repeating for 240 iterations, I. The sliding distance, S, of the window is inversely proportional to its length:

$$S = \frac{L_{max} - L}{I}. \quad [3.6]$$

For every iteration, a negative power law was fitted to all rockfall volumes that fell within the sliding window. The distribution of the 240 β values obtained for each window length was used to assess the influence of the scale of monitoring on rockfall magnitude-frequency relationships.

3.3 Results

Quantifying rockfall activity has proven problematic, particularly at the regional scale, with a range of approaches currently drawn upon (*Section 3.1*). In order to bridge this gap, a novel workflow was presented in *Section 3.2* that has been used to detect and characterise regional-scale rockfall activity from airborne LiDAR data, providing an inventory of > 58,000 rockfalls along 20.5 km of cliffs on the North Yorkshire coast, UK. The results of these procedures are presented and discussed in the following sections.

3.3.1 Rockfall magnitude, frequency, and cliff erosion

Over 58,000 rockfalls were observed along 20.5 km of cliffs along the North Yorkshire coast between August 2014 and March 2017. The area monitored constitutes *ca.* 805,739 m^2 of cliff face, with an average cliff height of *ca.* 40 m (Table 3.03). Rockfalls ranged in volume from $< 0.0001 \pm 0.00$ m^3 to $15{,}498.05 \pm 552.36$ m^3, with a mean rockfall volume of 2.15 ± 0.24 m^3 (Table 3.03). Rock yield totalled 124,843.31 m^3, equalling an average erosion rate of 0.06 m yr^{-1}, which is the same order of magnitude as rates derived from previous terrestrial monitoring of rockfalls between Boulby and Staithes (Table 2.01, *p.* 19) and represents the best estimate available for erosion along this stretch of coastline. Across the inventories, the average meshing error for the total eroded volume is ± 10.73%, which is relatively low despite the conservative approach used to calculate error margins in *Section 3.2.5* (Abellán *et al.*, 2014).

The magnitude-frequency distributions for rockfalls captured over the three monitoring periods were modelled using negative power law scaling relationships (Figure 3.11a), where the exponent β ranged from 1.54 (2016 – 2017) to 1.69 (2014 – 2015). These values fall inside the 1.00 – 2.00 range commonly found for non-cumulative plots of rockfall volume-frequency density (see *Appendix D, p. 187* for relationships derived from previous terrestrial monitoring of rockfalls). In all cases, the data only follow a negative power law for events greater than 1×10^{-3} m^3. This is

attributed to censoring by under-sampling and other biases, such as the threshold that was set for the minimum detectable change (0.10 m) during data processing, as well as differences in the way that cloud-to-cloud comparison methods identify insignificant change. Another important difference is that DBSCAN requires the user to set a minimum number of points to be defined as a cluster, meaning that the smallest changes (here $< 0.1\%$) are unlikely to be resolved using meshing approaches. All parameters quoted hereafter are for power laws fitted to the uncensored data only. The superimposition and coalescence of rockfalls has the effect of lowering the power law coefficient of the single change detection over a period (2014 – 2017) relative to that derived from more frequent sampling over the same period (Figure 3.11b). This explains the decrease in the overall number of rockfalls observed (from 58,032 to 25,969), and a corresponding increase in individual rockfall volumes. Yearly monitoring periods were therefore used for further analysis.

The mean erosion rate varied between years, increasing by an order of magnitude from 0.02 m yr^{-1} (2014 – 2015) to 0.10 m yr^{-1} (2016 – 2017; Table 3.03). This change is partly driven by an increase in the rate of rockfalls year-on-year, but is mostly accounted for by the occurrence of eight large ($> 1{,}000$ m^3) cliff collapses, comprising half of the total volumetric flux observed during 2016 – 2017. The mean rockfall volume more than trebled in this time, from 0.99 ± 0.04 m^3 (2014 – 2015) to 3.31 ± 0.28 m^3 (2016 – 2017), while the median (*ca.* 0.01 m^3) and mode

Table 3.03 *Variations in rockfall activity along the North Yorkshire coast, UK, from 2014 – 2017.*

	Date		
	2014 – 2015	*2015 – 2016*	*2016 – 2017*
Cliff length (m)	20,459	20,459	20,459
Cliff area (m^2)	746,539	854,958	815,719
Number of rockfalls (-)	14,460	18,729	24,843
Mean rockfall volume (m^3)	0.99 ± 0.04	1.51 ± 0.11	3.31 ± 0.28
Median rockfall volume (m^3)	0.02	0.02	0.01
Rockfall density (m^{-2})	0.02	0.02	0.03
Minimum eroded volume (m^3)	11,467	21,600	69,727
Average eroded volume (m^3)	14,375	28,291	82,177
Maximum eroded volume (m^3)	15,076	30,344	89,223
Dry cliff volume eroded (%)	92	95	97
Wet cliff volume eroded (%)	8	5	3
Erosion rate (m yr^{-1})	0.02	0.04	0.10
Standardised yield (m^3 m^{-1} yr^{-1})	0.87	1.63	4.13

Notes: Monitored cliff area calculated by measuring the surface area of a point cloud-derived mesh. Standardised yield is calculated per linear coastline m, per annum.

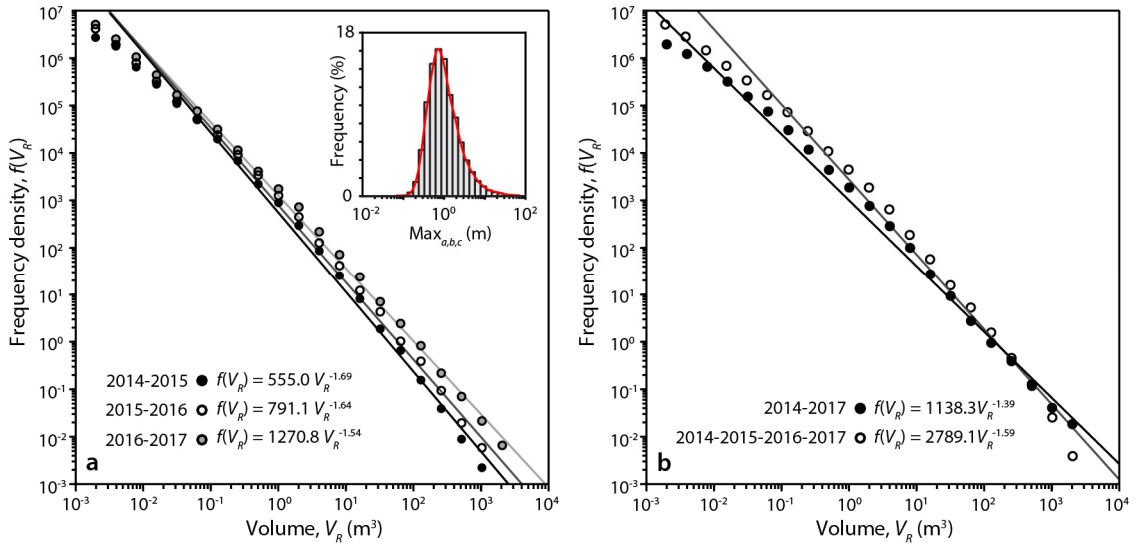

Figure 3.11 *Power law scaling and parameter estimations for (a) 2014 – 2015 (r^2 = 0.95), 2015 – 2016 (r^2 = 0.95) and 2016 – 2017 (r^2 = 0.98). Inset: histogram and corresponding kernel density estimate of the longest rockfall axis across all three inventories, and (b) the effect of superimposition of rockfall scars on power law plots. Data with a ca. 10-month sampling resolution (r^2 = 0.97) are plotted alongside that derived from a ca. 32 month sampling resolution (r^2 = 0.91).*

(*ca.* 0.2×10^{-2} m^3) remained relatively constant. The dominance of larger events is also reflected in the volume-frequency scaling exponent, β, which decreases through time (Figure 3.11a). Year-on-year, events of all magnitudes increased in frequency, marking an overall increase in the rate of rockfall activity along the coastline. Rock yield averaged 2.32 m^3 per linear meter of coastline per year, which approximates a mean areal cliff erosion rate of 0.06 m yr^{-1} (Table 3.03).

3.3.2 Spatial variations in erosion rates

Erosion rates derived in 100 m bins along the coast are highly variable within years (Figure 3.12), ranging from as much as 1.12×10^{-5} – 1.63 m yr^{-1} (2016 – 2017). Erosion rates at a number of cliff sections sharply increased over the monitoring period, most notably at Port Mulgrave, which eroded at an average rate of < 0.002 m yr^{-1} during 2014 – 2015. Due to a number of large rockfalls and landslips (31,943.47 m^3 in total), this rate increased to 0.04 m yr^{-1} (2015 – 2016) and then 0.28 m yr^{-1} (2016 – 2017). Although erosion rates along the coast are highly variable, in other places there are consistent patterns of spatial variation over time and space (Figure 3.12). Variations in erosion rates are often systematic across contiguous sections of the coastline, rather than showing a more random distribution where erosion rates vary independently between adjacent cliff sections. Sections with notably high rates include the *ca.* 3.5 km stretch of cliffs between Boulby and Cowbar Nab, which eroded at an average rate of 0.02 m yr^{-1} during 2014 – 2015, increasing to a rate of 0.07 m yr^{-1} during 2016 – 2017 (Figure 3.12). The highest rates of erosion along the coastline are observed here, with local erosion rates regularly exceeding 0.05 m yr^{-1} and reaching 1.47 m yr^{-1} in the event of a cliff collapse (15,498.05 ± 552.36 m^3, 2016

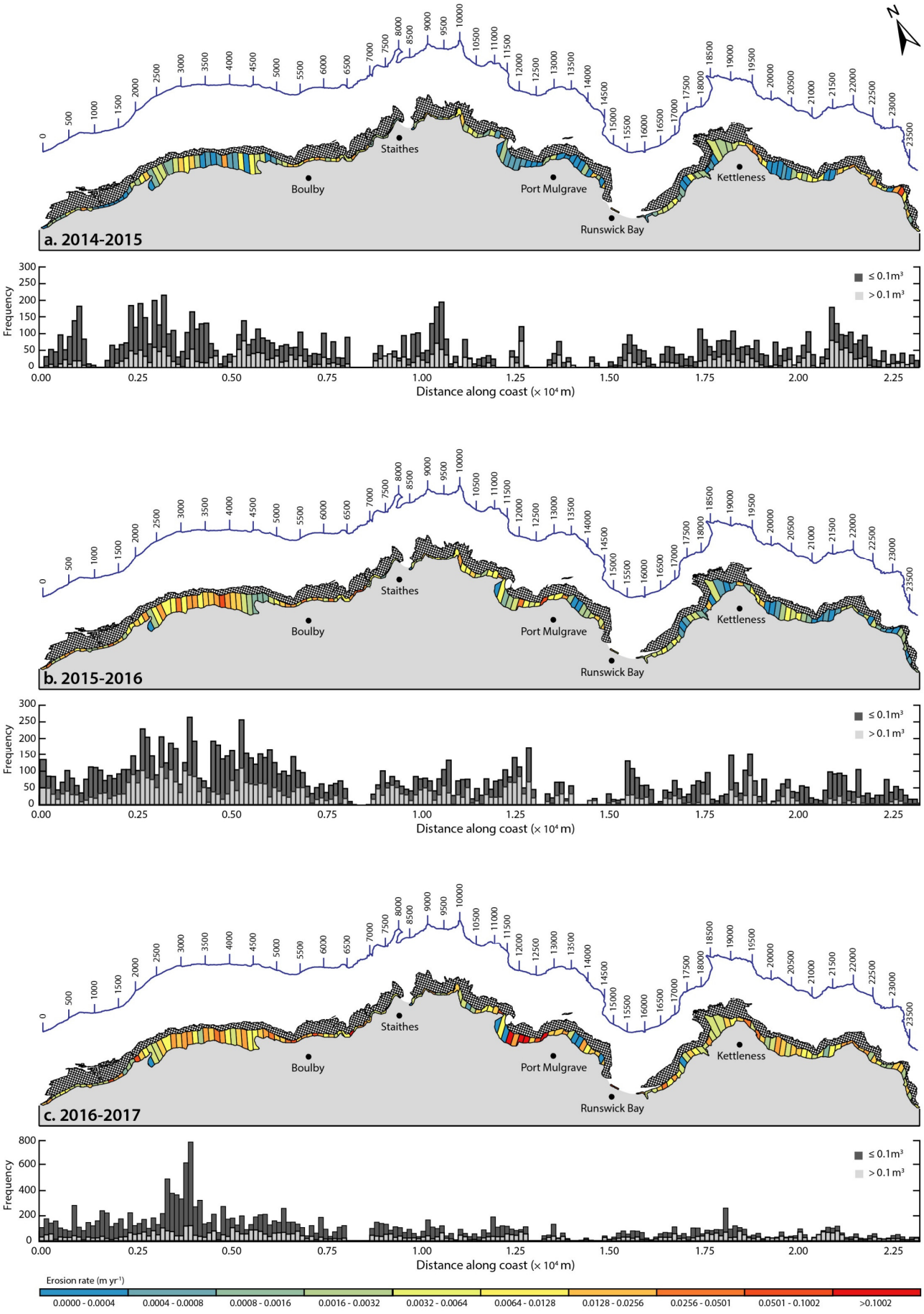
N
Staithes
Boulby
Port Mulgrave
Runswick Bay
Kettleness
a. 2014-2015
b. 2015-2016
c. 2016-2017
Frequency
≤ 0.1m³
> 0.1 m³
Distance along coast (× 10⁴ m)
Erosion rate (m yr⁻¹)
0.0000 - 0.0004
0.0004 - 0.0008
0.0008 - 0.0016
0.0016 - 0.0032
0.0032 - 0.0064
0.0064 - 0.0128
0.0128 - 0.0256
0.0256 - 0.0501
0.0501 - 0.1002
>0.1002

Figure 3.12 *Overleaf. Rates of erosion monitored along the North Yorkshire coast, UK, from (a) 2014 – 2015, (b) 2015 – 2016, and (c) 2016 – 2017. The monitored cliff area is divided into 100 m bins and coloured by erosion rate. The frequency of small (≤ 0.1 m³) and large (> 0.1 m³) rockfalls is also shown.*

– 2017). The highest frequencies of both small (≤ 0.1 m^3) and larger (> 0.1 m^3) rockfalls occurred along this stretch of cliffs (Figure 3.12), with over 11,000 of the recorded 58,032 rockfalls having occurred here. This is partly attributable to the fact that the cliffs between Boulby and Staithes are the highest along the coastline, reaching up to 150 m towards Boulby. North-facing sections of the coast such as Boulby show the highest rates of erosion, most likely due to their exposure to easterly and northerly North Sea storm wave events in comparison to the relatively sheltered embayments such as Runswick Bay, which eroded at an average rate of 0.005 m yr^{-1} between 2014 and 2017. Erosion rates also remained low at Kettleness throughout the monitoring period.

3.3.3 Spatial variations in power law scaling parameters

The relationship between β and the window length, L, was modelled using a two-term power series model (Figures 3.13a-b). Over each monitoring period, an inflection occurred at $L \approx 2.5$ km (Figure 3.13a), indicating that monitoring at length scales < 2.5 km has a significant effect on the frequency estimates of the largest events, potentially giving rise to considerably higher frequencies than is the case. This similarity occurs despite differences in β between years. The inflection implies that a magnitude-frequency distribution that is physically meaningful for modelling regional cliff erosion only becomes stable when captured at measurement length scales that exceed this distance (equivalent to a cliff area of *ca.* 1×10^5 m^2 assuming an average cliff height of 40 m), when surveyed at approximately annual intervals. This is pertinent for research using terrestrial LiDAR to monitor rockfall activity, of which there is an abundance, as this typically operates over only short length scales (see Abellán *et al.*, 2014 for a review).

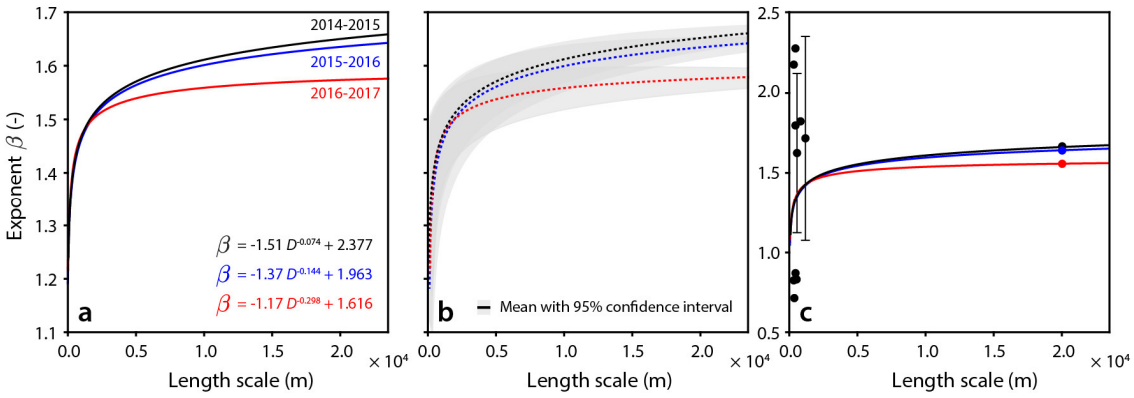

Figure 3.13 *Relationships between β and the length scale of monitoring, L, from (a) 2014 – 2015 (r^2 = 0.97), 2015 – 2016 (r^2 = 0.98), and 2016 – 2017 (r^2 = 0.99). The relationships were modelled using a two-term power series model, with confidence intervals shown in (b), and in (c) the data are plotted alongside β values derived from previous monitoring of rockfalls along the North Yorkshire coast (Table 3.04).*

Rates of erosion derived from previous monitoring vary between 0.004 m yr^{-1} and 0.128 m yr^{-1}, capturing well the mean rate of erosion along the coastline but poorly representing the extremes of the rockfall volume distribution and, importantly, their contribution to coastal erosion rates (Figures 3.14a-b). Values of β derived from previous terrestrial monitoring of rockfalls at a number of sites along the North Yorkshire coast range between *ca.* 0.60 and 2.40 (Figure 3.13c). These sites were monitored at length scales ≤ 600 m and at approximately equal monitoring intervals (*ca.* 30 days). Given that the data indicate that values of β converge when the spatial extent of monitoring is increased beyond $L \approx 2.5$ km, the influence of monitoring over a continuous section as compared to monitoring multiple segments that in total are at least this length scale is considered. Neighbourhood differences in the erosion rates shown in Figure 3.12 indicate that, for years with less intra-annual variability, there is a relatively small difference between each 100 m bin and its neighbours (Figure 3.14c), suggesting that there is more structure (or less variation) in the erosional signal if contiguous cliff sections are monitored. This suggests that, to overcome local (10^2 m) structure in the data and to assess more general behaviour of the coastline, the 2.5 km of monitoring should be distributed along-coast in multiple segments, rather than concentrated in one continuous stretch.

3.3.4 Vertical distribution of erosion

Measurements of cliff top recession (Lee and Clark, 2002) do not record the processes of undercutting and small scale, iterative failures that occur across the cliff face and lead to profile form adjustment through time. Here, erosion profiles show the pattern of net cliff change over each monitoring period, representing how erosion results from the cumulative imprint of rockfalls,

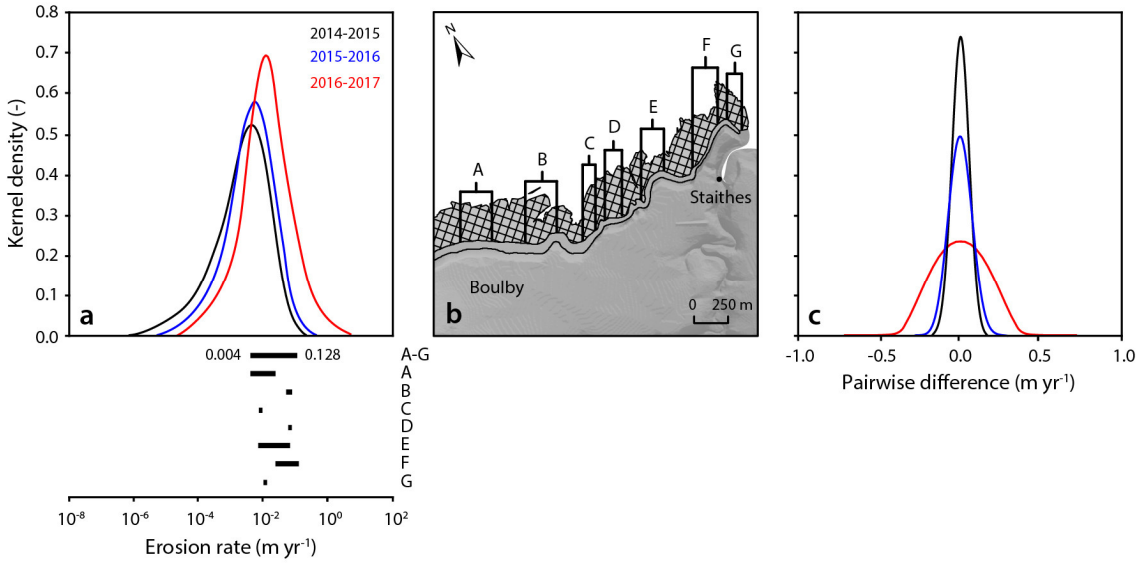

Figure 3.14 *(a) Distribution of the rates of erosion monitored along the North Yorkshire coast (shown in Figure 3.12), with rates derived from previous terrestrial monitoring at the sites shown in (b) also plotted (Table 2.01, p. 19), and (c) pairwise differences in erosion rate between each 100 m bin and its neighbours.*

Table 3.04 *Absolute β values derived from previous terrestrial monitoring of rockfalls along the North Yorkshire coast. Data are used in Figure 3.13c.*

Location	*Cliff dimensions*		*β*	*Date*	*Interval*	*Reference*
	width, m	*height, m*	-	*mm/yy*	*days*	-
N. Yorkshire	20,459	20 – 150	1.69	08/14 – 06/15	294	This study
N. Yorkshire	20,459	20 – 150	1.64	06/15 – 04/16	310	This study
N. Yorkshire	20,459	20 – 150	1.54	04/16 – 03/17	356	This study
Boulby – Staithes	604	22 – 55	1.12 – 2.37	09/02 – 05/05	~30	Rosser *et al.* (2013)*
Boulby – Staithes	482	35 – 71	1.80	10/03 – 04/05	~30	Lim *et al.* (2010)
Boulby – Staithes	482	22 – 55	1.12 – 2.12	09/03 – 03/05	~30	Barlow *et al.* (2012)*
Boulby	88	55	2.17	07/08 – 06/10	~30	Norman (2012)
Boulby	300	60	0.82	05/12 – 06/14	~30	Whadcoat (2017)
Cowbar	130	37	0.71	05/12 – 06/14	~30	Whadcoat (2017)
Cowbar	85	37	0.82	05/12 – 06/14	~30	Whadcoat (2017)
Staithes	220	33	0.86	05/12 – 06/14	~30	Whadcoat (2017)
Whitby	215	60	2.27	03/15 – 12/15	1 h	Williams *et al.* (2018)
Whitby	215	60	1.78	03/15 – 12/15	30	Williams *et al.* (2018)

** Denotes papers that provide monthly variations in β, which is given here as a range.*

which may map more directly onto potential drivers (Figures 3.15a-c). Year-on-year, the distribution of eroded depths varies up cliff. Erosion at the toe is marked by a pronounced inflection in β, indicating that the size distribution of rockfall activity below the elevation of the highest astronomical tide is dominated by relatively large, more episodic failures. This contradicts the widely-accepted notion that cliff toe erosion occurs iteratively through abrasion, attrition, and rapid void pressure changes that lead to fracture and detachment (for example, Trenhaile, 1987; Carter and Guy, 1988; Sunamura, 1992; Hampton, 2002; Young and Ashford, 2008). However, the small number of relatively large rockfalls occurring in the wet zone contributes little to the overall erosion: an average of only 5.13% of the eroded volume occurred in this zone, despite representing 10.70% of the total cliff area (Table 3.03). Profiles of erosion rate up cliff show similar trends, with some of the lowest rates of erosion occurring at the cliff toe (Figure 3.16).

Above the cliff toe, the value of β remains stable up to a height of *ca.* 60 m, indicating that, year-on-year, the relative volume of material contributed by events of varying sizes stabilises above the limit of marine influence, where the majority of change is driven by episodic, larger-scale failures (Figures 3.15a-c). This suggests that, where subaerial processes begin to dominate, erosion is primarily driven by incremental wasting, and that the onset of these processes can be constrained using variations in rockfall magnitude-frequency up cliff. These gradual changes in β

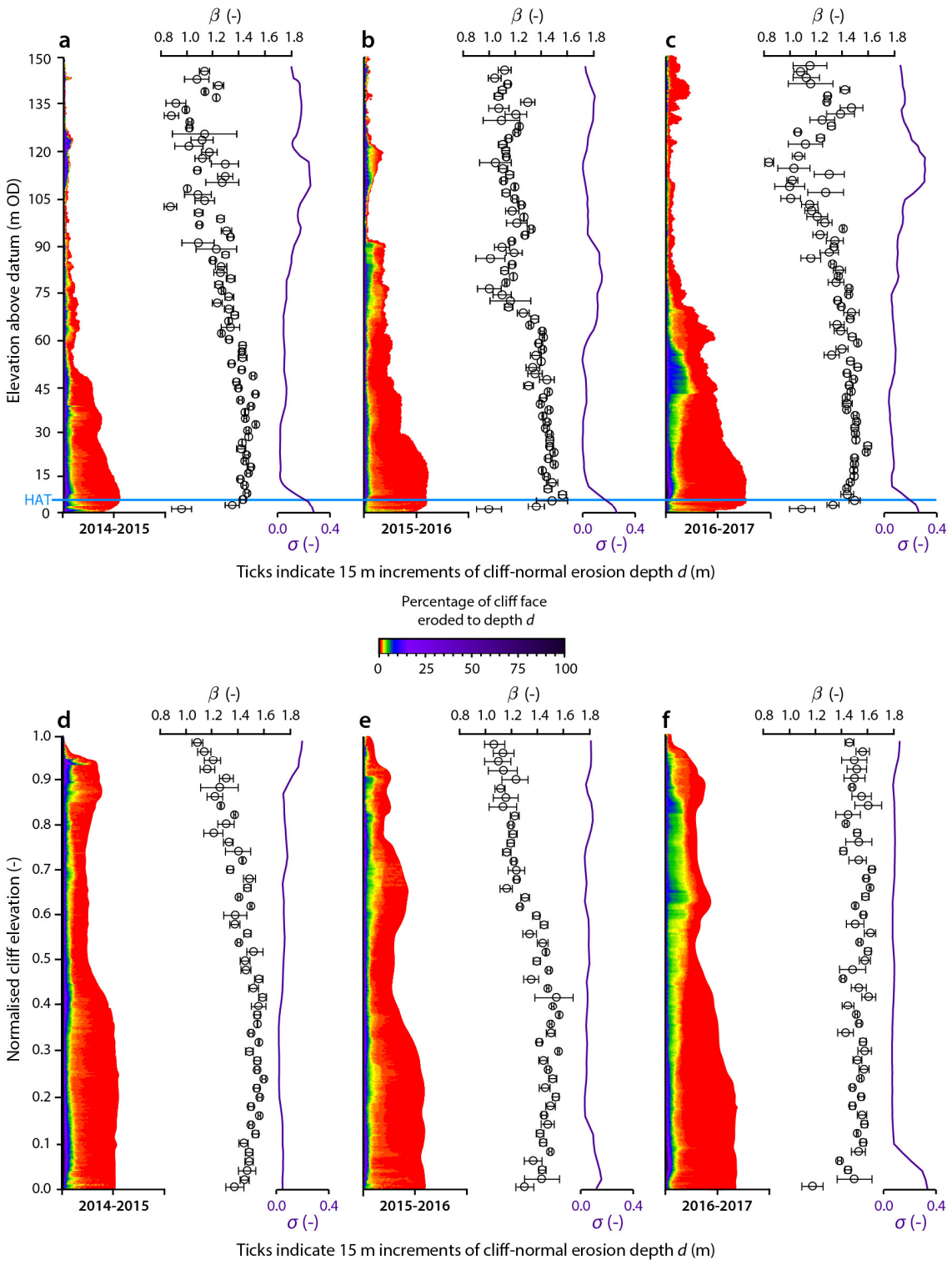

Figure 3.15 *Erosion monitored along the North Yorkshire coast, UK, between (a) 2014 – 2015, (b) 2015 – 2016 and (c) 2016 – 2017. In the upper panel, the vertical distribution of erosion depths (d) is shown in coloured shading (0.2 m bins). The exponent of the magnitude-frequency distribution, β, is shown alongside (2.0 m bins). In the lower panel, local cliff heights have been normalised to illustrate the effect of relative position up cliff between (d) 2014 – 2015, (e) 2015 – 2016 and (f) 2016 – 2017. The vertical distribution of erosion depths is shown in coloured shading (bin width = 0.002) and β is shown alongside (bin width = 0.02). Error bars were derived using minimum and maximum possible rockfall volumes. The variation in the exponent is shown in purple as the moving standard deviation, σ, of β (window length = 3) in both panels.*

may be linked to changes in the groundwater regime, weathering environment and the stress field up cliff. Above a height of *ca.* 60 m, the value of β begins to decrease. This trend is broadly consistent over time and is also evident when considering profiles of erosion depth that are normalised by cliff height (Figures 3.15d-f). Normalising the profiles by cliff height acts to smooth the vertical distribution of erosion depths, particularly in the lower half of the cliffs (normalised cliff elevation < 0.5). The high rates of toe incision evident in the raw data are largely smoothed out, as are large variations in β at the cliff tops, although there remains a general decrease in β from the cliff toe upwards. However, in both the raw and normalised data, the vertical distribution of material loss across the coastline in 2016 – 2017 is dominated by eight large ($> 1{,}000$ m^3), full-scale cliff collapses (Figures 3.15c and 3.15f).

The highest cliffs (at Boulby, for example) are prone to isolated zones of rockfalls, which often erode to a consistent depth (Figures 3.15a-c). These areas, which commonly occur at elevations > 100 m, are apparently uncoupled from erosion at the toe and are also characterised by large variations in β ($\sigma > 0.3$) and locally high erosion rates (Figure 3.16). With the exception of these rockfalls, rates of erosion are generally higher below *ca.* 70 m and decrease with height, implying that the average cliff profile is steepening over time (Figures 3.16a-b). This suggests that, over the shorter term, the dominant mode of cliff erosion leads to steepening with less frequent failures of the cliff top, resetting the global profile form by a number of full-scale cliff collapses (Figure 3.16c).

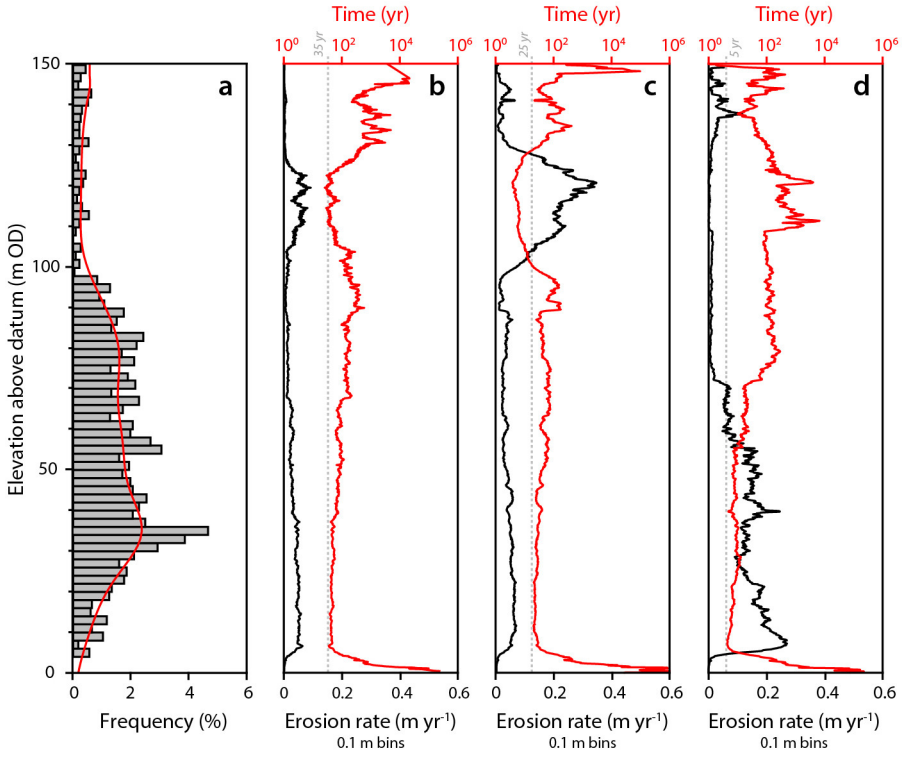

Figure 3.16 *(a) Distribution of cliff heights along the North Yorkshire coast, UK. The vertical distribution of erosion rates is also shown between (b) 2014 – 2015, (c) 2015 – 2016, and (d) 2016 – 2017. For each year, the erosion rate is plotted in 0.1 m bins (black) alongside its reciprocal, time, on a log scale (red).*

3.3.5 Cliff toe erosion

In the inundated toe (at elevations of *ca.* 0 – 4 m OD), the majority of change is driven by episodic, large-scale failures, across over 24 km of coastline. The vertical distribution of erosion at the toe is often modelled as a direct function of inundation duration (Sunamura, 1975, 1977; Trenhaile and Layzell, 1981; Carr and Graff, 1982; Belov *et al.*, 1999; Trenhaile, 2000, 2009, 2011; Walkden and Dickson, 2008; Ashton *et al.*, 2011), a relationship that has been incorporated into a number of widely-used numerical erosion models, including SCAPE (Walkden and Hall, 2005, 2011). The relationship between inundation duration and the vertical distribution of erosion at the toe of the cliffs along the North Yorkshire coast was therefore explored to assess whether such assumptions hold in respect of these data.

To approximate conditions across the coastline, monitored distal waves and tidal data are modelled using a transformation based on Battjes and Stive (1985) derived by Norman *et al.* (2013, Supporting Information). Data were used from the nearest available tide gauge (UK National Tide Gauge Network, Whitby, *ca.* 25 km south) and hourly significant wave heights obtained from an offshore wave buoy (CEFAS Wave Net, Whitby) to populate the model, which is run on 20 equally-spaced profiles along the coastline. The modelled tide, wave, and set-up elevations are then averaged across the profiles to give an approximation of the inundation durations along the coastline, over 2014 – 2017.

Aggregating monitored and modelled water elevation leads to a net elevation increase in the combined tide, wave and set-up signature in comparison to the observed tidal inundation duration alone. Over the monitoring period, erosion rates at the cliff toe appear to lag behind

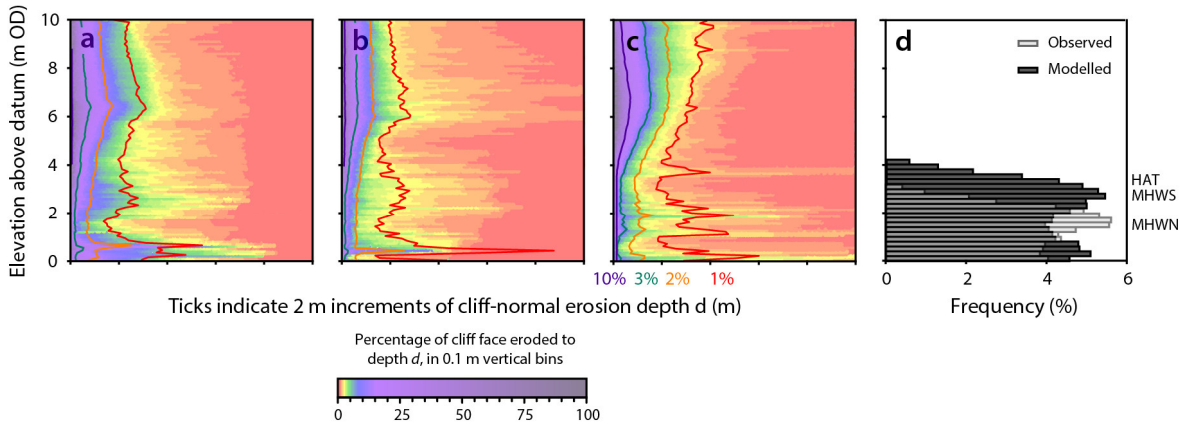

Figure 3.17 *Cliff toe erosion monitored along the North Yorkshire coast, UK, between (a) 2014 – 2015, (b) 2015 – 2016, and (c) 2016 – 2017. For each year, the vertical distribution of erosion depths (d) up the first 10 m of the cliffs is shown, with contours marking the position of the 1%, 2%, 3% and 10% depths. The observed tidal inundation frequency and combined tide and surge (monitored), wave and set-up elevations (modelled) are shown in (d) for the whole monitoring period (2014 – 2017). The highest astronomical tide (HAT), mean high water spring (MHWS), and mean high water neap (MHWN) are also labelled. These consider only tidal inundations, and not set-up and wave effects.*

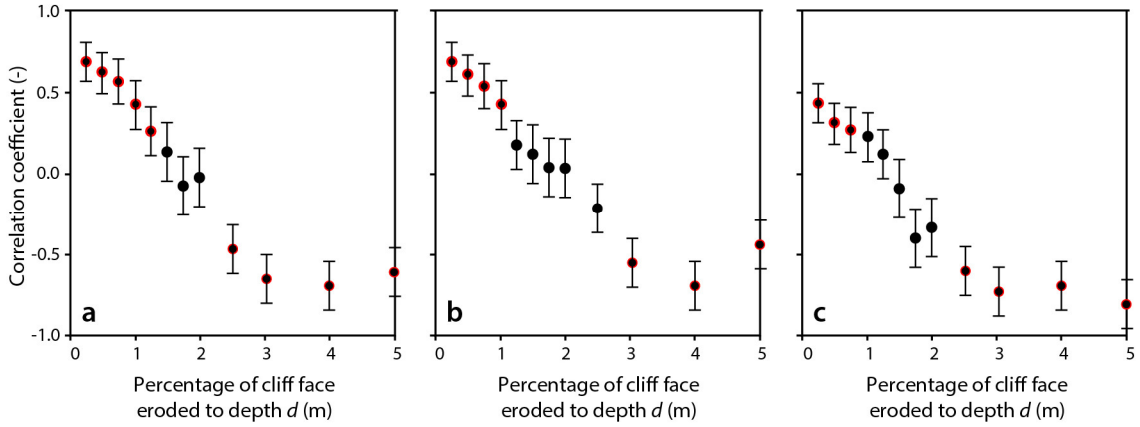

Figure 3.18 *Correlations between the vertical distribution of erosion depth (d) and inundation frequency (by height), plotted against the percentage of the cliff face eroded to depth d, between (a) 2014 – 2015, (b) 2015 – 2016, and (c) 2016 – 2017. Error bars show 95% confidence intervals. Red outlines indicate correlations that are statistically significant ($p < 0.05$).*

those of the cliff above (Figures 3.17a-c), although this is likely to vary in space based on variations in local rock mass strength and structure, and wave energy, which is conditioned by nearshore and foreshore bathymetry. The vertical distribution of erosion throughout the wet zone correlates well with modelled wave and set-up elevations, but only where erosion is most active (Figure 3.17d). Statistically significant ($p < 0.05$) correlations between inundation duration and erosion depth are only found across an equivalent of *ca.* 1.50% of the cliff toe between 2014 and 2017 (Figure 3.18). Across a greater proportion of the monitored cliff area this trend is reversed, and the cliff face is instead eroded to greater depths on and above the highest astronomical tide line (Figures 3.16 and 3.17), as indicated by a shift towards negative correlations (Figures 3.18a-c). This suggests that rising sea level may have a lesser impact upon this stretch of coastline than previous modelling may have predicted.

3.4 Summary

Using high-resolution, multi-temporal airborne LiDAR data, this chapter has explored regional-scale variations in rockfall magnitude and frequency, the extent to which these relations are sensitive to the spatial scale of monitoring, and patterns in the vertical distribution of erosion along the North Yorkshire coast. This work has shown that high-resolution airborne LiDAR provides a robust means to monitor rockfall activity and the resulting cliff retreat continuously (in space), in 3D, and over large spatial scales ($> 10^3$ m). The workflow presented here is semi-automatic, providing a 3D mesh, centres of mass and gravity, principal axes, and, uniquely, the volumetric uncertainty for each rockfall. The resulting inventory of rockfall activity has been used to show that:

1) Although erosion rates along the coast are highly variable, in many places there are consistent patterns of spatial variation over time.

2) With the exception of isolated zones of rockfall activity occurring at the cliff tops, the exponent of the magnitude-frequency distribution, β, and the erosion rate decrease with elevation. This is likely to be driven by changes in the weathering environment and stress field up cliff. Over time, this effect would cause the average cliff profile to steepen before being reset by numerous full-scale cliff collapses.

3) Year-on-year, inundation duration constitutes a significant control on erosion at the cliff toe, but only for $< 2\%$ of the monitored cliff length. Instead, the majority of the cliffs surveyed are consistently eroded to greater depths at elevations on and above the highest astronomical tide line. This suggests that, while there may be considerable impacts upon wave climate, rising sea levels may have a lesser effect upon this stretch of coastline than previous models would have predicted.

4) Rockfall magnitude-frequency relationships are highly sensitive to the spatial scale of monitoring, such that monitoring at length scales < 2.5 km significantly increases the frequency estimates of the largest events. This has considerable implications for research using terrestrial LiDAR to monitor rockfall activity, both in coastal and non-coastal environments, as any scaling relationships obtained previously may have incorrectly informed measures of risk reduction. However, it may be possible to assess more general patterns of rockfall occurrence across large length scales, provided that the 2.5 km of monitoring is distributed along the site in multiple segments, rather than concentrated in one continuous stretch.

The work presented in this chapter has upscaled previous work undertaken using terrestrial LiDAR on the North Yorkshire coast and shifted the focus towards understanding changes in rock slope morphology at the regional scale, allowing variability in drivers to be considered at scales previously inaccessible using terrestrial monitoring campaigns alone. The patterns of rockfall activity and distribution of erosion shown in this chapter will therefore be evaluated with respect to structural controls in *Chapter 4*, where other properties, including rockfall shape, are derived.

This page is intentionally left blank

Chapter 4

Evaluating structural controls on variations in rockfall activity

The relative importance of various conditioning factors for rockfall remains difficult to isolate on a regional scale. This is partly due to the methodological shortcomings associated with collecting high-resolution data at large scales ($> 10^3$ m). However, it also reflects the wider challenges associated with the fact that the local-scale causes of rockfalls occurring on individual rock slopes are likely to contrast with those that are causative over regional scales, due to emergent system behaviour and increasing system complexity with spatial scale (Messenzehl *et al.*, 2017). Although rock mass structure is known to play an important role in determining when, where, and how a rockfall may occur, regional-scale observations of variations in rockfall activity (*Chapter 3*) and rock mass structure (this chapter) remain scarce. The following discussion reviews rock mass structural properties and their roles as conditioning factors for rockfalls in *Section 4.1*. In *Section 4.2*, a workflow is presented that derives a detailed, quantitative appraisal of along-coast variations in the geometric properties of exposed discontinuity surfaces, which are known, to some extent, to control rockfall release. This section also describes the methods used to quantify rockfall shape and the clustering (or coalescence) of events over time, given that both are known to be defined by rock mass strength and structure. *Section 4.3* presents the results of this analysis: first by describing both up-cliff and alongshore variations in a number of rock mass structural properties (including joint spacing, density, dip, and the difference between joint orientation and cliff aspect), before assessing rockfall shape and identifying patterns in the distribution of rockfall shape as a function of volume. The results presented in *Section 4.3* are then used to explore how rock mass structure varies along the coastline, and to what extent patterns in the size and shape of rockfalls are related to differences in rock mass structure (*RQ2*). These findings are then summarised in *Section 4.4*.

4.1 Structural controls on rockfall activity

The stability of a rock slope is controlled by the mechanical properties and stress state of the rock mass, as well as the effectiveness of environmental forcing (Moore *et al.*, 2009). Although the relative importance of these controls on the mechanisms of erosion and overall cliff retreat are locally specific, both the role of intact rock strength and the presence and geometry of discontinuities (for example, spacing/density, orientation, persistence, and surface roughness) are known to play a major role in determining when, where, and how rockfalls occur (for example, Douglas *et al.*, 1991; Coe and Harp, 2007; Stead and Wolter, 2015). More specifically, the structural setting and spatial distribution of joint sets control rock mass fragmentation and eventual modes of failure, both in terms of block geometry and in terms of size. Rockfalls have previously been observed in areas with low intact rock strength (Selby, 1980; Vehling *et al.*, 2015), a high joint density (Sass, 2005; Loye *et al.*, 2012), and an unfavourable joint orientation relative to the cliff face strike (Cruden and Hu, 1994; Moore *et al.*, 2009). An illustrated example of some of the features of jointing, and their role in defining the broader scale surface topography of a rock mass, is provided in Figure 4.01.

Numerical modelling suggests that once a rockfall has occurred, critical levels of stress propagate along the failure surfaces at the near-surface, and that shear stresses along this surface reduce significantly with depth from the fracture surface (Wolters and Müller, 2008; Styles *et al.*, 2011). High-resolution monitoring of progressive collapses has given a considerable insight into the rates and patterns of failure propagation on rock-slopes (for example, Rosser *et al.*, 2007a; Abellán *et al.*, 2010; Stock *et al.*, 2011; Royán *et al.*, 2015). Stock *et al.* (2012b) considered a sequence of 14 progressive rockfall events that occurred over 15 months, highlighting the importance of stress redistribution from preceding rockfalls in conditioning subsequent instability in adjoining areas over time. Specifically, rockfalls propagated both upwards and laterally along sheeting joints, leading to high stress concentrations at the intersections of these discontinuities and promoting the development of new joints and failures. This effect has been observed elsewhere, with weathering, erosion, and eventually rockfalls favourably exploiting areas where there are high joint densities (Sturzenegger *et al.*, 2007). Similarly, Rohmer and Dewez (2015) applied spatial statistics to several thousand rockfall scars, inferring that progressive incremental failure is manifest as small rockfall events (10^{-3} – 10^{-2} m^3) that aggregate in clusters across the cliff face. On coastal cliffs, the propagation of rockfalls has been observed to facilitate the transmission of marine loading up the cliff face over time (Rosser *et al.*, 2013). These observations are supported by numerical modelling of the response of the rock mass to marine loading, which confirms the role of upward migration of shear strain through the cliff in causing tensile failure and crack growth at the cliff top (Styles *et al.*, 2011). The connectivity between events attests to the importance of stress redistribution following previous rockfalls in promoting damage accumulation and, eventually, further rock slope failure (Amitrano, 2006).

On coastal cliffs, the intersection between rock mass structure and marine forcing drives observable patterns in rockfall activity over time, where rockfalls facilitate the transmission of marine loading up the cliff face by exploiting structurally- or lithologically-defined discontinuities (for example, Rosser *et al.*, 2013; Vann Jones *et al.*, 2015). Although these observations have previously been made on a site-specific basis, they imply that consistencies in the spatial distribution of rockfall activity and cliff retreat observed in *Chapter 3* could be related to along-coast variations in, and interactions between, rock mass structure, cliff surface topography, and loading/unloading cycles driven by ocean waves (both in terms of the magnitude, frequency, and orientation of loading relative to existing fracture sets). This chapter therefore focuses on identifying structural controls on the rockfall activity observed in *Chapter 3*, before considering the local scale influences of wave impacting in *Chapter 5*.

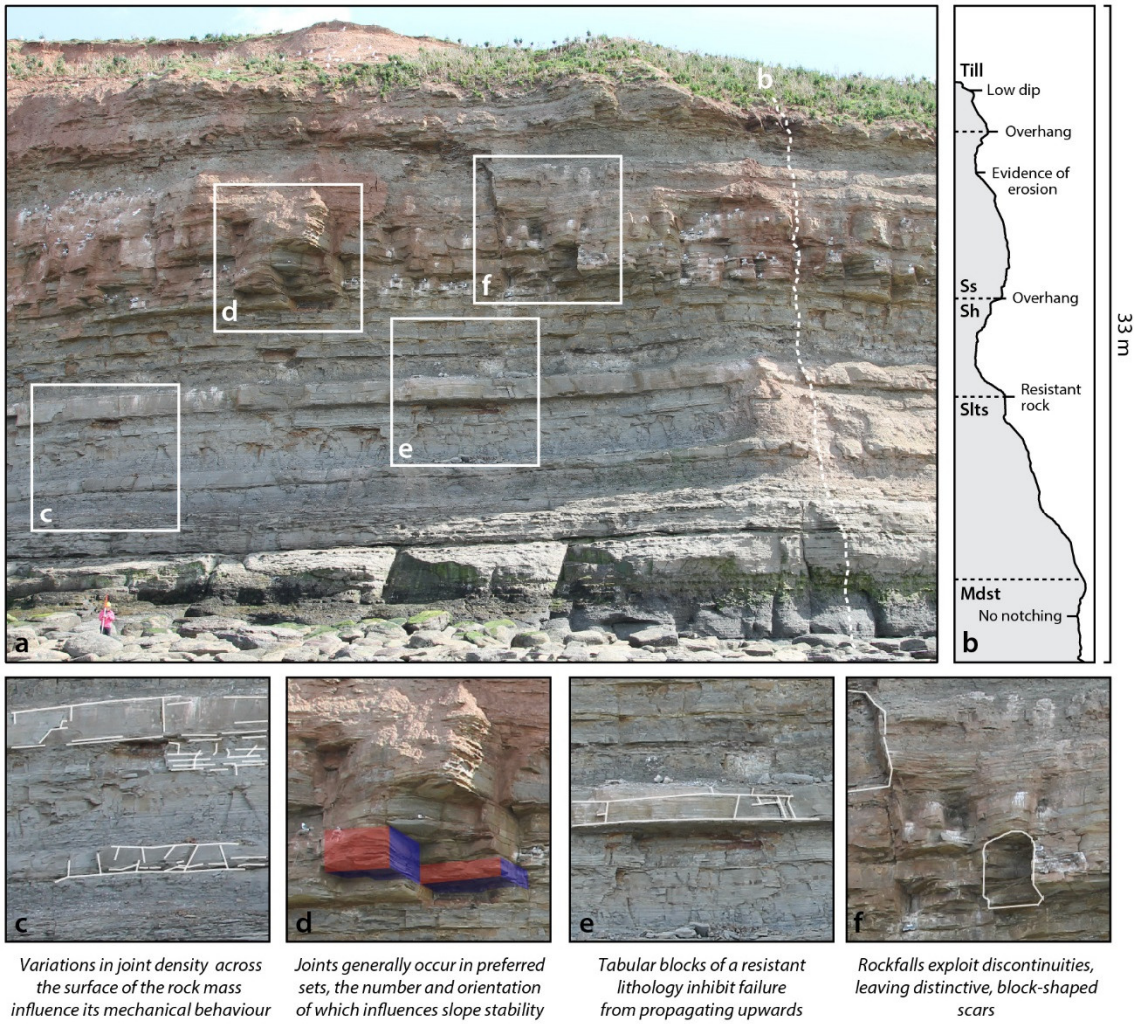

Figure 4.01 *Features of joints and jointing observed at Staithes, North Yorkshire, including (a) an image of the rock face at Staithes, with a profile of this section in (b), (c) evidence of variations in joint density across the surface of the cliffs, (d) variation in the orientation, or dip-direction, of joint sets. Here, three continuous and regular joint sets intersect an excavation surface to generate potentially removable blocks, and (e-f) show the role of lithology and block/scar shape in determining cliff face topography.*

4.2 Extracting surface structural information from point clouds

The findings in *Chapter 3* demonstrate that an entirely 3D approach to processing high-resolution airborne LiDAR data can provide a robust means to monitor rockfall activity. This allows cliff retreat to be characterised continuously in space, in 3D, and over large spatial scales ($> 10^4$ m). When mounted on a helicopter, continuous swaths from this type of LiDAR can be used to collect data along steep, near-vertical slopes, presenting a considerable advantage over mobile terrestrial LiDAR when scanning large areas that are limited by range and occlusion (Lato *et al.*, 2009a; Dunham *et al.*, 2017). Point cloud data obtained from close range applications of terrestrial LiDAR (scanner-object distances < 300 m) yield enhanced precision on slope angle, aspect, and, on bare rock faces, lineaments, and other structural features (see reviews by Sturzenegger and Stead, 2009 and Jaboyedoff *et al.*, 2012). Terrestrial LiDAR therefore enables measurement across the entire rock mass (Slob *et al.*, 2005; Assali *et al.*, 2014), with good agreement generally found between field measurements and LiDAR-derived estimates of several geometric properties of discontinuities (for example, Oppikofer *et al.*, 2009; Sturzenegger and Stead, 2009; Slob, 2010; Umili *et al.*, 2013; Riquelme *et al.*, 2015). However, it is crucial to recognise that both approaches measure only the exposed surfaces of discontinuities. These are subject to weathering and alteration by other surface processes, therefore requiring an assumption to be made regarding how representative they are of the surrounding rock mass.

Given that rock mass structure plays a critical role in defining both block geometry and size (*Section 4.1*), this section aims to derive a detailed, quantitative appraisal of along-coast variations in the geometric properties of exposed joint surfaces. A number of parameters known to influence rock slope stability, including the orientation of discontinuities (Slob *et al.*, 2005; Jaboyedoff *et al.*, 2007; Ferrero *et al.*, 2009; Gigli and Casagli, 2011; Sturzenegger *et al.*, 2011; Riquelme *et al.*, 2014), the spacing of discontinuities (Slob *et al.*, 2005; Oppikofer *et al.*, 2009; Riquelme *et al.*, 2015), and surface roughness (Haneberg, 2007; Sturzenegger and Stead, 2009; Oppikofer *et al.*, 2011), are extracted from the point cloud data described in *Chapter 3*. These are then related to individual rockfall properties, such as block shape and volume, as well as wider-scale variations in rockfall activity up-cliff and along-coast.

4.2.1 Data acquisition

Variations in rockfall activity along the North Yorkshire coast were characterised using the data and methods presented in *Chapter 3*. The data were collected at three approximately equal intervals between August 2014 and March 2017, giving four high-resolution point clouds captured along *ca.* 20.5 km of cliffs (Table 3.01, *p.* 29). During the surveys, the LiDAR system was housed in a protective pod on the front of the helicopter, to provide a 180° downward and sideways-looking field-of-view. This reduced the likelihood of an orientation bias in any surface dip and orientation data extracted from the resulting point clouds, as the data were not captured

at a single preferential incidence angle (Lato *et al.*, 2010). The system was deployed at an average flying height of *ca.* 100 m above the ground, yielding an average point density across the four surveys of *ca.* 50 points m^{-2} (corresponding to an average point spacing of *ca.* 0.15 m). Although this introduces a scale bias where discontinuity sets are below the point spacing (Sturzenegger and Stead, 2009), any data collected on discontinuities, field-derived or otherwise, must ultimately contain a cut-off below which certain features are not examined. Here, and in other research using LiDAR for the characterisation of discontinuities, the point spacing imposes a systematic cut-off that is approximately uniform across datasets. Though there is inevitably some variation between settings, Assali *et al.* (2014) found that variations in point spacing had little effect on the interpretation of discontinuities below a sampling resolution of 0.50 m.

4.2.2 Surface structural information

Following the processing steps undertaken in *Section 3.2.2* (*p.* 29), the open source software 'Facets' (Dewez *et al.*, 2016) was used to isolate and extract the geometry of exposed planar discontinuity surfaces, a process that is described in detail in *Section 4.2.2.1*. Given that the shape of rockfalls and their tendency to cluster (or coalesce) over time are, to an extent, defined by rock mass strength and structure (*Section 4.1*), both are quantified in *Sections 4.2.2.2* and *4.2.2.3*.

The 'Facets' detection routine (Dewez *et al.*, 2016), which is a plug-in to the open source point cloud processing software CloudCompare, was used to divide the cliffs into subgroups of geometrically similar, visually persistent, and exposed surfaces using the point clouds obtained in *Chapter 3*. These were then post-processed to derive a number of geometric properties, including facet spacing (both horizontal and vertical), area, density, dip angle, and aspect (the orientation of the facet). The extracted properties were then used to assess the influence of structural controls on the size distribution and characteristics of rockfalls observed in *Chapter 3*. The term 'facets' is used here to describe the extracted discontinuities, while acknowledging that some discontinuities may be too subtle for identification in point cloud data alone.

The plug-in performs planar facet extraction by sub-dividing a point cloud into clusters of adjacent points, each of which shares some user-defined degree of co-planarity (Dewez *et al.*, 2016). First, the algorithm spatially partitions the point cloud using a form of tree-structuring (Preparata and Shamos, 1985) known as a K-D tree, which recursively subdivides the points into balanced subcells, leaving each subcell with approximately the same number of points. Once the space has been sub-divided, these small planes are then clustered using a co-planarity criterion. The main parameters used to define the criterion in this work were as follows: minimum number of points per facet (5); maximum angle between neighbouring patches (25°); and a distance or roughness criterion (0.15 m), which is used to determine the planarity of a facet. Here, this requires that $> 99\%$ of the points that make up a facet are within 0.15 m of the facet plane. Of these

parameters, the overall output is most sensitive to changes in the minimum number of points per facet. This parameter was selected after a process of trial and error, where a visual comparison of the facets with the point cloud (coloured by RGB values derived from orthophotos) was used alongside a comparison of photographs, hillshades (derived from point cloud data), and facets along certain sections of the coastline where photographs of the cliffs were available. An example of the facets derived on the cliffs at Staithes is shown in Figure 4.02.

Once extracted, the facets were converted into meshes. These break each facet into a series of triangular faces, allowing a number of parameters known to influence rock slope stability, including the facet spacing (both horizontal and vertical), area, density, dip, and facet aspect to be calculated. The horizontal and vertical spacing were calculated for each facet by determining its overall width and height, and the surface area was then calculated by the sum of the areas of all the constituent faces. An approximation of facet density was then calculated by searching for all of the facets within a 1 m radius of the centroid of each facet and dividing the total number of facets by their combined area.

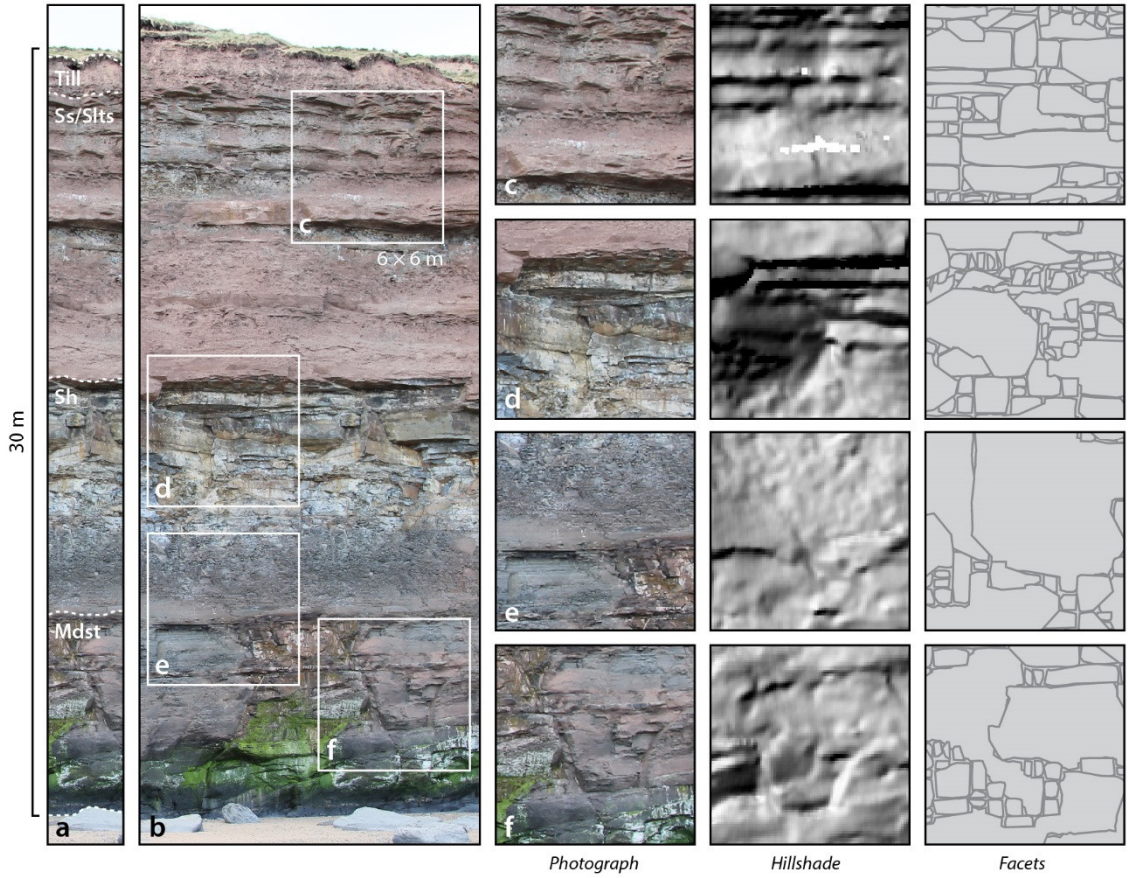

Figure 4.02 *Demonstration of facet analysis undertaken on a cliff section at Staithes. The point cloud and derivatives (hillshade, facets) were processed using airborne LiDAR data obtained in June 2015. The lithologies are labelled in (a), including mudstone (Mdst), shale (Sh), interbedded sandstone (Ss) and siltstone (Slts), which are capped by glacial till. In panel (b) four 6 × 6 m subsections are shown, which are used to demonstrate the outcomes of the facet analysis in panels (c – f). These include a photograph, a 0.10 m hillshade, and polygons of the facets.*

To calculate the facet dip and aspect, the points that make up each facet are fitted with a plane. This is achieved by computing the singular value decomposition (SVD) of the covariance matrix of each group of points, a process that yields the principal components (directions) of variation in the data. The equation of the plane, which describes the relationship between a query point, q, at the centroid of the plane and its normal vector, $\vec{n}$, has the following form:

$$\vec{n}_u q_x + \vec{n}_v q_y + \vec{n}_w q_z + d = 0, \quad [4.1]$$

where u (easting), v (northing), and w (vertical) are the indices of the surface normal, which is the vector perpendicular to the plane, and d is a constant determined by the vector dot product:

$$-\vec{q}_{(x,y,z)} \cdot \vec{n}_{(u,v,w)}. \quad [4.2]$$

Given a set of points in 3D, the surface normal is approximated by the third eigenvector, which represents the direction of the least variance, such that:

$$\vec{n} = (u, v, w). \quad [4.3]$$

However, the orientation of surface normals computed through SVD is ambiguous, meaning that they are unlikely to be consistently oriented over an entire point cloud dataset. Surface normals can be reoriented to point consistently towards a known viewpoint; a common procedure when post-processing point cloud data derived using terrestrial LiDAR (for example, Jaboyedoff *et al.*, 2007; Matasci *et al.*, 2017; Williams *et al.*, 2018). However, this is difficult when considering airborne or mobile data acquired from an unknown, nonstationary viewpoint and is increasingly complex for lengths of rock face with highly variable aspect. To ensure all surface normals were oriented consistently, the point cloud data were processed block-by-block, as in *Section 3.2.2*, to introduce artificial viewpoints for each facet. A point, p_i, central to each block and set back from the cliff face, was defined using the point cloud, p_c, as follows:

$$p_i(x, y, z) = \left[min(p_{c_x}) + \frac{range(p_{c_x})}{2}, min\left(p_{c_y}\right), min(p_{c_z}) \right]. \quad [4.4]$$

The centroid of each facet was then calculated using the arithmetic mean of its constituent points. The facets were then translated into a local coordinate system by subtracting p_i from the centroid of each facet. The point cloud was scaled by a factor of 1.5 before being converted back into the original coordinate system by adding p_i. This process is illustrated on the headland at Old Nab in Figure 4.03, providing an artificial viewpoint, s, for each facet that is always offshore. This ensures that all normals are oriented consistently even along a coastline of changing aspect.

The sign ambiguity of the normals is corrected using the position of each query point, q, relative to the artificial viewpoint, s, by:

$$\vec{s} = (s_x, s_y, s_z) - (q_x, q_y, q_z) \quad [4.5]$$

$$In\ \mathbb{R}^3: \alpha = (\|\vec{s} \times \vec{n}\|_2), \quad [4.6]$$

where $\times$ denotes the vector cross product, $\|$ denotes the Euclidean norm of the cross product, and α denotes the angle between the unit normal vector $\vec{n}$ at q, and $\vec{s}$ the vector between q and s (as in Williams *et al.*, 2018). If $\alpha > \frac{\pi}{2}$ or $\alpha < -\frac{\pi}{2}$, i.e. if the angle between the direction of the normal vector and that between the surface and the artificial sensor is not within ± 90°, then the normal direction is reversed as follows:

$$\vec{n}_r(u, v, w) = \vec{n}(-u, -v, -w). \quad [4.7]$$

Once the normals are oriented consistently, the dip and aspect of each facet is calculated. The dip is the angle between the facet surface and a horizontal plane through the facet (Figure 4.04):

$$\theta_{dip} = \cos^{-1} w. \quad [4.8]$$

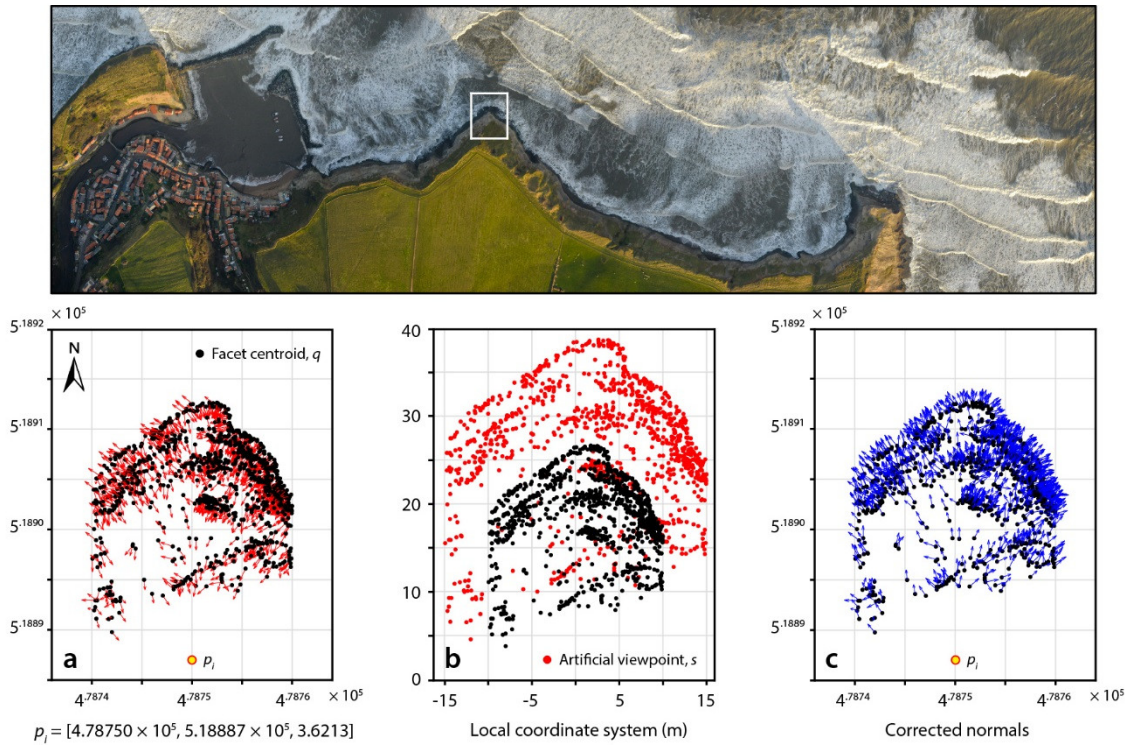

Figure 4.03 *Reorientation of surface normals around a headland. For each facet centroid, q, shown in (a), its surface normal is shown in red. The normals show an orientation bias around the headland, which is corrected in (b) by using a point p_i to translate the points into a local coordinate system. The centroids are scaled by a factor of 1.5 and used as artificial viewpoints, s, to reverse incorrectly oriented normals (c).*

The dip angle calculated for each facet represents the declination of the plane with respect to the horizontal but, crucially, the angle calculated here differs with respect to conventional measures of dip, which vary between 0° (horizontal plane) and 90° (vertical plane). The dip angle calculated here is not wrapped between 0° and 90° but is instead allowed to vary to 180° (Figure 4.04), in order to visually distinguish between gently sloping ($\vartheta_{dip} < 90°$), vertical ($\vartheta_{dip} = 90°$), and overhanging surfaces ($\vartheta_{dip} > 90°$). The aspect of a facet is then the azimuth of its normal vector, $\vec{n}$. That is, the angle (ϑ') between the horizontal component of the normal vector of the facet and the positive x-axis (or the direction of true north), such that:

$$\theta' = \cos^{-1}\left(\frac{u}{\sqrt{u^2 + v^2}}\right). \quad [4.9]$$

However, Equation 4.9 only gives an angular range of 0 – 90°. In order to calculate the correct aspect, the quadrant in which the aspect falls should be established (Feng *et al.*, 2001; Slob, 2010; Kissi, 2016). The correct aspect, ϑ_{dir}, can be determined using the following conditional equations:

$$\theta_{dir} = \theta', if\ u \geq 0\ and\ v \geq 0, \quad [4.10]$$

$$\theta_{dir} = 180 - \theta', if\ u \geq 0\ and\ v < 0, \quad [4.11]$$

$$\theta_{dir} = 180 + \theta', if\ u < 0\ and\ v < 0, \quad [4.12]$$

$$\theta_{dir} = 360 - \theta', if\ u < 0\ and\ v \geq 0, \quad [4.13]$$

which equate to facet aspects between 0° and 90° (Equation 4.10), 90° and 180° (Equation 4.11), 180° and 270° (Equation 4.12), and 270° and 360° (Equation 4.13).

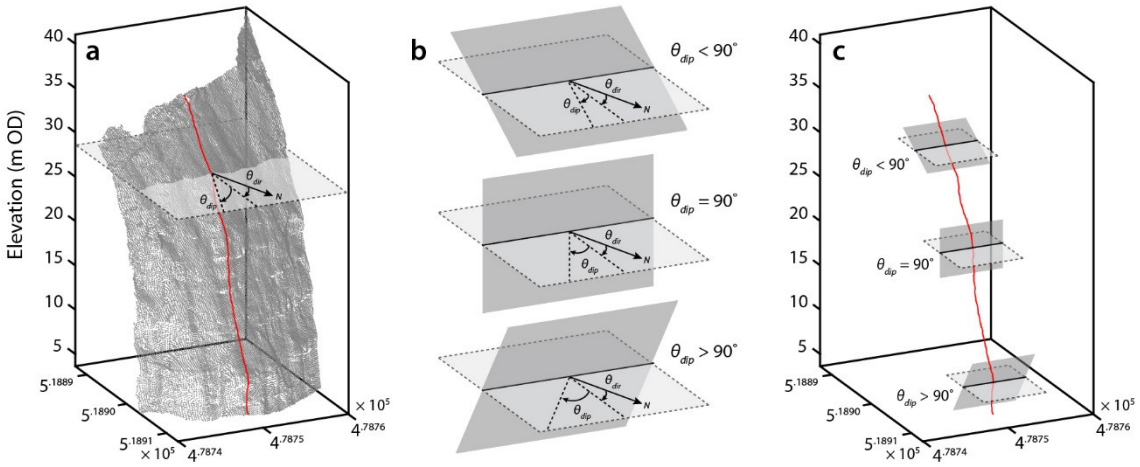

Figure 4.04 *Calculation of facet dip. In (a) this is demonstrated on a point cloud of the headland shown in Figure 4.03. For each facet, represented as a plane in (b) for simplicity, the dip is defined as the angle between the facet surface and a horizontal plane through the facet. The dip angle is not wrapped between 0° and 90°, but is instead allowed to vary to 180°, as shown in (c), in order to easily distinguish between gently sloping surfaces ($\vartheta_{dip} < 90°$), vertical surfaces ($\vartheta_{dip} = 90°$), and overhangs ($\vartheta_{dip} > 90°$).*

This analysis produced a database of 1,279,508 facets spanning the length of the North Yorkshire coastline, with an average density of *ca.* 16.8 facets m^{-2}. An example of the different properties extracted from the facets on the headland at Old Nab is shown in Figure 4.05. These illustrate several patterns in the surface structure of the cliffs. For example, the spacing, area, and density of the facets varies both with elevation and around the headland itself (Figures 4.05b–d). The toe of the cliffs is steep and slightly concave in profile (Figure 4.05e). Dip also varies up-cliff, with distinctive bands in the profile that vary in concavity up to an elevation of *ca.* 20 m, above which the cliff slopes gently backwards (Figures 4.05a and 4.05e). These bands are often associated with an increase in facet density. In order to understand the extent to which regional scale variations in the surface structure of the cliffs plays a role in defining rockfall activity, the geometric properties of the facets extracted here are related to local rockfall properties, such as block shape and scar contiguity, which are derived in *Sections 4.2.3* and *4.2.4*.

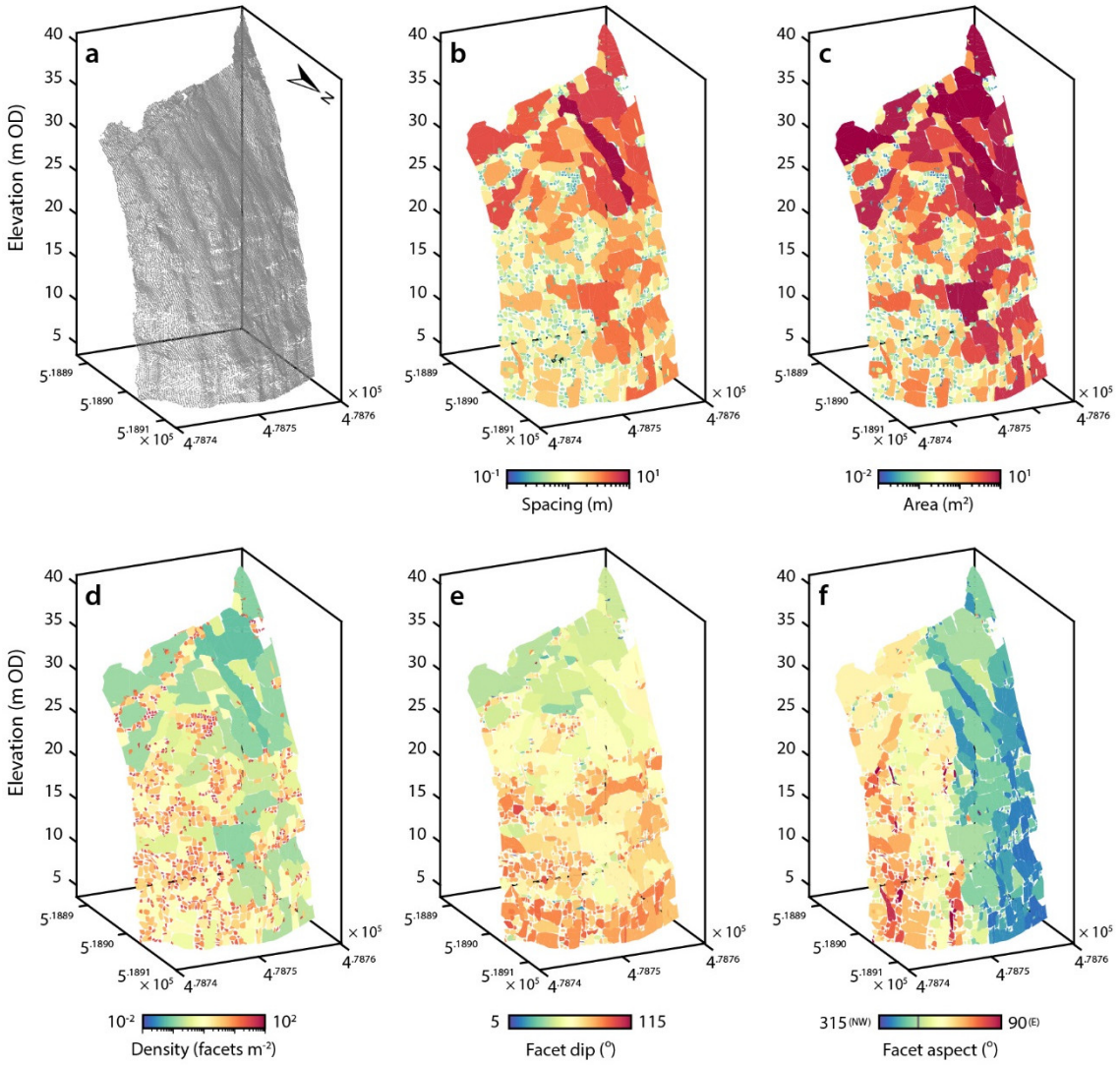

Figure 4.05 *Different facet properties, as demonstrated on a point cloud of the headland shown in Figure 4.03, in (a). Properties derived from the facets include (b) facet spacing, (c) facet area, (d) facet density, (e) facet dip, and (f) facet aspect. Note that colour bars for facet spacing, area, and density are log-scaled.*

4.2.3 Deriving rockfall shape

The shape of each rockfall that occurred along the North Yorkshire coast between August 2014 and March 2017 was quantified in order to, at least in part, account for the influence of structural discontinuities on block generation. Here, 'shape' is defined as the broad and medium-scale aspects of the morphology of a rockfall, while surface texture would refer to surface features that are small-scale relative to the size of a rockfall. The shape of rockfalls and their scars partially reflects the permissible kinematics of failure, as well as potential structural control (*Section 4.1*). Although the shape of large-scale instabilities is often characterised using LiDAR datasets (for example, Oppikofer *et al.*, 2009; Viero *et al.*, 2010), the shape of rockfalls is rarely quantified other than by visual interpretation (van Veen *et al.*, 2017). Shape typically comprises four main characteristics, which include the form, roundness, irregularity, and sphericity, detailed descriptions of which are provided by Blott and Pye (2008).

Rockfalls were classified in relation to the aspect ratios of the principal length axes (a, b, and c), where $a > b > c$ (Sneed and Folk, 1958; Graham and Midgley, 2000; Lukas *et al.*, 2013). This gave one of three end-member shapes, either blocky ($a = b = c$), slab-like ($a = b$, $c = 0$), or elongate ($a > 0$, $b = c = 0$), which themselves were divided into 10 sub-categories (Sneed and Folk, 1958). An example of the outputs of this process is shown in Figure 4.06, which provides an overall indication of the ratios of the principal length axes as they appear in a ternary plot. The ratios of the three axes vary linearly, resulting in a continuum of rockfall shapes. This type of analysis, where particle form is defined by its so-called 'tri-dimensional characteristics', has been used extensively in the field of geomorphology, principally for clast fabric analysis in glacial deposits (including, but not limited to, Barrett, 1980; Illenberger, 1991; Benn and Ballatyne, 1993; Bennett *et al.*, 1997), but also to determine particle form in arid environments (Higgitt and Allison, 1999) and fluvial reaches (Allan *et al.*, 2006; Byers *et al.*, 2015), to distinguish between storm and tsunami deposits (Costa *et al.*, 2017), and to quantify the shape of rockfalls (Rosser *et al.*, 2005b; van Veen *et al.*, 2017; Williams, 2017) and mass movement deposits (Šilhán and Pánek, 2010).

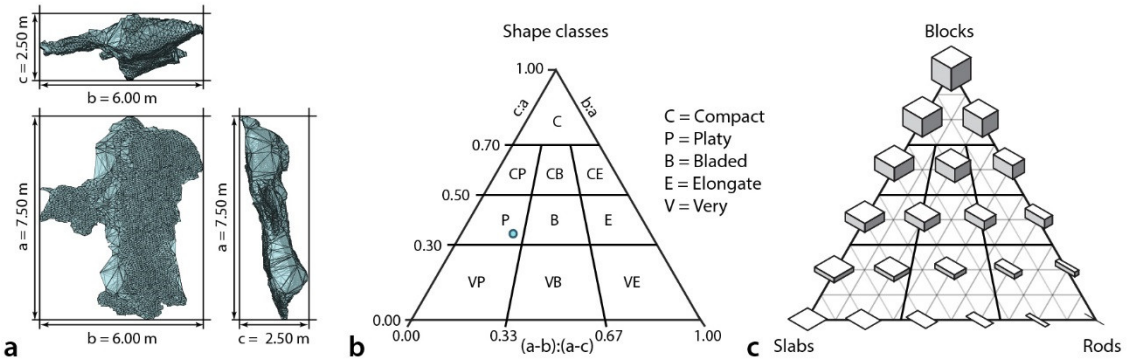

Figure 4.06 *Derivation of rockfall shape, as demonstrated on a rockfall captured at Staithes (a). Rockfall shapes are divided into 10 sub-categories, defined by Sneed and Folk (1958), and are shown in (b). Examples of the shapes are shown in (c), which is adapted from Figure 3 in Blott and Pye (2008, p. 36).*

4.2.4 Rockfall contiguity

The tendency for rockfall scars to coalesce over time has been observed using terrestrial LiDAR at a number of sites (Rosser *et al.*, 2005a, 2005b, 2007, 2013; Rohmer and Dewez, 2015; Royán *et al.*, 2015) and is a clear indicator that, where kinematically permissible to do so, rockfalls often propagate from the scars of previous rockfalls in a manner moderated by the local strength and structure of the rock mass. Landslides also demonstrate the existence of path-dependency (Samia *et al.*, 2017a, 2017b), which is a concept that originates from complexity theory and dictates that the current state of a system depends on its past state (Phillips, 2006; Temme *et al.*, 2015). When applied to mass movement processes, such as rockfalls, path dependency implies that previous activity affects (the susceptibility for) future activity through one or more legacy effects. These can include the effect of earthquakes (Parker *et al.*, 2015) as well as antecedent rainfall, hydrological properties, and accumulated damages in hillslopes (Fan *et al.*, 2015). In order to understand the degree to which rockfalls along the North Yorkshire coast were spatially associated, the proportion of rockfalls in the inventory whose scars coalesced with those of other rockfalls was calculated. This assumes that each rockfall occurred as a single event, given that this analysis considers the longer-term (*ca.* 10 – 12 month) spatial associations between rockfall scars. To assess the extent to which rockfalls can be considered a statistically independent, or random, process, these results were then compared to those of a randomised control.

Between two monitoring periods m_1 and m_2, a rockfall, R_1, was considered to have coalesced with another rockfall, R_2, if any points belonging to R_2 fell inside the mesh of R_1 or if any points belonging to R_2 fell within 0.20 m (approximately the maximum possible point spacing) of any points belonging to R_1, such that the scars of the two rockfalls were spatially contiguous (Figure 4.07). For each rockfall, this gave the IDs of any rockfalls captured in other monitoring

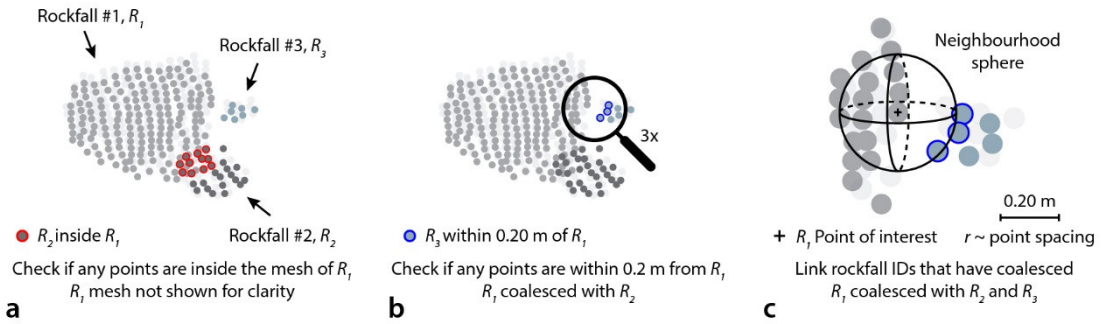

Figure 4.07 *Schematic diagram illustrating how levels of coalescence were determined between the rockfall inventories. The example uses three rockfalls, each of which occurred during separate monitoring periods. Every rockfall in the database is first tested to determine whether any rockfall points lie within the mesh of R_1. Any rockfall whose points fall inside the mesh, in this case those of R_2, is labelled as having coalesced with R_1, shown in (a). Any rockfall whose points are touching those of R_1, in this case those of R_3, is also labelled as having coalesced with R_1, shown in (b). A rockfall touches another rockfall when any of its points are < 0.20 m (approximately the maximum possible point spacing) from those of the rockfall of interest.*

periods that were spatially associated with the scar of that rockfall. Three possible scenarios of rockfall coalescence were then considered, including 1) year-on-year coalescence, where a rockfall in m_2 or m_3 had coalesced with the scar of one that occurred in m_1 or m_2, 2) sporadic coalescence, where a rockfall in m_2 or m_3 had coalesced with the scar of one that occurred in m_1, and 3) concentrated coalescence, where a rockfall in both m_2 and m_3 had coalesced with the scar of one that occurred in m_1, and also each other.

The proportion of rockfalls that coalesced in the same scenarios but under complete spatial randomness was also tested, in order to assess the extent to which the patterns observed along the coastline are indicative of path-dependency among rockfalls. This was achieved by randomly generating a new centroid for each rockfall by sampling points from the entire cliff surface. Each rockfall was then registered to its new centroid by using the iterative closest point (ICP) algorithm, producing a randomly positioned and oriented rockfall. The outcome of this process for rockfalls that occurred over a 500 m section of cliffs is shown in Figure 4.08. Although computationally intensive, this procedure was repeated 50 times and the proportion of rockfalls that coalesced was then averaged for each scenario. The inventory was split into rockfalls that had/not coalesced, and the properties of facets associated with rockfalls in the two sub-inventories were examined to assess whether any differences could be attributed to variations in rock mass structure.

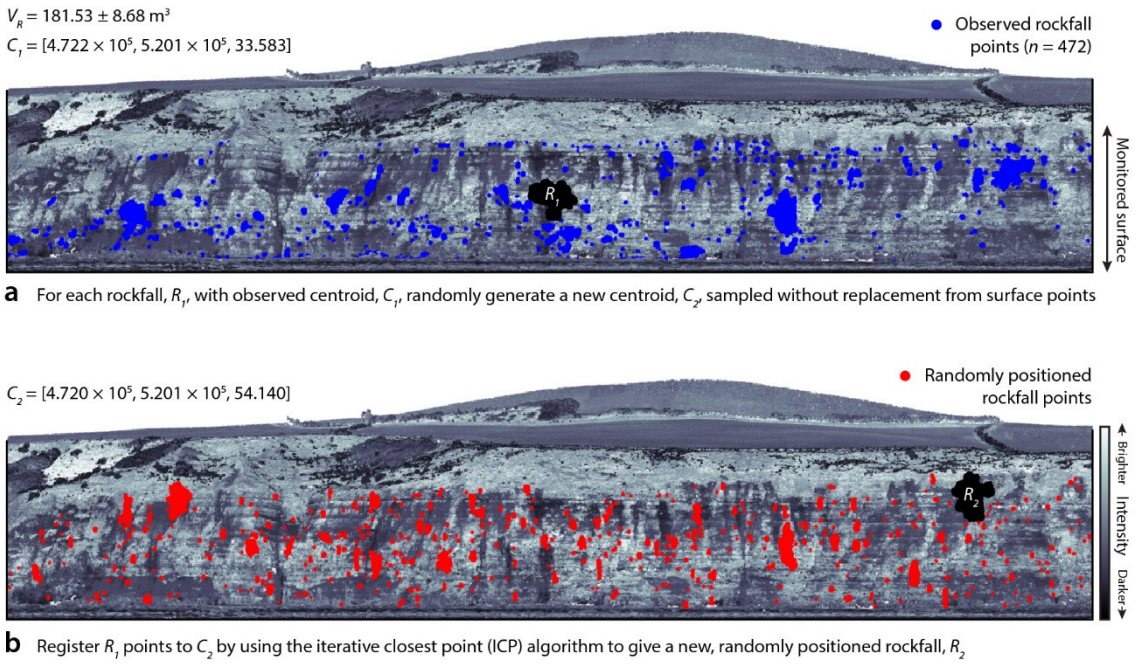

Figure 4.08 *Schematic diagram illustrating how rockfalls in each of the rockfall inventories were randomly assigned new locations. For each rockfall in (a), a new centroid was randomly generated by sampling points from the entire surface. Each rockfall was registered to its new centroid by using the iterative closest point (ICP) algorithm, giving a new, randomly positioned rockfall. The outcome of this process for rockfalls that occurred over a 500 m section of cliffs at Skinningrove is shown in (b). This process was repeated 50 times and the proportion of rockfalls that coalesced was then averaged for each scenario.*

4.3 Results

Although a wealth of publications concern the extraction of rock mass structural data from LiDAR point clouds, this work has largely been focussed on individual rock outcrops (Olariu *et al.*, 2008; Sturzenegger and Stead, 2009; Gigli and Casagli, 2011; Vöge *et al.*, 2013; Riquelme *et al.*, 2014, 2015). The results presented here describe alongshore and up-cliff variations in LiDAR-derived estimates of the geometric properties of exposed joint surfaces, or facets, observed along 20.5 km of cliffs on the North Yorkshire coast. Many of the major sources of error associated with field measurements of discontinuities are not applicable to the dataset used in this chapter. For example, (1) there is little censoring of discontinuities (Baecher and Lanney, 1978; Priest, 1993) and no length bias (Zhang and Einstein, 2000; Sturzenegger *et al.*, 2011) as the entire rock face was sampled, and (2) there is little or no orientation bias as there was no preferential viewing angle during data collection (Terzaghi, 1965; Sturzenegger *et al.*, 2007; Lato *et al.*, 2009b).

However, the facet analysis undertaken here must be appropriately caveated: as with all surveys, truncation occurs where discontinuities are too small to measure (Baecher and Lanney, 1978; Zhang and Einstein, 2000; Sturzenegger *et al.*, 2011), and, in LiDAR surveys, a scale bias is introduced where discontinuity sets are below the point spacing, although this bias is systematic and approximately uniform, both spatially and across datasets (here *ca.* 0.15 m; Sturzenegger and Stead, 2009). It is also crucial to recognise that only exposed joint surfaces were measured, which themselves are subject to weathering and alteration by other surface processes. With this in mind, the geometric properties of the facets measured here are considered to be indicative of the condition of the damaged 'skin' (Williams, 2017) of the rock mass, which is assumed to have accumulated to shallow depths (*ca.* 10^1 m) through weathering and the exploitation of microcracks. All of the facet data were validated using a visual comparison of the facets with the point clouds (coloured by RGB values) alongside oblique aerial photographs and high-resolution hillshades derived from the point cloud data, due to difficulties in accessing the foreshore and the large volumes of data involved. The data are therefore interpreted with caution but deemed suitable for examining relative variations in cliff structure alongshore and up-cliff, as shown in the following example.

An example of the geometric properties of the facets observed along the North Yorkshire coast is shown in Figure 4.09. The figure shows different facet properties derived for a point cloud of the cliffs at Boulby (Figure 4.09a), demonstrating the facet analysis undertaken in Figure 4.05 on a broader scale ($> 10^2$ m). The cliffs at Boulby constitute a geological conservation review site, which reflects their (inter)national importance both in terms of geology and geomorphology (Simms *et al.*, 2004). They are the highest in England, forming a vertical exposure through the Redcar Mudstone, Staithes Sandstone, Cleveland Ironstone, and Whitby Mudstone formations, which together constitute the Pleinsbachian and Toarcian stages of the Cleveland Basin (Figure 2.03, *p.* 14).

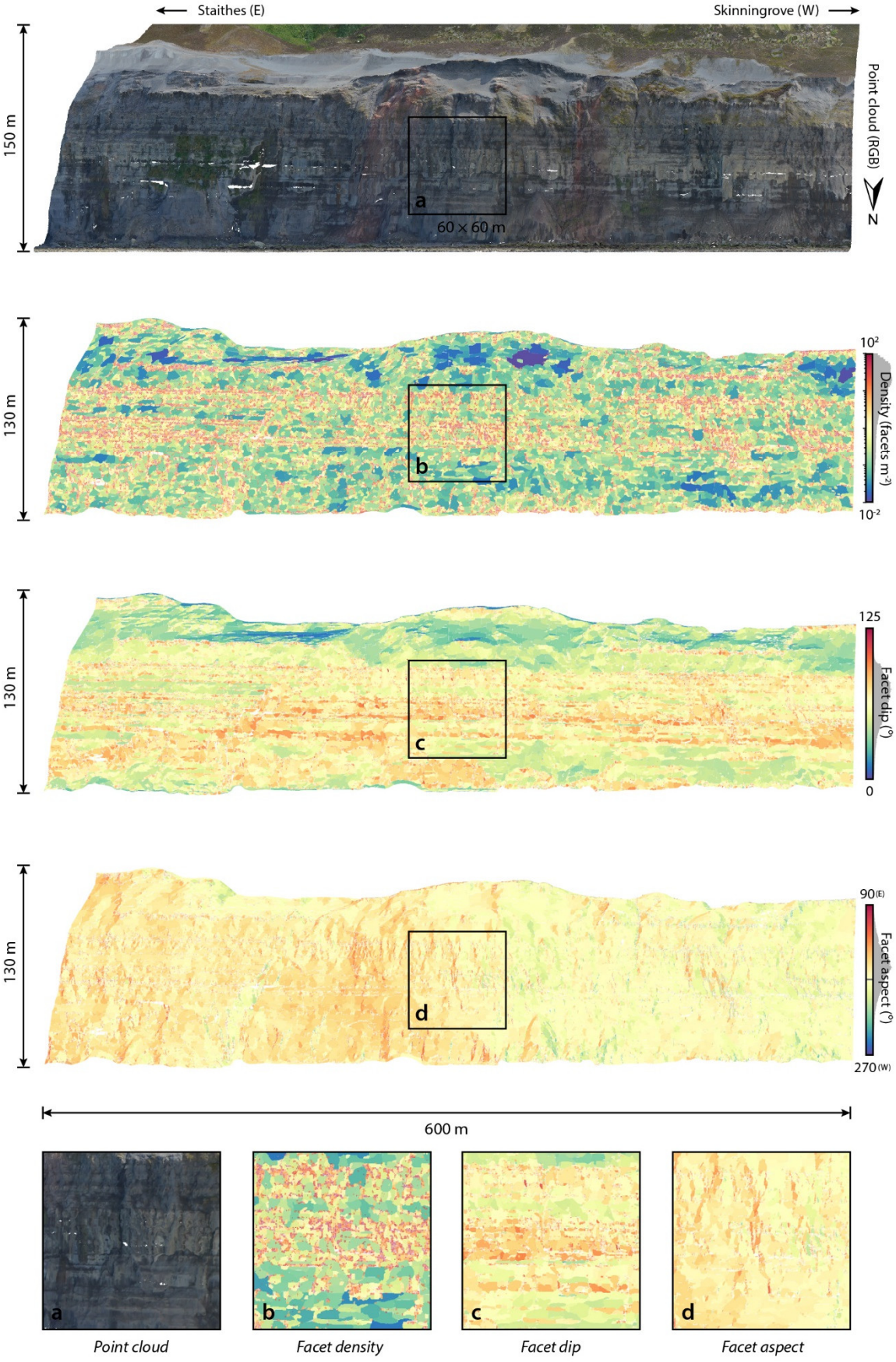

Figure 4.09 *Different facet properties, as demonstrated on a point cloud of the cliffs at Boulby, in (a). Properties derived from the facets include (b) facet density, (c) facet dip, and (d) facet aspect. Note that the colour bar for facet density is log-scaled. The stratigraphical range can be found in Figure 2.03 (p. 14).*

Approximately 45 m of shales and siltones of the upper part of the Ironstone Shale Member of the Redcar Mudstone Formation are exposed on the foreshore and at the toe of the cliff. The upper two thirds of the cliff expose the full thickness of the Staithes Sandstone (*ca.* 24.5 m thick) and Cleveland Ironstone (*ca.* 25.5 m thick) formations, the top of which forms a broad shelf, and behind which a further cliff rises to the summit, exposing the entire Whitby Mudstone Formation (*ca.* 72.0 m thick). The succession is unbroken by faults, and lies on the axis of a broad, gentle anticline that stretches from east of Staithes westwards towards Skinningrove (Simms *et al.*, 2004). The influence of lithology on cliff structure is evident when considering facet density and dip (Figures 4.09b and 4.09c), which clearly show the westward dipping ironstone bands and intervening seams of shale that are characteristic of the Cleveland Ironstone Formation.

4.3.1 Spatial variations in cliff structure

The geometric properties of the facets extracted along the North Yorkshire coast are summarised in Figure 4.10, with alongshore variations shown in Figure 4.11. Both horizontal and vertical spacing are lognormally distributed (Figure 4.10a), which is common in discontinuity spacing data (Priest and Hudson, 1981; Sen and Kazi, 1984; Rouleau and Gale, 1985; Narr and Suppe, 1991). The surface areas of the facets are also lognormally distributed (Figure 4.10b), with a median facet area of 0.07 m^2. It therefore follows that facet density is lognormally distributed, but negatively skewed (Figure 4.10c), with a median density of 12.3 facets m^{-2}. These distributions are illustrative of the fact that, in an extreme case, kilometre-scale discontinuities such as regional faults are exponentially less frequent than metre-scale joints, which in turn are less frequent than microcracks. Although larger spacings (here $> 10^0$ m) occur less frequently, their relative influence on the overall rock mass structure is greater given that they are more likely to generate larger block sizes (Ortega *et al.*, 2006). The negative exponential distribution has also been applied to discontinuity spacing (Priest and Hudson, 1976; La Pointe and Hudson, 1985; Villaescusa and Brown, 1990), while normally spaced discontinuities are rare (Huang and Angelier, 1989).

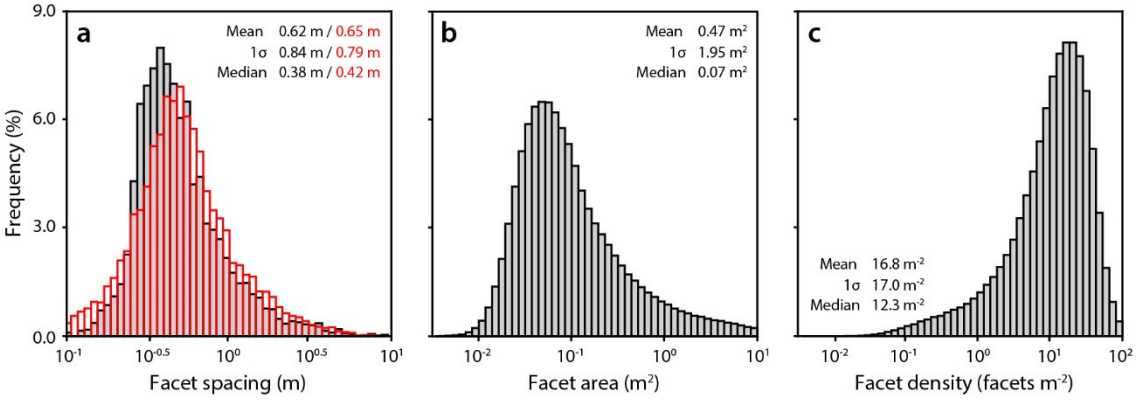

Figure 4.10 *Histograms of (a) facet spacing (horizontal in black and vertical in red), (b) facet area, and (c) facet density along the North Yorkshire coast, UK. Note that the x-axis for each plot is log-scaled.*

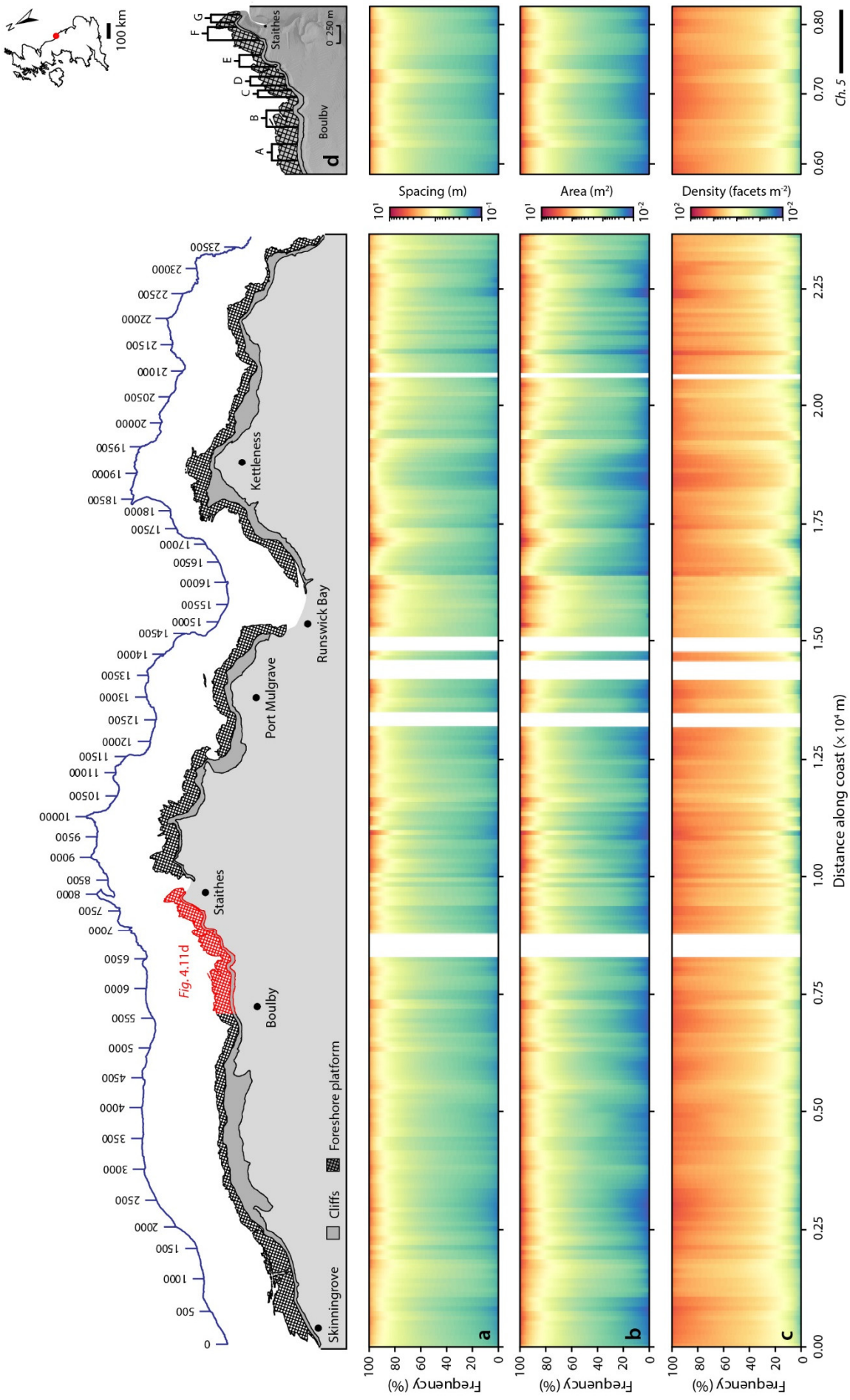
N
100 km
Skinningrove
Cliffs
Foreshore platform
Staithes
Boulby
Kettleness
Port Mulgrave
Runswick Bay
Fig. 4.11d
0
500
1000
1500
2000
2500
3000
3500
4000
4500
5000
5500
6000
6500
7000
7500
8000
8500
9000
9500
10000
10500
11000
11500
12000
12500
13000
13500
14000
14500
15000
15500
16000
16500
17000
17500
18000
18500
19000
19500
20000
20500
21000
21500
22000
22500
23000
23500
A
B
C
D
E
F
G
Staithes
Boulby
0 250 m
d
Spacing (m)
Area (m²)
Density (facets m⁻²)
Frequency (%)
a
b
c
Distance along coast (× 10⁴ m)
Ch. 5

Figure 4.11 *Overleaf. Variations in (a) facet spacing, (b) area, and (c) density along the North Yorkshire coast, UK. Facet properties are plotted as stacked bar graphs, with distance along the coastline divided into 100 m bins. The inset in (d) shows in detail the previously monitored sites (Table 2.01, p. 19) as well as the sites monitored in Chapter 5. Note that the colour bars are log-scaled. White bands denote harbours, beachy embayments and other gaps in the point cloud data where cliffs are absent or densely vegetated.*

Alongshore variations in the distribution of facet spacing, area, and density are shown in Figure 4.11, while variations in facet dip and aspect are shown in Figure 4.12. Areas with a larger average facet spacing and area, and therefore a lower density, primarily include Runswick Bay (at distances of *ca.* $1.50 - 1.65 \times 10^4$ m, 10.3 facets m^{-2}) and Sandsend ($> 2.30 \times 10^4$ m, 11.4 facets m^{-2}), both of which are characterised by lower cliffs of drift materials that separate steeper headlands, such as Kettleness (1.85×10^4 m). Although many of the cliffs composed of glacial drift are subject to erosion throughout their profile (Agar, 1960), the majority of the cliffs in bays such as Runswick are characterised by shallow dips ($< 50°$) with a slipping face (Figure 4.12). Conversely, the headlands at Boulby ($0.22 - 0.25 \times 10^4$ m, 19.9 facets m^{-2}), Cowbar Nab (0.75×10^4 m, 19.7 facets m^{-2}), Staithes (0.82×10^4 m, 17.4 facets m^{-2}), Penny Nab (0.90×10^4 m, 20.1 facets m^{-2}), Old Nab (1.00×10^4 m, 21.9 facets m^{-2}), and Kettleness (1.85×10^4 m, 25.7 facets m^{-2}) are characterised by high facet densities. These cliffs are near-vertical, with mean dips exceeding 70° (Figure 4.12), and are the product of marine erosion on a landscape of high relief, with alternating ridges and valleys abutting on the coast roughly at right angles (*Section 2.1.1*, *p.* 12).

More locally, the 900 m stretch of cliffs between Staithes and Cowbar ($0.73 - 0.82 \times 10^4$ m; marked on Figures 4.11d and 4.12e), which is the focus of a field investigation into the spatial variations in ground motion response to wave impacting (*Chapter 5*), is approximately uniform in geology and structure (see *Appendix E*, *p.* 191 for a diagram of the facets along this stretch of cliffs; Howarth, 1955; Simms *et al.*, 2004; Powell, 2010). There is little variation in mean facet density (16.4 ± 2.5 facets m^{-2}, $\pm 2\sigma$) or dip ($67.0° \pm 2.7°$, $\pm 2\sigma$), and variations in mean facet aspect are primarily controlled by the geometry of the coastline. Elsewhere, abrupt changes in facet properties between bins appear to coincide with a number of conditions (Figures 4.11 and 4.12): for example, from Penny Nab to Port Mulgrave ($1.00 - 1.25 \times 10^4$ m), sharp changes in facet density, which ranges from a mean value of 12.4 – 24.7 facets m^{-2} over a distance of 1.5 km, appear to occur where cliffs are dissected by landslide activity. Landsliding has occurred along this stretch of coastline where the deposits from repeated cliff collapses have accumulated over time, decreasing the gradient in places ($< 50°$). Towards Kettleness, a sharp increase in facet density from a mean value of 8.7 facets m^{-2} to 21.0 facets m^{-2} (at a distance of *ca.* 1.64×10^4 m) marks the transition from cliffs formed predominantly of more deformable drifts to cliffs formed of harder, lithified rock types (see *Appendix E*, *p.* 189 for a diagram of the facets at Kettleness). At Sandsend ($> 2.20 \times 10^4$ m), variations in facet density (11.5 ± 6.0 facets m^{-2}, $\pm 2\sigma$) appear to be associated with a series of crenulous coves separated by till cliffs.

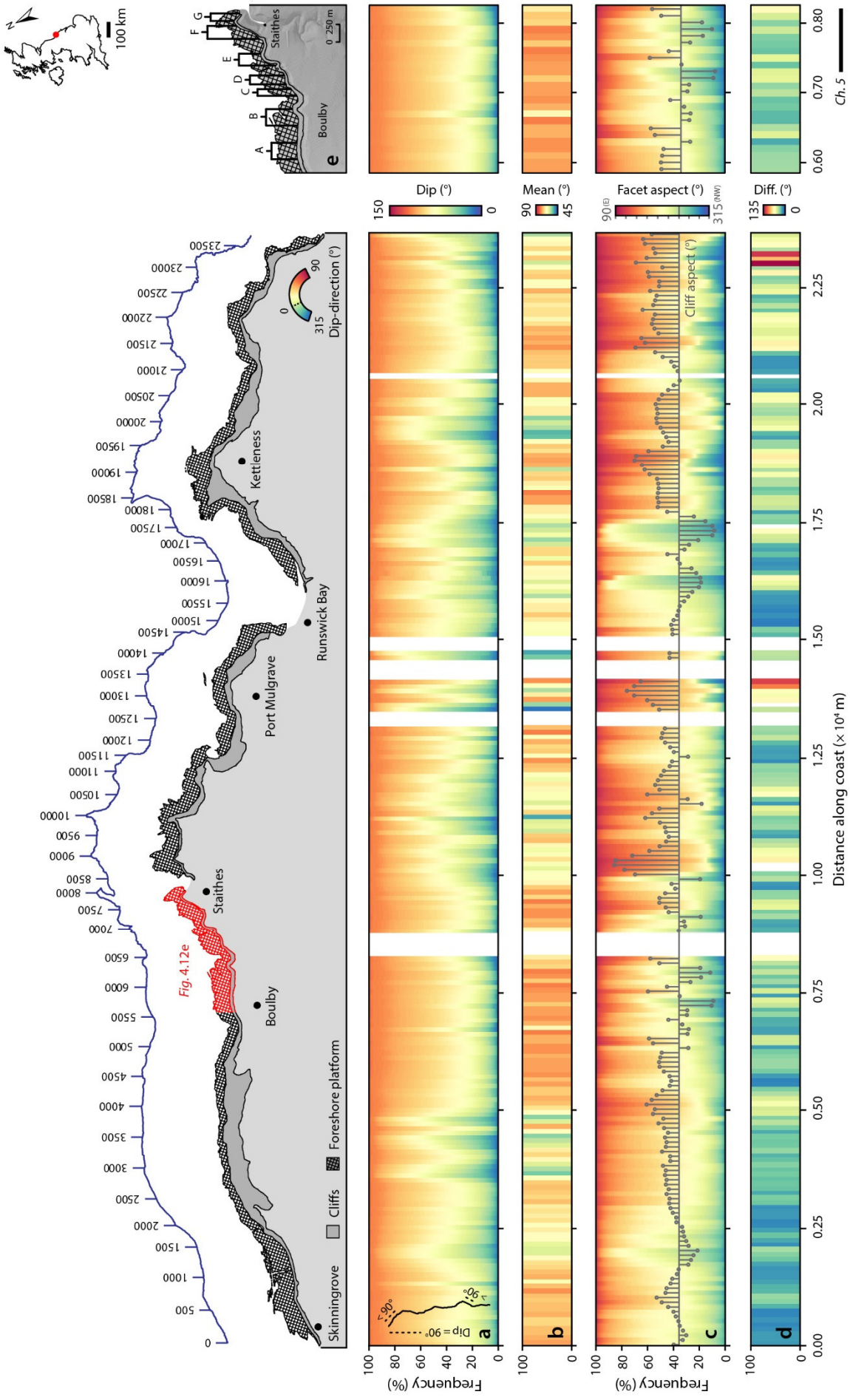
N
100 km
Skinningrove
Cliffs
Foreshore platform
Boulby
Staithes
Port Mulgrave
Runswick Bay
Kettleness
Fig. 4.12e
Dip-direction (°)
0
90
180
270
315
0
500
1000
1500
2000
2500
3000
3500
4000
4500
5000
5500
6000
6500
7000
7500
8000
8500
9000
9500
10000
10500
11000
11500
12000
12500
13000
13500
14000
14500
15000
15500
16000
16500
17000
17500
18000
18500
19000
19500
20000
20500
21000
21500
22000
22500
23000
23500
A
B
C
D
E
F
G
Staithes
Boulby
0 250 m
e
Dip (°)
150
0
Mean (°)
90
45
Facet aspect (°)
90 (E)
315 (NW)
Diff. (°)
135
0
Cliff aspect (°)
Dip = 90°
a
b
c
d
Frequency (%)
Frequency (%)
0.00
0.25
0.50
0.75
1.00
1.25
1.50
1.75
2.00
2.25
Distance along coast (× 10⁴ m)
0.60
0.70
0.80
Ch. 5

Figure 4.12 *Overleaf. Variations in (a) facet dip, (b) mean dip, (c) facet aspect (with mean aspect overlaid), and (d) the mean difference between facet and cliff aspect along the North Yorkshire coast, UK. Facet properties are plotted as stacked bar graphs, with distance along the coastline divided into 100 m bins. In (d), cliff aspect was calculated using a 20 m moving window. The inset in (e) shows in detail the previously monitored sites (Table 2.01, p. 19) as well as the sites monitored in Chapter 5. White bands denote harbours, beachy embayments and other gaps in the point cloud data where cliffs are absent or densely vegetated.*

4.3.2 Vertical variations in cliff structure

Variations in the geometric properties of facets as a function of cliff elevation are shown in Figure 4.13. The considerable along-coast variability in facet spacing, area, and density means that much of the variation in these properties is averaged out, although there is a slight decrease in both facet spacing and area up-cliff, with a corresponding increase in facet density. The distribution of facet dip, and the difference between facet and the cliff aspect measured over the surrounding 20 m window, vary considerably up-cliff. The bases of the cliffs ($<$ 6 m OD) are characterised by shallower dips (*ca.* 50°, global mean of *ca.* 60°) and larger differences (*ca.* 53°, global mean of *ca.* 36°) on average, further highlighting the apparent absence of notching along much of the coastline. Mean values of dip remain stable (*ca.* 63° $\pm$ 1°, 2σ) up to an elevation of *ca.* 90 m, while mean differences progressively decrease, stabilising between elevations of *ca.* 50 – 90 m (*ca.* 33° $\pm$ 2°, 2σ). Above elevations of *ca.* 100 m, the cliffs at Boulby form a broad shelf, resulting in low dips (*ca.* 47° $\pm$ 4°, 2σ). A further cliff rises behind this shelf, up to a summit of *ca.* 150 m, causing dips to briefly return to a mean of *ca.* 63°. The large differences, which increase to mean values of up to *ca.* 58°, are likely to be the result of extensive quarrying activity in the Alum Shale Member of the Whitby Mudstone Formation (Simms *et al.*, 2004).

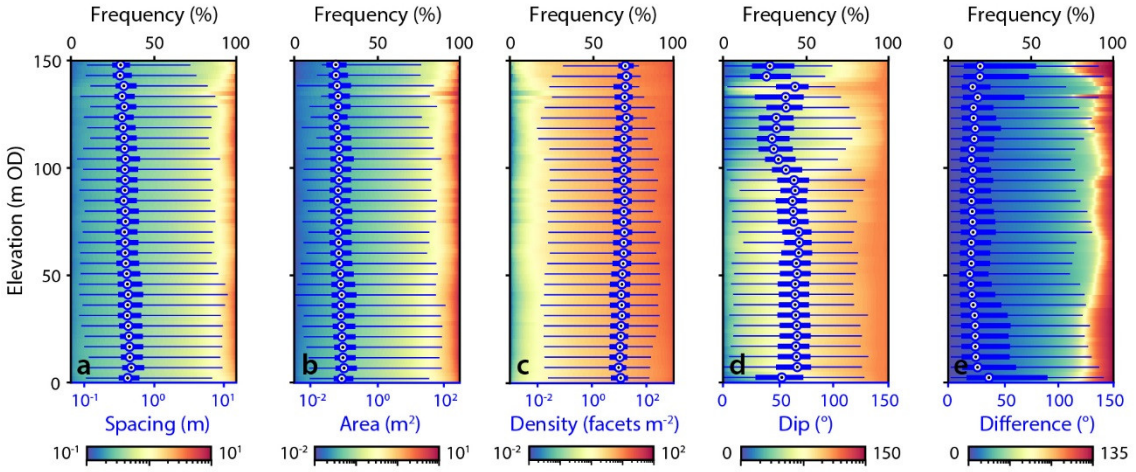

Figure 4.13 *Variations in (a) facet spacing, (b) facet area, (c) facet density, (d) facet dip, and (e) the difference between facet and cliff aspect along the North Yorkshire coast, UK. Facet properties are plotted as stacked bar graphs (coloured) and as compact box plots (blue) against elevation. Bins are in 2 m increments from an elevation of 0 m OD.*

4.3.3 Rockfall shape

Both the shape and size of rockfalls is governed by failure along joint planes or discontinuities (Jaboyedoff, 2011; Lambert and Nicot, 2011), such that they can be associated with the specific geological settings of the rock mass from which they were released (Fityus *et al.*, 2013). Rockfall shape along the North Yorkshire coast is therefore shown for each monitoring period in Figure 4.14. The shapes correspond to 10 sub-categories of three end-member shapes, blocky, slab-like, or rods, as defined by Sneed and Folk (1958). In each year, rockfall shapes are distributed throughout the ternary plot, with no distinctive patterns evident year-on-year. The majority of rockfalls (> 60% in each dataset) are compact (or blocky), lying in the top half of the ternary plot, with relatively few very platy, bladed, or elongate shapes (< 10% in each dataset). There appears to be little correlation between rockfall shape and volume for the largest 50 rockfalls in each inventory. To investigate this further, rockfall volumes are plotted on logarithmic axes using logarithmically binned data, as in the magnitude-frequency analysis undertaken in *Section 3.2.6*, and their shape class plotted as a stacked bar graph. In the combined inventory (n = 58,032), which is shown in Figure 4.15, rockfalls occurring at the tails of the distribution

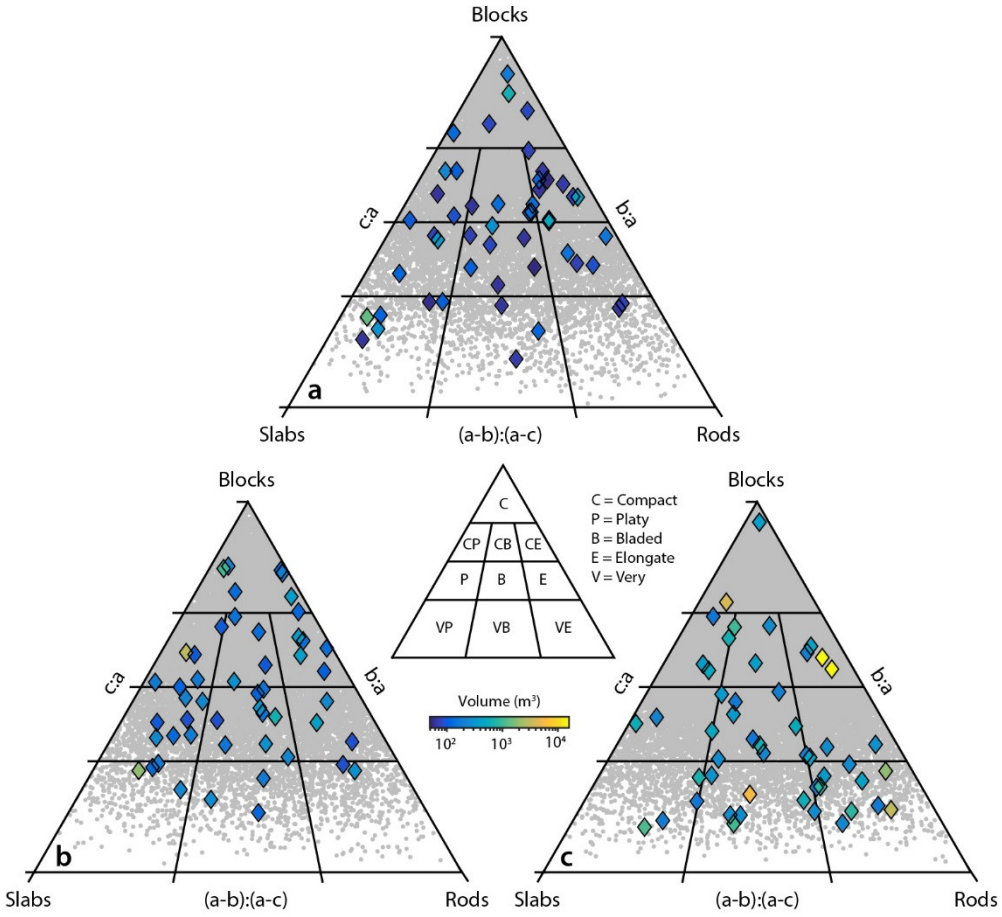

Figure 4.14 *Rockfall shape monitored along the North Yorkshire coast, UK, from (a) 2014 – 2015, (b) 2015 – 2016, and (c) 2016 – 2017. Diamonds represent the largest 50 rockfalls in each inventory. Colours correspond to rockfall volume. Shapes are divided into 10 sub-categories, defined by Sneed and Folk (1958).*

($< 10^{-3}$ m^3 and $> 10^1$ m^3) comprise approximately equal proportions of blocky, slab-like, and rod shapes, with a tendency towards very platy and elongate forms, particularly for rockfalls of $V_R > 10^2$ m^3. However, there is a clear peak in the stacked bar graph for rockfalls of volume 0.002 m^3 – 0.064 m^3 (n = 30,766), the majority of which ($> 70\%$) are blocky in shape. This equates to a cube of dimensions between *ca.* 0.13 m and *ca.* 0.40 m, which is of a similar order of magnitude to discontinuity-defined structural control on block size and shape at this scale (de Vilder *et al.*, 2017; observations made at the Boulby cliffs). Importantly, this peak does not coincide with the peak in the probability density of rockfall frequency as a function of volume (Figure 4.15), ruling out any influence of the observed frequency, or censoring, of rockfalls on the distribution of their shapes.

The results shown in Figure 4.15 show that, along the North Yorkshire coast, the probability distribution of rockfall shape as a function of volume is broadly predictable, and critically that rockfall shape is scale dependent. While a greater proportion of very small ($< 10^{-3}$ m^3) and very large ($> 10^1$ m^3) rockfalls tend towards very platy and elongate forms, the majority of rockfalls ($> 70\%$) of volume 0.002 – 0.064 m^3 (n = 30,766) are blocky in shape. This occurs year-on-year (Figure 4.16), potentially marking a transition from rockfall as a structurally-defined process to rockfall as either small scale consequences of incremental weathering ($V_R < 10^{-3}$ m^3), or fracturing-related mass-movements that break through rock bridges to generate larger, predominantly cliff face-parallel rockfall ($V_R > 10^2$ m^3; de Vilder *et al.*, 2017). The possibility of a structural control on rockfall shape is therefore investigated in *Section 4.3.5*. This relationship also holds important consequences for modelling future cliff erosion, both along cliffed shorelines and in non-coastal settings. This is the case if such relationships are used to place limits on the dimensions of modelled rockfalls, and the step-back events that result (for example, Dong and Guzzetti, 2005; Young *et al.*, 2011), using rockfall magnitude-frequency relationships.

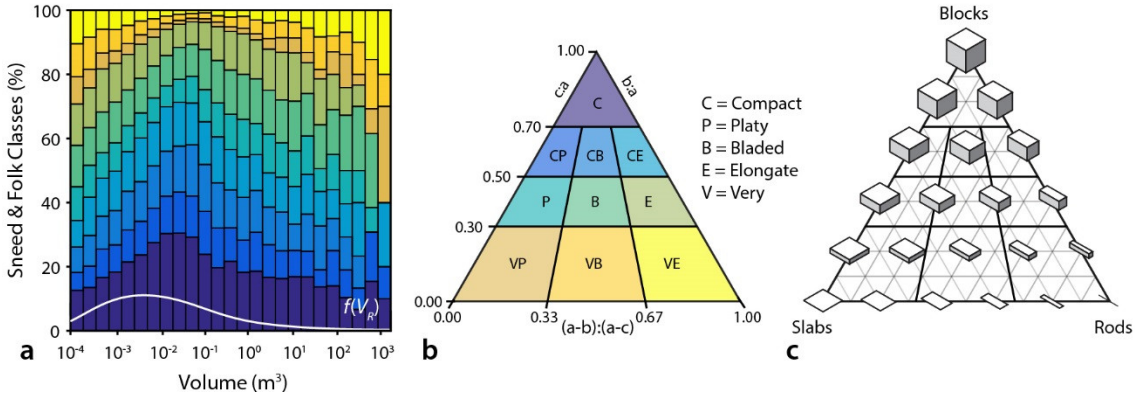

Figure 4.15 *Rockfall shape, derived for all 58,032 rockfalls in the inventory, plotted as a stacked bar graph in (a). The probability density of rockfall frequency as a function of volume is overlaid in white. Colours correspond to the 10 sub-categories shown in (b), defined by Sneed and Folk (1958). Examples of the shapes are shown in (c), which is adapted from Figure 3 in Blott and Pye (2008, p. 36).*

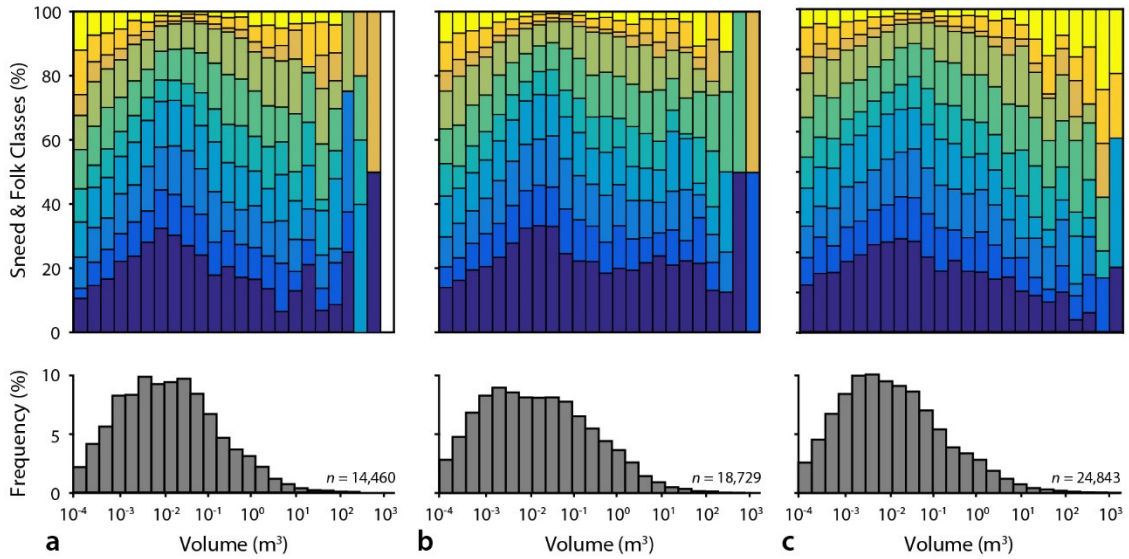

Figure 4.16 *Rockfall shape monitored along the North Yorkshire coast, UK, from (a) 2014 – 2015, (b) 2015 – 2016, and (c) 2016 – 2017. The results are plotted as a stacked bar graph, with colours corresponding to the 10 sub-categories shown in Figure 4.15b, defined by Sneed and Folk (1958). Histograms show the frequency of rockfalls in each volume bin.*

Beyond weathering processes, the shape and size of rockfalls are primarily governed by the geometric properties of discontinuities, including orientation and spacing (Wyllie and Mah, 2004; Jaboyedoff, 2011; Lambert and Nicot, 2011). The ability to monitor at length scales where there are variations in these factors is therefore crucial in aiding our understanding of the sensitivity of sea cliffs, such as those on the North Yorkshire coast, to future change. Alongshore variations in the distribution of rockfall shape are therefore shown for each year of monitoring in Figures 4.17a–c. The distribution of rockfall shape varies along the coastline, and the structure of this variation is generally consistent year-on-year. If each 100 m bin of cliffline consistently produces similar shapes of rockfall, then the existence of these patterns at least partly confirms the assertion that rockfall shape is controlled by the geometric relationships of rock mass discontinuities. To further test this, a moving correlation (± 200 m) was applied to the frequency data presented in Figure 4.17. Correlation coefficients were calculated for each rockfall shape class, in each 100 m bin along the coastline, using the rockfalls observed in both 2014 – 2015 and 2015 – 2016, and 2015 – 2016 and 2016 – 2017. The results were displayed only if a statistically significant positive correlation was observed for both cases, in which case they were amalgamated and a mean correlation was calculated.

Figure 4.18 (*p.* 78) shows the extent to which different 100 m cliff sections along the North Yorkshire coast produced the same or similar distributions of rockfall shapes year-on-year. The headlands at Boulby (at distances of *ca.* 0.22 – 0.25 $\times 10^4$ m and 0.57 $\times 10^4$ m), Cowbar Nab (0.75 $\times 10^4$ m), Staithes (0.82 $\times 10^4$ m), Old Nab (1.00 $\times 10^4$ m), Port Mulgrave (1.35 $\times 10^4$ m), and Kettleness (1.85 $\times$ 10^4 m) show the strongest correlations, having all produced similar

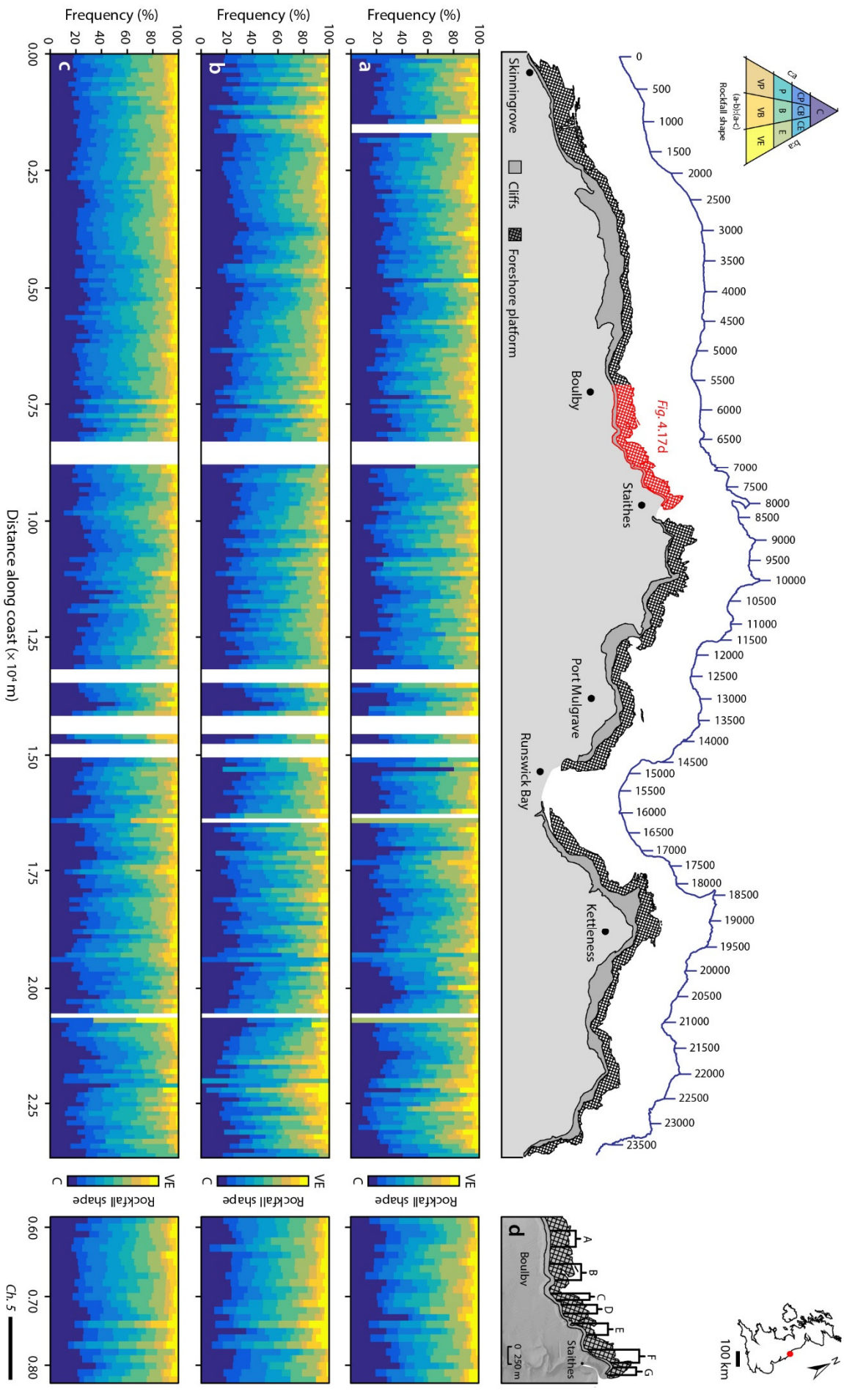
Frequency (%)
a
b
c
Rockfall shape
C
VE
Distance along coast (× 10⁴ m)
Ch. 5
Skinningrove
Cliffs
Foreshore platform
Boulby
Staithes
Port Mulgrave
Runswick Bay
Kettleness
Fig. 4.17d
Rockfall shape
(a-b)/(a-c)
b/a
C
CP
CB
CE
VP
P
B
E
VB
VE
d
A
B
C
D
E
F
G
0 250 m
100 km
N

Figure 4.17 *Overleaf. Rockfall shape monitored along the North Yorkshire coast, UK, from (a) 2014 – 2015, (b) 2015 – 2016, and (c) 2016 – 2017. Rockfall shape is plotted as a stacked bar graph, with distance along the coastline divided into 100 m bins. Colours correspond to the 10 sub-categories shown in Figure 4.15b, defined by Sneed and Folk (1958). The inset in (d) shows in detail the previously monitored sites (Table 2.01, p. 19) as well as the sites monitored in Chapter 5. White bands denote harbours, beachy embayments and other gaps in the point cloud data where cliffs are absent or densely vegetated.*

distributions in at least seven or more of the 10 shape classes (Figure 4.18b). These areas are sometimes separated by embayments, such as Runswick Bay and Sandsend, which have only produced similar distributions in fewer than four of the 10 shape classes. This implies that the geological setting of the coastline, where ridges of solid rock are separated by lower cliffs of drift (*Section 2.1.1*, *p.* 12), directly influences spatial variations in the distribution of rockfall shapes, and, by inference, rockfall volumes along the North Yorkshire coast.

Over 66% of the total monitored cliff length along the North Yorkshire coast consistently produced blocky (compact) shapes (Figure 4.18), with upwards of 35% of the cliffs also producing other sub-categories of blocky shapes (compact-platy, compact-bladed, or compact-elongate). Although a large proportion of the rockfalls observed were blocky ($> 23\%$), over the entire inventory they contributed a relatively small proportion ($< 11\%$) of the total eroded volume, with a mean volume of *ca.* 1.04 ± 0.16 m^3. This complements patterns observed in the volumetric data, which were derived using the same methods and show spatial variations in the correlation between the distribution of rockfall volumes observed along the North Yorkshire coast (*Appendix F*, *p.* 192). These data demonstrate a peak in volumes between 10^{-2} and 10^{-1} m^3, which approximately coincides with the peak observed in Figure 4.15a, and indicates that up to 50% of the coastline consistently produces rockfall material in this volume range. As in Figure 4.18b, the headlands at Boulby (at distances of *ca.* $0.22 - 0.25 \times 10^4$ m and 0.57×10^4 m), Cowbar Nab (*ca.* $0.70 - 0.75 \times 10^4$ m), and Old Nab (*ca.* 1.00×10^4 m) show the strongest correlations, having all produced statistically similar distributions in at least 14 or more of the 24 volume classes.

Both very elongate and very bladed shapes were consistently produced along much of the coastline (50% and 45% of the monitored cliff length, respectively). Although these contributed a small proportion (*ca.* 7%) of the rockfalls observed, together they constituted over 17% of the total eroded volume, with a mean volume of *ca.* 5.95 ± 1.37 m^3 and 4.93 ± 0.79 m^3, respectively. Areas with strongly positive correlations in these shapes often coincide with areas that produce blocky shapes (Figure 4.18a), with concentrations often around headlands. Although the largest rockfalls tend towards these shapes (Figure 4.15a), rockfalls with a volume greater than *ca.* 262 m^3 ($n = 53$) did not occur with any spatial consistency over the monitoring period (*Appendix F*, *p.* 192). However, rockfalls with a volume between *ca.* 131 m^3 and 262 m^3 ($n = 58$) did concentrate around the headland at Boulby (at a distance of *ca.* 0.57×10^4 m), with correlation coefficients there exceeding 0.70.

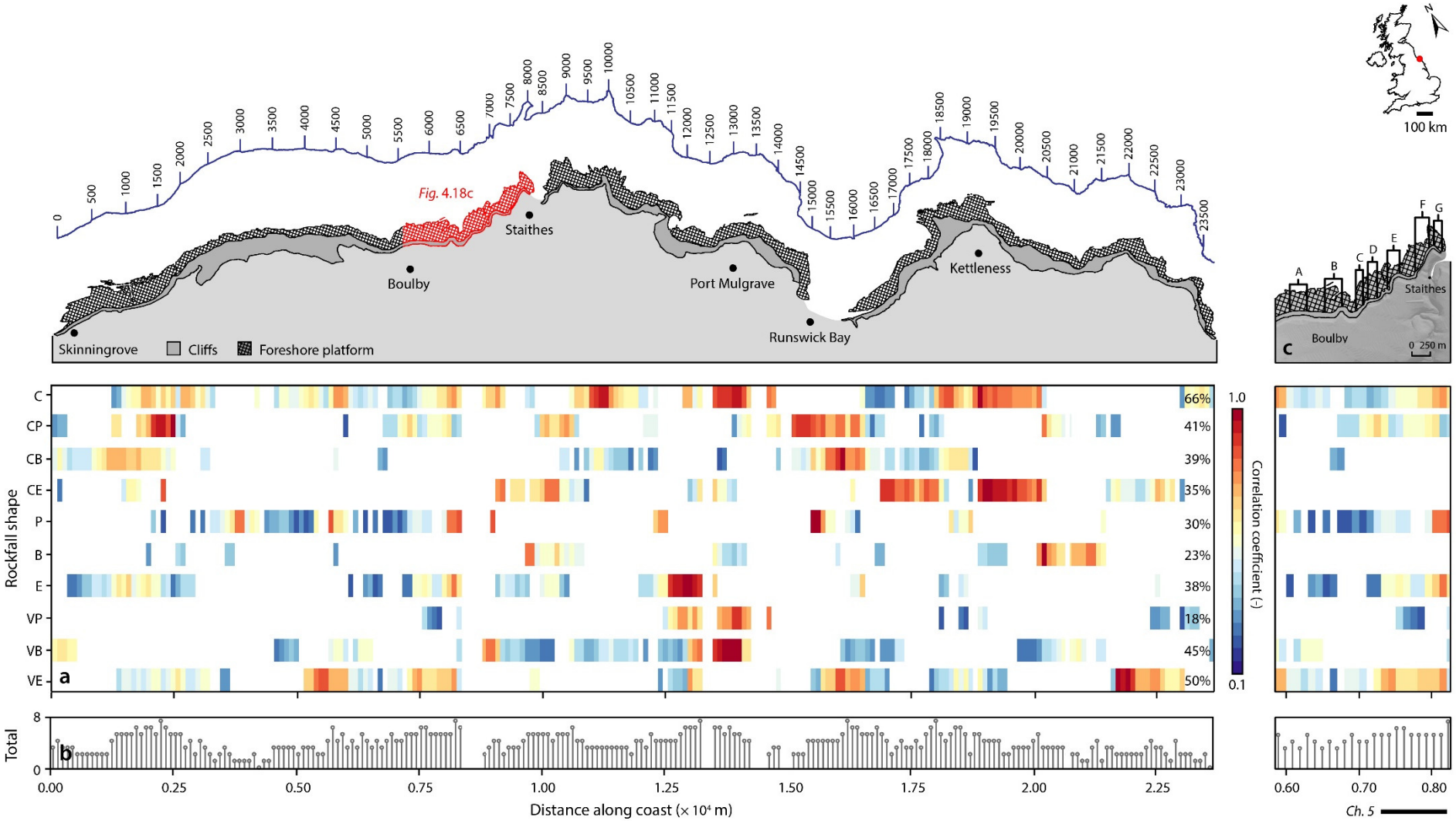
Fig. 4.18c
Staithes
Boulby
Port Mulgrave
Kettleness
Runswick Bay
Skinningrove
Cliffs
Foreshore platform
100 km
A
B
C
D
E
F
G
Staithes
Boulby
0 250 m
c
Rockfall shape
C
CP
CB
CE
P
B
E
VP
VB
VE
66%
41%
39%
35%
30%
23%
38%
18%
45%
50%
a
1.0
0.1
Correlation coefficient (-)
Total
8
0
b
0.00
0.25
0.50
0.75
1.00
1.25
1.50
1.75
2.00
2.25
Distance along coast (× 10⁴ m)
0.60
0.70
0.80
Ch. 5

Figure 4.18 *Overleaf. Spatial variations in the correlations between rockfall shapes shown in Figure 4.17. Correlations are windowed (± 200 m) and only shown in (a) if there is a positive correlation between shapes observed in both 2014 – 2015 and 2015 – 2016,* ***and*** *2015 – 2016 and 2016 – 2017. The total number of positively correlated shape classes for each 100 m bin is shown in (b). The inset in (c) shows in detail the previously monitored sites (Table 2.01, p. 19) as well as the sites monitored in Chapter 5.*

The distribution of rockfall shape and the exponent of the magnitude-frequency distribution, β, is shown in Figures 4.19a and 4.19b as a function of cliff elevation. In the combined inventory (n = 58,032), rockfalls occurring at the base of the cliffs (< 6 m OD) are more evenly distributed throughout the ternary diagram (Figure 4.19c). Over a third of rockfalls (*ca.* 33.9%) that occurred at these elevations are very platy, bladed or elongate, with relatively few compact (or blocky) shapes (*ca.* 9.7%). This is also marked by a pronounced inflexion in the exponent of the magnitude-frequency distribution β (Figure 4.19b), which indicates that the size distribution of rockfall activity at the cliff toe is dominated by relatively large failures (as in *Section 3.3.4*). The distribution of rockfall shapes remains stable up to an elevation of *ca.* 70 m OD; at these elevations, the majority of rockfalls (> 60%) are compact (or blocky) in shape, lying in the top half of the ternary plot. This approximately reflects the value of β, which remains stable at these elevations, indicating that the relative volume of material contributed by events of varying sizes stabilises above the limits of marine influence, as discussed in *Chapter 3*. These patterns could be related to changes in the groundwater regime, weathering environment, and the stress field up cliff, or to changes in structure, such as joint spacing and density (*Section 4.3.2*).

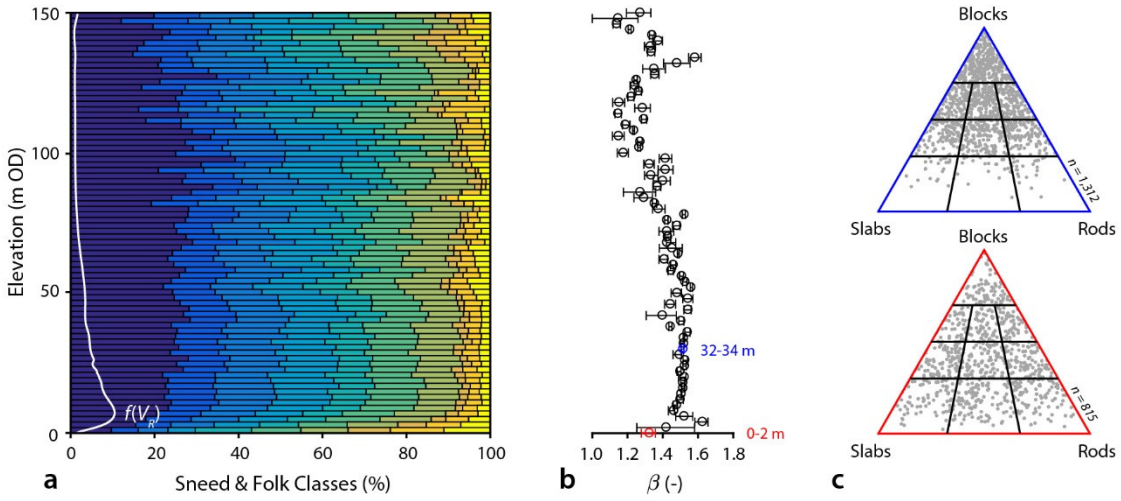

Figure 4.19 *Rockfall shape, derived for all 58,032 rockfalls in the inventory, plotted as a stacked bar graph against elevation in (a). The probability density of cliff elevation is overlaid in white. Colours correspond to the 10 sub-categories shown in Figure 4.15b, defined by Sneed and Folk (1958). Bins are in 2 m increments from an elevation of 0 m OD. The exponent of the magnitude-frequency distribution, β, of rockfall volumes is plotted against elevation in (b). A subset of the shape distributions for two bins at different elevations, and with different values of β, is shown in (c).*

4.3.4 Rockfall contiguity and relationships with cliff structure

When divided into separate inventories, the properties of contiguous and non-contiguous rockfalls differ considerably (Table 4.01). Despite contributing a relatively small proportion of the rockfalls observed (*ca.* 18%), together, contiguous rockfalls constituted > 83% of the total eroded volume, with a mean volume of *ca.* 9.82 ± 1.13 m^3, as compared with the mean volume of non-contiguous rockfalls (*ca.* 0.43 ± 0.08 m^3). This is likely because over half (*ca.* 53,721 m^3) of the total (*ca.* 104,326 m^3) volume eroded by contiguous rockfalls was contributed by 12 large (> 1,000 m^3) events. The proportion of rockfalls that occurred along the North Yorkshire coast that were spatially associated (contiguous), regardless of the scenario considered, is consistently an order of magnitude higher than those measured under complete spatial randomness. On average, 10.5% of rockfalls that occurred along the North Yorkshire coast had coalesced with the scars of those that had occurred the previous year, in comparison with a value of *ca.* 1.7% that would be expected under conditions of complete spatial randomness (Figure 4.20). Of the 58,032 rockfalls that occurred over the 32-month monitoring period, approximately 3.6% were part of a sequence of rockfalls that had propagated year-on-year ('concentrated coalescence') compared to *ca.* 0.1% estimated in the randomised control. Just as path-dependency has been observed among landslides (for example, Samia *et al.*, 2017a), these data demonstrate a clear spatial dependence among rockfalls occurring along the North Yorkshire coast, suggesting that they are not Poissonian processes. However, the linkage observed at this scale only applies to a small percentage of the

Table 4.01 *Summary of rockfall characteristics across three different inventories.*

	2014 – 2015, 2015 – 2016, 2016 – 2017		
	All rockfalls	*Contiguous*	*Non-contiguous*
Cliff length (m)	20,459	20,459	20,459
Cliff area (m^2)	805,739	805,739	805,739
Number of rockfalls (-)	58,032	10,622	47,410
Mean rockfall volume (m^3)	2.15 ± 0.24	9.82 ± 1.13	0.43 ± 0.08
Median rockfall volume (m^3)	0.014	0.104	0.010
Rockfall density (m^{-2})	0.072	0.013	0.059
Minimum eroded volume (m^3)	102,794.44	88,171.39	14,623.05
Average eroded volume (m^3)	124,843.31	104,326.48	20,516.83
Maximum eroded volume (m^3)	134,642.52	112,295.51	22,347.01
Annual retreat (m yr^{-1})	0.059	0.049	0.010
Standardised yield (m^3 m^{-1} yr^{-1})	2.320	1.939	0.381

Notes: Monitored cliff area is an average of the areas presented for each monitoring period in Table 3.01 (p. 29). Standardised yield is calculated per linear coastline metre, per annum.

total. Using the locations of previous events as an indicator of future rockfall risk from these cliffs is therefore problematic, as by far the majority appear unrelated to the location of those that have occurred in the two years monitored previously.

To establish whether differences in the properties of contiguous and non-contiguous rockfalls are driven by variations in cliff structure, the distribution of rockfall shape, facet spacing, area, density, dip, and the difference between facet aspect and cliff aspect as a function of rockfall volume was plotted for both inventories (Figure 4.21). There are few conspicuous differences between the inventories, as demonstrated by the box plots in Figure 4.21, although the differences for all inventories demonstrate a peak in volumes between 10^{-3} and 10^{-1} m^3, which approximately coincides with the peak observed in Figure 4.15a. These data illustrate the difficulties in elucidating any meaningful relationships between spatial variations in cliff structure and patterns of rockfall contiguity at regional scales. While the distribution of rockfall shape and volume through time have been shown to be spatially consistent, approximating the geological setting of the coastline (*Section 4.3.3*), relating the properties of individual rockfalls to variations in the geometric properties of exposed joint (or facet) surfaces at these scales remains difficult.

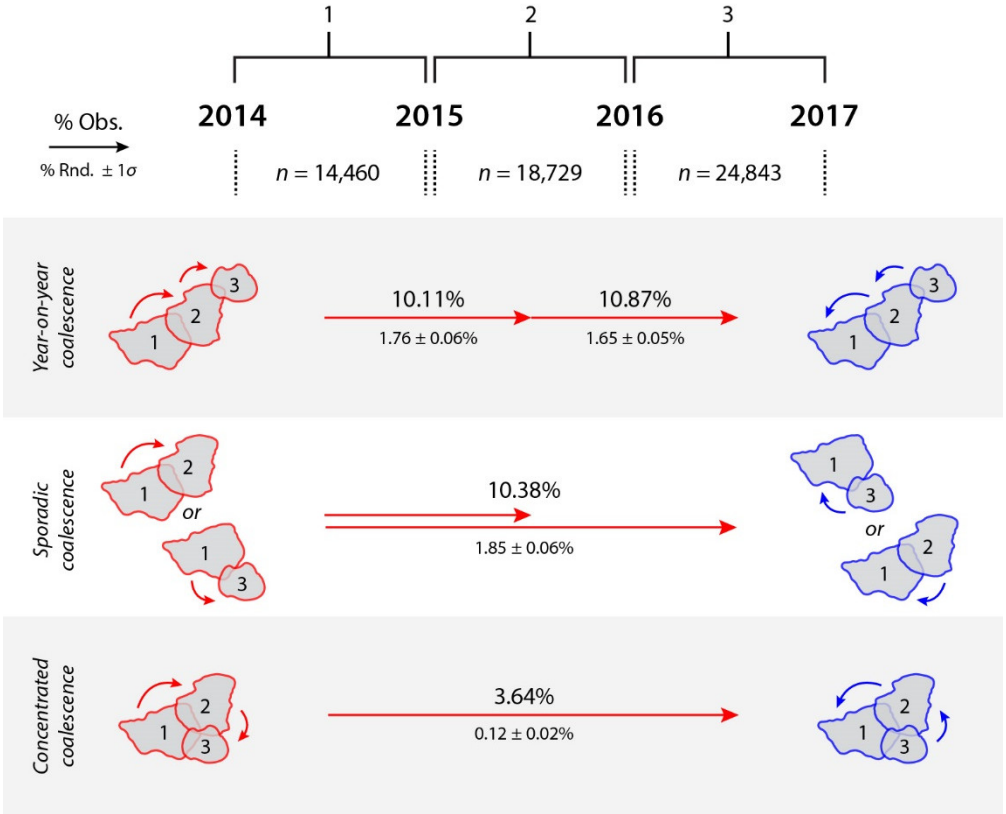

Figure 4.20 *Schematic diagram illustrating patterns of rockfall coalescence along the North Yorkshire coast between 2014 and 2017. Diagrams indicate possible coalescence scenarios. Colours indicate that percentages are applicable to both directions of coalescence. Numbers in large text were derived by dividing the number of rockfalls that coalesced by the total number of rockfalls that occurred across the monitoring periods of interest. Numbers in small text indicate the proportion of coalescence under complete spatial randomness.*

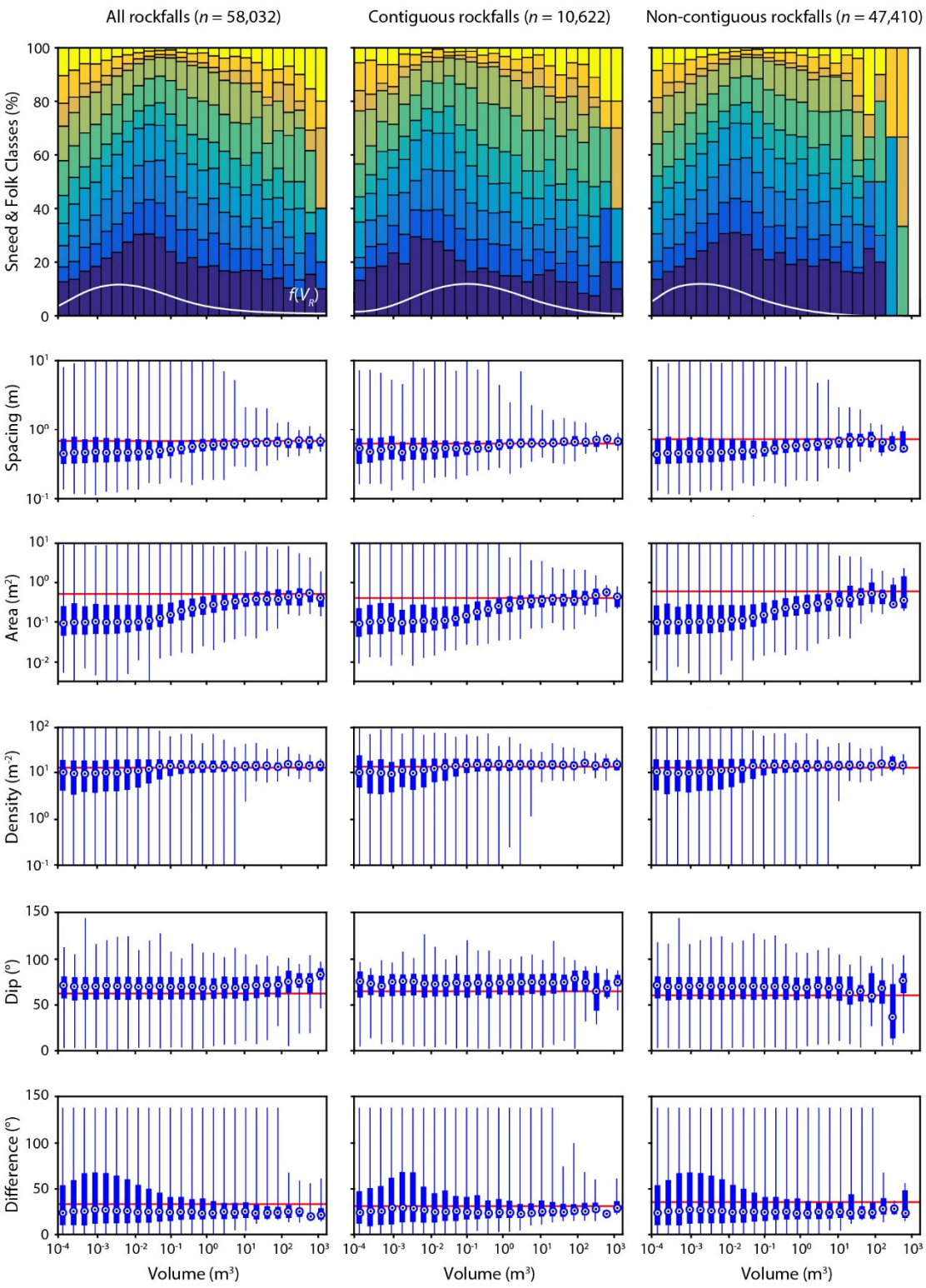

Figure 4.21 *Rockfall shape plotted as a stacked bar graph for three different inventories: all rockfalls (n = 58,032), contiguous rockfalls (n = 10,622), and non-contiguous rockfalls (n = 47,410). The probability density of rockfall frequency as a function of volume is overlaid in white. Colours correspond to the 10 sub-categories shown in Figure 4.15b, defined by Sneed and Folk (1958). Variations in facet spacing, area, density, dip, and the difference between facet and cliff aspect are plotted as compact box and whisker plots underneath for each volume bin. Red lines indicate the global mean in each case.*

4.4 Summary

Using high-resolution airborne LiDAR data, this chapter has derived a detailed, quantitative appraisal of variations in the geometric properties of exposed joint surfaces along the North Yorkshire coast. The chapter has explored how rockfall properties, such as block shape and volume, are related to wider-scale variations in these properties, both up-cliff and along-coast. Specifically, the resulting analyses have been used to show that:

1. Cliff structure, as defined by the geometric properties of exposed joint surfaces, varies alongshore. These variations appear to reflect variations in lithology, and are most clearly expressed in the headland and embayment sequences that are characteristic of the coastline, where lower cliffs composed of drift materials separate steeper headlands.
2. Rockfall shape is not scale invariant, and the relationship between rockfall volume and block shape is persistent year-on-year, providing the potential to predict future distributions of rockfall shape using magnitude-frequency relationships. Variations in mean rockfall shape with volume also imply a systemic shift in the underlying mechanisms of detachment with scale, questioning the validity of applying a single probabilistic model to the full range of observed rockfall volumes along the North Yorkshire coastline.
3. Spatial consistencies in the distribution of rockfall shape and volume through time approximately follow the geological setting of the coastline, where ridges of solid rock are separated by lower cliffs of drift. Spatial variations in the strength of correlations could be conditioned by differences in local processes (for example, nearshore wave impacts) and morphological controls between sites.
4. Rockfall occurrence at a regional scale is not a Poissonian phenomenon, although the proportion of contiguous rockfalls observed in this inventory is low enough (*ca.* 10.5%) to preclude hazard management using solely a database of precursory events. This finding has considerable implications for modelling future rockfall activity using magnitude-frequency distributions, which assume statistical independence between the observed events.

The results presented in this chapter have shown that variations in cliff structure can partially account for the consistent patterns of spatial variation in cliff retreat that were observed in *Chapter 3*. In order to understand the potential influence of spatial variations in cliff base wave impacting on these patterns, the ground motion response to wave impacting along a *ca.* 900 m stretch of cliffs of relatively uniform lithology and structure is therefore evaluated in *Chapter 5*.

This page is intentionally left blank

Chapter 5

Coastal cliff ground motions and response to wave loading

In (micro)seismically active zones, laboratory testing and numerical modelling have shown that repeated loading cycles involve variations in both the magnitude of dynamic stresses, their amplitude relative to baseline stress conditions, and their orientation relative to existing fracture sets and ground surface topography (*Chapter 1*). The cumulative effect of this (micro)seismicity has been suggested to play a crucial role in reducing rock slope stability by allowing macro-scale rock fracture to occur at stresses that are considerably less than the peak strength of intact rocks. If this is the case, then cyclic loading and consequent fatigue of rock slopes could hold important implications for the timing and distribution of landform and landscape susceptibility to change. In coastal settings, it is unknown how cliff response to wave impacting varies alongshore, or whether differences in the ground motion response between sites drive spatial variations in cliff erosion. Along-coast variations in coastal geometry and foreshore bathymetry should mean that spatial variations in cliff erosion are the product of differences in resisting and driving processes, meaning that coastal cliffs present an ideal case study for separating the effects of cliff structure from wave loading. The following discussion reviews the state of knowledge on the ground motions that occur on cliffed shorelines, and the conditions responsible for driving them (*Section 5.1*). *Section 5.2* outlines a workflow for integrating and processing data from a number of sources, with the aim of identifying relative variations in the ground motion response to wave impacting along a *ca.* 900 m stretch of cliffs, where other factors (lithology, structure, weather, groundwater regime) are broadly constant. *Section 5.3* presents the first concurrent observations of alongshore variations in wave impact-driven ground motions at coastal cliffs. Using the resulting inventory of wave impacting, this section explores how wave loading characteristics vary along the coastline, and how these are related to varying morphological controls and coastal processes (*RQ3*).

5.1 Ground motions on cliffed shorelines

Ambient vibrations of the ground, termed seismic noise or microseismicity, occur due to a range of natural and anthropogenic sources (Gutenberg, 1958). These vibrations have been used to forecast volcanic eruptions (Brenguier *et al.*, 2008), to constrain the seismic response of potentially unstable hillslopes (Burjánek *et al.*, 2012; Luo *et al.*, 2014; Del Gaudio *et al.*, 2015), to identify iceberg calving events (Amundson *et al.*, 2008), to detect and characterise mass movements (Amitrano *et al.*, 2005) such as precursory cracking prior to rockfall (Senfaute *et al.*, 2009) and the force-histories of rock avalanches (Allstadt, 2013; Ekstrom and Stark, 2013; Hibert *et al.*, 2014), and to measure fluvial discharge (Hsu *et al.*, 2011) and sediment transport (Roth *et al.*, 2014, 2016). Ground motions generated by ocean waves, which are often considered as noise in such studies, have been used for a range of purposes including monitoring of offshore oil and gas fields (de Ridder and Biondi, 2013), wave hindcasting (Powell *et al.*, 2010), tsunami monitoring (Yuan *et al.*, 2005), and for characterising coastal cliff ground motions as a proxy for wave loading and therefore erosion (Adams *et al.*, 2002, 2005; Young *et al.*, 2011, 2012, 2013, 2016; Dickson and Pentney, 2012; Norman *et al.*, 2013; Earlie *et al.*, 2015; Vann Jones *et al.*, 2015).

Recent seismic observations at coastal cliffs suggest that the ground motions generated by ocean waves may constitute a suitable proxy for wave impacting at the cliff. This is based on the assumption that the ground motions recorded reflect the timing, magnitude, and efficacy of wave forcing (Vann Jones *et al.*, 2015). Previously, due to challenges in collecting data on nearshore wave conditions, far-field observations were instead used to approximate conditions in the nearshore, such as wave power propagation and dissipation, through numerical transformations (for example, Collins and Sitar, 2008; Young *et al.*, 2009). These transformations have since been used, often without validation, to estimate cliff response to marine forcing (Trenhaile and Kanyaya, 2007) and to underpin models of past and future cliff evolution (Young *et al.*, 2009; Revell *et al.*, 2011; Castedo *et al.*, 2012). The vertical distribution of wave erosion in a number of these numerical models, including SCAPE (Walkden and Hall, 2005, 2011), is modelled as a direct function of inundation duration (Sunamura, 1975, 1977; Trenhaile and Layzell, 1981; Carr and Graff, 1982; Belov *et al.*, 1999; Trenhaile, 2000, 2009, 2011). However, on many non-carbonate coastlines there is little evidence of notching at the cliff toe (Pierre and Lahousse, 2006; Rosser *et al.*, 2007; Young *et al.*, 2009; Vann Jones *et al.*, 2015), meaning that the relationships between the vertical distribution of erosion, inundation duration, and wave impacting in these areas has remained poorly understood.

The absence of direct observations of wave-cliff interaction, and the resulting erosion, has led to the use of cliff-top microseismic ground motions as a proxy for wave impacting. Variations in cliff ground motions are driven by a range of local mechanisms that give rise to distinct microseismic frequencies (Figure 5.01). Superimposition of sea waves in the open ocean, which often propagate trans-continental distances, generates 'double frequency' microseisms that are

twice the frequency of ocean waves. Local sea, swell (Adams *et al.*, 2005), or infragravity (Young *et al.*, 2011, 2012, 2013) waves in nearshore waters generate low frequency cliff motion (0.01 – 0.10 Hz), or 'flexing'. This consists of downward and seaward ground motion and seaward ground tilt during wave loading and the opposite during unloading, amounting to a vertical ground displacement of *ca.* 0.5 – 10.0 μm at the cliff-top over each loading cycle when significant wave heights are > 3 m (Adams *et al.*, 2005). Cliff flexure occurs *ca.* 3 million times annually, with the

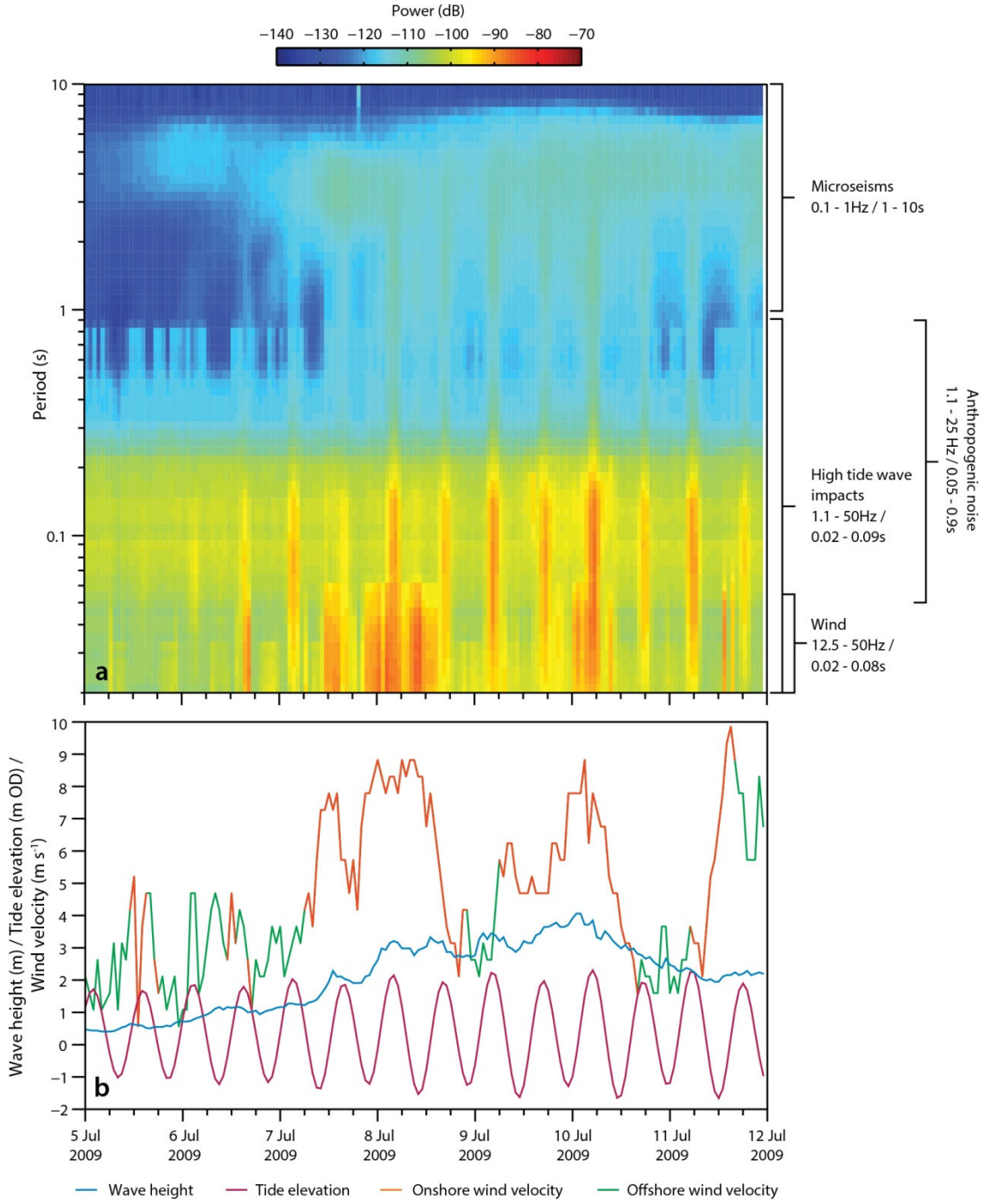

Figure 5.01 *Cliff-top ground motion response to wave height, tides, and wind over one week, where (a) is a power spectrogram (z-component) showing three frequency bands identified across the 0.1 – 50.0 Hz (0.02 – 10.00 s) spectrum of ground motions, and (b) is wave height, tide elevation, and wind velocity. Adapted from Figure 2 in Norman et al. (2013, p. 6811).*

amplitude of these cycles decaying exponentially with distance inland (Adams *et al.*, 2005). This cross-shore gradient in vertical displacements is suggested to fatigue the bedrock through microcracking, leaving the cliff face more susceptible to erosional processes associated with wave attack. Waves that directly impact the cliff generate higher frequency ground motion (> 0.3 Hz) or 'shaking' (Adams *et al.*, 2002), which is also caused by waves breaking in the nearshore (Poppeliers and Mallinson, 2015), on fronting shore platforms (Dickson and Pentney, 2012), wind buffeting (Norman *et al.*, 2013), and anthropogenic sources, including vehicle traffic. Frequency band widths and the number of peaks within these are likely to vary from site to site due to variations in local conditions, cliff geometry, and geological composition.

Previous research has shown that energy delivery to the cliff face is strongly modulated by tide, with both cliff shaking and cliff flexing increasing with water depth and incident wave height (Adams *et al.*, 2002, 2005; Young *et al.*, 2011), although this can vary with platform elevation and platform microtopography. For example, Dickson and Pentney (2012) found that the majority of wave energy at Okakari Point, New Zealand, was dissipated at the seaward edge of an elevated foreshore platform, which acted to amplify cliff-top ground motions at mid-low tides. Similarly, the extent (> 200 m) and microtopography of the foreshore platform at Boulby was shown to strongly condition wave energy flux and impact timing (Lim *et al.* 2011). Peak energy transfer occurs during the largest storm events, where bottom frictions and water depths are sufficient to maintain constant wave impacting, and therefore energy delivery, at the cliff face (Norman, 2012; Norman *et al.*, 2013). In Porthleven, Cornwall, significant wave heights of *ca.* 6 – 8 m in January/February 2014 generated vertical ground motions in excess of 50 – 100 μm at the cliff-top, driving rates of erosion up to two orders of magnitude higher than the long-term rate (Earlie *et al.*, 2015). A 32-day microseismic dataset obtained from the cliff-top at Boulby demonstrated that energetic storm events generate ground motions with a sustained cliff-normal component (Brain *et al.*, 2014), with the implication that changes in loading direction beyond those commonly experienced could lead to a change in the micro-scale stress field. This would act to extend microcracks beyond conditions achievable by low amplitude background displacements (those experienced during sea cliff flexure, for example), which are considered insufficient to damage the rock mass.

Previous studies lack quantitative analysis of spatial variations in cliff base waves and shaking, with many instead focussing on cross-shore variability (Adams *et al.*, 2005; Young *et al.*, 2011, 2012; Dickson and Pentney, 2012; Norman, 2012). Although a direct link between wave-induced ground shaking and cliff erosion is yet to be clearly demonstrated, findings presented in *Chapter 3* show consistent patterns of spatial variation in cliff retreat over time. Some of this variation can be accounted for by variations in cliff structure (*Chapter 4*); in this chapter, this variable is removed by monitoring variations in the ground motion response to wave impacting along a *ca.* 900 m stretch of cliffs, of relatively uniform lithology and structure, over one year.

5.2 Measuring cliff toe ground motions

The distribution of cyclic loading across a single rock slope, or an entire landscape, can be captured using a dense network of seismometers located on hillslopes likely to be affected by (micro)seismic ground motions. For example, Moore *et al.* (2011) and Burjánek *et al.* (2012) used a network of 12 tri-axial velocity sensors and nine digital seismic systems to record ambient vibrations on the Walkerschmatt rock slope in the southern Swiss Alps. Data obtained from installations such as these can be used to determine the site response characteristics of rock slopes subjected to variable loading conditions. This approach is adopted here in order to monitor relative variations in the cliff response to cyclic loading by wave impacting. Data are integrated from four sources. These include ground motion data, which were collected using an array of tri-axial accelerometers and treated as a proxy for the energy imparted to the cliff from the incoming wave field. Offshore wave conditions were recorded by a wave buoy and were combined with tidal data to populate a wave transformation model used for simulating nearshore wave conditions, including wave and set-up elevations, at each site. Spatial variations in rockfall activity were monitored using high-resolution, multi-temporal LiDAR (*Chapter 3*). Each dataset is outlined in detail below.

5.2.1 Data acquisition

Monitoring was undertaken along a stretch of cliffs west of Staithes and Cowbar Nab (Figure 5.02). Erosion along several cliff sections here has been extensively monitored using terrestrial LiDAR in the past, and this monitoring history is discussed in detail in *Section 2.2*. Airborne LiDAR surveys of the cliffs undertaken in *Chapter 3* show that retreat rates are highly variable, both within and between years (Figure 3.12, *p.* 43). Cliff retreat varied between

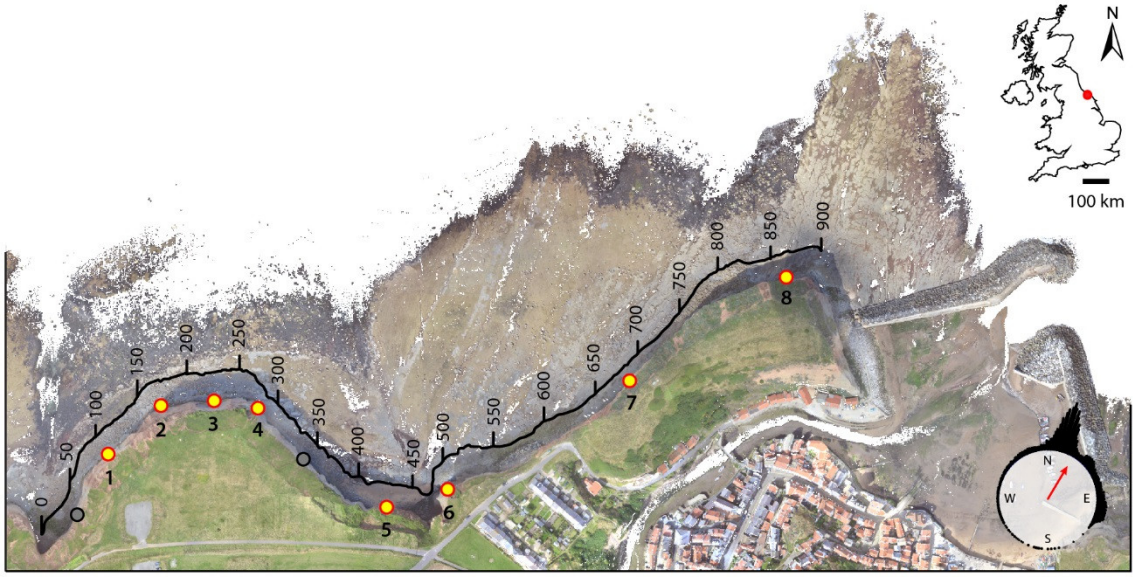

Figure 5.02 *Accelerometer installation sites west of the village of Staithes, North Yorkshire, plotted on top of a point cloud obtained in August 2014. Grey/yellow markers denote un/successful installations. Inset: circular histogram of wave directions recorded over the monitoring period, with the mean marked in red.*

4.010×10^{-4} m yr^{-1} and 0.006 m yr^{-1} from 2014 – 2015, 4.071×10^{-4} m yr^{-1} and 0.010 m yr^{-1} from 2015 – 2016, and 9.760×10^{-4} m yr^{-1} and 0.114 m yr^{-1} from 2016 – 2017. In places, locally high rates of change have been driven by the occurrence of large rockfalls, including one that caused a step-back of up to 6.50 m (636.19 ± 23.63 m^3, 2016 – 2017), threatening the access road from Staithes to Cowbar. The cliffs are relatively uniform in height and geology across the 900 m section. Cliff aspect ranges from 280° on the west side of Cowbar Nab to 80° in Staithes harbour, and the cliffs are fringed by as much as 270 m of foreshore platform in some places, and as little as 40 m in others. Given that the geology and wider environmental conditions over this section are broadly uniform (*Appendix E*, *p.* 191), large spatial variations in cliff aspect and nearshore bathymetry may drive differences in rockfall activity, and therefore erosion, at these sites.

5.2.1.1 Ground motion data

Ground motions were measured at eight sites with MSR 165 tri-axial accelerometers, which are optimised for recording high-frequency ground accelerations. The sensors were housed in a custom aluminium casing and set in the cliff face *ca.* 1.5 m above the cliff toe at each site, shown in Figure 5.03 (*p.* 92), using a 56 mm core drill. The instruments were set into the cliff toe in accordance with observations from other sites, where this elevation has provided the clearest indication of high frequency shaking induced by wave impacting (Dickson and Pentney, 2012). With the exception of S5, where a rockfall occurred on 12/01/2017 (Figure 5.03e), each position was occupied for a year between 6 September 2016 and 6 September 2017 in order to capture the full range of seasonal variations in ground motions. Recording was interrupted by 48 – 76 hour breaks approximately every 28 days for data download, recharging, and redeployment. The time lost during these periods equates to *ca.* 59 days, or 16.2% of the monitoring period, when synchronised across the eight sites. The sensor frequency was set to 200 Hz as the sensors had not previously been deployed to analyse cliff motion from wave impacting. Previous studies of cliff motion under wave loading have used seismometers monitoring at 100 Hz in order to determine cliff movement associated with the primary and secondary microseismic peaks (Adams *et al.*, 2002, 2005; Young and Adams, 2011). A GPS with Real Time Kinematic correction was used to determine the position and elevation of all the instruments, which are recorded in Table 5.01.

5.2.1.2 Oceanographic data

To approximate conditions across the cliffs, monitored distal waves and tidal data were modelled using a transformation based on Battjes and Stive (1985) derived by Norman *et al.* (2013) and summarised in *Appendix G* (*p.* 195). Half-hourly tidal elevations and residuals from the nearest available tide gauge (UK National Tide Gauge Network, Whitby, *ca.* 25 km south) and significant wave heights (H_s) obtained from an offshore wave buoy (CEFAS Wave Net, Whitby) were used to populate the model, which was run on 1,000 m long profiles taken at each site. An initial distance of 1,000 m was used as the water depth, and therefore wave conditions,

Table 5.01 *Accelerometer location, elevation, and aspect for each monitoring site.*

Site	*Easting*	*Northing*	*Elevation*	*Aspect*
	m	*m*	*m OD*	°
1	477633.43	518903.39	2.26	320
2	477676.08	518942.75	2.08	346
3	477729.80	518950.73	2.22	357
4	477758.23	518947.91	1.90	45
5	477860.81	518857.85	2.87	16
6	477931.51	518882.26	2.13	335
7	478076.23	518959.95	2.63	318
8	478205.81	519051.85	3.19	13

at that distance are approximately equal to those at the buoy according to linear wave theory. The modelled total water level was subsequently used to give an approximation of the inundation durations at each position of the array between 6 September 2016 and 6 September 2017.

Outputs from the model were validated using nearshore wave and tide information derived from an RBR*solo* water depth channel logger, which was deployed *ca.* 5 m seaward of the cliff toe at the site shown in Figure 5.03h. The instrument was deployed over a two-week period from 6 February 2017 to 21 February 2017, during which time significant wave heights observed at the offshore wave buoy exceeded 5 m. The instrument uses a pressure sensor with ± 0.05% accuracy, sampling 8 Hz bursts for *ca.* 17 minutes, every half an hour (totalling 8,192 samples per burst). Local water depths were computed as the mean water depth over the pressure sensor during each burst. Atmospheric pressure was removed from the record using half-hourly observations collected at the Loftus Met Office weather station, approximately 4 km northwest of the site. Timeseries were detrended and converted to hydrostatic elevation relative to the Ordnance Datum (m OD, at Newlyn, UK). Modelled total water level provides a good estimate of the observed maximum cliff base water level, with a comparison of modelled and measured water depths yielding a correlation coefficient of 0.93, with a mean absolute error of 0.09 m (*Appendix H, p.* 200).

5.2.1.3 Rockfall data

Longer-term variations in rockfall activity and the resulting cliff retreat between the sites were monitored using the data and methods presented in *Chapter 3*. The data were collected at three approximately equal intervals between August 2014 and March 2017. The aim of this chapter is not to demonstrate a direct physical link between wave-induced ground motions and cliff erosion, but rather to examine spatial variations in both in order to develop a more generalised understanding of how variations in loading magnitude, frequency, and direction may correlate with broader scale patterns of cliff erosion and retreat.

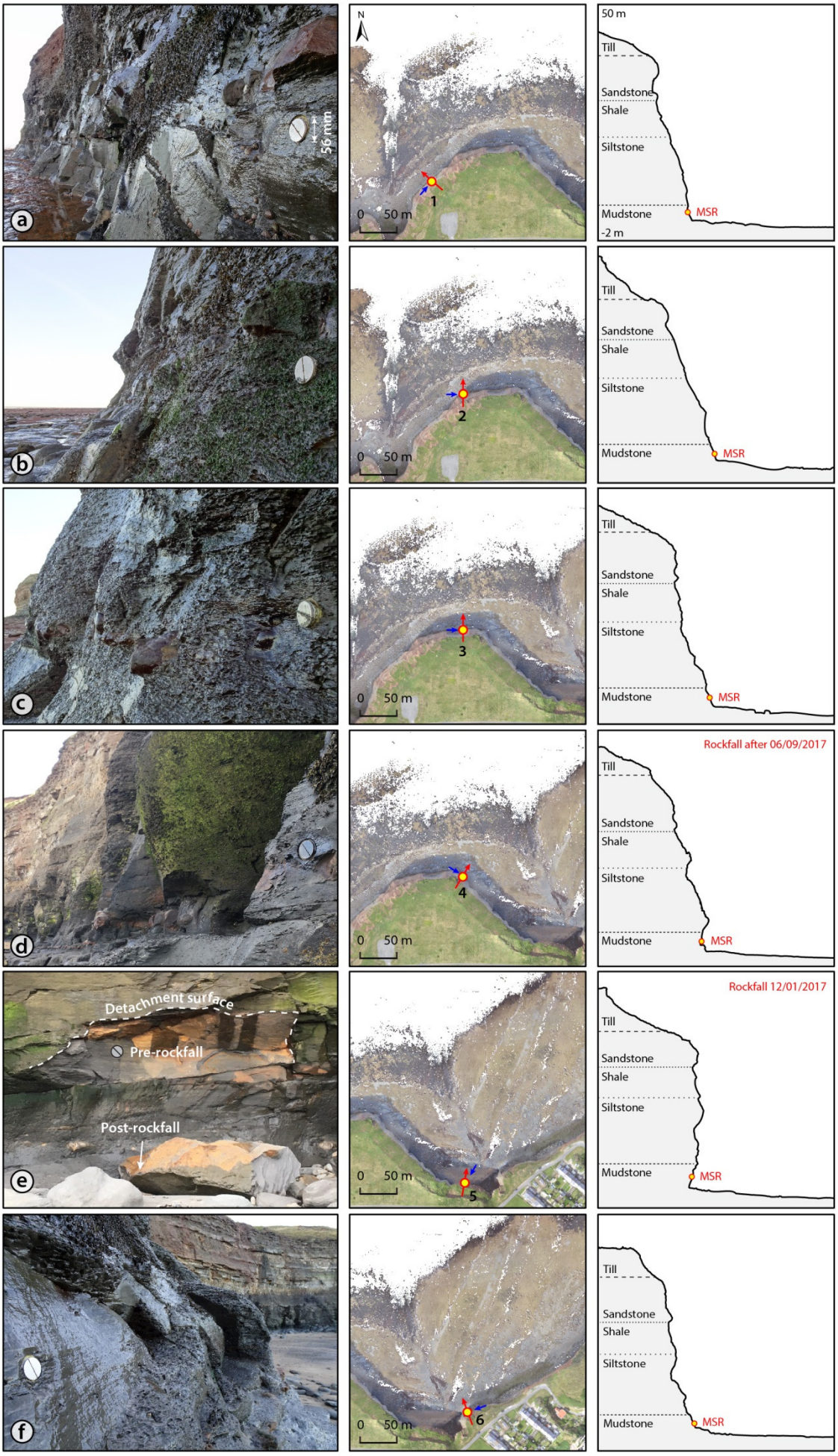
a
56 mm
N
0 50 m
1
50 m
Till
Sandstone
Shale
Siltstone
Mudstone
MSR
-2 m
b
2
c
3
d
4
Rockfall after 06/09/2017
e
Detachment surface
Pre-rockfall
Post-rockfall
5
Rockfall 12/01/2017
f
6

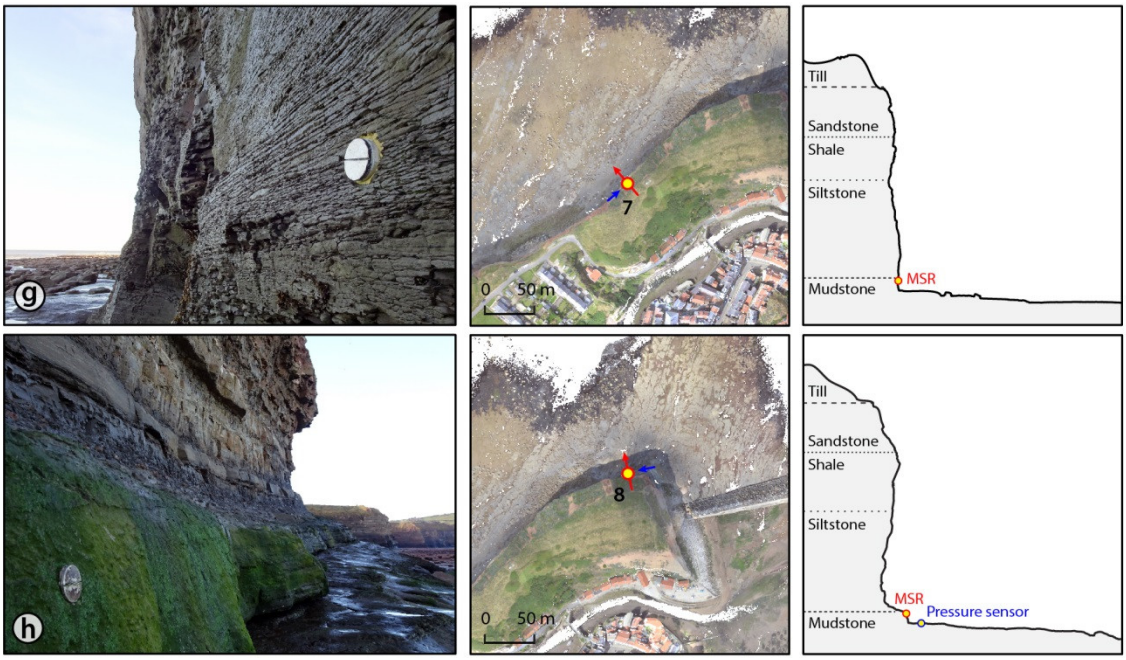

Figure 5.03 *Continued from overleaf. Vertical panels show photos of each installation site, as well as a location map and a cliff profile. Red arrows denote profile direction, while blue arrows denote the point of view from which each photograph was taken. Accelerometers 1 – 8 are shown in horizontal panels (a – h), respectively.*

5.2.2 Data processing

Processing ground motion data typically involves a number of steps, although it should first be noted that there are several differences between motion data recorded using an accelerometer and those recorded using a seismometer (as in the research outlined in *Section 5.1*). Firstly, previous research conducted using accelerometers to monitor ground motions at Mesnil-Val, France, has noted that microseismic events recorded during high tides are directly related to the action of waves on the cliff face and are often subject to high levels of signal attenuation (Senfaute *et al.*, 2009). The accelerometers used here measure ground accelerations that are driven purely by local (direct) wave impacting, which broadly equates to the high frequency shaking band (> 0.3 Hz), and removes the need to process the data in multiple frequency bands, as is the case with seismometer data. Secondly, in many seismic records observed at coastal cliffs, ground tilt maps part of the vertical gravitational acceleration onto the observed horizontal component of ground motions (Rodgers, 1968; Crawford and Webb, 2000), particularly at swell (0.04 – 0.10 Hz) and infragravity (0.01 – 0.04 Hz) frequencies (Young *et al.*, 2012), and therefore must be corrected. However, at high frequencies there is little contamination of cross-shore accelerations by ground tilt (Young *et al.*, 2012). This contribution is therefore ignored on the grounds that high frequency shaking, caused by waves directly impacting on the cliff, is the focus of this chapter. The workflow for processing the ground motion data collected in this chapter is detailed in Figure 5.04, which illustrates the main stages of data acquisition and processing.

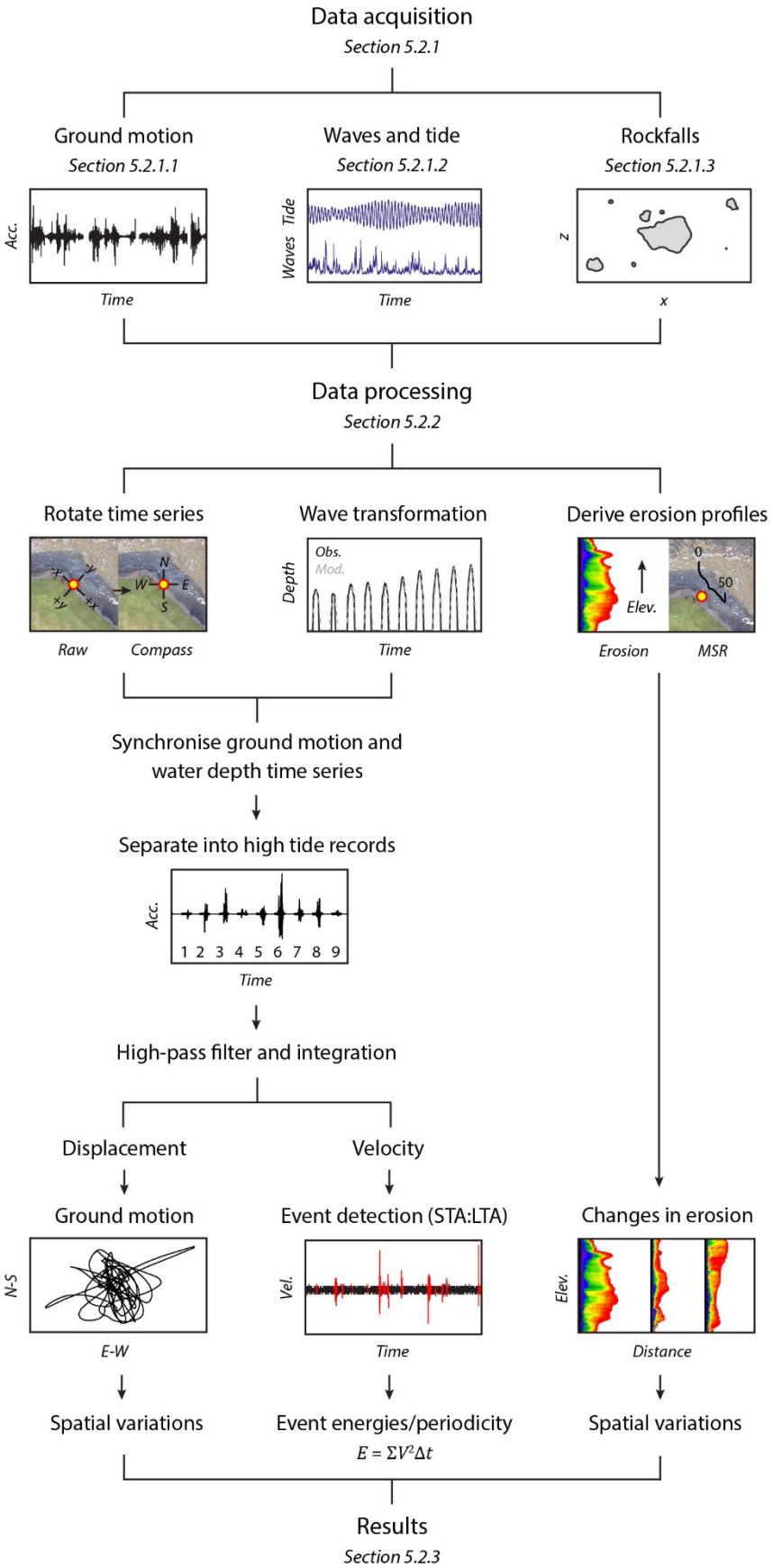

Figure 5.04 *Schematic diagram illustrating the main stages of data acquisition and processing detailed in this chapter. Rockfall data were acquired and processed for the coastline in Chapter 3, and a subset of the inventory from Staithes was used here.*

The raw data recorded at each site were processed to derive acceleration, velocity, displacement, and energy. Time series captured in the x (cliff-parallel), y (cliff-normal), and z (vertical) axes, which approximate the local shoreline orientation, were also rotated into compass coordinates (N-S and E-W) for all processing. The data were first synchronised using the system clock of the setup computer and, where appropriate, were adjusted for British Summer Time (BST). Hours containing significant ground motion from post-installation settlement were removed. The data were divided into 14 h epochs, each with *ca.* 1×10^7 observations, and were detrended and converted from g to m s^{-2}. The acceleration time series for each axis was high-pass filtered using a Butterworth filter with a cut-off frequency of 0.05 Hz, in order to ensure that signals with a longer period than the roll-off frequency of the instrument were not analysed. This prevents bias and drift in the signal upon integration, both of which are caused when the lower range of the instrument bandwidth is larger than 0 Hz. This is known as DC response, and the effects of integration on a signal with this bias are shown in Figure 5.05. A high-pass filter was

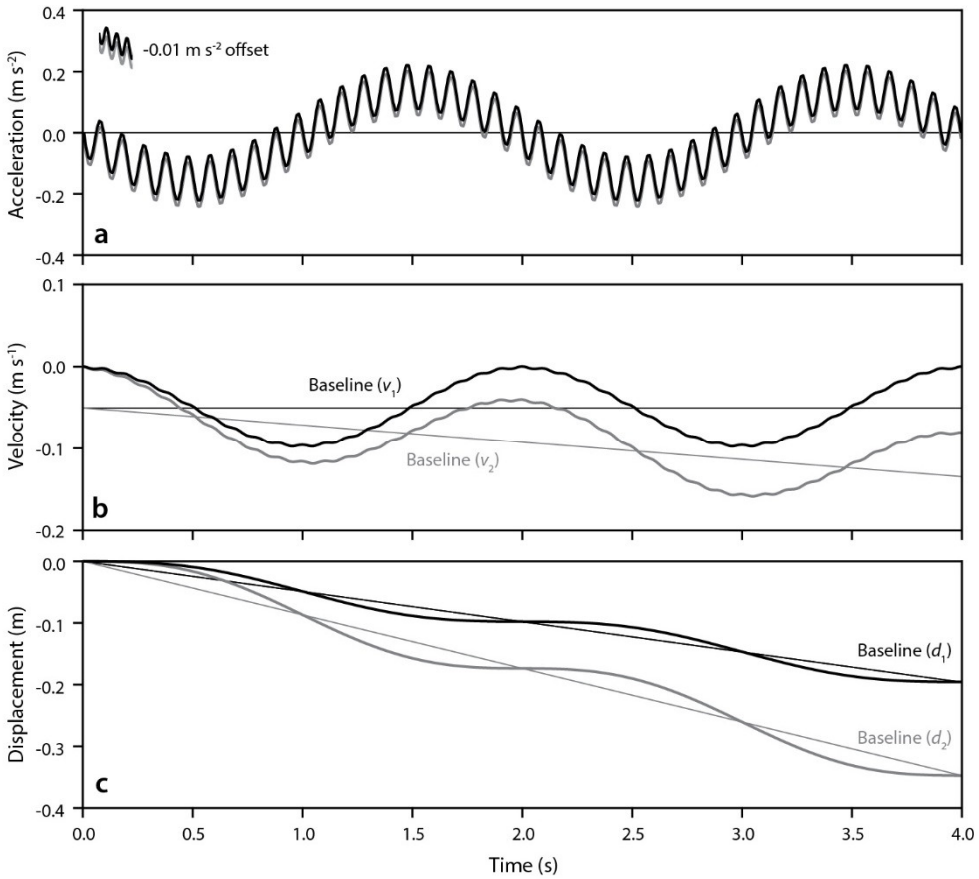

Figure 5.05 *Diagram illustrating the effect of DC bias on integration, using synthetic data, where (a) shows two identical acceleration waveforms, the latter of which is offset by -0.01 m s^{-2}, (b) shows trapezoidally integrated velocities of the acceleration signals shown in (a). The baselines v_1 and v_2 illustrate the influence of this offset, with baseline v_2 representing a linear drift, and (c) shows trapezoidally integrated displacements, which become unbounded over time. After each integration, the high frequency content of the original waveforms is increasingly diminished.*

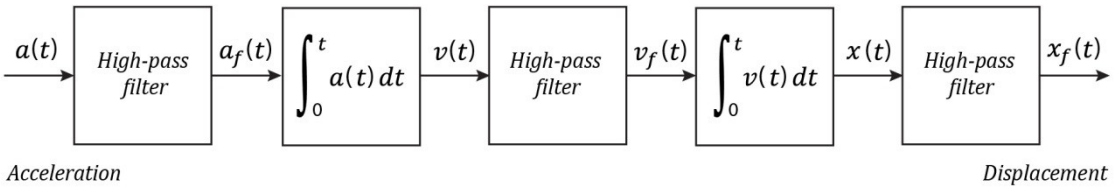

Figure 5.06 *Diagram of the double integration process. Each signal is filtered, both before and after integration, using a high-pass Butterworth filter in order to remove bias and drift in the signal.*

therefore used following integration to remove the DC component of the resulting velocity and displacement signals (Figure 5.06).

The ground motion data were synchronised with linearly interpolated observations of tide elevations before being divided into individual high tide records. This gave a total of 541 high tides monitored at each accelerometer with the exception of S5, which recorded ground motions for a total of 183 high tides. The data were divided in this way on the basis that cliff shaking signals were only above noise levels during periods of wave-cliff interaction. Individual impact events were then extracted using a moving short-term average/long-term average (STA/LTA) ratio, with an STA of 1 s and an LTA of 60 s, in order to prevent false triggering by noise. Event start and end times were then used to generate an inventory of impact events at each site, using the N-S velocity time series. The compass direction (azimuth) and the vector magnitude (displacement) were then calculated for each impact event using its particle motion ellipsoid.

5.3 Results

5.3.1 Cliff toe ground motions

A representative series of contemporaneous acceleration records of microseismic response to variations in tide and nearshore wave height for one of the accelerometers (S4) is presented in Figure 5.07. Horizontal accelerations (N-S and E-W) are much greater than vertical accelerations,

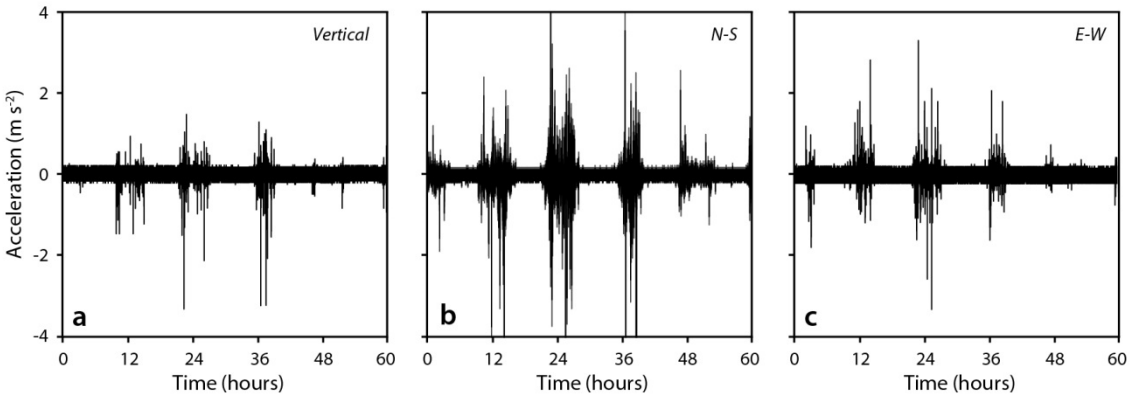

Figure 5.07 *Ground motions observed at S4, where (a) is vertical ground motion, (b) is north-south ground motion, and (c) is east-west ground motion. Note the influence of the tide in the acceleration record.*

and the semidiurnal tidal influence is apparent in all three directions of ground motion. The greatest variations in microseismic accelerations occurred during periods of high tide for north-south ground motions, while the least variation in accelerations occurred at low tide, where instrument noise (*ca.* ± 0.05 m s^{-2}) dominates the recorded signal.

When high tides and large swells coincide (H_s = 4.12 m, H_{max} = 7.69 m), a 12 – 15 s periodicity is clearly visible in the ground motion data (Figure 5.08), particularly in the horizontal components of motion where accelerations are greatest (> 4 m s^{-2}). Ground motion at high tide during smaller or more moderate swells (H_s = 0.23 m, H_{max} = 0.51 m) is diminished. Particle motion plots of the ground motions captured in these conditions are presented in Figure 5.09. The particle motion observed by the sensor is plotted during a single 15 s interval, which is marked in Figure 5.08. As observed by Adams *et al.* (2005), the cliff sways simultaneously downwards and towards the incoming wave field, which maps out an ellipsoid approximately parallel to the nearshore wave direction. The particle motion pattern observed when the cliff is impacted by small waves (Figure 5.09a) is consistent in shape with that during impacting by large waves (Figure 5.09b), although the length of the longest axis of the particle motion ellipsoid is *ca.* $^1/_5$ of the length.

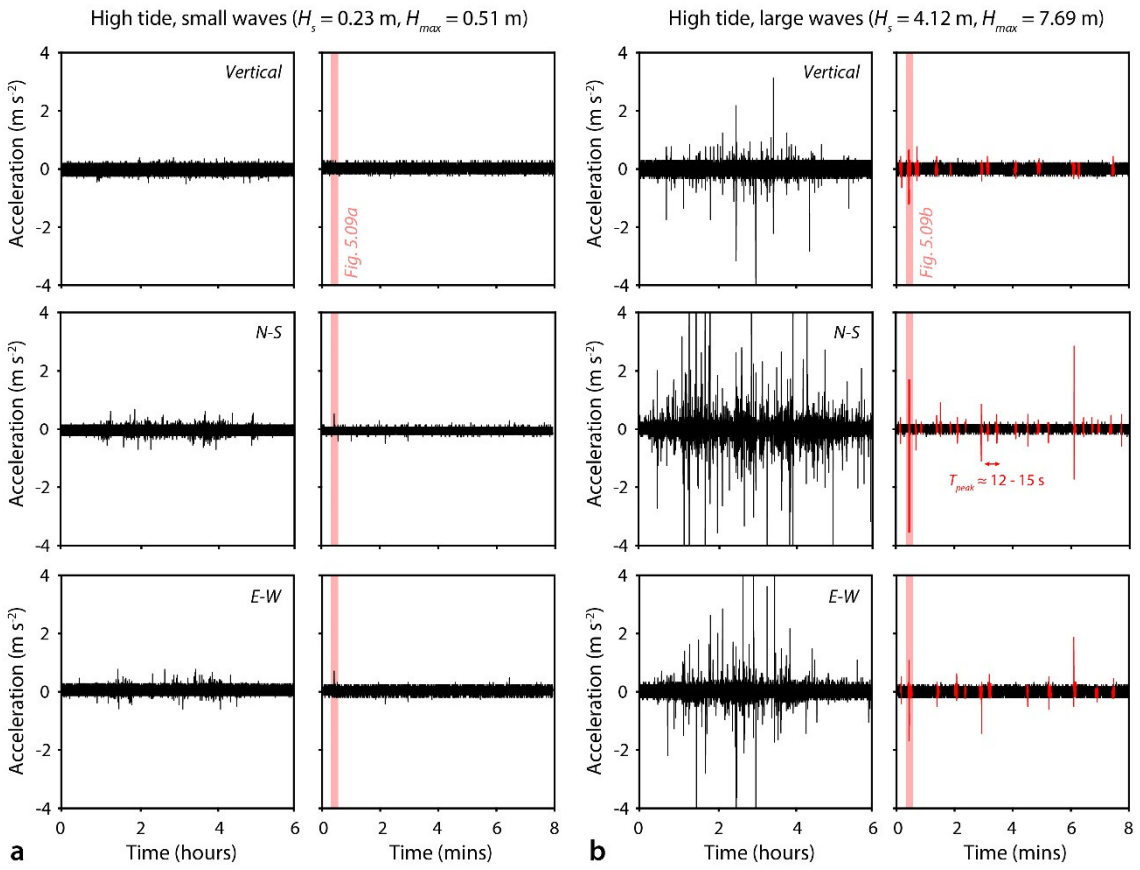

Figure 5.08 *Samples of ground motions captured at S4 over a 6 hour and an 8 minute window, at (a) high tide, with small waves, and (b) high tide, with large waves. When waves are large, note the strong 9 – 12 s periodicity (T_{peak}) and higher frequency crashers (T_z) that ride along on the longer period sway.*

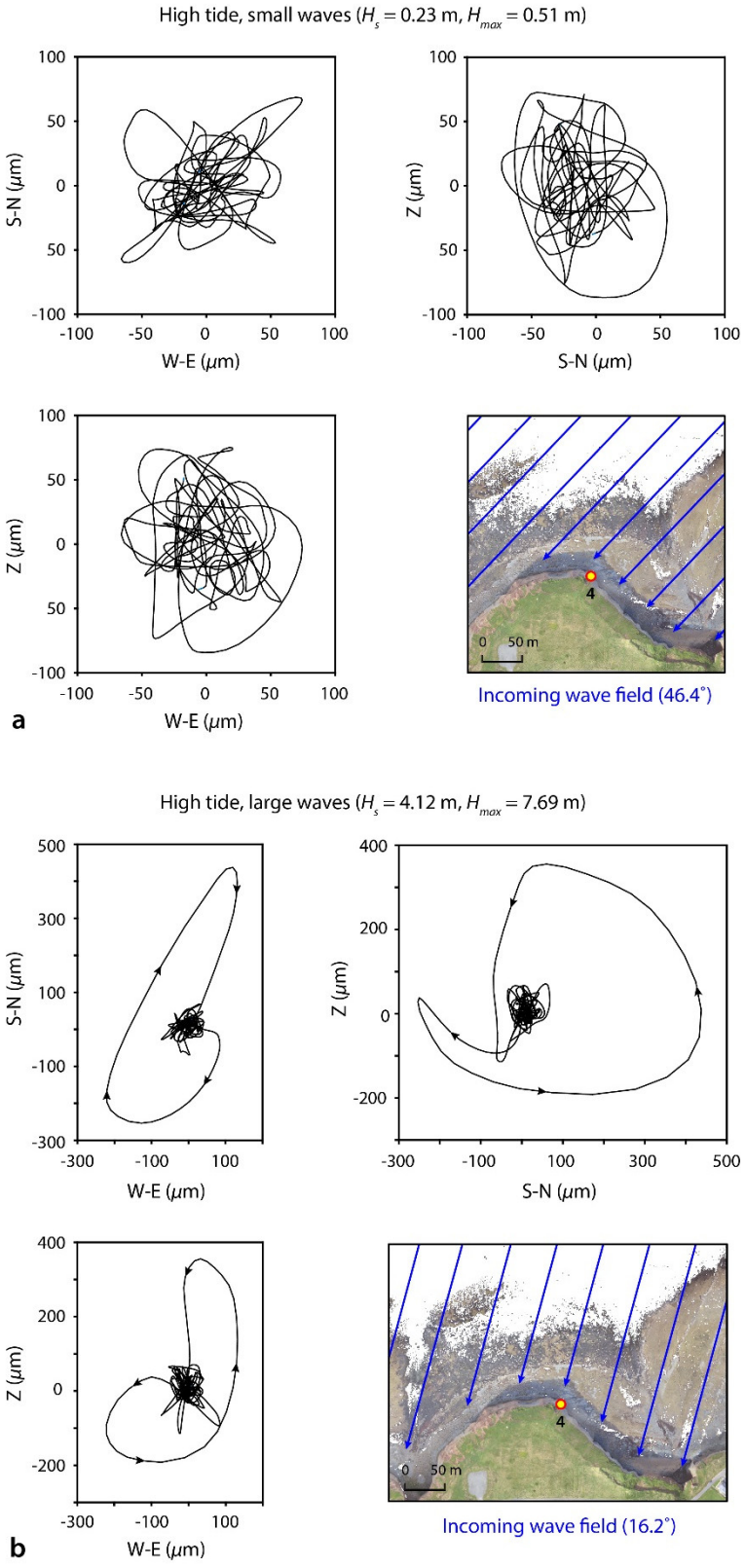

Figure 5.09 *Simultaneous particle motion plots of ground motions captured at S4, at (a) high tide, with small waves, and (b) high tide, with large waves. The plots correspond to the acceleration plots shown in Figure 5.08 and are of individual wave events captured over a 15 s interval. Note that the cliff sways simultaneously downwards and towards the wave field (approximated from the offshore wave buoy), which maps out an ellipsoid approximately parallel to the nearshore wave direction. This effect can be seen for both small and large waves.*

5.3.2 Spatial variations in ground motions

Although cross-shore decay of cliff top ground motions is well understood (Adams *et al.*, 2005; Young *et al.*, 2011, 2012; Dickson and Pentney, 2012; Norman, 2012), previous studies lack quantitative analysis of alongshore variations in cliff base waves and shaking, which require detailed observations of cliff impacts in both space and time. Figure 5.10 illustrates a yearlong time series of the cliff toe ground motions observed at eight sites along *ca.* 900 m of coastline between Staithes and Cowbar. Assuming an average wave period of 8.25 s over the monitoring period, as recorded at the nearest offshore wave buoy, these cliffs undergo $> 3.8 \times 10^6$ nearshore wave-induced flexing cycles per year (Adams *et al.*, 2005). However, the observed ground motions vary considerably alongshore, with sheltered sites, such as S1 and S7, undergoing fewer impacting events and at lower amplitudes than exposed sites, such as S2 – S4. The number of impacts observed over the monitoring period, excluding those recorded at S5, ranges between *ca.* 1.00×10^6 at S8 to *ca.* 4.16×10^6 at S3, which corresponds to an average rate of between 10.9 and 20.6 impacts min^{-1} when waves are directly in contact with the cliff toe (Table 5.02). Sites undergoing consistently high rates and amplitudes of impacting generally exhibit greater average horizontal than vertical displacements on impact (for example, S2 – S5), a finding that is at odds with microseismic measurements of cliff toe ground motion undertaken at a separate site by Dickson and Pentney (2012).

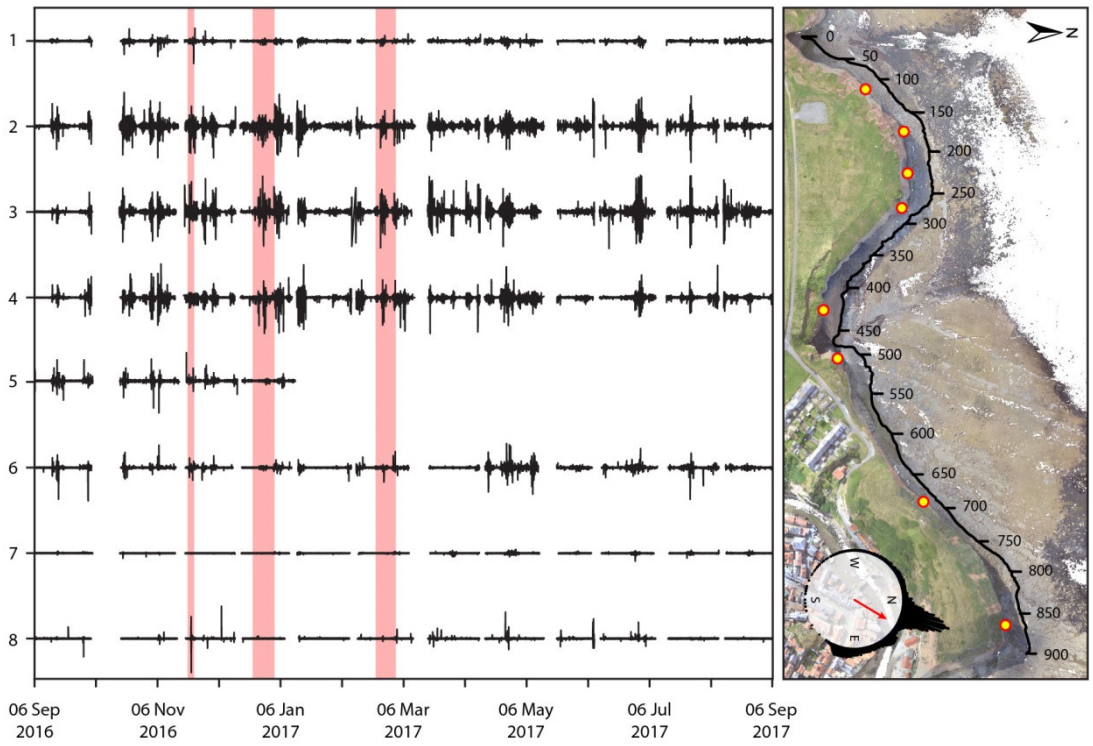

Figure 5.10 *Simultaneous plots of the ground motions captured at each site throughout the monitoring period (06 September 2016 – 06 September 2017). The ground motions plotted are those observed in the N-S axis. Monitoring at S5 was interrupted on 12 January 2017 by a rockfall. Red bands denote the passing of named storms and white bands denote missing data.*

Table 5.02 *Impact events observed at each site over the monitoring period.*

Site	*Impacts*	*Rate of impacts*	*Average displacement on impact*	
			Horizontal	*Vertical*
	-	min^{-1}	µm	µm
1	2,677,956	14.1	75.9	97.3
2	3,213,238	17.0	118.9	106.1
3	4,160,598	20.6	127.2	97.8
4	3,120,380	15.6	106.4	89.1
5*	441,860	19.2	111.8	110.1
6	2,825,580	14.2	89.9	97.6
7	1,310,992	10.9	73.7	101.8
8	1,000,892	16.4	113.0	98.4

* *Observations at this site were recorded over 102 days (as opposed to 306) due to a rockfall that occurred on 12/01/2017.*

Simultaneous particle motion plots of the ground motions and wave conditions captured at six of the eight sites show considerable variability in ground motion patterns, and hence energy delivery, alongshore (Figure 5.11). The acceleration time series, particle motion plots, and aerial photographs shown in Figures 5.11a and 5.11b were captured concurrently and are shown here as representative results that demonstrate the differences in ground motions captured across the sites, and at different times after high tide. As shown on a site-specific basis in Figures 5.07b and 5.08b, large swells (H_s = 4.49 m, H_{max} = 7.26 m) drive a *ca.* 12 – 15 s periodicity (T_{peak}, also observed at an offshore wave buoy) in ground motions approximately an hour after high tide (1.56 m OD), with the impact of higher frequency 'crashers' (T_z) that ride along on the longer period sway also evident at some sites (Figure 5.11a). The particle motion ellipsoids observed at the sites where strong impacting occurred, S2 – S6, are oriented approximately parallel to the nearshore wave direction, as is also shown in Figure 5.09. However, these patterns are only evident where instruments are not sheltered and where the instrument, and hence cliff toe, elevation is well within the range of modelled tide, wave, and set-up elevations (referred to from herein as the total water level). This is indicative of a strong relationship between impact ground motions observed at the cliff toe and the total water level, which is consistent with previous research undertaken using cliff top seismometers (Young *et al.*, 2016) and is investigated further in *Section 5.3.3*. The ground motions and wave conditions captured approximately two and a half hours after high tide (0.66 m OD) are further illustrative of this relationship: the long axes of the particle motion ellipsoids at each site are at least $^1/_2$ of the length of those captured an hour and a half previously (Figure 5.11b). Very sheltered sites (S1, S6, and S7), as well as sites that lie consistently on or above the total water level (S7 and S8), therefore receive very little impacting.

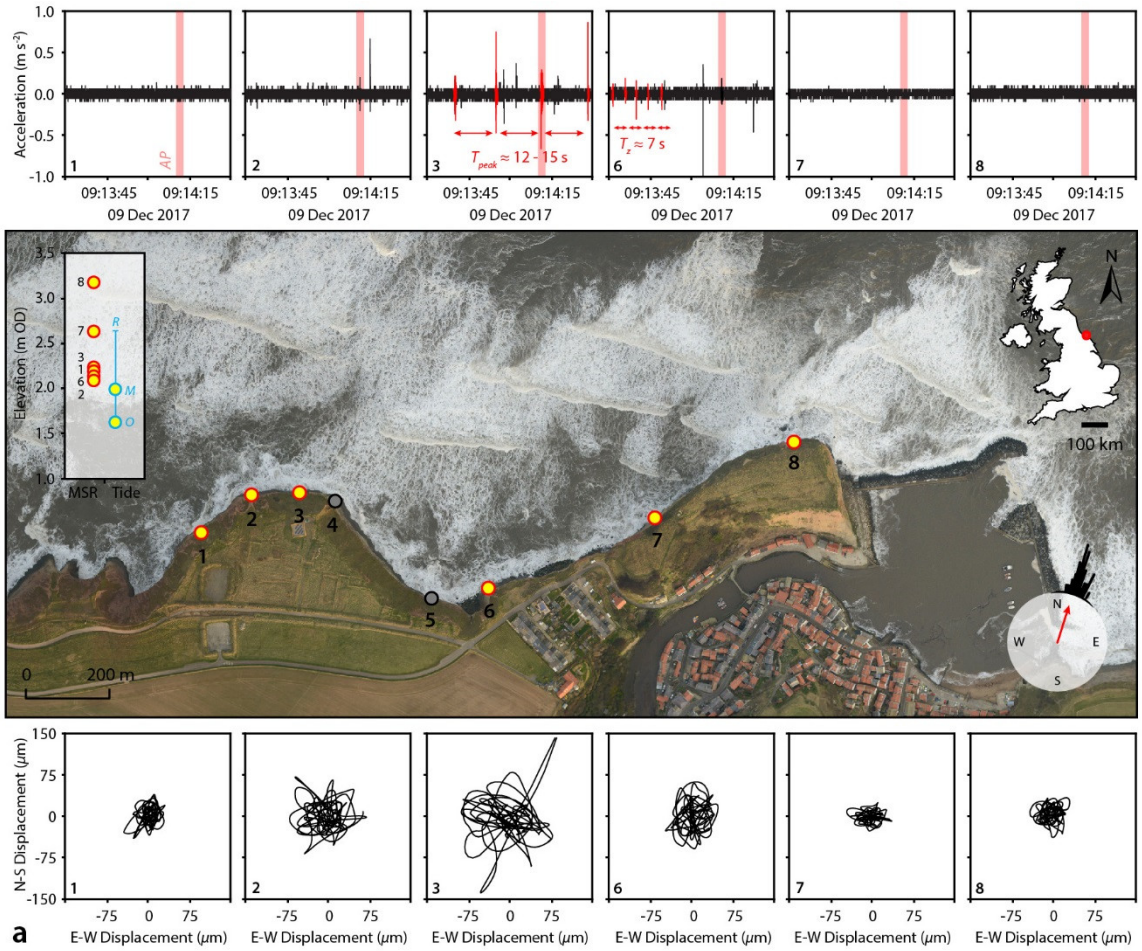
Acceleration (m s-2)
AP
$T_{peak} \approx 12 - 15$ s
$T_z \approx 7$ s
09:13:45
09:14:15
09 Dec 2017
Elevation (m OD)
MSR
Tide
R
M
O
100 km
200 m
N
S
E
W
N-S Displacement (μm)
E-W Displacement (μm)
a

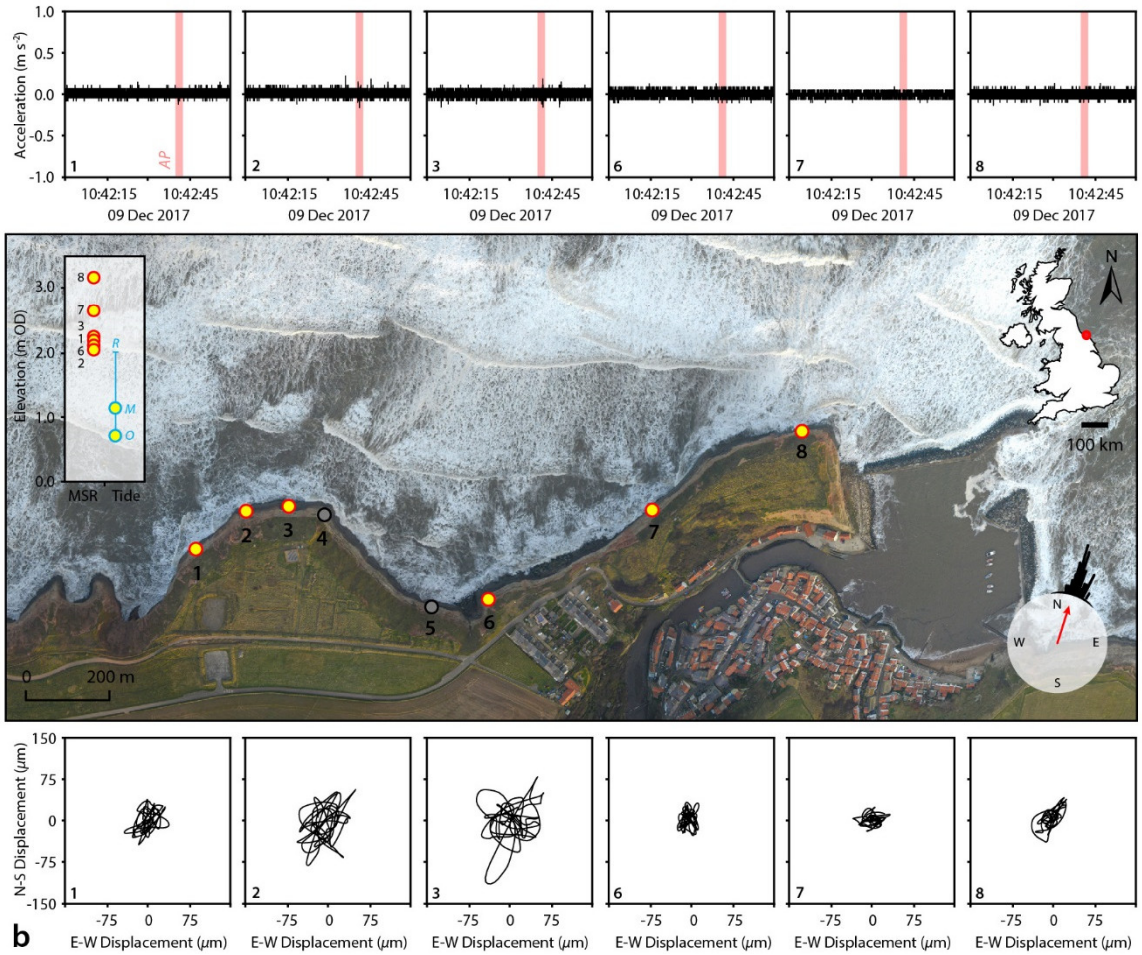
Acceleration (m s-2)
AP
10:42:15
10:42:45
09 Dec 2017
Elevation (m OD)
MSR
Tide
R
M
O
100 km
200 m
N
S
E
W
N-S Displacement (μm)
E-W Displacement (μm)
b

Figure 5.11 *Overleaf. Simultaneous particle motion plots of ground motions captured at six accelerometers, (a) an hour after high tide, and (b) two and a half hours after high tide. The plots correspond to the accelerations shown in the top panel and are of individual wave events captured over a 10 s interval, shown in red. This interval is captured in the aerial photograph (AP) in the middle panel. Inset: instrument elevations plotted against the observed tide, O, average modelled tide, wave, and set-up elevations, M, and the range in these elevations, R. Sites S4 and S5 were unable to be included in this analysis due to rockfall.*

Over the 541 high tides recorded, the ground motions captured at each site are highly directional, with strong peaks at azimuths ranging between *ca.* 25° and 65° (Figure 5.12). The rose plots shown in Figure 5.12 illustrate the characteristic impact ground motions observed at each site over the monitoring period, where the directional data are derived using the azimuth of the particle motion ellipsoid for each impact and plots are coloured by vector magnitude. Variations in the direction and strength of the concentration peaks are likely caused by the combined effects of variations in the incoming wave height (mean H_s over the monitoring period = 0.95 m) and direction (mean = 30.9°) relative to the cliff strike.

The lowest average displacements are observed at sites S1, S6, and S7 (ranging from 73.7 µm to 89.9 µm), which are relatively sheltered. The sites are similar in aspect, which ranges from 318° to 335°, and are characterised by strong directionality under weak impacting (displacements < 50 µm). For these displacements, ground motions are preferentially oriented at angles *ca.* 45° to the main concentration peak. The directionality of ground motion recordings obtained along exposed coastal sections, such as sites S2 – S5 and S8, does not show a preferential orientation at these displacement magnitudes. Ground motions at sites S2 – S5, located around the headland at Cowbar, show strong directionality at azimuths of between *ca.* 40° and 60°. This stretch of coastline is characterised by varying wave exposure and, with the exception of S5, a short foreshore platform and low cliff toe/instrument elevation. These sites, where impacting at high magnitudes and frequencies occurred throughout the monitoring period, show little directionality for relatively small impacts (displacements < 50 µm), but highly directional ground motion for the largest impacts (displacements > 1000 µm). During these events, ground motions predominantly occur in a direction that is approximately perpendicular to the main concentration peak, a behaviour unique to these four sites.

Given that the sensors were installed at an approximately uniform height relative to the cliff toe, and across sites of uniform geologic composition, variations in the magnitude, frequency, and azimuth of impacting recorded at each sensor are highly likely to be driven by variations in cliff aspect and platform geometry, as well as variations in total water level and incoming wave direction. Although the influence of total water level on cliff motion is well known (Lim *et al.*, 2011; Norman *et al.*, 2013; Vann Jones *et al.*, 2015; Adams *et al.*, 2016), previous studies lack concurrent observations of cliff shaking alongshore, such that the effects of variations in wave direction relative to cliff strike have remained difficult to isolate.

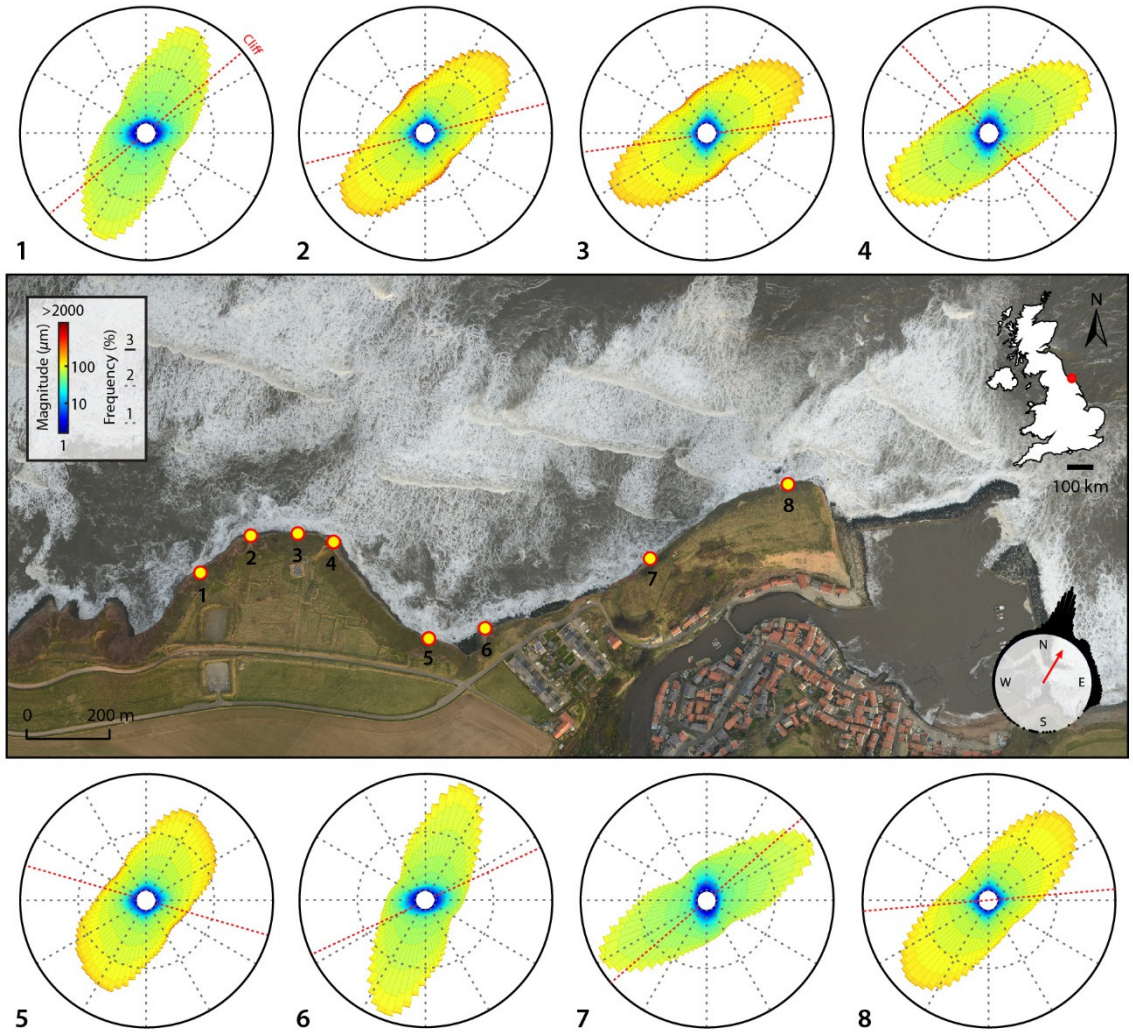

Figure 5.12 *Rose plots of the characteristic impact ground motions observed at each site over the monitoring period, ca. 306 days (with the exception of S5, where recordings were undertaken for a total of 102 days). Directional data are derived using the azimuth of the particle motion ellipsoid for each impact, and plots are coloured by vector magnitude (in μm, log scale). The direction of the cliff strike at each site is marked by a red dashed line.*

5.3.3 Energy transfer and environmental conditions

Temporal patterns of energy transfer to the cliffs between Staithes and Cowbar correspond, in part, to changing environmental conditions (Figure 5.13a). The tidal range along the North Yorkshire coast is largely macro-tidal, experiencing two daily tides that cycle between spring and neap highs over a range of *ca.* 6 m (Figure 5.13b). The bases of the cliffs are often submerged during high spring tides, in places up to a depth of at least 3 m. The coincidence of mean high water springs (*ca.* 2.59 m OD) with storm events, which drive high swells (maximum H_s = 10.82 m, T_{peak} = 28 s; Figures 5.13c and 5.13d) and peaks in precipitation and wind speeds (maximum rainfall accumulation = 27.40 mm, wind speed = 33 km h^{-1}; Figures 5.13e and 5.13f), appears to accentuate ground motions at the cliff toe at all sites, but to varying degrees, and with the exception of S7.

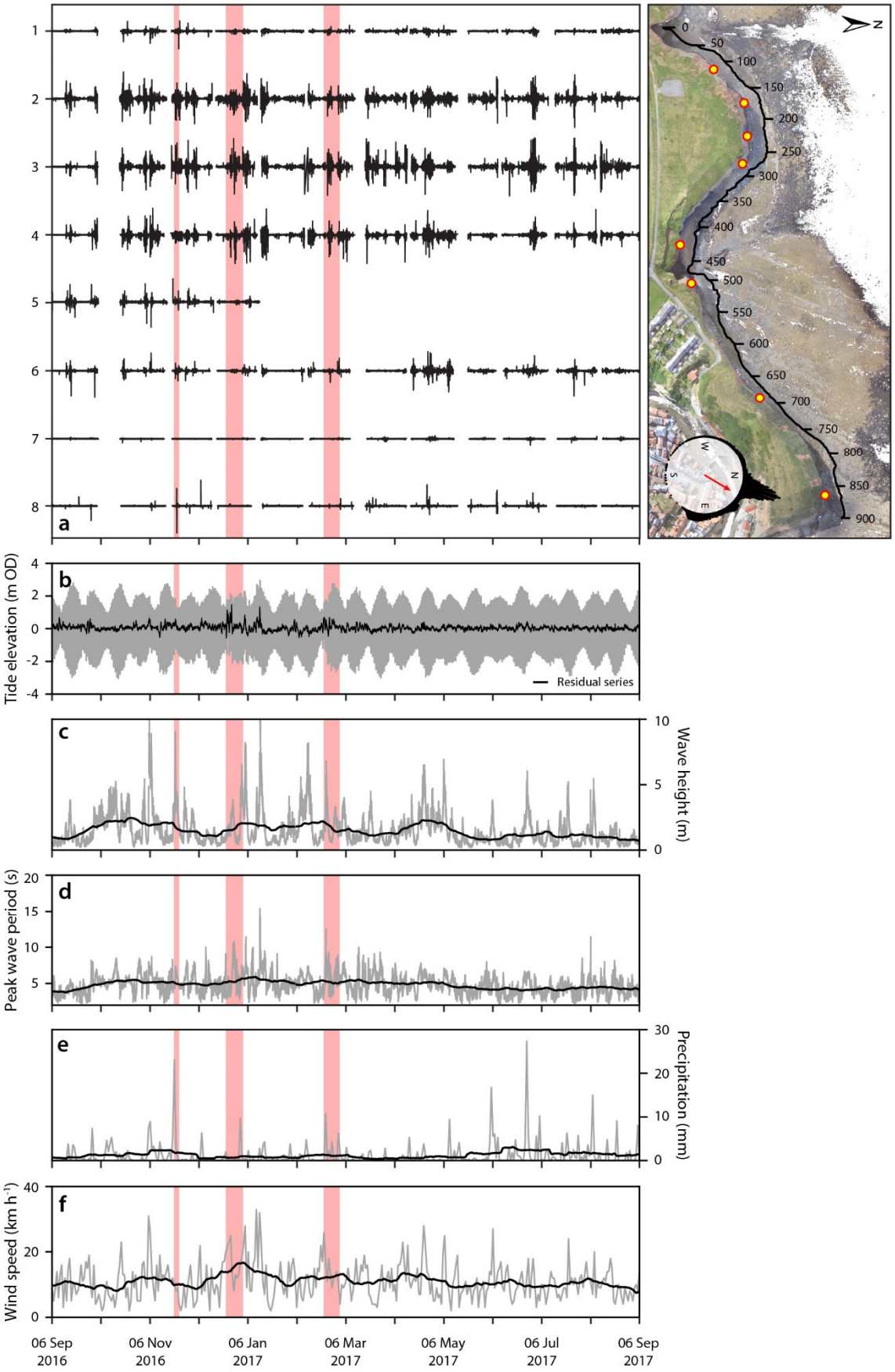

Figure 5.13 *(a) Ground motions captured at each site, plotted alongside observations of (b) tide elevations, (c) significant wave height, (d) peak wave period, (e) precipitation accumulation, and (f) mean wind speed. In subplots (b – f), data presented are raw (grey) and smoothed using a 30-day moving average (black).*

The total water level exceeded the elevation of the cliff toe at each of the sites for between *ca.* 41.83 and 148.08 days, excluding at S5 (Table 5.03). Continuous wave-cliff interaction therefore occurred for between 13.68% and 48.40% of the monitoring period across the sites, as waves did not reach any of the sites at low tide. Continuous wave-cliff interaction at the elevations of each of the sensors, which were installed at an approximately uniform height relative to the cliff toe, occurred for between 0.03% and 12.85% of the monitoring period (Table 5.03). As the spatial range of detectable wave-cliff impacts is highly limited, bursts of elevated ground motion are almost always coincident with an increase in cliff base water levels. Similarly, wave breaking at the fronting foreshore platform does not excite ground motion at any of the sensors, as observed by Young *et al.* (2013, 2016).

To examine any potential relationships between tidal forcing and the recorded impacting at each site, the timing of impact events was compared to periodic components of the observed tidal cycle (Figures 5.14 and 5.15). Classical tidal harmonic analysis was performed on the half-hourly tidal elevations and residual series shown in Figures 5.14a and 5.14b, which show a tidal variation superimposed on subtidal variability. The analysis tested the significance of 35 tidal constituents, where significant constituents were identified if the signal-to-noise ratio exceeded 1. Of the 35 tidal constituents tested, 18 were judged to be significant (Figure 5.14c). The majority of the significant constituents are in the diurnal (0.04 cycles hour^{-1}) and semidiurnal (0.08 cycles hour^{-1}) frequency bands, although a number of higher frequency constituents are also significant, including those in the terdiurnal (0.13 cycles hour^{-1}), quarter-diurnal (0.17 cycles hour^{-1}), and sixth-diurnal (0.25 cycles hour^{-1}) bands. Despite the large amount of energy in the fortnightly band (0.002 cycles hour^{-1}), which approximates the spring-neap tidal cycle, the fitted constituents are not significant.

Table 5.03 *Time elapsed where the total water level exceeded the cliff toe and instrument elevations.*

Site	*Cliff toe*	*Instrument*	*Water on/above cliff toe*		*Water on/above instrument*	
	m OD	*m OD*	*dd:hh:mm*	*%*	*dd:hh:mm*	*%*
1	0.66	2.26	132:21:10	43.43	16:11:47	5.39
2	0.68	2.08	131:21:40	43.11	27:02:22	8.86
3	0.54	2.22	140:13:45	45.94	18:18:31	6.13
4	0.42	1.90	148:02:14	48.40	39:08:00	12.85
5*	1.81	2.87	16:14:52	16.29	00:08:31	0.35
6	0.55	2.13	140:01:48	45.78	23:21:07	7.80
7	1.35	2.63	83:22:44	27.43	03:14:11	1.17
8	1.86	3.19	41:20:27	13.68	00:01:50	0.03

* *Observations at this site were recorded over 102 days (as opposed to 306) due to a rockfall that occurred on 12/01/2017.*

The power spectral density of the ground motion time series recorded at each sensor is shown in the periodograms in Figure 5.15. Coloured lines correspond to different false-alarm probabilities (P_{fa}), each of which indicate the probability that a peak with power exceeding this threshold is the result of random statistical fluctuations. With the exception of the ground motions recorded at S8, all of the time series exhibit significant ($P_{fa} < 1\%$) semidiurnal periodicity, which reflects the twice-daily tidal cycle. This semidiurnal component is superimposed on subtidal variability of differing frequencies, including the terdiurnal component at S6 and S7; the quarter-diurnal component at S3, S4, and S7; the fifth-diurnal component at S3; and the sixth-diurnal component at S1, S2, and S5 (Figure 5.15). The presence of statistically significant peaks at frequencies that correspond to those of significant tidal constituents (Figure 5.15) indicates that the frequency of cliff impacting is tidally modulated at these sensors. The elevated foreshore platform and cliff toe at S8 (1.861 m OD) means that wave-cliff interaction only occurred for 13.68% of the monitoring period, with total water levels only reaching the instrument for less than two hours (Table 5.03), and therefore precludes any significant periodicity in the ground motion time series.

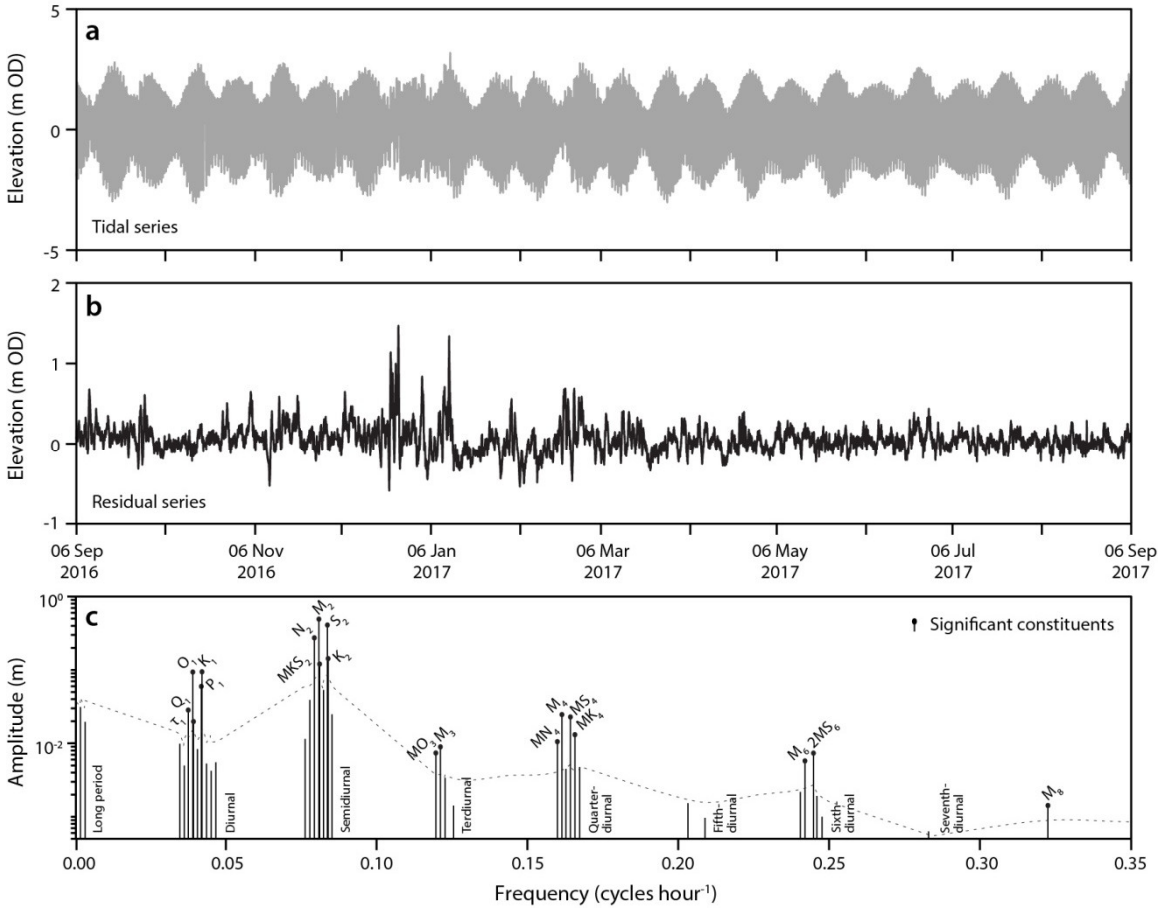

Figure 5.14 *Tidal harmonic analysis for Whitby, showing (a) tidal elevations, (b) tidal residuals, and (c) amplitude of all the analysed components with the 95% significance level. Significant constituents are marked with a solid circle. Full details of the analysis are given in Appendix I (p. 201). Analysis undertaken using the* `T_TIDE` *toolbox developed by Pawlowicz et al. (2002).*

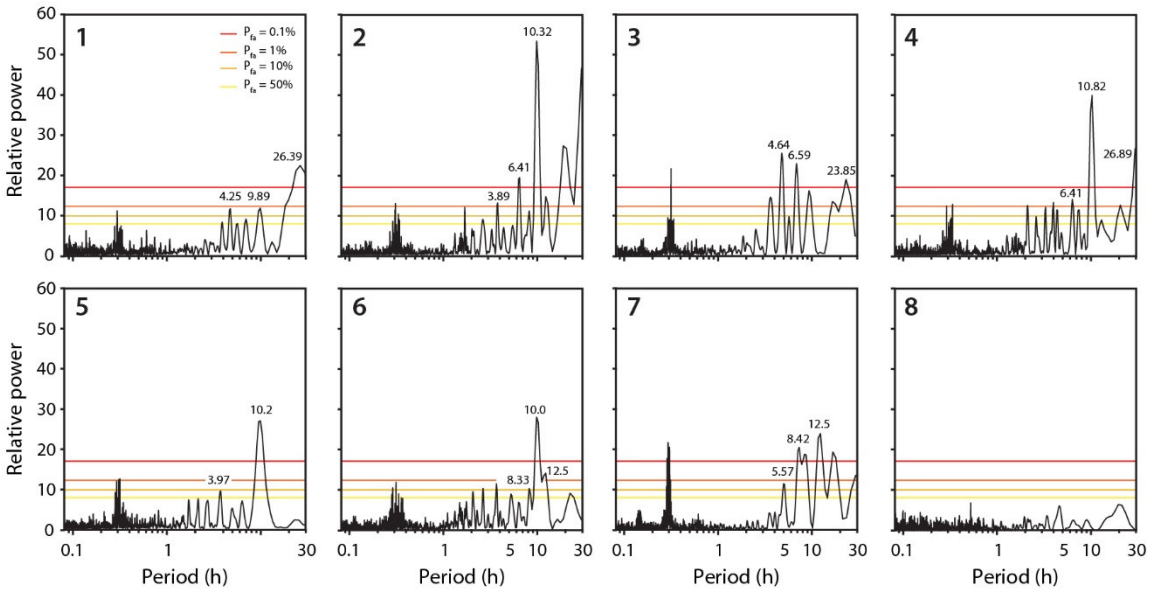

Figure 5.15 *Lomb-Scargle periodograms illustrating the power spectral density of the ground motion time series shown in Figure 5.10. Levels corresponding to false-alarm probabilities of 50%, 10%, 1%, and 0.01% are annotated. The false-alarm probability denotes the probability that at least one out of M independent power values in a prescribed frequency band of a power spectrum computed from a white-noise time series is as large as or larger than the threshold, P_{fa}.*

Although the magnitude of displacements observed at each instrument trend consistently during hours of wave-cliff interaction, there is considerable scatter around displacement magnitudes independent of the total water depth (Figure 5.16a, *p.* 108). Cliff toe impacting at all sites is most elevated at high tide, but the amount of spread around this time differs by as much as two hours either side of high tide. Similarly, the largest displacements observed at each site are driven by total water levels of varying depths, sometimes by as much as 2 m; both of these observations are most likely due to differences in site morphological controls such as foreshore elevation, which are considered in *Section 5.3.4*. To further illustrate this, the proportion of events of different displacement magnitudes occurring at specified total water levels is plotted for each site as a stacked bar graph in Figure 5.16b (*p.* 108). Up to a particular threshold, the displacements recorded at sites that are elevated, such as S5, S7, and S8 (Table 5.03), are driven by total water levels that vary in approximately equal proportions. Given that this occurs at all sites, although it is sharper at some more than others, it most likely represents the impact events that occur under subdued wave conditions (Figure 5.09a), which result in relatively small event magnitudes (displacements < 100 µm). Above this threshold, the largest displacements occurring at S5, S7, and S8 are almost entirely driven by the deepest waters (> 3.0 m OD), which only reach the sensors for $< 1.17\%$ of monitoring period (Table 5.03). The other sensors, which are characterised by approximately equal inundation durations (Table 5.03), instead show gradual trends whereby an increasing proportion of high magnitude events are associated with deeper total water levels (Figure 5.16b, *p.* 108).

The spatial differences in energy transferred to the cliffs can therefore be partly explained by differences between total water level and foreshore elevation. The observations of locally wave-generated ground motions shown in Figure 5.13a, which are tidally modulated at most sites, are consistent with previous research (Adams *et al.*, 2002, 2005; Young *et al.*, 2011, 2012, 2016). However, beyond foreshore elevation, spatial variations in tidal influence point towards important differences in local processes and morphological controls between sites, which could also explain differences in the directionality of the ground motions observed at each site (Figure 5.12).

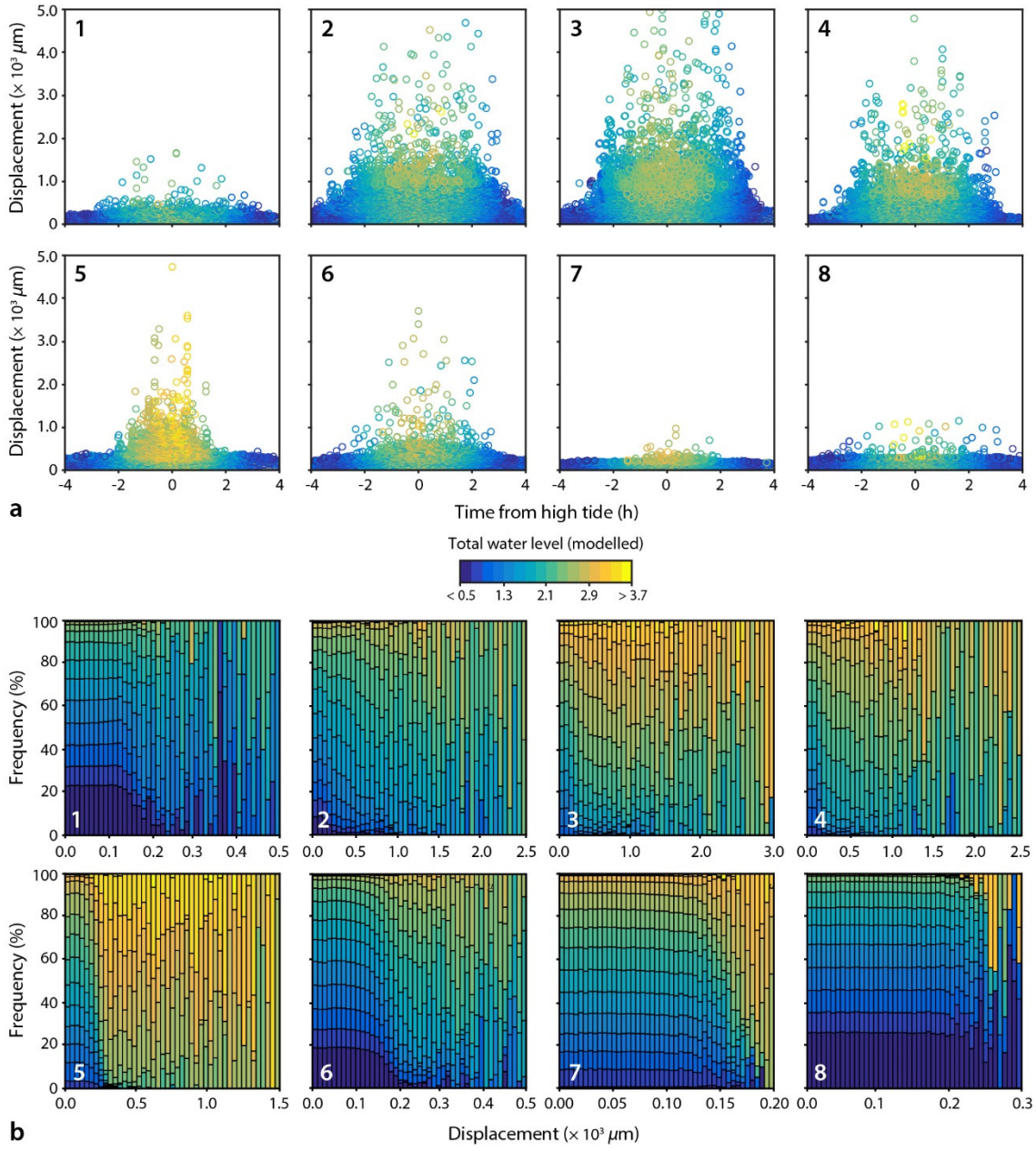

Figure 5.16 *(a) Time from high tide versus displacement magnitude for each impact, as recorded at each instrument, and (b) displacement magnitudes plotted as a stacked bar graph. Note that the axes are scaled differently for each site. The maximum displacement used corresponds to the upper quartile (0.75) of the distribution for each site in order to maintain a representative number of samples in each bar. Both plots are coloured by total water level (modelled).*

5.3.4 Energy transfer and local characteristics

Observations at S2 and S6 offer a comparison between instruments with the same elevation (± 0.048 m OD; Table 5.03), and aspect (346° and 335°; Table 5.01), but with different platform morphologies. Shaking at S2 is elevated on the shoulders of the tide (± 4 hours) while shaking at S6 is less frequent, lower in magnitude but concentrated around high tide (± 2 hours; Figure 5.17a). At S2, as well as S3 and S4, the short platform (< 100 m; Figure 5.02 and Figure 5.03b) and deeper water allows waves to approach the cliffs without much tidal change in dissipation. Conversely, due to the long (> 150 m), gently sloping foreshore platform at S6 (Figure 5.03f), shallower water depths on the shoulders of the tide cause wave shoaling and breaking prior to wave-cliff interaction. The gentle slope therefore drives tidal modulation of wave dissipation and brings energy closer to the cliff at high tide, an effect that can be seen in the aerial photos shown in Figure 5.11. Similarly, although S5 is elevated in comparison to S2 and S6 (+ 0.736 m), the platform fronting the cliffs drops off abruptly over a short distance (Figure 5.03e; *Appendix G, p.* 195). Deeper water, as at S2 – S4, and the aspect of the sensor (16°) exposes S5 to the mean wave direction (30.9°). These findings are consistent with previous research undertaken in a variety of settings (for example, Lim *et al.*, 2011; Dickson and Pentney, 2012), which has demonstrated that platform morphology influences wave energy delivery to cliffs.

Morphological control of the ground motions recorded between Staithes and Cowbar is further demonstrated by the signal directionality shown in Figure 5.12. At each site, the azimuth of the recorded impacts deviates from the local cliff strike in a systematic manner that varies along the coast (Figure 5.17). At sites facing north-west, such as S1 – S3 and S7, the majority of

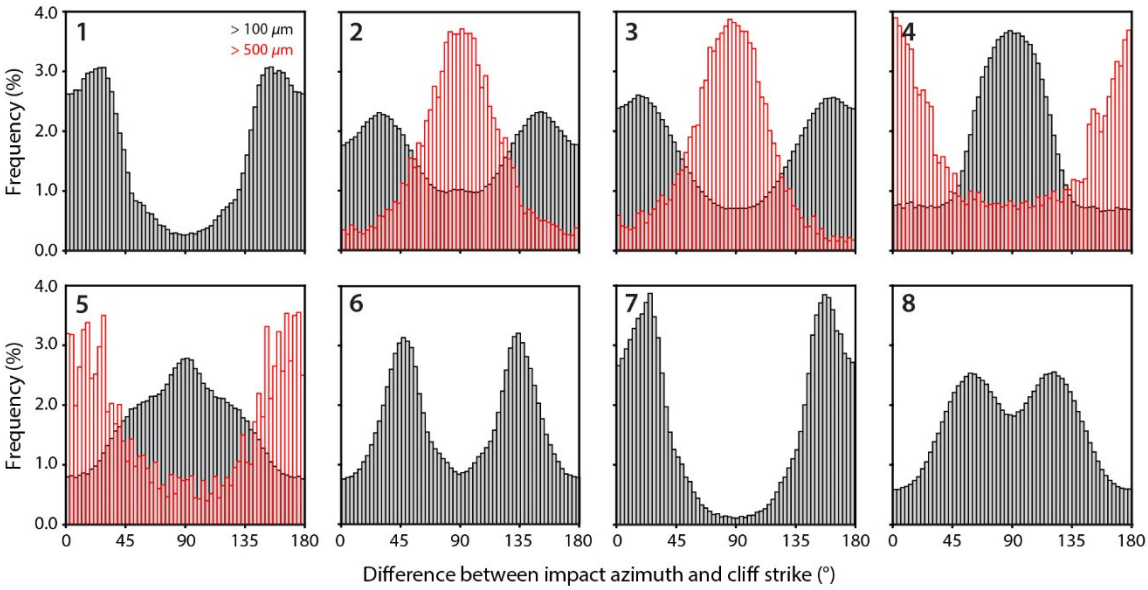

Figure 5.17 *Distribution of the differences between impact azimuth and the local cliff strike, as observed at each site. Low-level impacting that occurs under subdued wave conditions is not shown (displacements < 100 μm). At sensors that experienced frequent, high magnitude impacting (displacements > 500 μm) this distribution is also shown in red.*

impacts are oriented between *ca.* 20°/160° and 30°/150° to the local cliff strike, although the peaks in the distributions are not uniform across these sites. For example, ground motions display strong preferential directivity at S1 and S7, which are more sheltered from the predominant wave direction than S2 and S3 and therefore have limited exposure to any incoming waves. At S4 and S5, which face northeast, the majority of impacts are oriented *ca.* 80° – 100° to the local cliff strike. However, this distribution inverts at those sites where high magnitude displacements were recorded (displacements $>$ 500 µm), implying that, during abnormal loading conditions, a preferential loading direction is sustained that is approximately perpendicular to that of those most frequently experienced (displacements $<$ 100 µm). This effect is also demonstrated in the rose plots shown in Figure 5.12, where the orientation of the inner ellipsoid is consistently oriented *ca.* 75° – 90° to the main concentration peak.

5.3.5 Establishing the controls on energy transfer

The spatial differences in energy transferred to the cliffs between Staithes and Cowbar appear to correspond with differences in local processes and morphological controls between sites (*Sections 5.3.3* and *5.3.4*). A number of variables discussed above, including the instrument aspect (which acts as a proxy for cliff aspect), foreshore platform morphology/geometry (both length and slope), and inundation duration at the cliff toe are therefore compared to measures of impact magnitude and frequency in Figure 5.18. The impact magnitude was derived using the overall vector magnitude of the particle motion ellipsoid for each impact, and the mean, median, and maximum values recorded at each site are presented in Figure 5.18.

The magnitude and frequency of impacting are both conditioned by the instrument (or cliff) aspect (Figures 5.18a and 5.18e). Peaks in both impact magnitude and frequency are observed at *ca.* 357° – 13°, which approximately corresponds with peaks in the distribution of wave directions observed at both the Whitby (*ca.* 25 km south) and Tees (*ca.* 40 km north) offshore wave buoys. A correlation or relationship between the magnitude and frequency of impacting with aspect is also apparent in Figure 5.13a. Given that the accelerometers used here measure ground accelerations driven purely by local (direct) wave impacting, if a cliff face is fully exposed to the predominant wave direction then a correlation between the magnitude and frequency of impacting and aspect is to be expected, local morphological influences aside. However, given that instruments facing the same or similar aspects record different ground motion responses (for example, S5 and S8), as observed in Figure 5.13a, the influence of aspect is clearly moderated by other conditions.

Observations at two sites that offer a comparison between instruments with the same elevation and aspect, but with different platform morphologies, indicate that platform length and/or morphology at this site influences wave energy delivery to the cliffs (*Section 5.3.4*). Both the magnitude and, to a lesser extent, the frequency of impacting are conditioned by platform length (Figures 5.18b and 5.18f), with sites fronted by a short ($<$ 100 m) platform experiencing

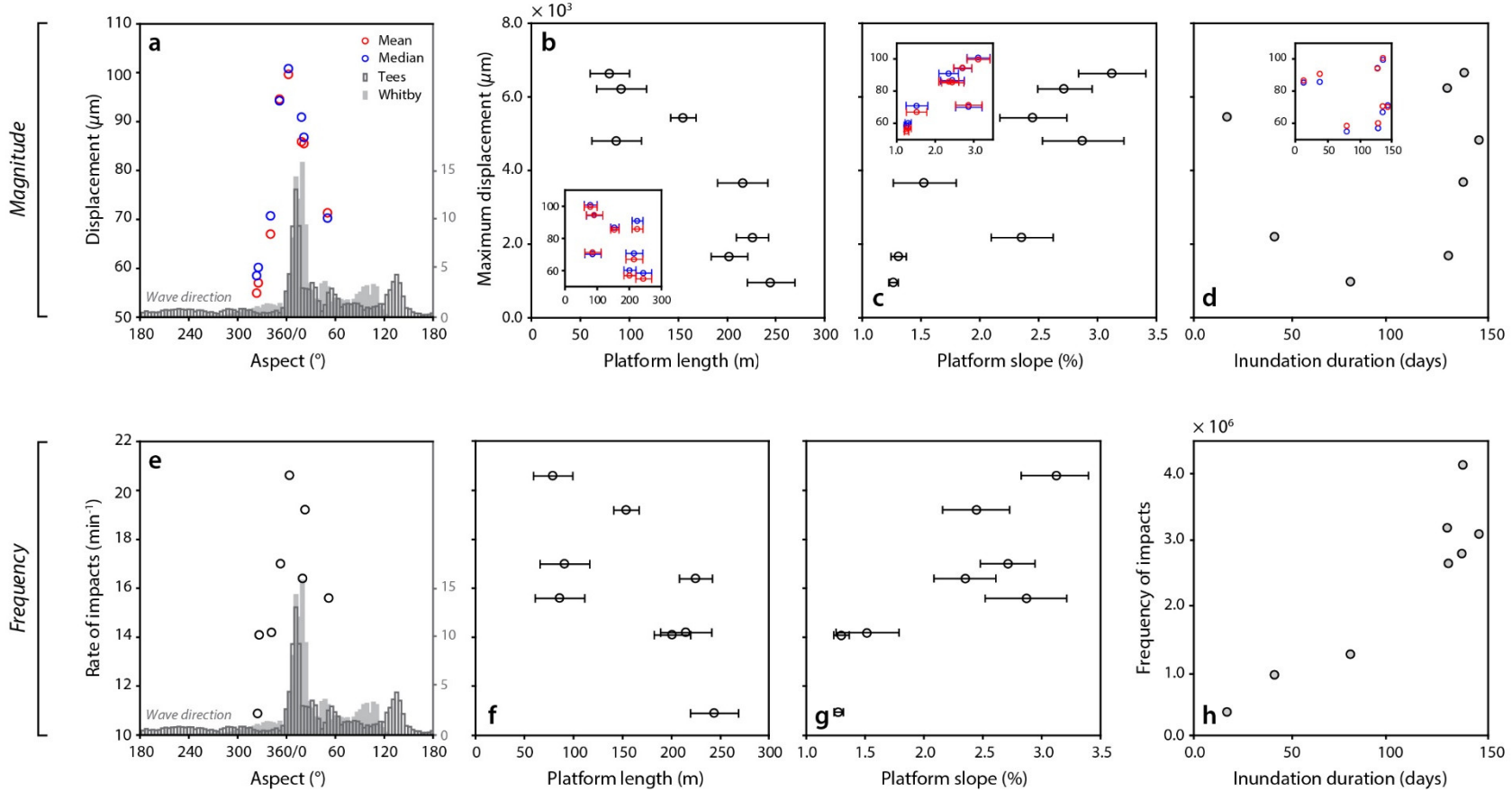

Figure 5.18 *Measures of impact magnitude (mean, median, and maximum) and frequency (number and rate of impacts) plotted against the aspect (a,e), platform length (b,f), platform slope (c,g), and inundation duration (d,h) observed at each site. For measures of impact magnitude, the strongest relationship is plotted for each variable, with the alternatives plotted as an inset. Both the platform length and slope were measured in the predominant wave direction (30.9°). Measurements of both in other probable directions based on cliff aspect and the incoming wave direction are also included using the standard deviation of these measurements (± 1σ), which are included as error bars. All values are given in Appendix J (p. 203).*

higher mean, median, and maximum impact displacements than elsewhere. A similar relationship is observed for platform slope (Figures 5.18c and 5.18g), where, on average, high gradients are associated with impacts of a greater magnitude, which occur at higher rates. These findings are consistent with previous research, which has demonstrated that the presence of foreshore platforms can cause wave shoaling and breaking prior to wave-cliff interaction (Trenhaile and Kanyaya, 2007; Porter *et al.*, 2010), filtering the incoming wave energy to levels as low as 5% as waves propagate across the platform (Stephenson and Kirk, 2000). These findings also explain why there is no coherent relationship between impact magnitude and inundation duration (Figure 5.18d): for example, the instrument at S5 recorded large impacts ($> 4.0 \times 10^3$ µm) despite being exposed more frequently than elsewhere. Although it is one of the most elevated sites, the platform fronting the cliffs drops off abruptly over a short distance (*Appendix G, p.* 195). Deeper water allows waves to approach the cliffs at S5 without much tidal change in dissipation, such that the sensor is exposed to large waves when spring tides and large swells coincide.

5.3.6 Rockfall activity and cliff erosion

Variations in rockfall activity across the sites were monitored between August 2014 and March 2017 using the data and methods presented in *Chapter 3*. These data are used here to examine spatial variations in wave-induced ground motions and rockfall activity in order to develop a more generalised understanding of how variations in loading magnitude, frequency, and direction may correlate with broader scale patterns of cliff erosion and retreat. However, it should again be noted that it is not the aim of this chapter to demonstrate a direct physical link between wave-induced ground motions and cliff erosion.

Erosion profiles show the pattern of net cliff change observed over the 50 m of cliffs surrounding each instrument between August 2014 and March 2017 (Figure 5.19). Although some tendency for notching appears to occur at certain sites (for example, S1 and S5), relatively little erosion occurs below the elevation of the highest astronomical tide (HAT), with erosion rates at the cliff toe at all sites appearing to lag behind those of the cliff above. This reflects the patterns of erosion observed along the entire coastline, which are presented in *Section 3.3.4*, where statistically significant ($p < 0.05$) correlations between inundation duration and erosion depth are only found across an equivalent of *ca.* 1.50% of the cliff toe between 2014 and 2017. Except for the occurrence of a large (15.83 ± 0.47 m^3), isolated rockfall at S7, low rates of face-parallel cliff retreat occur at S6 – S8, which are either sheltered from the predominant wave direction (30.9°), elevated in comparison to the other sites, or both. Conversely, at S1, S2, and S4, isolated zones of rockfalls occur at elevations > 15 m. These rockfalls appear to erode to approximately consistent depths, and they are largely uncoupled from any erosion that has occurred at the cliff toe. Although the cliffs are not necessarily more exposed where this occurs, they often have a shorter fronting platform.

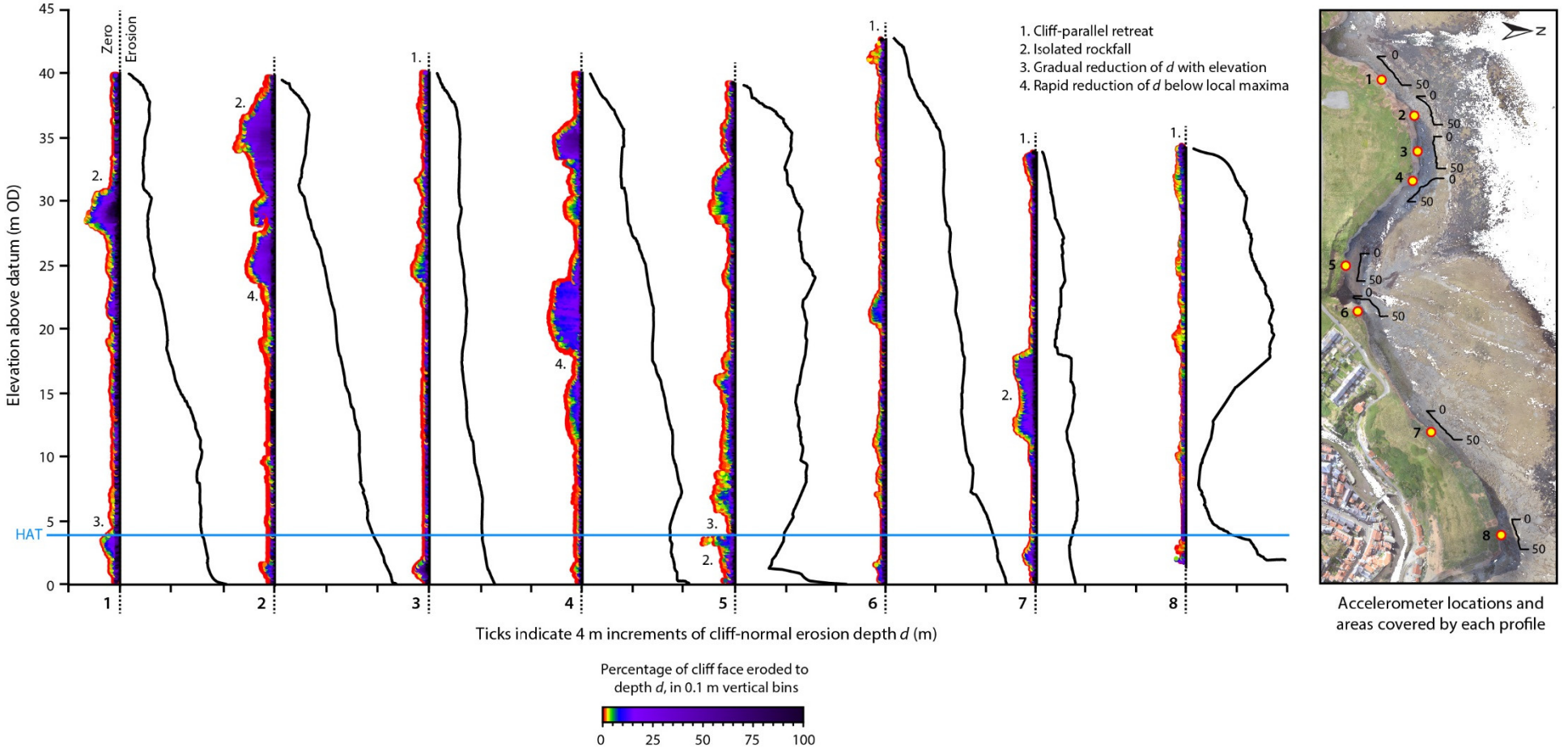

Figure 5.19 *Vertical distribution of erosion depths monitored between Staithes and Cowbar Nab. Profiles show the pattern of net cliff change observed over the 50 m of cliffs surrounding each instrument, between August 2014 and March 2017. Erosion depths are shown in coloured shading (0.1 m bins). Note that the aspect ratios of the profiles are not exactly equal. See Figure 5.03.*

Plots of the net cliff change accumulated across all eight of the instrumented sites are illustrative of the trends described above: generally low rates of erosion at the cliff toe are outpaced at the HAT line, above which the cliffs are eroded to progressively greater depths (Figure 5.20a). The vertical distribution of erosion across the sites is also representative of the net cliff change observed over the entire 900 m section of cliffs monitored between Staithes and Cowbar Nab (Figure 5.20b). This suggests that, over the shorter term, the dominant modes of cliff erosion at this site are operating such that the slope profile can reach an equilibrium (near-vertical) state. This is also evident when considering the profile form of the cliffs (Figures 5.03 and 5.19), many sections of which are steep (S6, S7) and even concave (S5, S8).

To assess the relationship between wave impact-driven ground motions and rockfall activity, the total volume of erosion that occurred at each site between 2014 and 2017 is plotted against measures of wave impact magnitude and frequency in Figure 5.21. The eroded volume correlates well with the maximum impact displacements, yielding a correlation coefficient of 0.51 (Figure 5.21a). When S3 is removed, this coefficient increases to 0.90. There is a less coherent

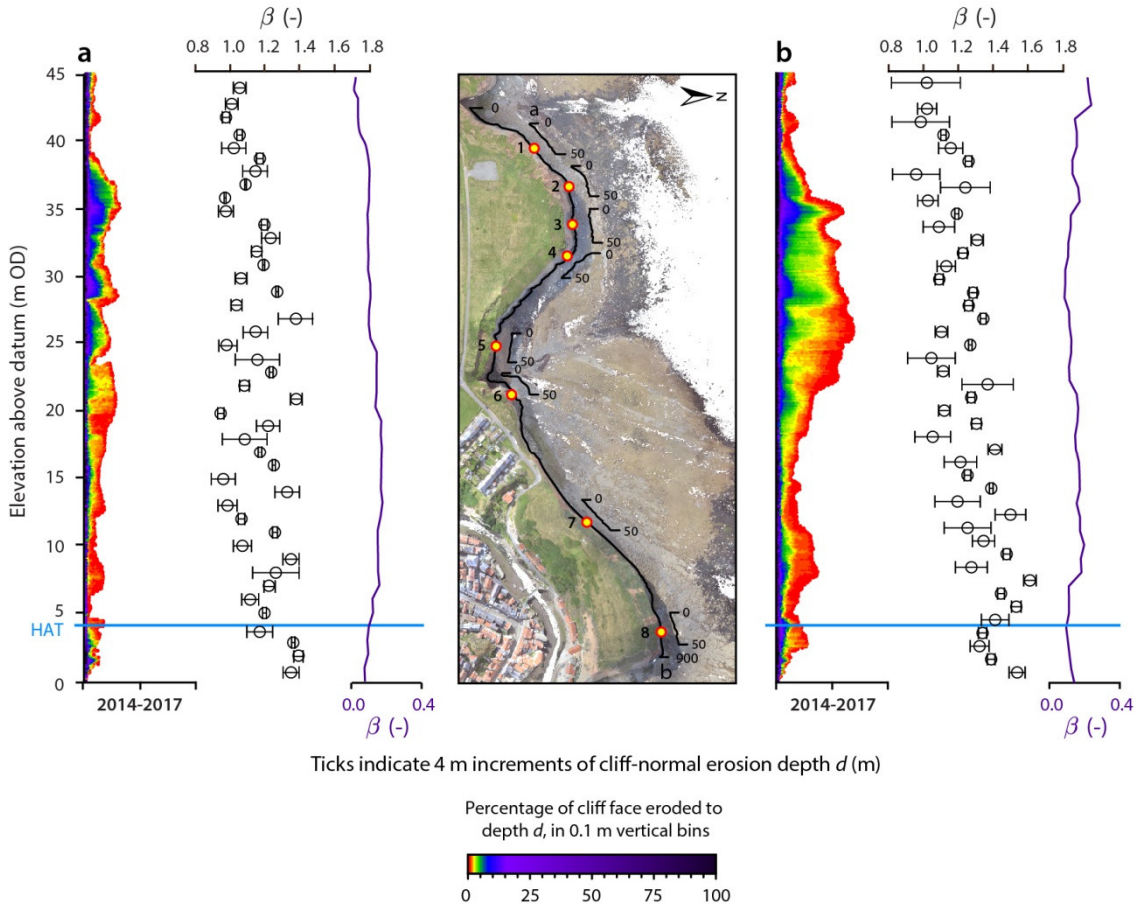

Figure 5.20 *Vertical distribution of erosion depths monitored between Staithes and Cowbar Nab. Profiles in (a) show the combined pattern of net cliff change observed over the 50 m of cliffs surrounding each instrument, and profiles in (b) show the pattern of net cliff change observed along the entire 900 m section, between August 2014 and March 2017. Erosion depths are shown in coloured shading (0.1 m bins). The exponent of the magnitude-frequency distribution, β, is plotted alongside (2.0 m bins).*

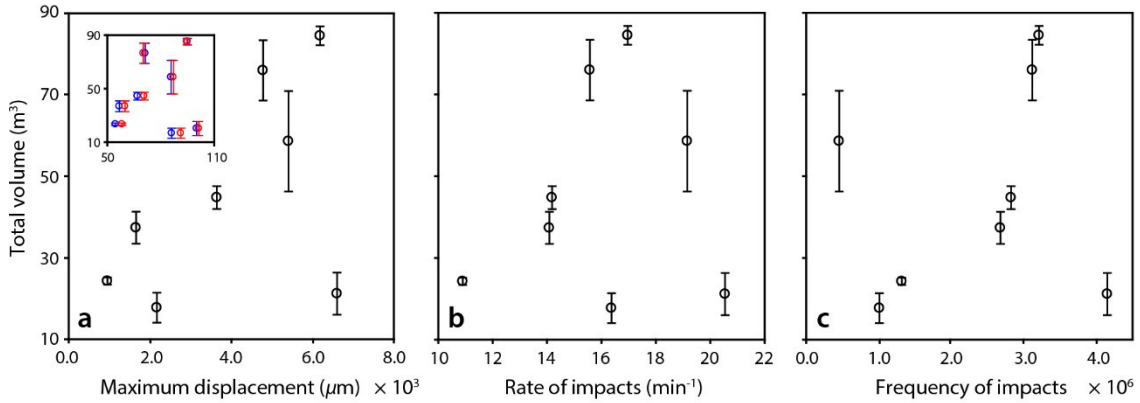

Figure 5.21 *Total rockfall volume plotted against (a) the magnitude (mean, median and maximum), (b) the rate, and (c) the number of impacts observed at each site. Volume was calculated as the total volume of the rockfalls that occurred over the 50 m of cliffs (± 25 m) surrounding each instrument, between August 2014 and March 2017. Error bars are included and reflect the minimum and maximum possible meshing volumes derived in Section 3.2.5 (p. 36). All values given in Appendix J (p. 203).*

relationship between the total volume eroded and measures of impact frequency (Figures 5.21b and 5.21c), with two sites that typically undergo high rates of impacting (S3 and S8) experiencing little erosion (21.05 ± 5.17 m^3 and 17.57 ± 3.71 m^3). This may be explained by site-specific factors, including those discussed in *Section 5.3.5*, or it may simply imply that monitoring was not undertaken over a long enough period to capture fully the conditions occurring at these sites. Relationships between the erosion flux and the local processes and morphological controls discussed in *Section 5.3.5* attest to the former (Figure 5.22). There is some correlation between the total eroded volume and aspect (Figure 5.22a), although S5 and S8, which are of similar aspect (16° and 13°), recorded different ground motion responses (Figure 5.13a) and volume fluxes (58.67 ± 12.39 m^3 and 17.57 ± 3.71 m^3). The influence of aspect is clearly moderated by other conditions: these include platform length, inundation duration, and, to a lesser extent, platform slope (Figure 5.22). By inference, these findings confirm observations from both modelling and site-specific field studies, which indicate the importance of bed or platform morphology on wave transformation in the surf zone (Nakamura *et al.*, 1966; Svendsen *et al.*, 1978). The observations presented here therefore confirm the importance of the amount of wave energy available for erosional work, and the way in which this energy is distributed alongshore.

5.4 Summary

Using concurrent observations of wave impact-driven ground motions, this chapter has explored how the cliff response to wave impacting varies alongshore, how these variations are related to morphological controls and coastal processes, and whether differences in the ground motion response between sites drives spatial variations in cliff erosion. The resulting inventory of $> 18 \times 10^6$ impacts, measured along a *ca.* 900 m stretch of cliffs, has been used in conjunction

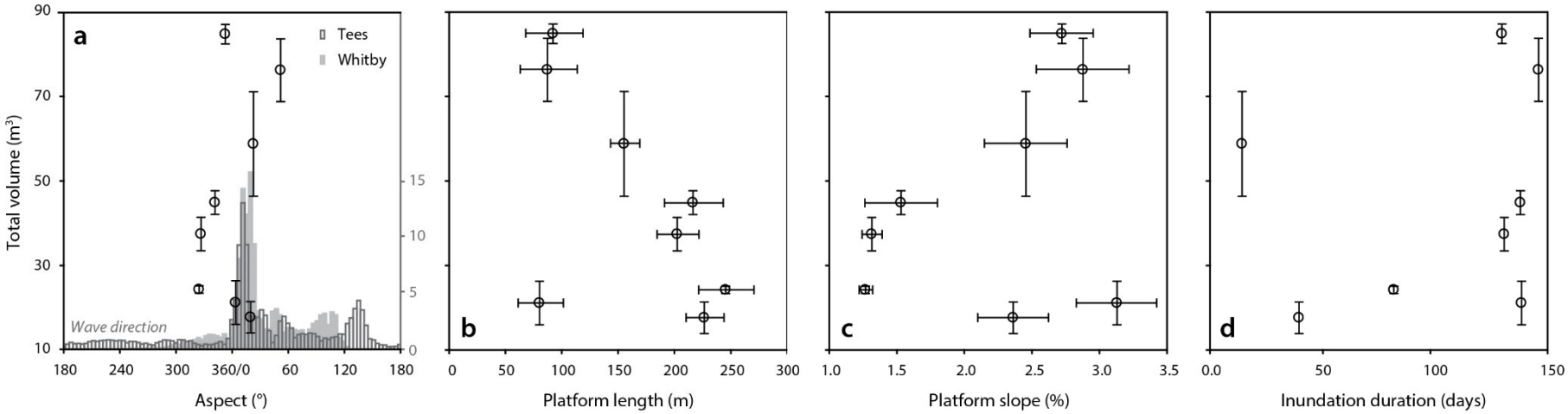

Figure 5.22 *Total rockfall volume plotted against (a) aspect, (b) platform length, (c) platform slope, and (d) inundation duration observed at each site. Volume was calculated as the total volume of the rockfalls that occurred over the 50 m of cliffs (± 25 m) surrounding each instrument, between August 2014 and March 2017. Error bars are included and reflect the minimum and maximum possible meshing volumes derived in Section 3.2.5 (p. 36). All values given in Appendix J (p. 203).*

with observed variations in rockfall activity to show that:

1) The cliff response to wave impacting varies considerably alongshore.
2) Observations of locally wave-generated ground motions at all sites are tidally modulated, consistent with previous research. However, spatial variations in the form and strength of this influence are conditioned by differences in local processes and morphological controls between sites.
3) Specifically, both the magnitude and frequency of wave impacting are strongly conditioned by cliff aspect, as well as foreshore platform morphology and geometry.
4) Longer-term variations in rockfall activity and the resulting cliff retreat between the sites are broadly correlated with wave impact-driven ground motions, and variations in the morphological conditions that drive them.

This chapter has presented the first concurrent observations of alongshore variations in wave impact-driven ground motions on coastal cliffs. The findings of this chapter will be synthesised with those of *Chapter 3* and *Chapter 4*, which together examined the patterns of rockfall activity and distribution of erosion with respect to structural controls, in order to gain new insights into the drivers of regional scale rockfall activity in *Chapter 6*.

This page is intentionally left blank

Chapter 6

Discussion

In this thesis, high-resolution field monitoring techniques were deployed in order to investigate how regional-scale variations in cliff structure and wave loading conditions relate to variations in rockfall activity (*Chapters 3*, *4*, and *5*). This was undertaken as one of the first attempts to consider the relative importance of intrinsic versus extrinsic controls on rockfalls, and therefore erosion, at spatial scales where these controls vary. To constrain variations in rockfall frequency, magnitude, and the resulting rockwall retreat over regional scales ($> 10^4$ m), the work presented in *Chapter 3* developed an approach for using high-resolution, multi-temporal airborne LiDAR data for detecting and characterising changes in the morphology of near-vertical rock slopes in 3D. In *Chapter 4*, these data were drawn upon to derive a quantitative appraisal of regional scale variations in the geometric properties of exposed discontinuity surfaces, and the extent to which these geometries drive patterns in the occurrence, size, and shape of observed rockfalls. A representative subsection of the coastline (10^2 m), where cliff lithology and structure are approximately uniform, was selected for higher-resolution field monitoring in *Chapter 5* to quantify spatial variations in loading characteristics, here via wave action, and to relate these to morphological and prevailing environmental conditions.

In this chapter, these findings are synthesised in *Section 6.1*, which evaluates the relationships between key metrics of erosion (*Chapter 3*), structural controls (*Chapter 4*), and morphological controls (as a proxy for wave loading; *Chapter 5*). Spatial variations in these relationships are then examined along the North Yorkshire coastline, and are used to identify whether erosion in this setting can be quantitatively shown to be dominated by either structural (intrinsic) or morphological (as a proxy for extrinsic) controls, a mixture of both, or simply random (no correlation). Patterns in erosion rates and their dominant controls are then explored, and examples of 'type sites' for the conditions and controls are presented. Notably, this analysis allows the 20.5 km of coastal cliffs to be classified based on the dominant controls on change, thereby

enabling a first order identification of sections of the coast that may be either more or less susceptible to changes in the rates of driving processes, such as those induced by future sea level rise. The aim of this chapter is then to set the findings of the work presented in *Chapters 3, 4*, and *5*, and synthesised in *Section 6.1*, within the wider context of (1) the implications for monitoring and modelling rockfall activity over wide extents (*Section 6.2*), (2) understanding patterns of rockfall occurrence, the resulting cliff erosion, and their drivers (*Section 6.3*), and (3) the associated implications for cliff evolution (*Section 6.4*). *Section 6.5* concludes the chapter by presenting a summary of these findings. Based on the understanding gained from the research undertaken in this thesis, this highlights the conditions that promote or inhibit rockfalls, and therefore cliff erosion, along hard rock coastlines.

6.1 Synthesis: intrinsic or extrinsic controls on rockfalls?

In order to understand how regional-scale variations in cliff structure and wave loading drive variations in rockfall activity, this section aims to derive relationships between metrics of erosion (rockfall frequency, total volume eroded, and erosion rate; derived in *Chapter 3*), structural controls (mean facet density, facet dip, and the difference between facet and cliff aspects; derived in *Chapter 4*), and morphological controls as a proxy for wave loading (cliff toe elevation, platform length, slope, and wave approach angle; derived in *Chapter 5*). For each 100 m bin along the North Yorkshire coast, shown in Figure 3.12 (*p.* 43), the total number of rockfalls (frequency), the total volume eroded, and the mean erosion rate over the whole monitoring period (August 2014 – March 2017) were calculated. The data were then aggregated by the mean of each control, in each bin, in order to consider correlations with the observed rockfalls and resulting erosion. For structural controls, the mean values of all of the facets within each bin were assessed, while for morphological controls, the mean value of estimates taken for every 10 m of cliff length along the coastline were assessed. This reduces the effect of noise inherent in estimating values of the controls at shorter length scales ($< 10^0$ m), while avoiding the effect of smoothing at longer length scales ($> 10^2$ m; Matsumoto *et al.*, 2017). The full results of this analysis are presented in *Appendix K* (*p.* 204), and only statistically significant controls are considered in Figures 6.01 and 6.02.

There are a several statistically significant structural (mean facet density, dip, and the difference between facet and cliff aspects) and morphological (cliff toe elevation, platform slope, and wave approach angle) controls on both the total volume eroded and the erosion rate (*Appendix K*, *p.* 204). These are summarised in Figures 6.01 and 6.02, and spatial variations in these controls are shown in Figure 6.03 (*p.* 124). Figures 6.01 and 6.02 illustrate several important observations, including (1) that the relationships between erosion and both structural and morphological controls are not random, (2) that substantial erosion is more likely with an increase in facet density, dip, and, to an extent, cliff toe elevation and platform slope, and also with a decrease in wave approach angle and the difference between facet and cliff aspects, and (3) that, while a broad

range of outcomes is possible at any given value of any of these controls, this range in outcomes varies significantly as a function of the controlling variable in question. Where the frequency distributions converge, this most likely represents a small number of samples observed for certain conditions (for example, Figures 6.01c and 6.02c).

The highest mean erosion rate observed over the monitoring period (at a distance of *ca.* 0.67×10^4 m along the coastline; VR_{max} = 1,633.58 ± 767.04 m^3, ER_{max} = 0.54 m yr^{-1}) coincided with a high facet density (15.7 facets m^{-2}), dip (65°), and platform slope (6.7%), and a moderate difference between facet and cliff aspects (58°), cliff toe elevation (1.19 m OD), and wave approach angle (47°). Conversely, the lowest mean erosion rate observed (at a distance of *ca.* 1.42×10^4 m; VR_{min} = 0.04 ± 0.01 m^3, ER_{min} = 1.90×10^{-6} m yr^{-1}) coincided with a lower facet density (12.7 facets m^{-2}), dip (58°), platform slope (0%, no platform), and wave approach angle (24°), and a similar difference between facet and cliff aspects (69°) and cliff toe elevation (1.41 m OD). The existence of these patterns on a regional scale, and the implications of having identified these patterns, are outlined below for both structural and morphological controls.

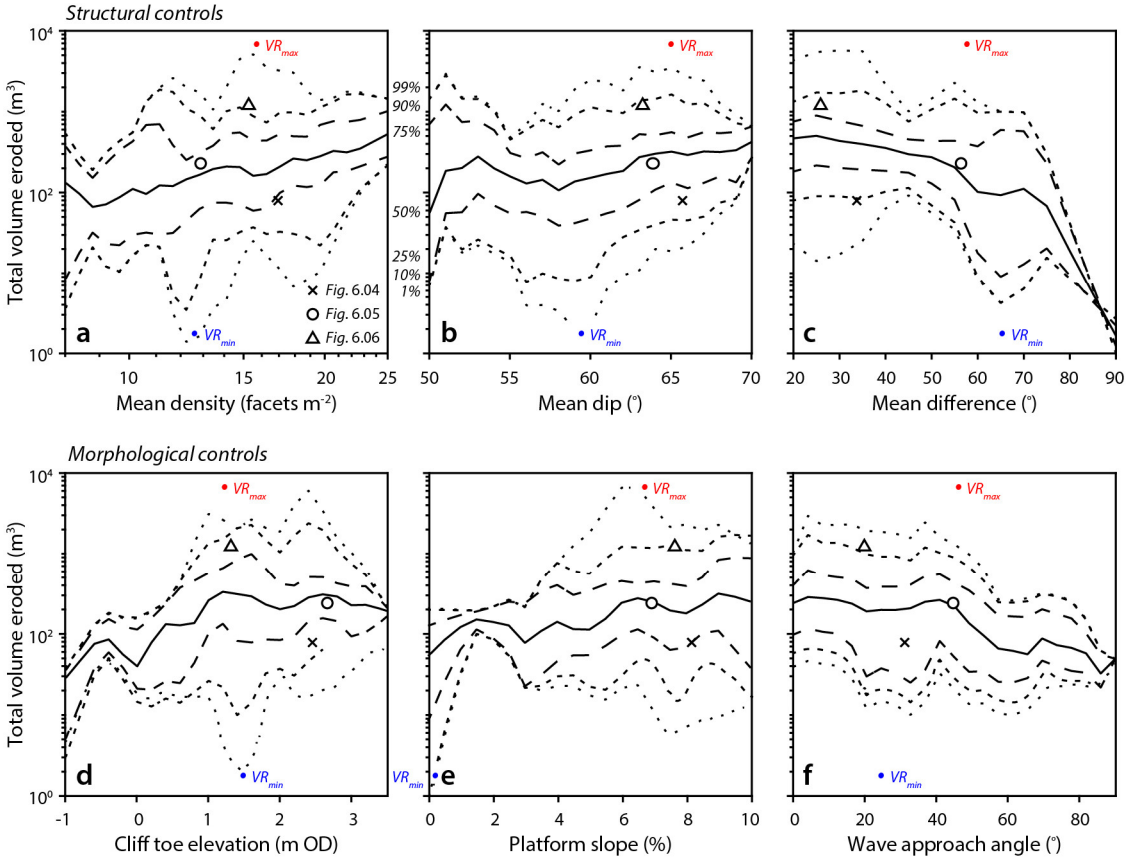

Figure 6.01 *Percentile plot of a bin-by-bin comparison of the total volume eroded against a selection of structural (a – c) and morphological (d – f) controls, including (a) mean facet density, (b) mean facet dip, (c) the mean difference between facet and cliff aspects, (d) cliff toe elevation, (e) platform slope, and (f) wave approach angle. Ensemble of percentile lines illustrates frequency distribution of the total volume eroded for any given control. Symbols represent the properties of key sites selected from Figure 6.03.*

Previous observations of individual rockfalls, and rockfall sequences, have demonstrated that the structural setting and spatial distribution of joint sets control rock mass fragmentation and eventual modes of failure, both in terms of block geometry and in terms of detachment size (*Section 4.1, p.* 54). Here, both facet density and facet dip appear to control rockfall activity when observed at the regional scale (Figures 6.01a,b and 6.02a,b), reflecting local observations made elsewhere. These include alpine environments, where high rates of rockwall retreat ($> 1 \times 10^{-3}$ m yr^{-1}) are typically associated with the weakening of bedrock due to a combination of high joint densities and steep rockwalls, as well as post-glacial stress relaxation (André, 1997; Arsenault *et al.*, 2005). The rate of cliff erosion is shown here to be inversely related to the relative orientations of the cliff face and their constituent facets beyond a mean angle of *ca.* 45° (Figures 6.01c and 6.02c), although there is considerable scatter for angles below *ca.* 30°. Along the North Yorkshire coast, these patterns are likely to reflect discontinuity-defined structural controls on block size and shape (*Section 4.3.3, p.* 73). For example, very platy, elongate, and bladed rockfalls dominate the erosional flux ($> 25\%$), despite representing $< 10\%$ of the inventory (mean volume

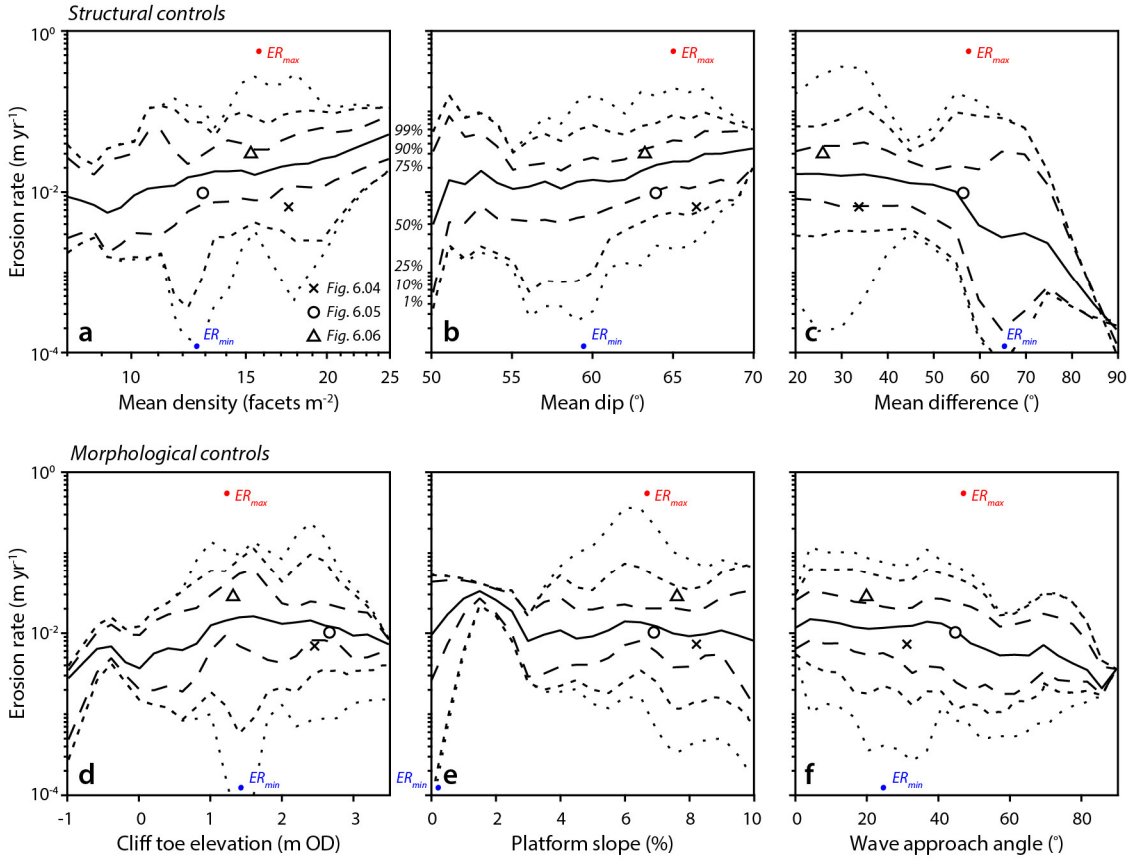

Figure 6.02 *Percentile plot of a bin-by-bin comparison of the erosion rate against a selection of structural (a – c) and morphological (d – f) controls, including (a) mean facet density, (b) mean facet dip, (c) the mean difference between facet and cliff aspects, (d) cliff toe elevation, (e) platform slope, and (f) wave approach angle. Ensemble of percentile lines illustrates frequency distribution of the erosion rate for any given control. Symbols represent the properties of key sites selected from Figure 6.03.*

of *ca.* 5.48 ± 1.13 m^3). These are shallow slabs and rods with a slope-parallel orientation and therefore a small mean difference between block orientation and cliff aspect, and are similar in behaviour to sheeting joints (Martel, 2006; Moore *et al.*, 2009). Conversely, rockfalls that are blocky, and therefore more three-dimensional, in shape are more likely to have a large orientation angle relative to the cliff surface. Along the North Yorkshire coastline, however, these are largely limited to small volumes < 0.064 m^3, contributing a small proportion of the total eroded volume ($< 11\%$), despite representing $> 23\%$ of rockfalls.

Relationships between cliff erosion and morphological controls, here acting as a proxy for the efficacy of wave impacting at the cliff toe (*Chapter 5*), are less clear than those observed for structural controls. Both cliff toe elevation and platform slope appear to control cliff erosion at the regional scale (Figures 6.01d,e and 6.02d,e). This broadly reflects previous observations, which have demonstrated that platform morphology can strongly influence wave shoaling and breaking prior to wave-cliff interaction (Trenhaile and Kanyaya, 2007; Porter *et al.*, 2010). Rates of erosion sharply increase with cliff toe elevation between *ca.* -1 m and 0 m OD, before gradually levelling off above 2 m OD, although there is considerable scatter in this range. Similarly, rates of erosion sharply increase with platform slope between values of *ca.* 0% and 2%, before decreasing and levelling off above slopes of 4%. Cliff erosion is inversely related to the wave approach angle (Figures 6.01e and 6.02e). This contradicts relationships between the angle of wave approach and wave-sustained sediment transport, which has been previously suggested to peak at angles of *ca.* 45° (Ashton *et al.*, 2001; Nienhuis *et al.*, 2013). This may be a function of the relatively short duration of observations here (made over a total period of 2 years and 7 months) as compared to the time required for an erosion signal to fully develop, such that this could retain an impression of the wave loading signal over and above noise.

To understand how regional-scale variations in cliff structure and wave loading drive variations in cliff erosion, and how these patterns manifest themselves spatially in contiguous compartments, a windowed correlation (± 200 m) was applied to the data presented in Figure 6.02. Sliding-window correlations are commonly used for estimating time-varying relationships between signals, where correlation coefficients are calculated on overlapping segments of time series data. Here, this concept was applied spatially. For each 100 m bin along the site, correlation coefficients were calculated between the mean of each control and the mean rate of erosion observed in each window. Figure 6.03 therefore shows the extent to which patterns in erosion rates in the ± 200 m surrounding each bin are preferentially correlated with (hereafter 'conditioned' by) different structural and morphological controls. These controls are assumed to strongly condition erosion rates where the correlation coefficient is greater than ± 0.75. Rates of erosion are strongly conditioned by solely structural controls along *ca.* 19% of the total monitored cliff length, and by morphological controls along *ca.* 25% of the coastline. Along *ca.* 31% of the coastline, erosion rates are strongly conditioned by both structural and morphological controls.

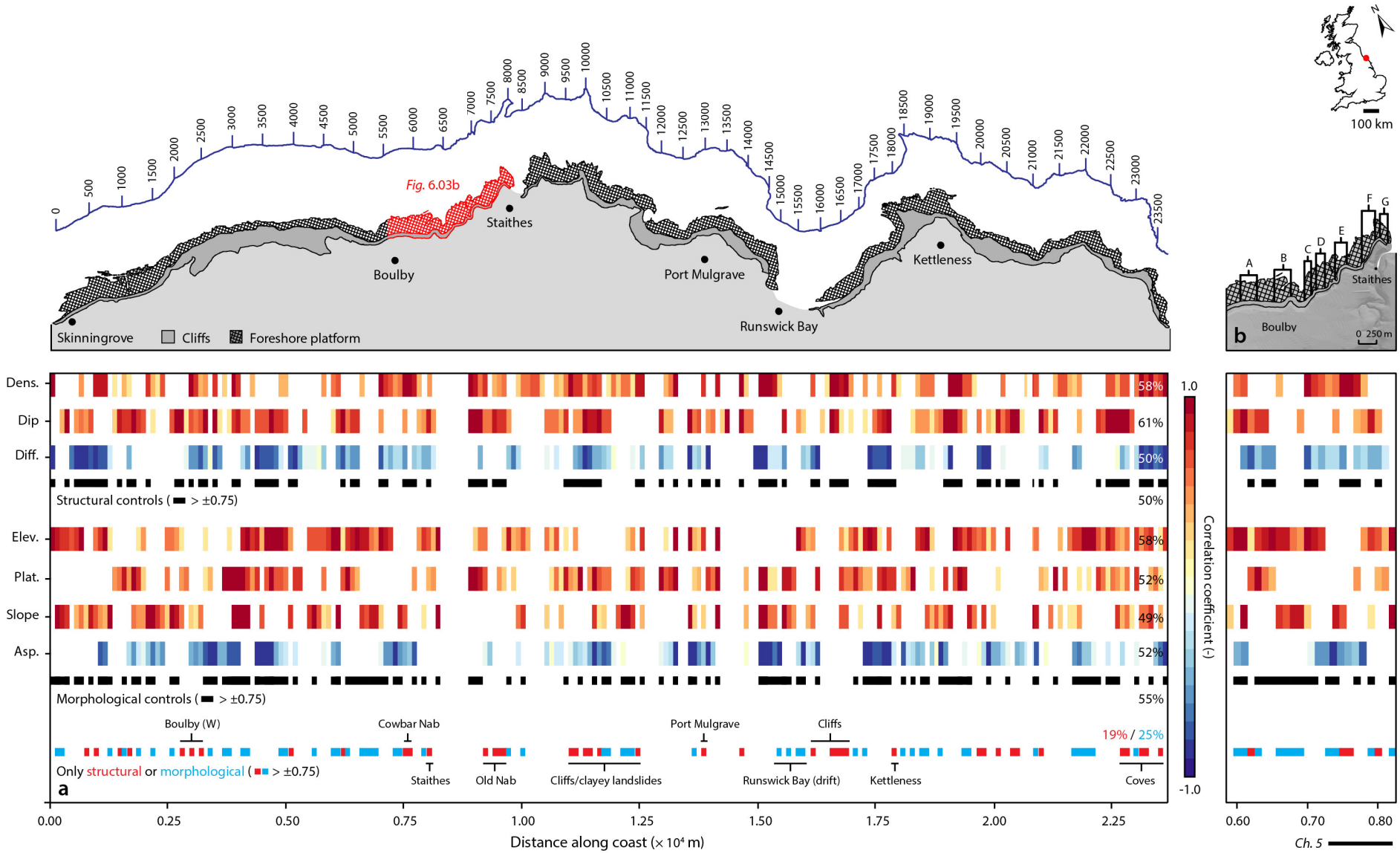
Fig. 6.03b
Staithes
Boulby
Port Mulgrave
Kettleness
Runswick Bay
Skinningrove
Cliffs
Foreshore platform
100 km
A
B
C
D
E
F
G
Staithes
Boulby
0 250 m
b
Dens.
Dip
Diff.
Structural controls (> ±0.75)
Elev.
Plat.
Slope
Asp.
Morphological controls (> ±0.75)
58%
61%
50%
50%
58%
52%
49%
52%
55%
Boulby (W)
Cowbar Nab
Port Mulgrave
Cliffs
19% / 25%
Only structural or morphological (> ±0.75)
Staithes
Old Nab
Cliffs/clayey landslides
Runswick Bay (drift)
Kettleness
Coves
a
1.0
-1.0
Correlation coefficient (-)
0.00
0.25
0.50
0.75
1.00
1.25
1.50
1.75
2.00
2.25
Distance along coast (× 10⁴ m)
0.60
0.70
0.80
Ch. 5

Figure 6.03 *Overleaf. Spatial variations in the correlations between the total volume eroded in each bin and a selection of structural and morphological controls. These include the mean facet density, dip, difference between facet and cliff aspects, cliff toe elevation, platform length (displayed here, although not statistically significant in Appendix K, p. 204), platform slope, and the wave approach angle. Correlations are windowed (± 200 m) and only shown in (a) if there is a positive/negative correlation, depending on the relationships observed in Appendix K. Where erosion is defined as being only structurally (or morphologically) controlled, this requires the presence of at least one strongly (± 0.75) correlated structural (or morphological) variable, and an absence of any morphological (or structural) controls. The inset in (b) shows in detail the previously monitored sites (Table 2.01, p. 19) as well as the sites monitored in Chapter 5.*

Cliff erosion at Boulby (0.28 – 0.33 × 10^4 m), Cowbar Nab (0.75 × 10^4 m), Staithes (0.82 × 10^4 m), Old Nab (1.00 × 10^4 m), Port Mulgrave (1.35 × 10^4 m), and also Kettleness (1.85 × 10^4 m) appears to be structurally controlled (Figure 6.03). Each of these sites are headlands that generally project seaward from the general line of the coast. These headlands also coincide with areas that were observed to produce similar distributions of rockfall shapes year-on-year (Figure 4.18, *p.* 78). This implies that the geological setting of the coastline, where ridges of solid rock with an absence of faulting are separated by lower cliffs and embayments, directly influences spatial variations in the distribution of rockfall shapes and the volume of material eroded. Between Old Nab and Port Mulgrave (1.10 – 1.25 × 10^4 m), rates of erosion are conditioned by a combination of structural and morphological controls where cliffs are dissected by landslide activity. At Sandsend (> 2.20 × 10^4 m), erosion appears to be associated with a series of crenulous coves, which are separated by mainly till cliffs. A subsection of the coastline at Staithes, which is a type site for these conditions, is shown in Figure 6.04. The cliff surface is characterised by a relatively high facet density and dip (17.0 facets m^{-2} and 67°, respectively), and a low difference between facet and cliff aspect (34°; values for all controls shown in Figures 6.01 and 6.02). The headland eroded at a mean rate of *ca.* 6.30 × 10^{-3} m yr^{-1} over the monitoring period, which is the same order of magnitude as the mean rate of erosion across all sites where patterns of erosion are conditioned by variations in rock mass structure (9.30 × 10^{-3} m yr^{-1}, median = 1.04 × 10^{-2} m yr^{-1}). These range over nearly three orders of magnitude, from 8.66 × 10^{-4} m yr^{-1} to 9.24 × 10^{-2} m yr^{-1} (Figure 6.04). Visual inspection of this section of the cliff shows a clear prominence of exposed joint surfaces on the rock face, where recent rockfall scars are apparently both exploiting and limited in extent by rock mass structure.

Rates of erosion in areas that are characterised by landsliding, such as Runswick Bay (1.50 – 1.65 × 10^4 m) and lower cliffs of drift materials, such as Sandsend (2.16 – 2.20 × 10^4 m), are primarily morphologically controlled (Figure 6.03). However, erosion along some stretches of rock cliffs, such as Boulby (0.34 – 0.50 × 10^4 m) and towards Cowbar Nab (0.59 – 0.74 × 10^4 m) is also strongly conditioned by morphological controls. At Kettleness, a change from predominantly morphological to structural controls on erosion (1.60 × 10^4 m) is coincident with

the transition from cliffs formed predominantly of more deformable drifts to cliffs of harder, lithified rock types. A subsection of the coastline at Kettleness, which is a type site for these conditions, is shown in Figure 6.05. Beyond the headland, where erosion reverts to being structurally controlled, rates of erosion along the cliffs are strongly conditioned by morphological controls, with a short platform length (144.6 m), a moderate cliff toe elevation and wave approach angle (2.65 m OD and 44°, respectively), and a high platform slope (6.9%; values for all controls shown in Figures 6.01 and 6.02). The cliffs at Kettleness eroded at a mean rate of *ca.* 9.70×10^{-3} m yr^{-1} over the monitoring period, with the mean rate of erosion across all sites where rates of erosion are strongly correlated with morphological controls ranging over three orders of magnitude, from 8.60×10^{-4} m yr^{-1} to 5.80×10^{-1} m yr^{-1} (Figure 6.05).

Patterns of erosion along approximately one third of the coastline (31%) were strongly correlated with both structural and morphological controls, rather than one of these alone or an apparently random behaviour shown by no correlation. The cliffs at Boulby (at a distance of *ca.* 0.40×10^{4} m) are a type site for these conditions, and are shown in Figure 6.06. The cliffs eroded

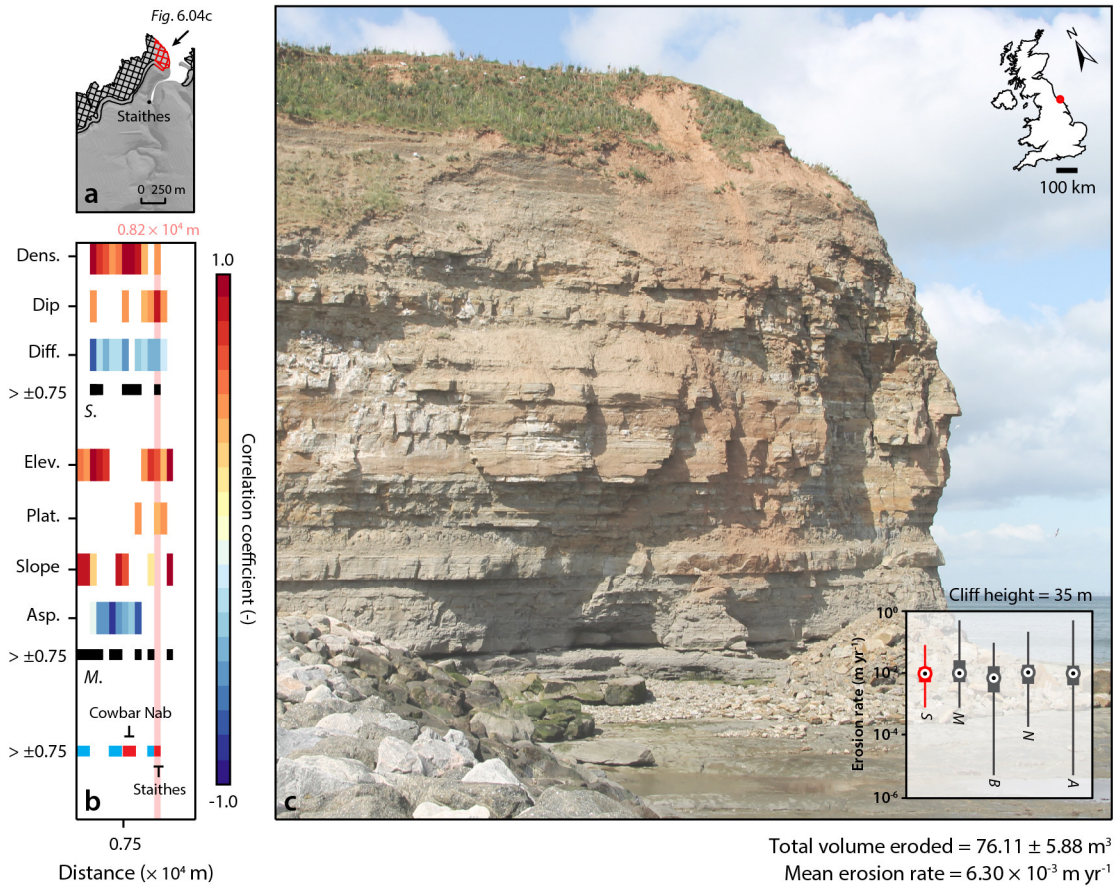

Figure 6.04 *A subsection of the North Yorkshire coastline at Staithes (a), where patterns of erosion are strongly correlated with structural controls, shown in (b). Erosion at the headland, pictured in (c), is one of a number of structurally controlled features along the coastline, with others marked in Figure 6.03. Inset: box plot of erosion rates along the coastline, grouped by structural (S), morphological (M), both structural and morphological (B), and no (N) controls. The data for all (A) erosion rates are also shown.*

at a mean rate of *ca.* 2.93 × 10^{-2} m yr^{-1} over the monitoring period (75th percentile). This high erosion rate is driven by a combination of high facet densities and steep rockwalls (15.4 facets m^{-2} and 64°, respectively), a similar orientation of the cliffs relative to their constituent facets (mean difference of 26°), a moderate toe elevation (1.31 m OD), a high platform slope (7.6%), and a relatively low angle of wave approach (20°; values for all controls shown in Figures 6.01 and 6.02). However, the mean rate of erosion across all sites with both structural and morphological controls (5.70 × 10^{-3} m yr^{-1}, median = 7.50 × 10^{-3} m yr^{-1}), is greater when they are considered separately (Figure 6.06).

These findings illustrate the importance of both cliff structure and wave loading (inferred using relationships with morphological controls observed on a local scale in *Chapter 5*) in driving regional-scale variations in rockfall activity and the resulting cliff erosion. Spatial patterns in the rates of erosion that occurred along over half of the 20.5 km of cliffs monitored in this research were strongly correlated with either structural or morphological conditions (50% vs. 55%). Oceanographic forcing has historically been viewed as the dominant driver of coastal cliff erosion

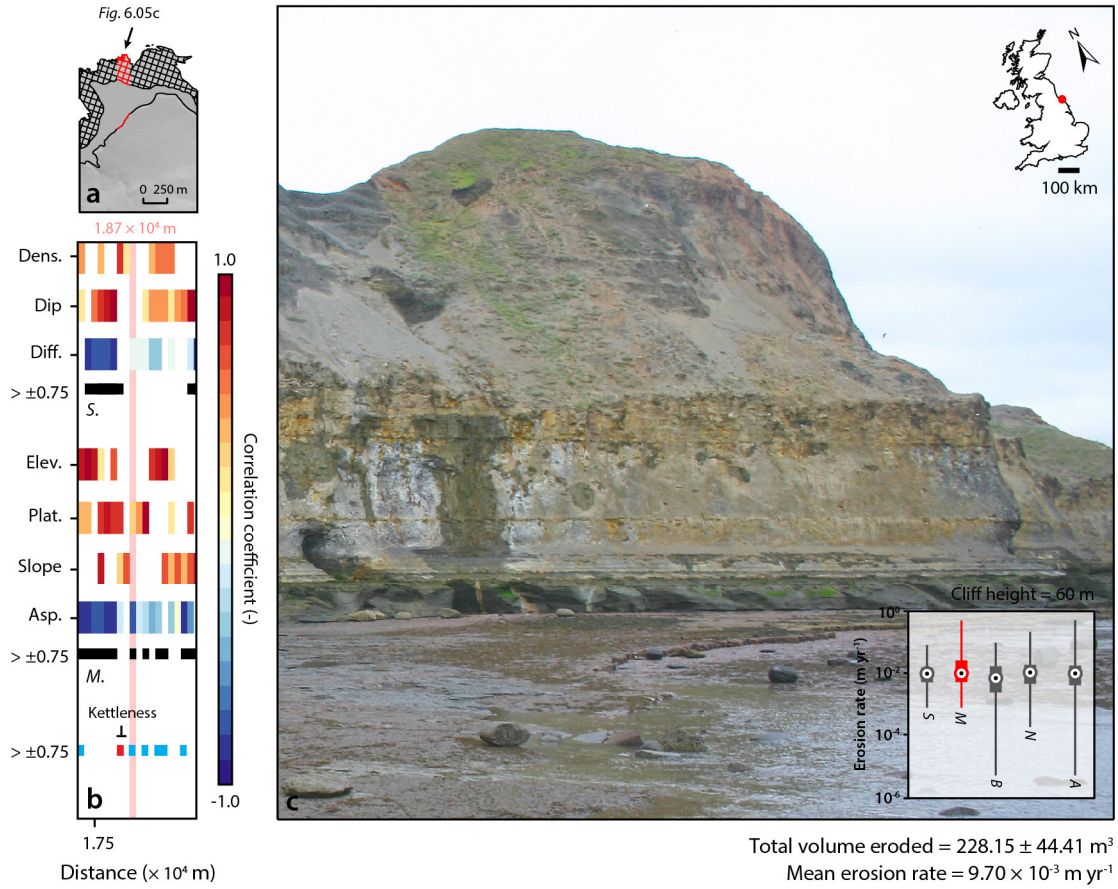

Figure 6.05 *A subsection of the North Yorkshire coastline at Kettleness (a), where patterns of erosion are strongly correlated with local morphological controls, shown in (b). Unlike the headland at Kettleness, the cliffs pictured in (c) are one of a number of stretches of morphologically controlled cliffs along the coastline. Inset: box plot of erosion rates along the coastline, grouped by structural (S), morphological (M), both structural and morphological (B), and no (N) controls. The data for all (A) erosion rates are also shown.*

(for example, Bartrum, 1926; Edwards, 1951; Sunamura, 1978a, 1978b; Tsujimoto, 1987; Trenhaile, 2000) and ultimately must, to some extent, set a base level for the rate of erosion along coastlines. However, these findings also attest to the importance of rock mass structure in controlling how rockfall and erosion respond to wave impacting and other processes occurring along rocky coasts. Here, this influence includes the role of joint density, the dip of the release surface, and the relative orientation of the joints to that surface, each of which vary on a regional scale and have been shown to relate to alongshore patterns in rockfall volume and shape. It is, however, acknowledged that the relative importance of these processes may also change over time, and may vary considerably year-on-year. The findings presented in *Chapters 3*, *4*, and *5*, and synthesised here, are now discussed in the following sections within the wider context of (1) the implications for monitoring and modelling rockfall activity over wide extents (*Section 6.2*), (2) understanding patterns of rockfall occurrence, the resulting cliff erosion, and the relative importance of intrinsic versus extrinsic controls on erosion (*Section 6.3*), and (3) the associated implications for cliff evolution (*Section 6.4*).

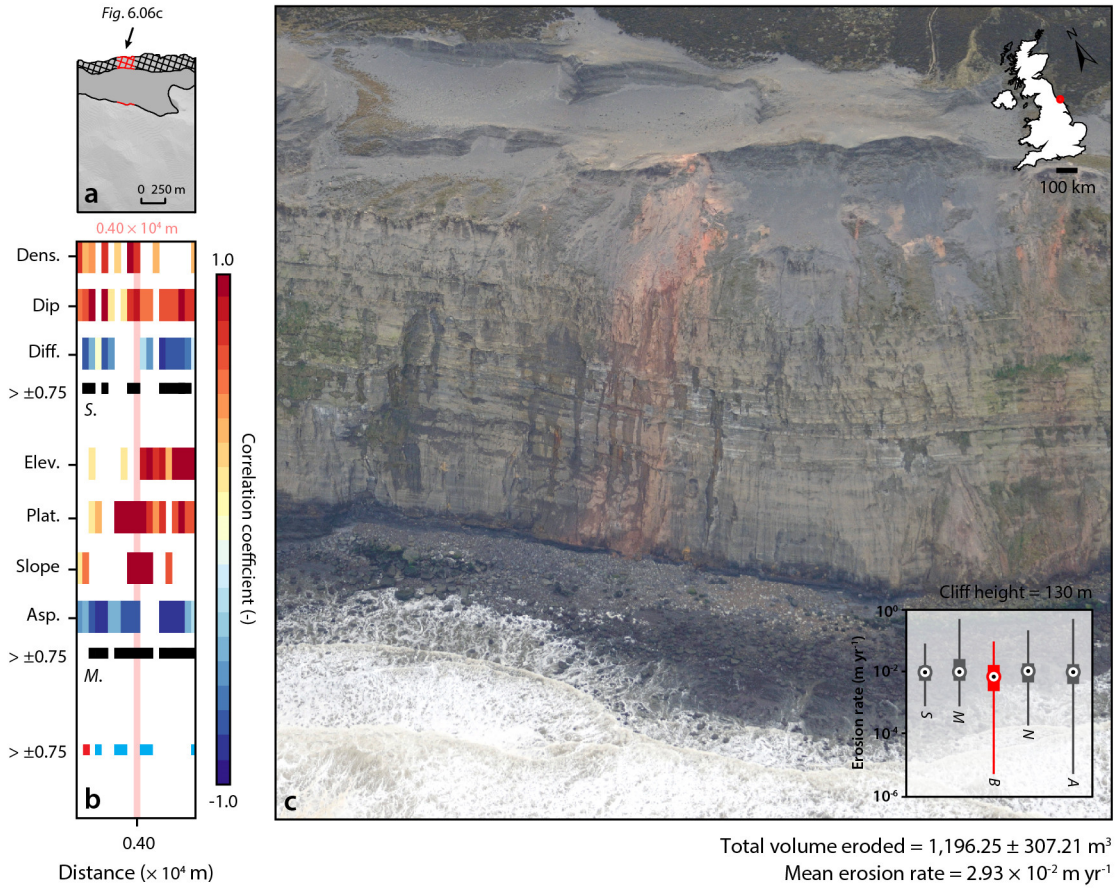

Figure 6.06 *A subsection of the North Yorkshire coastline at Boulby (a), where patterns of erosion are strongly correlated with both structural and morphological controls, shown in (b). A subsection of the cliffs is pictured in (c). Inset: box plot of erosion rates along the coastline, grouped by structural (S), morphological (M), both structural and morphological (B), and no (N) controls. The data for all (A) erosion rates are also shown.*

6.2 Implications for monitoring rockfall activity

The findings of this thesis demonstrate that a full 3D treatment of high-resolution airborne LiDAR provides a robust means to monitor rockfall activity and the resulting cliff erosion continuously (in space), in 3D, and over large spatial scales ($> 10^4$ m). When mounted on a helicopter, continuous swaths from this type of airborne LiDAR can be used to collect data along narrow corridors even with steep, near-vertical slopes, presenting a considerable advantage over mobile terrestrial LiDAR when scanning areas that are often limited by range, view direction, and can feature extensive occlusion (Lato *et al.*, 2009a; Dunham *et al.*, 2017). The point cloud data obtained from airborne LiDAR give increased precision on slope angle, aspect, and, on bare rock faces, joints, and other structural features. Multi return and colour data can be used during segmentation and classification routines (Axelsson, 1999; Sithole and Vosselman, 2004; Vosselman *et al.*, 2005) as a means of vegetation filtering (*Section 3.2.2, p.* 29). The workflow developed and used to process airborne LiDAR data in *Chapter 3* is semi-automatic and, uniquely, provides a means of analysing regional-scale variations in rockfall activity along rock slopes with a non-linear plan-form geometry. Most importantly, retaining the true 3D character of the data here has permitted comparisons with both structural and morphological controls at a comparable resolution. The approach outlined here gives a 3D watertight mesh, centre of gravity, principal axes, volume, and volumetric uncertainty for each rockfall. The 3D nature of the rockfall inventory derived here has permitted the shapes and volumes of real, observed rockfall detachments to be linked to variations in cliff structure and wave loading on a regional scale ($> 10^4$ m).

A key finding of the analysis presented in *Chapter 3* is that localised estimates of rockfall activity captured over small extents ($< 10^3$ m^2) do not generate stable magnitude-frequency distributions, and so cannot be upscaled for the purpose of modelling wider-scale or longer-term cliff evolution. Here, monitoring at length scales < 2.5 km (equivalent to *ca.* 1×10^5 m^2 assuming an average cliff height of 40 m) has a significant effect on the frequency estimates of the largest events, potentially giving rise to considerably higher (where, by chance, a large event is captured) or lower (where no large event occurs) frequencies than is actually the case. Here, the surface area of the largest recorded event is *ca.* 7.5×10^3 m^2, equating to 7.5% of this 'minimum' area. Along the North Yorkshire coast, this figure represents *ca.* 12% of the total cliff length or area monitored. This extent, which is a function of the probability of being able to capture a statistically valid sample of the largest possible events, is likely to vary between settings based on differences in weathering and other environmental conditions (for example, precipitation, temperature, and the frequency of triggering events), triggering mechanisms, and lithological characteristics, each of which are thought to influence the power law scaling of rockfalls (Barlow *et al.*, 2012).

In order to increase the likelihood of capturing a stable magnitude-frequency relationship and therefore a complete distribution of rockfall activity, monitoring of the cliffs under examination here should be undertaken at multiple sites totalling at least 2.5 km in length, rather

than in a single, continuous section (*Section 3.3.3*, *p.* 44). This length scale is likely to vary between settings based on, for example, variability in rock strength and structure, and ideally should be constrained elsewhere. This could reflect spatial variations in the dominant controls on erosion (Figure 6.03), which can remain approximately uniform over continuous sections of up to 1.7 km for areas where erosion is strongly structurally controlled (mean = 500 m), and 1.8 km where erosion is strongly morphologically controlled (mean = 700 m). These estimates also include areas where no strong, statistically significant controls on erosion have emerged. Assuming that the patterns of erosion observed form part of a longer-term cycle of cliff failure and profile-form adjustment that is not fully captured by the relatively short duration of monitoring undertaken here (2 years and 7 months), then neighbouring bins are more likely to be at a similar stage of this process than more distal sites. Previous research has demonstrated that the propagation of instability and failure along these cliffs operates at 10^1 year timescales. For example, Rosser *et al.* (2013) estimated an average resurfacing time of 28.1 yr along *ca.* 710 m of cliffs at sites A – G (*Section 2.2*, *p.* 17) based on extrapolating the spatial footprints of failures derived from monthly monitoring over a seven-year period. The assumption of similarities between neighbouring bins can be justified given the longer wavelength variations of rock mass structure along the coastline (*ca.* 10^3 m), which are likely to moderate the erosional effects of shorter wavelength variations in wave loading ($< 10^2$ m, observed in *Chapter 5*). If this cyclical nature of cliff erosion and retreat does exist, and it is characterised by time-dependent failure processes (for example, incremental oversteepening leading to large-scale failure), then a stable magnitude-frequency relationship can only be observed over a longer total duration of monitoring, or over a more widely-distributed area of monitoring. Moreover, sampling in a distributed manner is more likely to capture the erosional response of the cliffs to a wider variety of controls and, by inference, at different stages of the longer-term failure cycle.

Given the increasing tendency towards collecting large inventories on potentially hazardous geomorphic processes (Korup *et al.*, 2012), these findings attest to the importance of collecting a dataset that is both temporally and spatially complete. Although large pools of data were previously thought to enable a statistically robust analysis of magnitudes, frequencies, and the formulation of exceedance probabilities for hazard appraisals (Korup *et al.*, 2012), this is only the case if the quantitative input for these is complete over a large enough spatial scale relative to the scale of the events experienced. This is pertinent for research using terrestrial LiDAR to monitor rockfall activity, as such approaches typically operate at short length scales (see Abellán *et al.*, 2014 for a review). More widely, the analysis has considerable implications for monitoring the evolution of non-coastal slopes, where magnitude-frequency scaling is often used to inform hazard assessment and mitigation (Abellán *et al.*, 2011; Dewez *et al.*, 2013), and where accurately defining rockfall recurrence intervals is essential (for example, Budetta and Nappi, 2013; Budetta *et al.*, 2016; Moos *et al.*, 2017).

Just as path-dependency has been observed for landslides (for example, Samia *et al.*, 2017a, 2017b), the data presented in *Chapter 4* demonstrate a clear spatial dependence among rockfalls occurring along the North Yorkshire coast, suggesting that they cannot be considered a Poissonian process. However, the linkage observed at this scale only applies to a small percentage of the total: year-on-year, approximately 10.5% of rockfalls that occurred along the North Yorkshire coast between 2014 and 2017 had done so in locations where others had previously failed (compared to *ca.* 1.7% estimated under conditions of complete spatial randomness). It is, however, likely that with higher frequency monitoring, which has been shown elsewhere to disaggregate single scars observed over longer periods into multiple overlapping events, this tendency may be observed to increase. On a regional scale, using the locations of previous events or the quality of the rock mass (discussed in *Section 6.3*) as an indicator of future rockfall risk is therefore problematic, as by far the majority of rockfalls appear unrelated to the location of those that have occurred in the two years monitored previously.

Risk management using the magnitude-frequency distributions of rockfalls is therefore complicated: rockfall activity along the North Yorkshire coast, and likely elsewhere, is not sufficiently statistically independent for the purposes of rockfall frequency analyses, irrespective of the volume range considered. Conversely, levels of coalescence in the rockfall inventory derived here are not sufficiently high enough to reliably use precursory rockfall activity, here measured at annual intervals, as a means of forecasting future change. For example, Kromer *et al.* (2017) compiled a pre-failure deformation database of 90 rockfall events that occurred over a 1,252-day period. Of these events, 64 exhibited measurable deformation (movement) prior to failure, and the authors use these cases to present an empirical framework for forecasting the location, volume, and kinematics of potential rockfalls. However, the database of regional-scale rockfall coalescence derived in *Chapter 4* indicates that only a fraction of rockfalls that occurred along the coastline did so where others had occurred previously, leaving a large percentage with no observable pre-failure rockfall activity in the year immediately prior to monitoring ($>$ 0.10 m LoD defined in *Section 3.2.3*, *p.* 33). It may be that the rockfalls considered here are too small to exhibit observable pre-failure behaviour up to a year before the event itself, but nonetheless, this analysis shows a significant challenge to using previous behaviour as an indicator of future risk.

These findings also hold for variations in the total volume of rock eroded along the coastline. As demonstrated in *Chapter 4*, the proportion of the cliffs monitored that consistently (year-on-year) produced material in any given volume range did not exceed 50%, and more commonly remained below 35%. This reflects observations made elsewhere, where localised ($< 10^2$ m) comparisons between historical and recent retreat rates are often poorly correlated (Young, 2018). Using site-specific erosion rates, measured over short (sub-decadal) intervals, to predict or project future decadal scale cliff retreat is therefore problematic. This poses challenges for longer-term assessments of coastline responses to environmental change, as it is only recently

that the uncertainties in monitoring have been reduced to a point whereby erosion rates can be monitored with confidence. The findings presented in *Chapter 3*, which tested the sensitivity of rockfall magnitude-frequency distributions to the spatial scale of monitoring, also reflect this. Along the entire coastline, spatially averaged erosion profiles attest to the stochastic nature of cliff erosion, where two years of overall steepening were followed by a year in which the profile was effectively reset by a series of full-scale cliff collapses. Monitoring over a wider variety of timescales is therefore needed in order to quantify how long-term rates of erosion emerge from apparently sporadic changes that result from discrete, large events (Finnegan *et al.*, 2014; Ganti *et al.*, 2016), and to establish the minimum timescale over which time-averaged erosion rates are representative of the longer-term erosion signal. Ultimately, however, the findings presented in *Section 6.1* could be drawn upon to suggest that extrapolating historical rates of rockfall activity and the associated cliff erosion is problematic, without incorporating some measure of the forcing mechanisms and system feedbacks over the monitoring period (Lee, 2008).

6.3 Implications for cliff erosion

Much of the recent research into coastal cliff erosion has used case-specific approaches that infer a wider morphological model of the evolution of cliff and platform systems from only a limited selection of sites (Kennedy *et al.*, 2017). This reflects a wider issue in geomorphology, where undertaking regional-scale ($> 10^4$ m) monitoring of surface processes and their drivers at high resolutions is methodologically difficult, as discussed in *Chapter 1*. On coastal cliffs, previous research undertaken at these scales lacks observations of drivers and controls at resolutions that are commensurate with the detail of volumetric changes provided by airborne LiDAR surveys (Matsumoto *et al.*, 2017), potentially contributing to the poor correlations observed between recent rates of cliff erosion and metrics of wave-cliff impact, precipitation, and rock strength (Young, 2018). In addition, these shorelines transcend precipitation sub-regions or geological gradients, and comprise subsections of the monitored coastline that are either engineered or fronted by beaches, or both, introducing a number of geomorphic feedbacks that complicate the analysis of driver-effect relationships (Kline *et al.*, 2014; Young, 2015). The data presented in this thesis provide new insights into regional-scale cliff adjustment and retreat, constituting the first large-scale assessment of rockfall activity and the resulting coastal cliff erosion undertaken at high resolution. The significance of these findings, and their implications for our understanding of coastal processes, monitoring, and modelling, are discussed here.

The literature on coastal cliff behaviour and evolution often categorises cliffed coastlines into perceivably stable 'hard' rock cliffs and actively retreating 'soft' rock cliffs, with the implication of this distinction being that soft rock coasts are considered more vulnerable to instability and rapid change (Allison, 1989; Sherman and Gares, 2002). As demonstrated in *Chapter 3*, rates of cliff erosion can vary significantly both within and between regions. Along the

North Yorkshire coast, erosion rates ranged from as much as $1.12 \times 10^{-5} - 1.63$ m yr^{-1} over the monitoring period of this study. This reflects wider trends across the British Isles, where rates of landward retreat range from < 0.001 m yr^{-1} in what are apparently the most resistant rocks, to > 10 m yr^{-1} where cliffs are composed of soft, conformable glacial tills (Brooks and Spencer, 2012). The susceptibility of soft rock coastlines to erosion and retreat has meant that they are often prioritised in coastal management schemes (Lee and Clark, 2002), leaving the binary distinction implying some level of uniformity of behaviour or erosion within each subcategory.

The results presented in *Chapter 3*, however, demonstrate that local (10^2 m) erosion rates along stretches of perceivably 'hard' rock coastline can reach approximately the same order of magnitude as the highest rates of erosion occurring on soft rock coastlines, even over the annual timescales considered here. Along the North Yorkshire coast, almost half (*ca.* 53,721.72 m^3) of the total (*ca.* 124,843.31 m^3) volume eroded by rockfalls between August 2014 and March 2017 accrued in only 12 large ($> 1{,}000$ m^3) cliff collapses, eight of which occurred between April 2016 and March 2017, resulting in an instantaneous step-back of the coastline by up to 6 m in places. Assuming that the longest axis of these events is cliff-parallel (representing rockfall width) and the shortest axis is cliff-normal (representing rockfall depth), then these events alone caused an average step-back of *ca.* 1.92 m over 972 m of the coastline, equating to approximately 4.8% of the total cliff length monitored over a period of 2 years and 7 months. Present models of cliff retreat fail to capture the timing and scale of episodic events, and, at present, little is known of how the long-term rates of erosion derived by these models arise from the accumulation of individual, instantaneous events. Rising global sea-levels in conjunction with projected changes in winds, tides, precipitation, storm events, and wave climate are expected to accelerate coastal cliff retreat and threaten coastal populations in many areas (Sunamura, 1988; Bray and Hooke, 1997; Dickson *et al.*, 2007; Nicholls *et al.*, 2007; Trenhaile, 2010, 2014), resulting in a pressing need to understand and model the erosional response of hard rock coastlines like the North Yorkshire coast to these processes (Trenhaile, 2011).

6.3.1 Intrinsic controls on erosion

Determining the relative importance of intrinsic versus extrinsic controls on rockfalls, and the resulting erosion that they accumulate, is complex, particularly across different spatial and temporal scales. Although rockfalls have been monitored extensively in a variety of settings, high-resolution observations of rock slope erosion on a regional scale ($> 10^4$ m) are scarce. This is primarily due to difficulties in capturing data in a way that ensures a volumetrically complete inventory, and at length scales over which both resisting and driving stresses may vary. At the local scale, it is difficult to establish the extent to which variations in rockfall activity are actually part of inherent variability. The influence of subtle changes in different driving stresses (for example, thermal stresses, weathering, seismic loading, and, on coastal cliffs, wave impacting) is

also difficult to assess unless this is done at scale (Messenzehl *et al.*, 2017). The findings of this thesis demonstrate that, along a coastline where other controlling factors (tides, weather, offshore waves) are held approximately constant, rates of erosion are strongly conditioned by solely structural or morphological controls in approximately equal proportions (19% vs. 25%), where morphological controls act as a proxy for the erosional effects of wave impacting observed in *Chapter 5*. These patterns also hold when considering the locations where rates of erosion are strongly conditioned by structural and/or morphological controls (50% vs. 55%), amounting to *ca.* 10,229 m and 11,252 m of the coastline, respectively. Although oceanographic forcing has historically been viewed as the dominant driver of coastal cliff erosion (for example, Bartrum, 1926; Edwards, 1951; Sunamura, 1978a, 1978b; Tsujimoto, 1987; Trenhaile, 2000), the data presented in *Chapter 4* and synthesised here attest to the importance of cliff structure (primarily joint density, dip, and the relative orientation of joints to the cliff face) in defining regional-scale rates, the nature, and patterns of rockfall activity. This appears to override, at least in some places, the marine controls on erosion afforded by the macro-tidal, storm-dominated coast. Along coastal cliffs, previous research into the role of rock hardness and discontinuities on landform development has primarily been carried out on foreshore platforms (for example, Dickson *et al.*, 2004; Blanco-Chao *et al.*, 2007; Chelli *et al.*, 2010; Coombes *et al.*, 2013), although localised studies have also demonstrated the importance of rock mass characteristics in defining rates of cliff erosion (Budetta *et al.*, 2000; Duperret *et al.*, 2005; Lawrence *et al.*, 2013; Lee and Park, 2014). These have not managed to put local observations into a wider scale context, as here.

Along the North Yorkshire coast, spatial variations in cliff structure, as defined by the geometric properties of exposed joint surfaces, broadly follow the wider-scale geological setting of the coastline. In areas where high rates of erosion are strongly controlled by cliff structure, the cliff face is generally characterised by a combination of high joint densities, a steep gradient, and joints that lie sub-parallel to the topography, reflecting local observations made elsewhere (André, 1997; Moore and Griggs, 2002; Arsenault *et al.*, 2005; Dornbusch *et al.*, 2008). The strong relationship with joint density likely reflects small-scale transitions between different lithological units, which effectively promote failure due to contrasting hydraulic regimes and stress conditions (Evans and Hungr, 1993; Fischer, 2010). Previous research has identified the susceptibility of cataclinal slopes with surface-parallel joints, due to the pre-existence of sliding planes (Cruden and Hu, 1998; Moore *et al.*, 2009).

Cliff erosion at headlands is primarily structurally controlled (Valvo *et al.*, 2006), with headlands tending to produce similar distributions of rockfall shapes and volumes year-on-year, as compared to other areas. For example, rockfalls with a volume between *ca.* 131 m^3 and 262 m^3 ($n = 58$) consistently occurred around the headland at Boulby (at a distance of *ca.* 0.57×10^4 m). This implies that the geological setting of the coastline, where ridges of solid rock are separated by lower cliffs of drift, directly influences spatial variations in the distribution of rockfall shapes

and the volume of material eroded, while small differences in the strength of these patterns are likely to be driven by local processes and morphological controls. However, relating the properties of individual rockfalls to variations in the geometric properties of exposed joint (or facet) surfaces at these scales ($> 10^4$ m) remains difficult. Neither the distribution of rockfall shape, nor the distribution of different metrics of jointing as a function of rockfall volume, are sufficiently different between inventories of contiguous and non-contiguous rockfalls to conclude that rockfalls propagate along joints, conditioning subsequent instability in adjoining areas over time.

6.3.2 Extrinsic controls on erosion

At a local scale ($< 10^3$ m), over a stretch of cliffs that are relatively uniform in both geology and structure, longer-term variations in rockfall activity and the resulting cliff erosion are correlated with wave impact-driven ground motions, and variations in the morphological conditions that drive them: these include platform length, slope, cliff toe elevation, and wave approach angle (*Chapter 5*). These findings reflect the processes outlined in many conceptual models as well as previous observations made at other sites, which have demonstrated that platform morphology can strongly influence wave shoaling and breaking prior to wave-cliff interaction (for example, Nakamura *et al.*, 1966; Svendsen *et al.*, 1978; Trenhaile and Kanyaya, 2007). Although it is often assumed that the dissipation of higher frequency wave energy across a shore platform is a direct function of platform width (Johnson 1919; Stephenson and Thornton 2005), the results presented in *Chapter 5* also attest to the importance of the basic control of water depth (for example, Thornton and Guza 1982; Farrell *et al.* 2009; Marshall and Stephenson 2011; Ogawa *et al.* 2011, 2012). This reflects the known sensitivity of wave energy at higher (or 'gravity') frequencies to tidal-level changes (Ogawa *et al.*, 2016). For example, generalised observations of wave characteristics across six sites on the North Island, New Zealand, demonstrate that rapid attenuation of gravity waves occurs on wider and higher (and therefore shallow) foreshore platforms, while narrower and deeper platforms allow a greater proportion of higher frequency energies to propagate across the surface (Ogawa *et al.*, 2016). This coincides with observations at S4 and S5, which are detailed in *Chapter 5*: these sites have pronounced differences in cliff toe elevation (0.42 m vs. 1.81 m) and even platform widths (87 ± 25 m vs. 155 ± 13 m), but the platform fronting the cliffs at S5 drops off abruptly over a short distance. Although S4 is situated on a headland and is therefore more exposed, deeper water allows waves to approach the cliffs at S5 without much tidal change in dissipation. The sensor is therefore exposed to large waves when spring tides and large swells coincide. This could be the driver of comparative long-term erosional fluxes (76.17 ± 7.46 m^3 vs. 58.67 ± 12.39 m^3) despite S5 only being inundated for a fraction of the monitoring period (48.4% vs. 16.3%). If cliff-toe wave regimes are primarily determined by water depths, then this raises the possibility that certain platform geometries may be exposed to a persistent hydrodynamic regime regardless of the incident wave and tidal

conditions. The importance of total water level in driving both the magnitude and frequency of cliff toe wave impacting therefore holds implications for modelling future change under sea level rise, where certain stretches of coastline may transition towards gravity wave-dominated conditions over the long term.

On a regional scale ($> 10^4$ m), however, the analysis of driver-effect relationships between these processes is more difficult, with the data synthesised in this chapter demonstrating more scatter than for structural controls on cliff erosion. Variability in cliff structure (primarily joint density, dip, and the relative orientation of joints to the cliff face) could explain some of these discrepancies, with previous research highlighting that reversals in relationships between platform morphology and the expected environmental controls (tidal range, wave intensity) can be explained by rock mass structure, which can be locally dominant (Trenhaile, 1987). A more likely explanation is that the morphological conditions, used as a proxy for wave impacting at the cliff toe, simply introduce too much variability on a regional scale.

6.4 Implications for cliff evolution

The results presented in *Chapter 3* show that, within the inundated toe of the cliff, the majority of change is driven by episodic, large-scale failures, across over 24 km of coastline. However, the small number of relatively large rockfalls occurring in the wet zone contributes little to the overall erosion: an average of only 5.1% of the eroded volume occurred in this zone, despite representing 10.7% of the total cliff area. This appears to contradict the widely-accepted notion that cliff toe erosion occurs iteratively through abrasion, attrition, and rapid void pressure changes that lead to fracture, detachment, and subsequently undercutting (for example, Trenhaile, 1987; Carter and Guy, 1988; Sunamura, 1992; Hampton, 2002; Young and Ashford, 2008). On sections of the coast where erosion is most active, there is a statistically significant marine influence; however, this correlation only holds for an equivalent of *ca.* 2% of the monitored cliff length, even when monitored over multiple epochs. This is likely to reflect spatial variations in local rock mass strength and structure (*Chapter 4*; Sunamura, 1982; Allison and Kimber, 1998; Collins and Sitar, 2008; 2011; Dornbusch *et al.*, 2008), and wave energy, which is conditioned by nearshore and foreshore bathymetry (*Chapter 5*; Komar, 1998; Trenhaile and Kanyaya, 2007; Ogawa *et al.*, 2011). The limited marine influence evident in this data could explain why, as on many non-carbonate coastlines, there is little evidence of a wave cut notch at the base of these cliffs (Pierre and Lahousse, 2006; Rosser *et al.*, 2007; Young *et al.*, 2009; Vann Jones *et al.*, 2015).

The vertical distribution of wave erosion is often modelled as a direct function of inundation duration (Sunamura, 1975, 1977; Trenhaile and Layzell, 1981; Carr and Graff, 1982; Belov *et al.*, 1999; Trenhaile, 2000, 2009, 2011; Walkden and Dickson, 2008; Ashton *et al.*, 2011). This relationship has been incorporated into a number of widely used numerical models, including SCAPE (Walkden and Hall, 2005, 2011). Although the data presented in *Chapter 5* demonstrate

correlations between measurements of wave impacting recorded at the cliff toe and overall cliff erosion, these observations only hold for rockfalls occurring across the cliff face, and not solely below the highest astronomical tide line. The findings presented in this thesis call the processes that underpin many numerical models into question, and, in some cases, coastal retreat models could therefore overstate the role of cliff toe incision and subsequent cantilever collapse. In most cases, rising sea level will increase the depth of the water over sloping and horizontal foreshore platforms, acting to lower rates of wave attenuation and causing wave breaking zones to migrate landwards (Trenhaile, 2014). The data presented in *Chapter 3* appear to indicate that, year-on-year, the majority of the cliffs surveyed along the North Yorkshire coast are eroded to greater depths at elevations on and above the highest astronomical tide line. This suggests that, while the impacts upon wave climate may be profound, rising sea level may have a lesser effect upon this stretch of coastline than previous models would have predicted.

Along the North Yorkshire coast, the relative volume of material contributed by events of varying sizes stabilises above the limit of marine influence (*ca.* 10 m OD), where the majority of change is driven by episodic, large-scale failures. At a site-specific scale, the propagation of rockfalls has been observed to facilitate the transmission of marine undercutting up the cliff face over time (Rosser *et al.*, 2013). Where subaerial processes begin to dominate, erosion is primarily driven by incremental wasting, and the onset of these processes can be constrained using variations in rockfall magnitude-frequency and rockfall shape up-cliff. These gradual changes in β and in rockfall shape may be linked to changes in the groundwater regime, weathering environment, and the stress field up-cliff. These observations are supported by numerical modelling of the response of the rock mass to marine loading, which confirms the role of upward migration of shear strain through the cliff in causing tensile failure and crack growth at the cliff top (Styles *et al.*, 2011). The connectivity between events attests to the importance of stress redistribution following previous rockfalls in promoting damage accumulation and, eventually, further rock slope failure (Amitrano, 2006). On a regional scale, these processes are reflected in spatially-averaged erosion profiles, where two consecutive years of overall steepening are followed by a year in which the profile is effectively reset by full-scale cliff collapses, most likely related to an increased incidence in storms.

6.5 Summary

The research undertaken in this thesis has developed high-resolution field monitoring techniques with the aim of establishing the relative importance of intrinsic versus extrinsic controls on regional-scale ($> 10^4$ m) variations in rockfall activity. The analysis presented in *Section 6.1* builds on the research presented in *Chapters 3*, *4*, and *5* by synthesising these findings in order to develop a new, semi-empirical understanding of coastal cliff change behaviour. The coastline was discretised into 100 m compartments prior to testing the relationships between erosion in each bin

(the total volume eroded and the observed erosion rate), and a series of rock mass structural controls and local morphological controls (considered here as a proxy for wave loading). The findings have demonstrated observable, and in some cases strong, relationships between erosion and joint density, overall dip, and the relative orientation of joints to the cliff aspect (structural controls). Morphological controls that appear to exert an influence on erosion include cliff toe elevation (as a proxy for inundation duration), platform slope, and wave approach angle. Moving correlations (applied across each bin and its neighbours) were then used to assess the strength of relationships between spatial patterns in the observed erosion rate and these controls. This has highlighted the conditions that may promote or inhibit rockfalls and therefore cliff erosion, and shown how they vary along over 24 km of coastline.

The results presented here have enabled a unique insight into rockfall dynamics and how they vary on a regional scale. There are considerable implications for monitoring and modelling rockfall occurrence: extrapolating historical rates of rockfall activity and the associated cliff erosion is problematic without incorporating some measure of forcing mechanisms over the monitoring period, particularly when estimates have been made over short length scales ($< 10^3$ m; *Section 6.2*). Along a stretch of hard rock cliffs, rates of erosion have been shown to reach approximately the same order of magnitude as the highest rates of erosion occurring on soft rock coastlines, emphasising the importance of step-back events (*Section 6.3*). How the erosional work done by episodic, large-scale events accumulates into a long-term rate of erosion remains to be seen, with present models of cliff retreat failing to capture the timing, scale, or drivers of these events. More widely, these findings stress the importance of cliff structure and its ability to predispose particular stretches of coastline to increased (and also decreased) rates of erosion, reflecting local observations made in other settings (*Section 6.3.1*). In places, this influence can be negated or exacerbated by local morphological conditions, which control the dissipation of wave energy in the nearshore (*Section 6.3.2*).

Chapter 7

Conclusions

The aim of this research was *to understand how regional-scale variations in cliff structure and wave loading interact to condition variations in rockfall activity*. A series of research questions and objectives was outlined in *Chapter 1*, having identified key knowledge gaps in the literature, in order to address this aim. This thesis has identified a section of coastal cliffs along which micro-straining of the rock mass through wave impact loading varies considerably due to variable coastal geometry and bathymetry (*Chapter 2*). This variability, combined with variations in lithology and cliff structure, highlighted the importance of constraining the nature of rockfall occurrence beyond that observed on a single slope. To constrain variations in rockfall magnitude, frequency, and the resulting cliff erosion over regional scales ($> 10^4$ m), high-resolution, multi-temporal LiDAR data were used to detect and characterise changes in the morphology of rock slopes in 3D (*Chapter 3*). These data were used to undertake a quantitative appraisal of along-coast variations in the geometric properties of exposed discontinuity surfaces, to assess the extent to which these drive patterns in the size and shape of rockfalls observed (*Chapter 4*). A representative subsection of the coastline (10^2 m), but where cliff lithology and structure were approximately uniform, was chosen for high-resolution field monitoring for the purpose of quantifying spatial variations in wave loading characteristics, and relating these to local morphological conditions (*Chapter 5*). The findings of *Chapters 3*, *4*, and *5* have been synthesised to further our understanding of coastal cliff change behaviour (*Chapter 6*). The results have enabled unique insights into the regional-scale dynamics of rockfall activity, the importance of cliff structure and its ability to predispose particular stretches of coastline to increased rates of erosion, and the relationships between local morphological characteristics and longer-term variations in erosion. This marks a step-change in our ability to understand the competing effects of different processes in determining the magnitude and frequency of rockfall activity. *Section 7.1* summarises these findings in relation to the research questions outlined in *Chapter 1*, before discussing directions for future research in *Section 7.2*.

7.1 Summary of findings

The research presented in this thesis was based on a detailed study of actively failing rock slopes along a macro-tidal storm-dominated coast. The stretch of coastal cliffs that was the focus of this thesis offered the unique opportunity to investigate the relationships between rock mass structure, wave loading, and rockfall occurrence on a regional scale (*RO1*). This section revisits each of the research questions in *Section 1.2* (*p.* 8) and outlines the key findings of this thesis.

RQ1. How do rockfalls and the resulting cliff erosion vary over regional scales?

A workflow for detecting and characterising rockfalls across multiple scales was developed in *Chapter 3* (*RO2*). This workflow was then applied to high-resolution airborne LiDAR data in what is considered by the author as the first multi-temporal detection of regional-scale variations in rockfall magnitude, frequency, and the resulting cliff erosion in 3D (*RO3*). In total, over 58,000 rockfalls were observed along 20.5 km of coastal cliffs. Rock yield totalled 124,843.31 m^3, equating to an average erosion rate of 0.059 m yr^{-1}, which is the same order of magnitude as rates derived from previous terrestrial monitoring of rockfalls at local scales (10^2 m). The analysis presented takes into account spatial variations in both cliff profile- and plan-form, and considers the implications of these findings for wider monitoring of rockfall activity. Specifically, the resulting inventory of rockfall activity and cliff erosion has been used to show that:

- Local (10^2 m) rates of cliff erosion can vary over six orders of magnitude along a 20.5 km stretch of hard rock cliffs. The widespread occurrence of episodic step-back events, 12 of which accumulated an average step-back of *ca.* 1.92 m over nearly 5% of the cliff length monitored, dispels the concept that hard rock coastlines are relatively stable and highlights the importance of understanding and modelling the erosional response of hard rock coastlines under a changing climate.
- In the tidally inundated toe section of the cliffs, the majority of change is driven by episodic, large-scale failures. The small number of relatively large rockfalls occurring in the wet zone contributes little to its overall retreat, with an average of only 5.1% of the eroded volume having occurred here, despite representing 10.7% of the total cliff area.
- Inundation duration constitutes a significant control on erosion at the cliff toe, but only for $< 2\%$ of the monitored cliff length. Instead, the majority of the cliffs surveyed are consistently eroded to greater depths at elevations on and above the highest astronomical tide line. This contradicts the widely accepted notion that cliff toe erosion occurs iteratively, leading to notching, although it is acknowledged that the relatively short duration of observations here may preclude the full development of this signal.
- The relative volume of material contributed by events of varying sizes stabilises above the limit of marine influence. This suggests that, where the erosive action of subaerial processes begins to dominate, erosion is primarily driven by incremental wasting, and that

the onset of these processes can be constrained using variations in rockfall magnitude-frequency and shape. These gradual changes may be linked to changes in the groundwater regime, weathering environment, and the stress field up-cliff.

- Stress redistribution following rockfalls is crucial in promoting further rock slope failure, and evidence of this can be seen on a regional scale. Spatially averaged erosion profiles have been used to infer that, over the short term, the dominant mode of cliff erosion leads to steepening of the cliff profile, with less frequent failures at the cliff top. Two consecutive years of overall steepening are followed by a year in which the profile is effectively reset by full-scale cliff collapses, most likely related to an increased incidence in storms.
- Rockfall magnitude-frequency relationships are highly sensitive to the spatial scale of monitoring, such that monitoring at length scales < 2.5 km in this setting considerably increases the frequency estimates of the largest events. This window of monitoring should be distributed in multiple segments, rather than concentrated in one continuous stretch, to avoid bias. This has profound implications for research using methods of data acquisition that typically operate at short length scales, as any scaling relationships derived may be subject to significant bias as a function of spatial monitoring extent.

RQ2. To what extent does rock slope structure drive spatial variations in rockfall activity?

Chapter 4 details the methods used to extract the geometric properties of exposed discontinuity surfaces on near-vertical rock slopes, on a regional scale. In total, over 1.2×10^6 facets were extracted, which were then used to explore how the properties of rockfalls, such as block shape and volume, are related to wider-scale variations in the quality of the rock mass, both up-cliff and along-coast (*RO4*). The results of this analysis demonstrated that:

- Rockfall shape is scale dependent. The dominance of small ($10^{-3} < V_R < 10^{-1}$ m^3), blocky shapes and large ($V_R > 10^2$ m^3), slab-like shapes potentially marks a transition from rockfalls as a structurally-defined process to rockfall as either small-scale consequences of incremental weathering or fracturing-related mass movements that break through rock bridges to generate larger, predominantly face-parallel rockfalls. Variations in the distribution of rockfall shape with volume therefore imply a systemic shift in the underlying mechanisms of detachment with scale, questioning the validity of applying a single probabilistic model to the full range of rockfall volumes observed here.
- The scars of rockfalls are spatially associated through time. This complicates rockfall risk management using magnitude-frequency distributions, as they assume statistical independence between the observed events, irrespective of the volume range considered. However, the proportion of contiguous rockfalls observed here (10.5%) is not sufficiently high to reliably use a database of precursory rockfall activity, here measured at annual intervals, as a means of forecasting future change.

- Relating the properties of individual rockfalls to indicators of the quality of the rock mass on a regional scale is difficult. Neither the distribution of rockfall shape, nor the distribution of different metrics of jointing as a function of rockfall volume, are sufficiently different between inventories of contiguous and non-contiguous rockfalls to conclude that the contiguous rockfalls observed here propagate along joints, conditioning subsequent instability in adjoining areas over time.
- Spatial consistencies in the distribution of rockfall shape and volume through time follow the geological setting of the coastline, although variations in the strength of these patterns are likely to be driven by variations in local processes and morphological controls.

RQ3. Do spatial variations in cliff erosion reflect variations in wave loading conditions?

Chapter 5 presented a workflow for integrating and processing data from a number of sources, with the aim of quantifying local variations in the ground motion response to wave loading along a *ca.* 900 m stretch of cliffs, where other factors (lithology, structure, weather, groundwater regime) are held broadly constant, over one year. The findings were used to explore how wave loading characteristics vary along the coastline, whether these are related to varying morphological controls and coastal processes, and how these variations manifest themselves in relation to observed variations in rockfall activity (*R05*). Specifically, analysis of the resulting inventory of more than 1.8×10^7 impacts has shown that:

- Observations of locally wave-generated ground motions are tidally modulated, consistent with previous research.
- Spatial variations in the strength of the influence of total water level on ground motions are conditioned by morphological controls. The cliff response to wave impacting varies considerably alongshore, with variations in the magnitude, frequency, and directionality of impacting reflecting variations in platform length, slope, and the wave approach angle.
- Locally, longer-term variations in rockfall activity are broadly correlated with wave impact-driven ground motions, and the morphological conditions that drive them. These observations confirm the importance of the amount of wave energy available for erosional work, and reflect the processes outlined in many conceptual models of coastal processes, as well as observations made elsewhere.

RQ4. What is the relative importance of cliff structure and wave loading in determining rates of erosion, and is there an optimal scenario of conditions that lead to rockfalls and sustained cliff erosion?

The findings of this thesis were synthesised in *Chapter 6*, which evaluated the relationships between key metrics of erosion (derived in *Chapter 3*), structural controls (derived in *Chapter 4*), and morphological controls (as a proxy for wave loading, derived in *Chapter 5*). The analysis

presented takes into account spatial variations in these relationships, which are used to identify areas where patterns of erosion are dominated by either structural or morphological controls, or a mixture of both (*RO6*). The findings demonstrate that, along a macro-tidal, storm-dominated coastline:

- Rates of cliff erosion are strongly correlated with structural or morphological controls in approximately equal proportions along the coast (50% versus 55%), where morphological controls act as a proxy for the erosional effects of wave impacting.
- Specifically, regional-scale patterns of rockfall activity and the resulting cliff erosion are strongly conditioned by only structural controls along 19% of the coastline. In areas where high rates of erosion are strongly controlled by cliff structure, the cliff face is generally characterised by a combination of high joint densities, a steep gradient, and joints that lie sub-parallel to the topography, reflecting local observations made elsewhere.
- Regional-scale patterns of rockfall activity and the resulting cliff erosion are strongly conditioned by only morphological controls along 25% of the coastline. Where high rates of erosion are strongly controlled by coastal morphology, the coastline is generally characterised by a narrower and deeper foreshore platform, and a small wave approach angle.

7.2 Directions for future research

The methodological focus of this thesis was to develop novel workflows for undertaking regional-scale ($> 10^4$ m) assessments of rockfall activity at previously unprecedented resolutions (10^{-1} m), and to complement these observations with high-resolution field monitoring of both the intrinsic and extrinsic controls on rockfalls. The resulting inventory of rockfall activity and cliff erosion has demonstrated the importance of sea cliff retreat as an episodic process, where sudden, large ($> 1{,}000$ m^3) rockfall events punctuate periods of relative stability. The majority of models instead simulate future patterns of cliff retreat by time-averaging these processes, seemingly without any direct knowledge of what drives long-term rates of retreat: are they caused by the accumulation of several large events, or many smaller events? The challenges for developing future models of coastal retreat are therefore (1) to understand how long term rates of erosion emerge from the accumulation of individual, instantaneous events, and (2) to establish the minimum timescale of monitoring over which time-averaged retreat rates are representative of the longer-term cliff retreat signal. Along slowly eroding, hard rock cliffs such as those that were the focus of this study, this requires monitoring over 10^1 year timescales (rather than 10^0 year timescales, as here), which are commensurate with time-dependent failure processes operating alongshore.

In an idealised scenario, rock slope monitoring would be undertaken at relatively high frequencies ($< 10^0$ year) and over long timescales ($> 10^1$ year), in order to capture the full range of time-dependent failure processes that drive large-scale, profile-form change. For example,

observations of contiguous failure scars coalescing, and consequently destabilising the rock face above, are relatively common in previous research undertaken along the North Yorkshire coast. However, the coarse temporal resolution of monitoring undertaken here permitted the observation of only a small proportion of spatially contiguous rockfalls (10.5%), in comparison with a value of 1.7% that would be expected under conditions of complete spatial randomness. This attests to the importance of stress redistribution following previous rockfalls in promoting damage accumulation and, eventually, further rock slope failure, even on a regional scale. This tendency would likely increase with higher frequency monitoring, which has been shown elsewhere to disaggregate single scars observed over longer periods into multiple overlapping events. The method developed for assessing the 3D spatio-temporal contiguity of rockfalls in this research is advantageous over commonly-used approaches that rely on the analysis of point pattern processes, such as Ripley's K-function. Such approaches assume that the dimensions of a rockfall are negligible in relation to the surface from which they are released. With higher frequency monitoring, future research could therefore explore the propagation of failures through time (in 3D), rockfall scar geometries, and relationships with the quality of the rock mass.

A core motivation of this thesis has been to make a step-change in our understanding of the drivers of rockfalls, shifting the focus towards the regional scale. The findings of this research have demonstrated the importance of rock mass structure in conditioning spatial variations in both the shape and size of rockfalls, and the resulting erosion, at a regional scale. Here, variations in the geometric properties of exposed discontinuity surfaces have partly been treated as a proxy for the effect of lithology, in the absence of data recorded at a commensurate resolution. Previous local-scale observations of rockfall occurrence along the coast have stressed the importance of lithology in defining both rockfall shape and scar contiguity through time. With the increasing pervasiveness of low-cost platforms able to undertake high-resolution monitoring, a priority for research in this area should be in honing the ability to derive lithological models at scale. This could potentially involve UAV-acquired photography and Structure-from-Motion point cloud data to aid detailed mapping, or interpolating nearby borehole measurements and using the lithological boundaries from the resulting 3D geological model to subdivide point clouds into lithological classes.

Relationships between local scale (10^2 m) observations of cliff toe wave impacting and morphological controls (aspect, platform length, platform slope, and inundation duration) were stronger than those applied at regional scales ($> 10^4$ m). This difference could simply be driven by spatial variations in rock mass structure, or it could represent the effect of site-specific conditions, potentially introducing geomorphic feedbacks that complicate the analysis of driver-effect relationships. Given the known importance of nearshore and foreshore bathymetry in driving spatial variations in wave energy delivery to the cliffs, wave and water level conditions at the cliff toe should be monitored directly in the future. At a regional scale, a more appropriate means of

upscaling these observations would entail using nearshore wave models to model patterns of wave propagation and changes in wave properties due to refraction, diffraction, shoaling, and interactions with currents alongshore. This would allow for a stronger process-based understanding of the links between variations in morphological controls, wave impacting, and cliff erosion.

Along a stretch of cliffs where lithology and structure remain approximately uniform, the ground motion data collected here have demonstrated a clear correlation between the dynamic loading of coastal cliffs and observations of longer-term rockfall activity. Future research should aim to test whether there is a direct driver-effect relationship, or if the relationship observed here simply arises because cyclic loading acts as a proxy for other processes, such as variations in energy delivery. On coastal rock slopes, isolating the damage effects caused by each forcing variable is difficult due to the number of processes operating concurrently that are conducive to damage and subsequent fracture. Future research should therefore seek to test the role of variations in loading characteristics on damage accumulation in a laboratory setting, using stress magnitudes and frequencies of the same order of magnitude as those observed in the field, in order to establish their importance for the timing and distribution of rock slope susceptibility to failure.

This page is intentionally left blank

References

Abdalati, W. and Krabill, W.B. 1999. Calculation of ice velocities in the Jakobshavn Isbrae area using airborne laser altimetry. *Remote Sensing of Environment*, 67(2), pp. 194-204.

Abellán, A., Jaboyedoff, M., Oppikofer, T. and Vilaplana, J. 2009. Detection of millimetric deformation using a terrestrial laser scanner: Experiment and application to a rockfall event. *Natural Hazards and Earth System Sciences*, 9(2), pp. 365-372.

Abellán, A., Calvet, J., Vilaplana, J.M. and Blanchard, J. 2010. Detection and spatial prediction of rockfalls by means of terrestrial laser scanner monitoring. *Geomorphology*, 119(3-4), pp. 162-171.

Abellán, A., Oppikofer, T., Jaboyedoff, M., Rosser, N.J., Lim M. and Lato, M.J. 2014. Terrestrial laser scanning of rock slope instabilities. *Earth Surface Processes and Landforms,* 39(1), pp. 80-97.

Abellán, A., Vilaplana, J.M., Calvet, J., García-Sellés, D. and Asensio, E. 2011. Rockfall monitoring by Terrestrial Laser Scanning–case study of the basaltic rock face at Castellfollit de la Roca (Catalonia, Spain). *Natural Hazards and Earth System Sciences*, 11(3), pp. 829-841.

Adams, P.N., Anderson, R.S. and Revenaugh, J. 2002. Microseismic measurement of wave-energy delivery to a rocky coast. *Geology*, 30(10), pp. 895-898.

Adams, P.N., Storlazzi, C.D. and Anderson, R.S. 2005. Nearshore wave-induced cyclical flexing of sea cliffs. *Journal of Geophysical Research: Earth Surface*, 110(F2), 19 p.

Agar, R. 1960. Post-glacial erosion of the North Yorkshire Coast from the Tees Estuary to Ravenscar. *Proceedings of the Yorkshire Geological Society*, 32(4), pp. 409-428.

Alba, M., Fregonese, L., Prandi, F., Scaioni, M. and Valgoi, P. 2006. Structural monitoring of a large dam by terrestrial laser scanning. In Maas, H.-G. and Schneider, D. (Eds.) *Proceedings of the ISPRS Commission V Symposium: Image Engineering and Vision Metrology*, 6 p.

Allan, J.C., Hart, R. and Tranquili, J.V. 2006. The use of Passive Integrated Transponder (PIT) tags to trace cobble transport in a mixed sand-and-gravel beach on the high-energy Oregon coast, USA. *Marine Geology*, 232(1-2), pp. 63-86.

Allison, R.J. 1989. Rates and mechanisms of change in hard rock coastal cliffs. *Zeitschrift für Geomorphologie, Supplement Band*, 73, pp. 125-138.

ALLISON, R.J. AND KIMBER, O.G. 1998. Modelling failure mechanisms to explain rock slope change along the Isle of Purbeck coast, UK. *Earth Surface Processes and Landforms*, 23(8), pp. 731-750.

ALLSTADT, K. 2013. Extracting source characteristics and dynamics of the August 2010 Mount Meager landslide from broadband seismograms. *Journal of Geophysical Research: Earth Surface*, 118(3), pp. 1472-1490.

AMENTA, N., CHOI, S. AND KOLLURI, R.K. 2001. The Power Crust. In Anderson, D.C. and Lee, K. (Eds.) *Proceedings of the Sixth ACM Symposium on Solid Modelling and Applications,* pp. 249-266.

AMITRANO, D. 2006. Rupture by damage accumulation in rocks. *International Journal of Fracture*, 139(3-4), pp. 369-381.

AMITRANO, D., GRASSO, J. R. AND SENFAUTE, G. 2005. Seismic precursory patterns before a cliff collapse and critical point phenomena. *Geophysical Research Letters*, 32(8), 5 p.

AMUNDSON, J.M., TRUFFER, M., LÜTHI, M.P., FAHNESTOCK, M., WEST, M. AND MOTYKA, R.J. 2008. Glacier, fjord, and seismic response to recent large calving events, Jakobshavn Isbræ, Greenland. *Geophysical Research Letters*, 35(22), 5 p.

ANDRÉ, M.F. 1997. Holocene rockwall retreat in Svalbard: a triple-rate evolution. *Earth Surface Processes and Landforms*, 22(5), pp. 423-440.

ANSARI, M.K., AHMAD, M. AND SINGH, T.N. 2014. Rockfall risk assessment for pilgrims along the circumambulatory pathway, Saptashrungi Gad Temple, Vani, Nashik Maharashtra, India. *Geomatics, Natural Hazards and Risk*, 5(1), pp. 81-92.

ARSENAULT, A.M. AND MEIGS, A.J. 2005. Contribution of deep-seated bedrock landslides to erosion of a glaciated basin in southern Alaska. *Earth Surface Processes and Landforms*, 30(9), pp. 1111-1125.

ARYAL, A., BROOKS, B., REID, M., BAWDEN, G. AND PAWLAK, G. 2012. Displacement fields from point cloud data: Application of particle imaging velocimetry to landslide geodesy. *Journal of Geophysical Research: Earth Surface*, 117(F1), 15 p.

ASHTON, A.D., MURRAY, A.B. AND ARNOULT, O. 2001. Formation of coastline features by large-scale instabilities induced by high-angle waves. *Nature*, 414(6861), pp. 296-300.

ASHTON, A.D., WALKDEN, M.J.A. AND DICKSON, M.E. 2011. Equilibrium responses of cliffed coasts to changes in the rate of sea level rise. *Marine Geology*, 284(1-4), pp. 217-229.

ASSALI, P., GRUSSENMEYER, P., VILLEMIN, T., POLLET, N. AND VIGUIER, F. 2014. Surveying and modeling of rock discontinuities by terrestrial laser scanning and photogrammetry: Semi-automatic approaches for linear outcrop inspection. *Journal of Structural Geology*, 66, pp. 102-114.

ATTEWELL, P.B. AND FARMER, I.W. 1973. Fatigue behaviour of rock. *International Journal of Rock Mechanics and Mining Sciences & Geomechanics Abstracts*, 10(1), pp. 1-9

AVIAN, M. AND KELLERER-PIRKLBAUER, A. 2009. LiDAR for monitoring mass movements in permafrost environments at the cirque Hinteres Langtal, Austria, between 2000 and 2008. *Natural Hazards and Earth System Sciences*, 9(4), pp. 1087-1094.

AXELSSON, P. 2000. DEM generation from laser scanner data using adaptive TIN models. *International Archives of Photogrammetry and Remote Sensing*, 33(B4), pp. 111-118.

Ayoub, F., Leprince, S. and Avouac, J.P. 2009. Co-registration and correlation of aerial photographs for ground deformation measurements. *ISPRS Journal of Photogrammetry and Remote Sensing*, 64(6), pp. 551-560.

Baecher, G.B. and Lanney, N.A. 1978. Trace length biases in joint surveys. In *19thUS Symposium on Rock Mechanics (USRMS)*. American Rock Mechanics Association, 10 p.

Barlow, J., Lim, M., Rosser, N.J., Petley, D.N., Brain, M.J., Norman, E.C. and Geer, M. 2012. Modeling cliff erosion using negative power law scaling of rockfalls. *Geomorphology*, 139-140, pp. 416-424.

Barnhart, T.B., and Crosby, B.T. 2013. Comparing Two Methods of Surface Change Detection on an Evolving Thermokarst Using High-Temporal-Frequency Terrestrial Laser Scanning, Selawik River, Alaska. *Remote Sensing*, 5(6), pp. 2813-2837.

Barrett, P.J., 1980. The shape of rock particles, a critical review. *Sedimentology*, 27(3), pp. 291-303.

Bartrum, J.A. 1926. " Abnormal" Shore Platforms. *The Journal of Geology*, 34(8), pp. 793-806.

Battjes, J.A. and Stive, M.J.F. 1985. Calibration and verification of a dissipation model for random breaking waves. *Journal of Geophysical Research: Oceans*, 90(C5), pp. 9159-9167.

Bauer, A., Paar, G., and Kaltenböck, A. 2005. Mass movement monitoring using terrestrial laser scanner for rock fall management. In van Oosterom, P., Zlatanova, S. and Fendel, E.M. (Eds.) *Proceedings of the First International Symposium on Geo-Information for Disaster Management.* Delft, The Netherlands: Springer, pp. 393-406.

Beer, A., Turowski, J. and Kirchner, J. 2017. Spatial patterns of erosion in a bedrock gorge. *Journal of Geophysical Research: Earth Surface*, 122(1), pp. 191-214.

Belov, A.P., Davies, P. and Williams, A.T. 1999. Mathematical modeling of basal coastal cliff erosion in uniform strata: A theoretical approach. *The Journal of Geology*, 107(1), pp. 99-109.

Benjamin, J., Rosser, N.J. and Brain, M.J. 2016. Rockfall detection and volumetric characterisation using LiDAR. In Aversa, S., Cascini, L., Picarelli, L. and Scavia, C. (Eds.) *Landslides and Engineered Slopes. Experience, Theory and Practice: Proceedings of the 12th International Symposium on Landslides.* The Netherlands: CRC Press, pp. 389-395.

Benn, D.I. and Ballantyne, C.K. 1993. The description and representation of particle shape. *Earth Surface Processes and Landforms*, 18(7), pp. 665-672.

Bennett, G.L., Molnar, P., Eisenbeiss, H. and McArdell, B.W. 2012. Erosional power in the Swiss Alps: characterization of slope failure in the Illgraben. *Earth Surface Processes and Landforms*, 37(15), pp. 1627-1640.

Bennett, M.R., Hambrey, M.J. and Huddart, D. 1997. Modification of clast shape in high-Arctic glacial environments. *Journal of Sedimentary Research*, 67(3), pp. 550-559.

Berger, M., Tagliasacchi, A., Seversky, L., Alliez, P., Levine, J., Sharf, A. and Silva, C. 2014. State of the art in surface reconstruction from point clouds. In Lefebvre, S. and Spagnuolo, M. (Eds.) EUROGRAPHICS 2014 - State of the Art Reports, 1(1), pp. 161-185.

Bird, E.C.F. 2000. *Coastal Geomorphology.* Chichester: John Wiley & Sons, 322 p.

Blais-Stevens, A., Couture, R., Page, A., Koch, J., Clague, J.J. and Lipovsky, P. 2010. Landslide susceptibility, hazard and risk assessments along pipeline corridors in Canada. In *Proceedings of the 63rd Canadian Geotechnical Conference and 6th Canadian Permafrost Conference*, pp. 878-88.

Blais-Stevens, A., Behnia, P., Kremer, M., Page, A., Kung, R. and Bonham-Carter, G. 2012. Landslide susceptibility mapping of the Sea to Sky transportation corridor, British Columbia, Canada: comparison of two methods. *Bulletin of Engineering Geology and the Environment*, 71(3), pp. 447-466.

Blanco-Chao, R., Pérez-Alberti, A., Trenhaile, A.S., Costa-Casais, M. and Valcárcel-Díaz, M. 2007. Shore platform abrasion in a para-periglacial environment, Galicia, northwestern Spain. *Geomorphology*, 83, pp. 136–151.

Blasone, G., Cavalli, M., Marchi, L. and Cazorzi, F. 2014. Monitoring sediment source areas in a debris-flow catchment using terrestrial laser scanning. *Catena*, 123, pp. 23-36.

Blott, S.J. and Pye, K. 2008. Particle shape: a review and new methods of characterization and classification. *Sedimentology*, 55(1), pp. 31-63.

Borsa, A. and Minster, J. 2012. Rapid Determination of Near-Fault Earthquake Deformation Using Differential LiDAR. *Bulletin of the Seismological Society of America*, 102(4), pp. 1335-1347.

Brain, M.J., Rosser N.J., Norman, E.C., and Petley, D.N. 2014. Are microseismic ground displacements a significant geomorphic agent? *Geomorphology,* 207, pp. 161-173.

Bray, M.J. and Hooke, J.M. 1997. Prediction of soft-cliff retreat with accelerating sea-level rise. *Journal of Coastal Research*, pp. 453-467.

Brenguier, F., Campillo, M., Hadziioannou, C., Shapiro, N. M., Nadeau, R. M. and Larose, E. 2008. Postseismic relaxation along the San Andreas fault at Parkfield from continuous seismological observations. *Science*, 321(5895), pp. 1478-1481.

Brunetti, M.T., Guzzetti, F. and Rossi, M. 2009. Probability distributions of landslide volumes. *Nonlinear Processes in Geophysics* 16(2), pp. 179-188.

Budetta, P., Galietta, G. and Santo, A. 2000. A methodology for the study of the relation between coastal cliff erosion and the mechanical strength of soils and rock masses. *Engineering Geology*, 56(3-4), pp. 243-256.

Budetta, P. and Nappi, M. 2013. Comparison between qualitative rockfall risk rating systems for a road affected by high traffic intensity. *Natural Hazards and Earth System Sciences*, 13(6), pp. 1643-1653.

Budetta, P., De Luca, C. and Nappi, M. 2016. Quantitative rockfall risk assessment for an important road by means of the rockfall risk management (RO. MA.) method. *Bulletin of Engineering Geology and the Environment*, 75(4), pp. 1377-1397.

Bunce, C., Cruden, D. and Morgenstern, N. 1997. Assessment of the hazard from rock fall on a highway. *Canadian Geotechnical Journal*, 34(3), 344-356.

Burjánek, J., Moore, J.R., Yugsi Molina, F.X. and Fäh, D. 2012. Instrumental evidence of normal mode rock slope vibration. *Geophysical Journal International*, 188(2), pp. 559-569.

Burns, W.J., Coe, J.A., Kaya, B.S. and Ma, L. 2010. Analysis of Elevation Changes Detected from Multi-Temporal LiDAR Surveys in Forested Landslide Terrain in Western Oregon. *Environmental and Engineering Geoscience*, 16(4), pp. 315-341.

Byers, D.A., Hargiss, E. and Finley, J.B. 2015. Flake morphology, fluvial dynamics, and debitage transport potential. *Geoarchaeology*, 30(5), pp. 379-392.

Carr, A.P. and Graff, J. 1982. The tidal immersion factor and short platform development - discussion. *Transactions of the Institute of British Geographers*, 7, pp. 240-245.

Carrea, D., Abellán, A., Derron, M.-H., Gauvin, N., Jaboyedoff, M., Eberhardt, E., Froese, C., Turner, K. and Leroueil, S. 2012. Using 3D surface datasets to understand landslide evolution: From analogue models to real case study. In Eberhardt, E., Froese, C. and Turner, K. (Eds.) *Landslides and Engineered Slopes: Protecting Society Through Improved Understanding*. London: Taylor and Francis, pp. 575-579.

Carrea, D., Abellán, A., Derron, M.-H. and Jaboyedoff, M. 2015. Automatic rockfalls volume estimation based on terrestrial laser scanning data. In Lollino, G., Giordan, D., Crosta, G.B., Corominas, J., Azzam, R., Wasowski, J. and Sciarra, N. (Eds.) *Engineering Geology for Society and Territory – Volume 2: Landslide Processes,* Switzerland: Springer International Publishing, pp. 425-428.

Carter, C.H. and Guy, D.E. 1988. Coastal erosion: processes, timing and magnitudes at the bluff toe. *Marine Geology*, 84(1-2), pp. 1-17.

Castedo, R., Murphy, W., Lawrence, J. and Paredes, C. 2012. A new process–response coastal recession model of soft rock cliffs. *Geomorphology*, 177, pp. 128-143.

Chau, K.T., Wong, R., Liu, J. and Lee, C.F. 2003. Rockfall hazard analysis for Hong Kong based on rockfall inventory. *Rock Mechanics and Rock Engineering,* 36(5), pp. 383-408.

Chelli, A., Pappalardo, M., Llopis, I.A. and Federici, P.R. 2010. The relative influence of lithology and weathering in shaping shore platforms along the coastline of the Gulf of La Spezia (NW Italy) as revealed by rock strength. *Geomorphology*, 118, pp. 93–104.

Clarke, B.A. and Burbank, D.W. 2011. Quantifying bedrock-fracture patterns within the shallow subsurface: Implications for rock mass strength, bedrock landslides, and erodibility. *Journal of Geophysical Research: Earth Surface*, 116(F4).

Coe J.A. and Harp E.L. 2007. Influence of tectonic folding on rockfall susceptibility, American Fork Canyon, Utah, USA. *Natural Hazards and Earth System Sciences,* 7, pp. 1–14.

Collins, B.D. and Sitar, N. 2008. Processes of coastal bluff erosion in weakly lithified sands, Pacifica, California, USA. *Geomorphology*, 97(3-4), pp. 483-501.

Collins, B.D. and Stock, G.M. 2012. Lidar-based rock-fall hazard characterization of cliffs. In *GeoCongress 2012: State of the Art and Practice in Geotechnical Engineering,* pp. 3021-3030.

Collins, B.D., Corbett, S., Fairly, H., Minasian, D., Kayen, R., Dealy, T. and Bedford, D. 2012. Topographic Change Detection at Select Archaeological Sites in Grand Canyon National Park, Arizona, 2007–2010. *US Geologic Survey Scientific Investigation Report 2012-5133.* Reston, VA: US Geological Survey, 77 p.

Collins, B.D. and Stock, G.M. 2016. Rockfall triggering by cyclic thermal stressing of exfoliation fractures. *Nature Geoscience*, 9(5), pp. 395-400

Cook, K.L. 2017. An evaluation of the effectiveness of low-cost UAVs and structure from motion for geomorphic change detection. *Geomorphology*, 278, pp. 195-208.

Coombes, M.A., Feal-Pérez, A., Naylor, L.A. and Wilhelm, K. 2013. A non-destructive tool for detecting changes in the hardness of engineering materials: application of the Equotip durometer in the coastal zone. *Engineering Geology*, 167, pp. 14–19.

Cordes, S.E., Stock, G.M., Schwab, B.E. and Glazner, A.F. 2013. Supporting Evidence for a 9.6±1 ka Rock Fall Originating from Glacier Point in Yosemite Valley, California9. 6±1 ka Rock Fall, Glacier Point, Yosemite Valley, California. *Environmental and Engineering Geoscience*, 19(4), pp. 345-361.

Corsini, A., Borgatti, L., Cervi, F., Dahne, A., Ronchetti, F. and Sterzai, P. 2009. Estimating mass-wasting processes in active earth slides – earth flows with time-series of High-Resolution DEMs from photogrammetry and airborne LiDAR. *Natural Hazards and Earth System Science,* 9(2), pp. 433-439.

Costa, P.J., Gelfenbaum, G., Dawson, S., La Selle, S., Milne, F., Cascalho, J., Lira, C.P., Andrade, C., Freitas, M.C. and Jaffe, B. 2017. The application of microtextural and heavy mineral analysis to discriminate between storm and tsunami deposits. *Geological Society Special Publications*, 456, pp. 456-457.

Couture, R., Blais-Stevens, A., Page, A., Koch, J., Clague, J.J. and Lipovsky, P.S. 2010. Landslide susceptibility, hazard and risk assessment along pipelines in Canada. In *Proceedings of the 11th International Association for Engineering Geology and the Environment Congress*, pp. 1023-1031.

Crawford, W.C. and Webb, S.C. 2000. Identifying and removing tilt noise from low-frequency ($<$ 0.1 Hz) seafloor vertical seismic data. *Bulletin of the Seismological Society of America*, 90(4), pp. 952-963.

Cruden, D.M. and Hu, X.Q. 1994. Topples on underdip slopes in the Highwood-Pass, Alberta, Canada. *Quarterly Journal of Engineering Geology and Hydrogeology,* 27(1), pp. 57–68.

Davidson-Arnott, R. 2010. *Introduction to Coastal Processes and Geomorphology.* Cambridge: Cambridge University Press, 458 p.

Day, S.S., Gran, K.B., Belmont, P. and Wawrzyniec, T. 2013. Measuring bluff erosion part 1: terrestrial laser scanning methods for change detection. *Earth Surface Processes and Landforms,* 38(10), pp. 1055-1067.

de Ridder, S.A.L. and Biondi, B.L. 2013. Daily reservoir-scale subsurface monitoring using ambient seismic noise. *Geophysical Research Letters*, 40(12), pp. 2969-2974.

de Vilder, S.J., Rosser, N.J. and Brain, M.J. 2017. Forensic analysis of rockfall scars. *Geomorphology*, 295, pp. 202-214.

Del Gaudio S., Festa G. and Causse M. 2015. Strong motion numerical simulations using the empirical Green's function method: application to 2009 L'Aquila earthquake. *Geophysical Journal International,* 203(1), pp. 720–736.

Dewez, T.J.B., Rohmer, J., Regard, V. and Cnudde, C. 2013. Probabilistic coastal cliff collapse hazard from repeated terrestrial laser surveys: case study from Mesnil Val (Normandy, northern France). *Journal of Coastal Research: Special Issue 65 - International Coastal Symposium Volume,* 1, pp. 702-707.

Dewez, T.J.B., Girardeau-Montaut, D., Allanic, C. and Rohmer, J. 2016. Facets: A CloudCompare plugin to extract geological planes from unstructured 3D point clouds. *The International Archives of Photogrammetry, Remote Sensing and Spatial Information Science*, 41(B5), 6 p.

Dickson, M.E., Kennedy, D.M. and Woodroffe, C.D. 2004. The influence of rock resistance on coastal morphology around Lord Howe Island, southwest Pacific. *Earth Surface Processes and Landforms,* 29(5), pp. 629–643.

Dickson, M.E., Walkden, M.J. and Hall, J.W. 2007. Systemic impacts of climate change on an eroding coastal region over the twenty-first century. *Climatic change*, 84(2), pp. 141-166.

Dickson, M.E. and Pentney, R. 2012. Micro-seismic measurements of cliff motion under wave impact and implications for the development of near-horizontal shore platforms. *Geomorphology*, 151, pp. 27-38.

Dietze, M., Turowski, J.M., Cook, K.L. and Hovius, N. 2017. Spatiotemporal patterns, triggers and anatomies of seismically detected rockfalls. *Earth Surface Dynamics*, 5(4), pp. 757-779.

Dong, P. and Guzzetti, F. 2005. Frequency-size statistics of coastal soft-cliff erosion. *Journal of Waterway, Port, Coastal, and Ocean Engineering*, 131(1), pp. 37-42.

Dornbusch, U., Robinson, D.A., Moses, C.A. and Williams, R.B. 2008. Temporal and spatial variations of chalk cliff retreat in East Sussex, 1873 to 2001. *Marine Geology*, 249(3-4), pp. 271-282.

Douglas G.R., Whalley W.B. and McGreevy J.P. 1991. Rock properties as controls on free-face debris fall activity. *Permafrost and Periglacial Processes*, 2(4), pp. 311–319.

Drake, A.R. and Phipps, P.J. 2007. Cliff recession and behavior studies, Hunstanton, UK. *Maritime Engineering*, 160(1), pp. 3-17.

Dunham, L., Wartman, J., Olsen, M.J., O'Banion, M. and Cunningham, K. 2017. Rockfall Activity Index (RAI): A lidar-derived, morphology-based method for hazard assessment. *Engineering Geology*, 221, pp. 184-192.

Duperret, A., Taibi, S., Mortimore, R.N. and Daigneault, M. 2005. Effect of groundwater and sea weathering cycles on the strength of chalk rock from unstable coastal cliffs of NW France. *Engineering Geology*, 78(3-4), pp. 321-343.

Dussauge-Peisser, C., Helmstetter, A., Grasso, J.-R., Hantz, D., Desvarreux, P., Jeannin, M. and Giraud, A. 2002. Probabilistic approach to rock fall hazard assessment: potential of historical data analysis. *Natural Hazards and Earth System Sciences*, 2, pp. 15-26.

Earlie, C.S., Masselink, G., Russell, P. and Shail, R. 2013. Sensitivity analysis of the methodology for quantifying cliff erosion using airborne LiDAR – examples from Cornwall, UK. *Journal of Coastal Research: Special Issue 65 - International Coastal Symposium Volume*, 1, pp. 470-475.

Earlie, C.S., Young, A.P., Masselink, G. and Russell, P.E. 2015. Coastal cliff ground motions and response to extreme storm waves. *Geophysical Research Letters*, 42(3), pp. 847-854.

Edwards, A.B. 1951. Wave action in shore platform formation. *Geological Magazine*, 88(1), pp. 41-49.

Ekström, G. and Stark, C.P. 2013. Simple scaling of catastrophic landslide dynamics. *Science*, 339(6126), pp. 1416-1419.

Ester, M., Kriegel, H.-P., Sander, J. and Xu, X. 1996. A Density-Based Algorithm for Discovering Clusters in Large Spatial Databases with Noise. *KDD*, 96(34), pp. 226-231.

Evans, S.G. and Hungr, O. 1993. The assessment of rockfall hazard at the base of talus slopes. *Canadian Geotechnical Journal*, 30(4), pp. 620-636.

Fan, L., Lehmann, P. and Or, D. 2015. Effects of hydromechanical loading history and antecedent soil mechanical damage on shallow landslide triggering. *Journal of Geophysical Research: Earth Surface*, 120(10), pp. 1990-2015.

Farrell E.J., Granja H., Cappietti L., Ellis J.T., Li B. and Sherman D.J. 2009. Wave transformation across a Rock Platform, Belinho, Portugal. *Journal of Coastal Research*, I56, pp. 44–48.

Feng, T., Liu, X., Scaioni, M. and Lin, X. 2012. Real-time landslide monitoring using close-range stereo image sequences analysis. In *International Conference on Systems and Informatics (ICSAI)*, pp. 249-253.

FENG, Q., SJÖGREN, P., STEPHANSSON, O. AND JING, L. 2001. Measuring fracture orientation at exposed rock faces by using a non-reflector total station. *Engineering Geology*, 59(1-2), pp. 133-146.

FERRERO, A.M., FORLANI, G., RONCELLA, R. AND VOYAT, H.I. 2009. Advanced geostructural survey methods applied to rock mass characterization. *Rock Mechanics and Rock Engineering*, 42(4), pp. 631-665.

FINNEGAN, N.J., SCHUMER, R. AND FINNEGAN, S. 2014. A signature of transience in bedrock river incision rates over timescales of 10^4 – 10^7 years. *Nature*, 505(7483), pp. 391-394.

FITYUS, S.G., GIACOMINI, A. AND BUZZI, O. 2013. The significance of geology for the morphology of potentially unstable rocks. *Engineering Geology*, 162, pp. 43-52.

FOWLER, H.J., KILSBY, C.G. AND O'CONNELL, P.E. 2000. A stochastic rainfall model for the assessment of regional water resource systems under changed climatic condition. *Hydrology and Earth System Sciences*, 4(2), pp. 263-281.

FOWLER, H.J., KILSBY, C.G., O'CONNELL, P.E. AND BURTON, A. 2005. A weather-type conditioned multi-site stochastic rainfall model for the generation of scenarios of climatic variability and change. *Journal of Hydrology*, 308(1-4), pp. 50-66.

GANTI, V., VON HAGKE, C., SCHERLER, D., LAMB, M.P., FISCHER, W.W. AND AVOUAC, J.P. 2016. Time scale bias in erosion rates of glaciated landscapes. *Science Advances*, 2(10), 11 p.

GARDNER, J.S. 1970. Rockfall: a geomorphic process in high mountain terrain. *Albertan Geographer*, 6, pp. 15-20.

GARDNER, J.S. 1980. Frequency, magnitude and spatial distribution of mountain rockfalls and rockslides in the Highwood Pass area, Alberta, Canada. In Coates, D.R. and Vitek, J.D. (Eds.) *Thresholds in Geomorphology.* New York: Allen and Unwin, pp. 267-295.

GAUDIO, V. AND WASOWSKI, J. 2011. Advances and problems in understanding the seismic response of potentially unstable slopes. *Engineering Geology*, 122(1-2), pp. 73-83.

GE, H. AND KANG, L. 2014. Ductile crack initiation and propagation in steel bridge piers subjected to random cyclic loading. *Engineering Structures,* 59, pp. 809-820.

GHUFFAR, S., SZÉKELY, B., RONCAT, A. AND PFEIFER, N. 2013. Landslide Displacement Monitoring Using 3D Range Flow on Airborne and Terrestrial LiDAR Data. *Remote Sensing*, 5(6), pp. 2720-2745.

GIGLI, G. AND CASAGLI, N. 2011. Semi-automatic extraction of rock mass structural data from high resolution LIDAR point clouds. *International Journal of Rock Mechanics and Mining Sciences*, 48(2), pp. 187-198.

GIRARDEAU-MONTAUT, D., ROUX, M., MARC, R. AND THIBAULT, G. 2005. Change detection on point cloud data acquired with a ground laser scanner. In Vosselman, G. and Brenner, C. (Eds.) *Proceedings of the ISPRS Workshop on Laser Scanning.* Enschede: ITC, pp. 30-35.

GISCHIG, V., PREISIG, G. AND EBERHARDT, E. 2016. Numerical investigation of seismically induced rock mass fatigue as a mechanism contributing to the progressive failure of deep-seated landslides. *Rock Mechanics and Rock Engineering*, 49(6), pp. 2457-2478.

GOLDSTEIN, M.L., MORRIS, S.A. AND YEN, G.G. 2004. Problems with fitting to the power-law distribution. *European Physical Journal B*, 41(2) pp. 255-258.

Graham, D.J. and Midgley N.G. 2000. Graphical representation of particle shape using triangular diagrams: An Excel spreadsheet method. *Earth Surface Processes and Landforms*, 25(13), pp. 1473-1477.

Gruen, A. and Akca, D. 2005. Least squares 3D surface and curve matching. *ISPRS Journal of Photogrammetry and Remote Sensing,* 59(3), pp. 151-174.

Guerin, A., D'Amato, J., Hantz, D., Rossetti, J.P. and Jaboyedoff, M. 2014. Investigating rockfall frequency using terrestrial laser scanner (Grenoble area, France). In Humair F., Matasci, B. Jaboyedoff, M., Abellán, A. Carrea, D., Derron, M.-H. and Wyser, M. (Eds.) *Vertical Geology, from remote sensing to 3D geological modelling. Proceedings of the first Vertical Geology Conference,* 4 p.

Gunzburger, Y., Merrien-Soukatchoff, V. and Guglielmi, Y. 2005. Influence of daily surface temperature fluctuations on rock slope stability: case study of the Rochers de Valabres slope (France). *International Journal of Rock Mechanics and Mining Sciences*, 42(3), pp. 331-349.

Gutenberg, B. 1958. Microseisms. In Landsberg, H.E. and Van Mieghem, J. (Eds.) *Advances in Geophysics*, 5(3-4), New York: Academic Press Inc., pp. 53-92.

Guthrie, R.H. and Evans, S.G. 2007. Work, persistence, and formative events: The geomorphic impact of landslides. *Geomorphology,* 88(3-4), pp. 266-275.

Guzzetti, F., Reichenbach, P. and Wieczorek, G.F. 2003. Rockfall hazard and risk assessment in the Yosemite Valley, California, USA. *Natural Hazards and Earth System Sciences,* 3(6), pp. 491-503.

Guzzetti, F., Reichenbach, P. and Ghigi, S. 2004. Rockfall hazard and risk assessment along a transportation corridor in the Nera Valley, central Italy. *Environmental Management*, 34(2), pp. 191-208.

Hall, J.W. Meadowcroft, I.C., Lee, E.M. and Van Gelder, P.H.A.J.M. 2002. Stochastic simulation of episodic soft cliff recession. *Coastal Engineering*, 46(3), pp. 159-174.

Hampton, M.A. 2002. Gravitational failure of sea cliffs in weakly lithified sediment. *Environmental and Engineering Geoscience*, 8(3), pp. 175-191.

Haneberg, W.C. 2007. Directional roughness profiles from three-dimensional photogrammetric or laser scanner point clouds. In Eberhardt, E., Stead, D. and Morrison, T. (Eds.) *Rock Mechanics: Meeting Society's Challenges and Demands.* London: Taylor & Francis, pp. 101–106.

Hemingway, J.E. 1974. Jurassic. In Raynor, D.H. and Hemingway, J.E. (Eds.) *The Geology and Mineral Resources of Yorkshire.* Leeds: Yorkshire Geological Society, pp. 161-233.

Hibert, C., Ekström, G. and Stark, C.P. 2014. Dynamics of the Bingham Canyon Mine landslides from seismic signal analysis. *Geophysical Research Letters*, 41(13), pp. 4535-4541.

Higgitt, D.L. and Allison, R.J. 1999. Clast exposure on boulder-covered desert slopes. *Earth Surface Processes and Landforms*, 24(2), pp. 111-125.

Hovius, N. and Stark, C.P. 2006. Landslide-driven erosion and topographic evolution of active mountain belts. In Evans, S.G., Mugnozza, G.S., Strom, A. and Hermanns, R.L. (Eds.) *Landslides from massive rock slope failure.* Dordrecht: Springer, pp. 575-590.

Howarth, M.K. 1955. Domerian of the Yorkshire coast. *Proceedings of the Yorkshire Geological Society*, 30(2), pp. 147-175.

Hsu, L., Finnegan, N.J. and Brodsky, E.E. 2011. A seismic signature of river bedload transport during storm events. *Geophysical Research Letters*, 38(13), 6 p.

Huang, Q. and Angelier, J. 1989. Fracture spacing and its relation to bed thickness. *Geological Magazine*, 126(4), pp. 355-362

Hungr, O., Evans, S.G. and Hazzard, J. 1999. Magnitude and frequency of rock falls and rock slides along the main transportation corridors of southwestern British Columbia. *Canadian Geotechnical Journal*, 36(2), pp. 224-238.

Illenberger, W.K. 1991. Pebble shape (and size!). *Journal of Sedimentary Research*, 61(5), pp. 756-767.

IPCC 2013. Climate Change 2013: The Physical Science Basis. In Stocker, T.F., Qin, D., Plattner, G.-K., Tignor, M., Allen, S.K., Boschung, J., Nauels, A., Xia, Y., Bex, V. and Midgley, P.M. (Eds.) *Contribution of Working Group I to the Fifth Assessment Report of the Intergovernmental Panel on Climate Change*. Cambridge: Cambridge University Press, 1535 p.

Jaboyedoff, M. 2011. *Slope tectonics.* London: Geological Society of London, 285 p.

Jaboyedoff, M., Metzger, R., Oppikofer, T., Couture, R., Derron, M.-H., Locat, J. and Turmel, D. 2007. New insight techniques to analyze rock-slope relief using DEM and 3D imaging cloud points: Coltop-3D software.In Eberhardt, E., Stead, D. and Morrison, T. (Eds.) *Rock Mechanics: Meeting Society's Challenges and Demands*. London: Taylor & Francis, pp. 61–68.

Jaboyedoff, M., Oppikofer, T., Abellán, A., Derron, M.-H., Loye, A., Metzger, R. and Pedrazzini, A. 2012. Use of LIDAR in landslide investigations: a review. *Natural Hazards*, 61(1), pp. 5-28.

Johnson. D.W. 1919. *Shore processes and shoreline development*. New York: Hafner, 584 p.

Kasperski, J., Delacourt, C., Allemand, P., Potherat, P., Jaud, M. and Varrel, E. 2010. Application of a Terrestrial Laser Scanner (TLS) to the Study of the Séchilienne Landslide (Isère, France). *Remote Sensing*, 2(12), pp. 2785-2802.

Katz, O., Reichenbach, P. and Guzzetti, F. 2011. Rock fall hazard along the railway corridor to Jerusalem, Israel, in the Soreq and Refaim valleys. *Natural Hazards*, 56(3), pp. 649-665.

Katz, O. and Mushkin, A. 2013. Characteristics of sea-cliff erosion induced by a strong winter storm in the eastern Mediterranean. *Quaternary Research*, *80*(1), pp. 20-32.

Kemeny, J. 2003. The time-dependent reduction of sliding cohesion due to rock bridges along discontinuities: a fracture mechanics approach. *Rock Mechanics and Rock Engineering*, 36(1), pp. 27-38.

Kennedy, D.M., Coombes, M.A. and Mottershead, D.N. 2017. The temporal and spatial scales of rocky coast geomorphology: a commentary. *Earth Surface Processes and Landforms*, 42(10), pp. 1597-1600.

Kidner, D.B., Thomas, M.C, Leigh, C., Robert, O.J. and Morgan, C.G. 2004. Coastal monitoring with LiDAR: challenges, problems, and pitfalls. *Proceedings of SPIE,* 5574, pp. 80-89.

Kissi, J. 2016. Automatic fracture orientation extraction from SfM point clouds. M.Sc. thesis. The University of Western Ontario, Canada, 118 p.

Kline, S.W., Adams, P.N. and Limber, P.W. 2014. The unsteady nature of sea cliff retreat due to mechanical abrasion, failure and comminution feedbacks. *Geomorphology*, 219, pp. 53-67.

KOMAR, P.D. 1998. *Beach Processes and Sedimentation.* 2nd edition. New Jersey: Prentice Hall, 544 p.

KORUP, O., GÖRÜM, T. AND HAYAKAWA, Y. 2012. Without power? Landslide inventories in the face of climate change. *Earth Surface Processes and Landforms*, 37(1), pp. 92-99.

KOONS, P.O., UPTON, P. AND BARKER, A.D. 2012. The influence of mechanical properties on the link between tectonic and topographic evolution. *Geomorphology*, 137(1), pp. 168-180.

KRAUTBLATTER, M. 2003. *The impact of rainfall intensity and other external factors on primary and secondary rockfall (Reintal, Bavarian Alps)*, Ph.D. thesis. University of Erlangen-Nuremberg, Germany.

KRAUTBLATTER, M. AND DIKAU, R. 2007. Towards a uniform concept for the comparison and extrapolation of rockwall retreat and rockfall supply. *Geografiska Annaler: Series A, Physical Geography*, 89(1), pp. 21-40.

KRAUTBLATTER, M., MOSER, M., SCHROTT, L., WOLF, J. AND MORCHE, D. 2012. Significance of rockfall magnitude and carbonate dissolution for rock slope erosion and geomorphic work on Alpine limestone cliffs (Reintal, German Alps). *Geomorphology*, 167, pp. 21-34.

KROMER, R., LATO, M., HUTCHINSON, D.J., GAUTHIER, D. AND EDWARDS, T. 2017. Managing rockfall risk through baseline monitoring of precursors using a terrestrial laser scanner. *Canadian Geotechnical Journal*, 54(7), pp. 953-967.

KUHN, D. AND PRÜFER, S. 2014. Coastal cliff monitoring and analysis of mass wasting processes with the application of terrestrial laser scanning: A case study of Rügen, Germany, *Geomorphology,* 213, pp. 153-165.

LA POINTE. P.R. AND HUDSON, J.A. 1985. Characterization and interpretation of rock mass joint patterns. *Geological Society of America*, 199, pp. 1- 37

LAGUE, D., BRODU, N. AND LEROUX, J. 2013. Accurate 3D comparison of complex topography with terrestrial laser scanner: Application to the Rangitikei canyon (NZ). *ISPRS Journal of Photogrammetry and Remote Sensing,* 82, pp. 1026-1054.

LAMBERT, S. AND NICOT, F. 2011. *Rockfall engineering.* London: John Wiley & Sons, 435 p.

LATO, M.J., HUTCHINSON, D.J., BALL, D. AND HARRAP, R. 2009a. Engineering monitoring of rockfall hazards along transportation corridors: using mobile terrestrial LiDAR. *Natural Hazards and Earth System Sciences*, 9(3), pp. 935-946.

LATO, M.J, DIEDERICHS, M.S., HUTCHINSON, D.J. AND HARRAP, R. 2009b. Optimization of LiDAR scanning and processing for automated structural evaluation of discontinuities in rock masses. *International Journal of Rock Mechanics and Mining Sciences*, 46(1), pp. 194-199.

LATO, M.J., DIEDERICHS, M.S. AND HUTCHINSON, D.J. 2010. Bias correction for view-limited Lidar scanning of rock outcrops for structural characterization. *Rock Mechanics and Rock Engineering*, 43(5), pp. 615-628.

LAWRENCE, J.A., MORTIMORE, R.N., STONE, K.J. AND BUSBY, J.P. 2013. Sea saltwater weakening of chalk and the impact on cliff instability. *Geomorphology*, 191, pp. 14-22.

LEE, E.M. 2008. Coastal cliff behaviour: Observations on the relationship between beach levels and recession rates. Geomorphology, 101(4), pp. 558-571.

LEE, E.M., HALL, J.W. AND MEADOWCROFT, I.C. 2001. Coastal cliff recession: the use of probabilistic prediction methods. *Geomorphology*, 40(3-4), pp. 253-269.

Lee, E.M. and Clark, A.R. 2002. *Investigation and Management of Soft Rock Cliffs*. London: Thomas Telford Publishing, 382 p.

Lee, S.K. and Park, H.D. 2014. Comparison of observation and laboratory slaking tests in the assessment of coastal erosion in Cheju Island, Korea. *Geosystem Engineering*, 17(2), pp. 136-141.

Leyland, J., Hackney, C.R., Darby, S.E., Parsons, D.R., Best, J.L., Nicholas, A.P., Aalto, R. and Lague, D. 2017. Extreme flood-driven fluvial bank erosion and sediment loads: direct process measurements using integrated Mobile Laser Scanning (MLS) and hydro-acoustic techniques. *Earth Surface Processes and Landforms*, 42(2), pp. 334-346.

Lim, M. 2006. *Coastal cliff evolution with reference to Staithes, North Yorkshire*. Ph.D. thesis. Durham University, UK, 378 p.

Lim, M. 2014. The rock coast of the British Isles: cliffs. *Memoirs of the Geological Society of London*, 40(1), pp. 19-38.

Lim, M., Petley, D.N., Rosser, N.J., Allison, R.J., Long, A.J. and Pybus, D. 2005. Combined Digital Photogrammetry and Time-of-Flight Laser Scanning for Monitoring Cliff Evolution. *The Photogrammetric Record,* 20(110), pp. 109-129.

Lim, M., Rosser, N.J., Allison, R.J. and Petley, D.N. 2010. Erosional processes in the hard rock coastal cliffs at Staithes, North Yorkshire. *Geomorphology,* 114(1-2), pp. 12-21.

Lim, M., Rosser, N.J., Petley, D.N. and Keene, M. 2011. Quantifying the Controls and Influence of Tide and Wave Impacts on Coastal Rock Cliff Erosion. *Journal of Coastal Research*, 27(1), pp. 46-56.

Lim, S.P. and Haron, H. 2014. Surface reconstruction techniques: a review. *Artificial Intelligence Review*, 42(1), pp. 59-78.

Loye, A., Pedrazzini, A., Theule, J.I., Jaboyedoff, M., Liébault, F., Metzger, R. 2012. Influence of bedrock structures on the spatial pattern of erosional landforms in small alpine catchments. *Earth Surface Processes and Landforms,* 37(13), pp. 1407–1423.

Lukas, S., Benn, D.I., Boston, C.M., Brook, M., Coray, S., Evans, D.J., Graf, A., Kellerer-Pirklbauer, A., Kirkbride, M.P., Krabbendam, M. and Lovell, H. 2013. Clast shape analysis and clast transport paths in glacial environments: A critical review of methods and the role of lithology. *Earth-Science Reviews*, 121, pp. 96-116.

Luo, Y., Del Gaudio, V., Huang, R., Wang, Y. and Wasowski J. 2014. Evidence of hillslope directional amplification from accelerometer recordings at Qiaozhuang (Sichuan - China). *Engineering Geology*, 183, pp. 193-207.

Malamud, B.D., Turcotte, D.L., Guzzetti, F. and Reichenbach P. 2004. Landslide inventories and their statistical properties. *Earth Surface Processes and Landforms*, 29(6), pp. 687-711.

Marques, F.M.S.F. 2008. Magnitude-frequency of sea cliff instabilities. *Natural Hazards and Earth System Sciences*, 8, pp. 1161-1171.

Marques, F.M.S.F., Matildes, R. and Redweik, P. 2013. Sea cliff instability susceptibility at regional scale: a statistically based assessment in the southern Algarve, Portugal. *Natural Hazards and Earth System Sciences*, 13(12), pp. 3185-3203.

Marshall R.J.E. and Stephenson, W.J. 2011. The morphodynamics of shore platforms in a micro-tidal setting: Interactions between waves and morphology. *Marine Geology,* 288(1–4), pp. 18–31.

Martel, S.J. 2006. Effect of topographic curvature on near-surface stresses and application to sheeting joints. *Geophysical Research Letters*, 33(1), 5 p.

Matasci, B., Stock, G.M., Jaboyedoff, M., Carrea, D., Collins, B.D., Guérin, A., Matasci, G. and Ravanel, L. 2017. Assessing rockfall susceptibility in steep and overhanging slopes using three-dimensional analysis of failure mechanisms. *Landslides*, doi: 10.1007/s10346-017-0911-y.

Matsumoto, H., Dickson, M.E. and Masselink, G. 2017. Systematic analysis of rocky shore platform morphology at large spatial scale using LiDAR-derived digital elevation models. *Geomorphology*, 286, pp. 45-57.

Matsuoka, N. 1990. The rate of bedrock weathering by frost action: field measurements and a predictive model. *Earth Surface Processes and Landforms*, 15(1), pp. 73-90.

Matsuoka, N. and Sakai, H. 1999. Rockfall activity from an alpine cliff during thawing periods. *Geomorphology*, 28(3), pp. 309-328.

McCoy, S.W., Kean, J.W., Coe, J.A., Staley, D.M., Wasklewicz, T.A. and Tucker, G.E. 2010. Evolution of a natural debris flow: In situ measurements of flow dynamics, video imagery, and terrestrial laser scanning. *Geology*, 38(8), pp. 735-738.

Messenzehl, K. and Dikau, R. 2017. Structural and thermal controls of rockfall frequency and magnitude within rockwall–talus systems (Swiss Alps). *Earth Surface Processes and Landforms*, 42(13), pp. 1963-1981.

Messenzehl, K., Meyer, H., Otto, J.C., Hoffmann, T. and Dikau, R. 2017. Regional-scale controls on the spatial activity of rockfalls (Turtmann valley, Swiss Alps)—a multivariate modeling approach. *Geomorphology*, 287, pp. 29-45.

Metternicht, G., Hurni, L. and Gogu, R. 2005. Remote sensing of landslides: An analysis of the potential contribution to geo-spatial systems for hazard assessment in mountainous environments. *Remote Sensing of Environment*, 98(2-3), pp. 284-303.

Michoud, C., Derron, M.-H., Horton, P., Jaboyedoff, M., Baillifard, F.-J., Loye, A., Nicolet, P., Pedrazzini, A. and Queyrel, A. 2012. Rockfall hazard and risk assessments along roads at a regional scale: example in Swiss Alps. *Natural Hazards and Earth System Sciences*, 12(3), pp. 615-629.

Midgley, N.G. and Tonkin, T.N. 2017. Reconstruction of former glacier surface topography from archive oblique aerial images. *Geomorphology*, 282, pp. 18-26.

Mitchell, T.M. and Faulkner, D.R. 2008. Experimental measurements of permeability evolution during triaxial compression of initially intact crystalline rocks and implications for fluid flow in fault zones. *Journal of Geophysical Research*, 113(B11), doi: 10.1029/2008JB005588.

Monserrat, O. and Crosetto, M. 2008. Deformation measurement using terrestrial laser scanning data and least squares 3D surface matching. *ISPRS Journal of Photogrammetry and Remote Sensing*, 63(1), pp. 142-154.

Moore, J.R., Sanders, J.W., Dietrich, W.E. and Glaser, S.D. 2009. Influence of rock mass strength on the erosion rate of alpine cliffs. *Earth Surface Processes and Landforms*, 34(10), pp. 1339-1352.

Moore, J.R., Gischig, V., Burjanek, J., Loew, S. and Fah, D. 2011. Site Effects in Unstable Rock Slopes: Dynamic Behavior of the Randa Instability (Switzerland). *Bulletin of the Seismological Society of America,* 101(6), pp. 3110-3116.

Moore, L.J. and Griggs, G.B. 2002. Long-term cliff retreat and erosion hotspots along the central shores of the Monterey Bay National Marine Sanctuary. *Marine Geology*, 181(1-3), pp. 265-283.

Moos, C., Dorren, L. and Stoffel, M. 2017. Quantifying the effect of forests on frequency and intensity of rockfalls. *Natural Hazards and Earth System Sciences*, 17(2), pp. 291-304.

Nakamura, M., Shiraishi, H. and Sasaki, Y. 1966. Wave decaying due to breaking. In *Proceedings of the 10th International Conference on Coastal Engineering*, New York: American Society of Civil Engineers, pp. 234-253.

Narr, W. and Suppe, J. 1991. Joint spacing in sedimentary rocks. *Journal of Structural Geology*, 13(9), pp. 1037-1048.

Nicholls, R.J., Wong, P.P., Burkett, V., Codignotto, J., Hay, J., McLean, R., Ragoonaden, S., Woodroffe, C.D., Abuodha, P.A.O., Arblaster, J. and Brown, B. 2007. *Coastal systems and low-lying areas.* Faculty of Science Papers – Archive, University of Wollongong.

Nienhuis, J.H., Ashton, A.D., Roos, P.C., Hulscher, S.J. and Giosan, L. 2013. Wave reworking of abandoned deltas. *Geophysical Research Letters*, 40(22), pp. 5899-5903.

Norman, E.C. 2012. *Microseismic monitoring of the controls on coastal rock cliff erosion.* Ph.D. thesis. Durham University, UK, 278 p.

Norman, E.C., Rosser, N.J., Brain, M.J., Petley, D.N. and Lim, M. 2013. Coastal cliff-top ground motions as proxies for environmental processes. *Journal of Geophysical Research: Oceans,* 118(12), pp. 6807-6823.

Ogawa H., Dickson M.E. and Kench P.S. 2011. Wave transformation on a sub-horizontal shore platform, Tatapouri, North Island, New Zealand. *Continental Shelf Research*, 31(14), pp. 1409–1419.

Ogawa H., Kench P.S. and Dickson M.E. 2012. Field measurements of wave characteristics on a near-horizontal shore platform, Mahia Peninsula, North Island, New Zealand. *Geographical Research,* 50(2), pp. 179–192.

Ogawa, H., Dickson, M.E. and Kench, P.S. 2016. Generalised observations of wave characteristics on near-horizontal shore platforms: Synthesis of six case studies from the North Island, New Zealand. *New Zealand Geographer*, 72(2), pp. 107-121.

Olariu, M.I., Ferguson, J.F., Aiken, C.L. and Xu, X. 2008. Outcrop fracture characterization using terrestrial laser scanners: deep-water Jackfork sandstone at Big Rock Quarry, Arkansas. *Geosphere*, 4(1), pp. 247–259.

Olsen, M.J., Kuester, F., Chang, B.J. and Hutchinson, T.C. 2010. Terrestrial laser scanning-based structural damage assessment. *Journal of Computing in Civil Engineering*, 24(3), pp. 264-272.

Olsen, M.J., Wartman, J., McAlister, M., Mahmoudabadi, H., O'Banion, M.S., Dunham, L. and Cunningham, K. 2015. To Fill or Not to Fill: Sensitivity Analysis of the Influence of Resolution and Hole Filling on Point Cloud Surface Modeling and Individual Rockfall Event Detection. *Remote Sensing*, 7(9), pp. 12103-12134.

Oppikofer, T., Jaboyedoff, M. and Keusen, H.-R. 2008. Collapse at the eastern Eiger flank in the Swiss Alps. *Nature Geoscience*, 1(8), pp. 531–535.

Oppikofer, T., Jaboyedoff, M., Blikra, L., Derron, M.-H. and Metzger, R. 2009. Characterization and monitoring of the Åknes rockslide using terrestrial laser scanning. *Natural Hazards and Earth System Sciences*, 9(3), pp. 1003-1019.

Oppikofer, T., Jaboyedoff, M., Pedrazzini, A., Derron, M.-H. and Blikra, L.H. 2011. Detailed DEM analysis of a rockslide scar to characterize the basal sliding surface of active rockslides. *Journal of Geophysical Research: Earth Surface*, 116(F2), 22 p.

Ortega, O.J., Marrett, R.A. and Laubach, S.E. 2006. A scale-independent approach to fracture intensity and average spacing measurement. *American Association of Petroleum Geologists Bulletin*, 90(2), pp. 193-208.

Parker, R., Petley, D., Densmore, A., Rosser, N.J., Damby, D. and Brain, M. 2013. Progressive failure cycles and distributions of earthquake-triggered landslides. In Ugai, K., Yagi, H. and Wakai, A. (Eds.) *Earthquake-induced landslides: Proceedings of the International Symposium on Earthquake induced landslides*. Berlin: Springer, pp. 755-762.

Parker, R.N., Hancox, G.T., Petley, D.N., Massey, C.I., Densmore, A.L. and Rosser, N.J. 2015. Spatial distributions of earthquake-induced landslides and hillslope preconditioning in the northwest South Island, New Zealand. *Earth Surface Dynamics*, 3(4), pp. 501-525.

Patwary, M.M.A., Palsetia, D., Agrawal, A., Liao, W., Manne, F. and Choudhary, A. 2012. A New Scalable Parallel DBSCAN Algorithm Using the Disjoint Set Data Structure. In Hollingsworth, J.K. (Ed.) *Proceedings of the International Conference on High Performance Computing, Networking, Storage and Analysis (Supercomputing, SC'12)*. Los Alimatos: IEEE Computer Society Press, pp. 1-11.

Pawlowicz, R., Beardsley, B. and Lentz, S. 2002. Classical tidal harmonic analysis including error estimates in MATLAB using T_TIDE. Computers and Geosciences, 28(8), pp. 929-937.

Phillips, J.D. 2006. Deterministic chaos and historical geomorphology: a review and look forward. *Geomorphology*, 76(1-2), pp. 109-121.

Pierre, G. and Lahousse, P. 2006. The role of groundwater in cliff instability: an example at Cape Blanc-Nez (Pas-de-Calais, France). *Earth Surface Processes and Landforms*, 31(1), pp. 31-45.

Poppeliers, C. and Mallinson, D. 2015. High-frequency seismic noise generated from breaking shallow water ocean waves and the link to time-variable sea states. *Geophysical Research Letters*, 42(20), pp. 8563-8569.

Porter, N.J., Trenhaile, A.S., Prestanski, K.J. and Kanyaya, J.I. 2010. Shore platform downwearing in eastern Canada: Micro-tidal Gaspé, Québec. *Geomorphology*, 116(1-2), pp. 77-86.

Powell, J.H. 2010. Jurassic sedimentation in the Cleveland Basin: a review. *Proceedings of the Yorkshire Geological Society*, 58(1), pp. 21-72.

Powell, M. D., Murillo, S., Dodge, P., Uhlhorn, E., Gamache, J., Cardone, V., Cox, A., Otero, S., Carrasco, N., Annane, A. and St Fleur, R. 2010. Reconstruction of Hurricane Katrina's wind fields for storm surge and wave hindcasting. *Ocean Engineering*, 37(1), pp. 26-36.

Preparata, F.P. and Shamos, M.I. 2012. *Computational geometry: an introduction*. New York: Springer Science & Business Media, 399 p.

Priest, S.D. 1993. *Discontinuity analysis for rock engineering*. London: Chapman & Hall, 473 p.

Priest, S.D. and Hudson, J.A. 1976. Discontinuity spacings in rock. *International Journal of Rock Mechanics and Mining Sciences & Gemechanics Abstracts*, 13(5), pp. 135-148

PRIEST, S.D. AND HUDSON, J.A. 1981. Estimation of discontinuity spacing and trace length using scanline surveys. *International Journal of Rock Mechanics and Mining Sciences & Gemechanics Abstracts*, 18(3), pp. 183-197

RABATEL, A., DELINE, P., JAILLET, S. AND RAVANEL, L. 2008. Rock falls in high-alpine rock walls quantified by terrestrial lidar measurements: A case study in the Mont Blanc area. *Geophysical Research Letters*, 35(L10502), 5 p.

RAWSON, P.F. AND WRIGHT, J.K. 2000. *The Yorkshire Coast*. The Yorkshire Coast Geologists' Association Guide No. 34. London: Geologists' Association, 130 p.

REVELL, D.L., BATTALIO, R., SPEAR, B., RUGGIERO, P. AND VANDEVER, J. 2011. A methodology for predicting future coastal hazards due to sea-level rise on the California Coast. *Climatic Change*, 109(1), pp. 251-276.

RIEGL 2014. *RIEGL VQ-450 - High Speed 2D Laser Scanner with Online Waveform Processing*. Available at: http://products.rieglusa.com/Asset/10_DataSheet_VQ-450_rund_2014-09-02.pdf (Accessed: 16 February 2017).

RIQUELME, A.J., ABELLÁN, A., TOMÁS, R. AND JABOYEDOFF, M. 2014. A new approach for semi-automatic rock mass joints recognition from 3D point clouds. *Computers and Geosciences*, 68, pp. 38-52.

RIQUELME, A.J., ABELLÁN, A. AND TOMÁS, R. 2015. Discontinuity spacing analysis in rock masses using 3D point clouds. *Engineering Geology*, 195, pp. 185-195.

ROBINSON, L.A. 1974. *Towards a process response model of cliff retreat - the case of North East Yorkshire*. Ph.D. thesis. University of Leeds, UK, 535 p.

RODGERS, P.W. 1968. The response of the horizontal pendulum seismometer to Rayleigh and Love waves, tilt, and free oscillations of the Earth. *Bulletin of the Seismological Society of America*, 58(5), pp. 1385-1406.

ROHMER, J. AND DEWEZ, T. 2013. On the deviation of extreme sea-cliff instabilities from the power-law frequency-volume distribution: practical implications for coastal management. *Journal of Coastal Research: Special Issue 65 - International Coastal Symposium Volume*, 2, pp. 1698-1703.

ROHMER, J. AND DEWEZ, T. 2015. Analysing the spatial patterns of erosion scars using point process theory at the coastal chalk cliff of Mesnil-Val, Normandy, northern France. *Natural Hazards and Earth System Sciences*, 15(2), pp. 349-362.

ROSSER, N.J., PETLEY, D.N., LIM, M., DUNNING, S.A. AND ALLISON, R.J. 2005a. Terrestrial laser scanning for monitoring the process of hard rock coastal cliff erosion. *Quarterly Journal of Engineering Geology and Hydrogeology,* 38(4), pp. 363-375.

ROSSER, N.J., DUNNING, S.A., LIM, M. AND PETLEY, D.N. 2005b. Terrestrial laser scanning for quantitative rockfall hazard assessment. In Hungr, O., Fell, R., Couture, R. and Eberhardt, E. (Eds.) *Landslide Risk Management*. Vancouver, Canada, 31 May – 3 June. London: Taylor & Francis, pp. 359-368.

ROSSER, N.J., LIM, M., PETLEY, D.N., DUNNING, S.A AND ALLISON, R.J. 2007. Patterns of precursory rockfall prior to slope failure. *Journal of Geophysical Research: Earth Surface,* 112(F4), 14 p.

ROSSER, N.J., BRAIN, M.J., PETLEY, D.N., LIM, M. AND NORMAN, E.C. 2013. Coastline retreat via progressive failure of rocky coastal cliffs. *Geology,* 41(8), pp. 939-942.

Roth, D.L., Finnegan, N.J., Brodsky, E.E., Cook, K.L., Stark, C.P. and Wang, H.W. 2014. Migration of a coarse fluvial sediment pulse detected by hysteresis in bedload generated seismic waves. *Earth and Planetary Science Letters*, 404, pp. 144-153.

Roth, D.L., Brodsky, E.E., Finnegan, N.J., Rickenmann, D., Turowski, J.M. and Badoux, A. 2016. Bed load sediment transport inferred from seismic signals near a river. *Journal of Geophysical Research: Earth Surface*, 121(4), pp. 725-747.

Rouleau, A. and Gale, J.E. 1985. Statistical characterization of the fracture system in the Stripa Granite, Sweden. *International Journal of Rock Mechanics and Mining Sciences & Gemechanics Abstracts,* 22(6), pp. 353-367.

Royán, M.J., Abellán, A., Jaboyedoff M., Vilaplana J.M. and Calvet J. 2013. Spatio-temporal analysis of rockfall pre-failure deformation using Terrestrial LiDAR. *Landslides,* 11(4), pp. 697-709.

Royán, M.J., Abellán, A. and Vilaplana, J.M. 2015. Progressive failure leading to the 3 December 2013 rockfall at Puigcercós scarp (Catalonia, Spain). *Landslides*, 12(3), pp. 585-595.

Samia, J., Temme, A., Bregt, A., Wallinga, J., Guzzetti, F., Ardizzone, F. and Rossi, M. 2017a. Do landslides follow landslides? Insights in path dependency from a multi-temporal landslide inventory. *Landslides*, 14(2), pp. 547-558.

Samia, J., Temme, A., Bregt, A., Wallinga, J., Guzzetti, F., Ardizzone, F. and Rossi, M. 2017b. Characterization and quantification of path dependency in landslide susceptibility. *Geomorphology*, 292, pp. 16-24.

Sanche, D. 2016. *PowerCrust - MATLAB® GitHub Repository.* Available at: https://github.com/sanche21/Power-Crust-MATLAB (Accessed: 15 November 2014).

Sander, J., Ester, M., Kriegel, H.P. and Xu, X. 1998. Density-based clustering in spatial databases: The algorithm gdbscan and its applications. *Data Mining and Knowledge Discovery*, 2(2), pp. 169-194.

Santana, D., Corominas, J., Mavrouli, O. and Garcia-Sellés, D. 2012. Magnitude–frequency relation for rockfall scars using a Terrestrial Laser Scanner. *Engineering Geology,* 145-146, pp. 50-64.

Sass, O. 2005. Spatial patterns of rockfall intensity in the northern Alps. *Zeitschrift für Geomorphologie. Neue Folge,* 138, pp. 51–65.

Scheidl, C., Rickenmann, D. and Chiari, M. 2008. The use of airborne LiDAR data for the analysis of debris flow events in Switzerland. *Natural Hazards and Earth System Sciences*, 8(5), pp. 1113-1127.

Schürch, P., Densmore, A.L., Rosser, N.J., Lim, M. and McArdell, B.W. 2011. Detection of surface change in complex topography using terrestrial laser scanning: application to the Illgraben debris-flow channel. *Earth Surface Processes and Landforms*, 36(14), pp. 1847-1859.

Schwalbe, E., Maas, H.-G. and Dietrich, R. 2008. Glacier velocity determination from multi temporal terrestrial long range laser scanner point clouds. *The International Archives of the Photogrammetry, Remote Sensing and Spatial Information Sciences*, 37, pp. 457-462.

Schwartz, M.L. 2005. *Encyclopedia of Coastal Science*. The Netherlands: Springer, 1213 p.

Selby, M.J. 1980. A rock mass strength classification for geomorphic purposes: with tests from Antarctica and New Zealand. *Zeitschrift für Geomorphologie. Neue Folge*, 24, pp. 31–51.

Selby, M.J. 1982. *Hillslope Materials and Processes.* Oxford: Oxford University Press, 451 p.

Semechko, A. 2014. *Using Divergence Theorem to Compute Exact Rigid-Body Parameters of Objects Represented by Triangular Surface Meshes,* 9 p. Available at: https://uk.mathworks.com/matlabcentral/fileexchange/48913-compute-exact-rigid-body-parameters-of-objects-represented-by-triangular-surface-meshes (Accessed: 23 January 2015).

Sen Z. and Kazi A. 1984. Discontinuity spacing and RQD estimates from finite length scanlines. *International Journal of Rock Mechanics and Mining Sciences & Gemechanics Abstracts*, 21(4), pp. 203–212.

Senfaute, G., Duperret, A. and Lawrence, J.A. 2009. Micro-seismic precursory cracks prior to rock-fall on coastal chalk cliffs: a case study at Mesnil-Val, Normandie, NW France. *Natural Hazards and Earth System Sciences*, 9(5), pp. 1625-1641.

Sherman, D.J. and Gares, P.A. 2002. The geomorphology of coastal environments. *Geomorphology*, 48, pp. 1–6.

Šilhán, K. and Pánek, T. 2010. Fossil and recent debris flows in medium–high mountains (Moravskoslezské Beskydy Mts, Czech Republic). *Geomorphology*, 124(3), pp. 238-249.

Simms, M.J., Chidlaw, N., Morton, N. and Page, K.N. 2004. British Lower Jurassic stratigraphy: an introduction. *Geological Conservation Review Series*, 30, pp. 1-50.

Sithole, G. and Vosselman, G. 2004. Experimental comparison of filter algorithms for bare-Earth extraction from airborne laser scanning point clouds. *ISPRS Journal of Photogrammetry and Remote Sensing*, 59(1), pp. 85-101.

Skorupa, M. 1999. Load interaction effects during fatigue crack growth under variable amplitude loading - a literature review. Part II: qualitative interpretation. *Fatigue & Fracture of Engineering Materials and Structures,* 22(10), pp. 905-926.

Slob, S. 2010. *Automated Rock Mass Characterisation Using 3-D Terrestrial Laser Scanning.* Ph.D. thesis. Delft University of Technology, The Netherlands, 301 p.

Slob, S., van Knapen, B., Hack, R., Turner, K. and Kemeny, J. 2005. Method for automated discontinuity analysis of rock slopes with three-dimensional laser scanning. *Transportation Research Record: Journal of the Transportation Research Board*, 1913, pp. 187–194

Smets, B., d'Oreye, N., Kervyn, M. and Kervyn, F. 2016. Gas piston activity of the Nyiragongo lava lake: First insights from a Stereographic Time-Lapse Camera system. *Journal of African Earth Sciences*, 134, pp. 874-887.

Sneed, E.D. and Folk, R.L. 1958. Pebbles in the lower Colorado River, Texas, a study in particle morphogenesis. *The Journal of Geology*, 66(2), pp. 114-150.

Stead, D. and Wolter, A. 2015. A critical review of rock slope failure mechanisms: The importance of structural geology. *Journal of Structural Geology,* 74, pp. 1-23.

Stephenson W.J. and Thornton L.E. 2005. Australian rock coasts: Review and prospects. *Australian Geographer,* 36(1), pp. 95–115.

Stephenson, W.J. and Kirk, R.M. 2000. Development of shore platforms on Kaikoura Peninsula, South Island, New Zealand: Part one: the role of waves. *Geomorphology*, 32(1-2), pp. 21-41.

Stock, G.M., Luco, N., Collins, B.D., Harp, E.L., Reichenbach, P. and Frankel, K.L. 2012a. Quantitative rock-fall hazard and risk assessment for Yosemite Valley, Yosemite National Park, California. *National Park Service Report*, 92 p.

Stock, G.M., Martel, S.J., Collins, B.D. and Harp, E.L. 2012b. Progressive failure of sheeted rock slopes: The 2009–2010 Rhombus Wall rock falls in Yosemite Valley, California, USA. *Earth Surface Processes and Landforms*, 37(5), pp. 546-561.

Stock, G.M., Bawden, G.W., Green, J.K., Hanson, E., Downing, G., Collins, B.D., Bond, S. and Leslar, M. 2013. High-resolution three-dimensional imaging and analysis of rock falls in Yosemite Valley, California. *Geosphere*, 7(2), pp. 573-581.

Strunden, J., Ehlers, T. A., Brehm, D. and Nettesheim, M. 2015. Spatial and temporal variations in rockfall determined from TLS measurements in a deglaciated valley, Switzerland. *Journal of Geophysical Research: Earth Surface*, 120(7), pp. 1251-1273.

Stumpf, A., Malet, J.P., Allemand, P., Pierrot-Deseilligny, M. and Skupinski, G. 2015. Ground-based multi-view photogrammetry for the monitoring of landslide deformation and erosion. *Geomorphology,* 231, pp. 130-145.

Sturzenegger, M., Yan, M., Stead, D. and Elmo, D. 2007. Application and limitations of ground-based laser scanning in rock slope characterization. In Eberhardt, E., Stead, D. and Morrison, T. (Eds.) *Rock Mechanics: Meeting Society's Challenges and Demands. Proceedings of the 1st Canada-US Rock Mechanics Symposium.* 27-31 May. London: CRC Press, pp. 29-36.

Sturzenegger, M. and Stead, D. 2009. Quantifying discontinuity orientation and persistence on high mountain rock slopes and large landslides using terrestrial remote sensing techniques. *Natural Hazards and Earth System Sciences*, 9(2), pp. 267-287.

Sturzenegger, M., Stead, D. and Elmo, D. 2011. Terrestrial remote sensing-based estimation of mean trace length, trace intensity and block size/shape. *Engineering Geology*, 119(3-4), pp. 96-111.

Styles, T.D., Coggan, J.S. and Pine, R.J. 2011. Back analysis of the Joss Bay chalk cliff failure using numerical modelling. *Engineering Geology*, 120(1), pp. 81-90.

Sunamura, T. 1975. Laboratory study of wave-cut platform formation. *The Journal of Geology*, 83(3), pp. 389-397.

Sunamura, T. 1977. Relationship between wave-induced cliff erosion and erosive force of waves. *The Journal of Geology*, 85(5), pp. 613-618.

Sunamura, T. 1978a. A model of the development of continental shelves having erosional origin. *Geological Society of America Bulletin*, 89(4), pp. 504-510.

Sunamura, T. 1978b. Mechanisms of shore platform formation on the southeastern coast of the Izu Peninsula, Japan. *The Journal of Geology*, 86(2), pp. 211-222.

Sunamura, T, 1988. Projection of future coastal cliff resession under sea level rise induced by the green house effect: Nii-jima Island, Japan. *Trans Japanese Geomorphological Union*, 9, pp. 17-33.

Sunamura, T. 1992. *Geomorphology of Rocky Coasts.* New York: John Wiley & Sons, 302 p.

Svendsen, I.A., Madsen, P.Å. and Hansen, J.B. 1978. Wave characteristics in the surf zone. In *Proceedings of the 16th International Conference on Coastal Engineering*, New York: American Society of Civil Engineers, pp. 520-539.

Teixeira, S.B. 2006. Slope mass movements on rocky sea-cliffs: a powerlaw distributed natural hazard on the Barlavento Coast Algarve, Portugal. *Continental Shelf Research*, 26(9), pp. 1077-1091.

TEMME, A.J., KEILER, M., KARSSENBERG, D. AND LANG, A. 2015. Complexity and non-linearity in earth surface processes–concepts, methods and applications. *Earth Surface Processes and Landforms*, 40(9), pp. 1270-1274.

TERZAGHI, R.D. 1965. Sources of error in joint surveys. *Geotechnique*, 15(3), pp. 287-304.

THORNTON E.B. AND GUZA R.T. 1982. Energy saturationand phase speeds measured on the natural beach. *Journal of Geophysical Research,* 87(C12), pp. 9499-9508.

TRAVELLETTI, J., OPPIKOFER, T. AND DELACOURT, C. 2008. Monitoring landslide displacements during a controlled rain experiment using a long-range terrestrial laser scanning (TLS). *The International Archives of the Photogrammetry, Remote Sensing and Spatial Information Sciences*, 37(B5), pp. 485-490.

TRAVELLETTI, J., MALET, J.-P. AND DELACOURT, C. 2014. Image-based correlation of Laser Scanning point cloud time series for landslide monitoring. *International Journal of Applied Earth Observation and Geoinformation*, 32, pp. 1-18.

TRENHAILE, A.S. 1987. *Geomorphology of Rock Coasts.* Oxford: Oxford University Press, 384 p.

TRENHAILE, A.S. 2000. Modeling the development of wave-cut shore platforms. *Marine Geology*, 166(1-4), pp. 163-178.

TRENHAILE, A.S. 2002. Rock coasts, with particular emphasis on shore platforms. *Geomorphology*, 48(1-3), pp. 7-22.

TRENHAILE, A.S. 2009. Modeling the erosion of cohesive clay coasts. *Coastal Engineering*, 56(1), pp. 59-72.

TRENHAILE, A.S. 2010. Modeling cohesive clay coast evolution and response to climate change. *Marine Geology*, 277(1-4), pp. 11-20.

TRENHAILE, A.S. 2011. Predicting the response of hard and soft rock coasts to changes in sea level and wave height. *Climatic Change*, 109(3), pp. 599-615.

TRENHAILE, A.S. 2014. Climate change and the impact on rocky coasts. *Rock Coast Geomorphology: A Global Synthesis*, 40, pp. 7-17.

TRENHAILE, A.S. AND LAYZELL, M.G.J. 1981. Shore platform morphology and the tidal duration factor. *Transactions of the Institute of British Geographers*, 6, pp. 82-102.

TRENHAILE, A.S. AND KANYAYA, J.I. 2007. The role of wave erosion on sloping and horizontal shore platforms in macro-and mesotidal environments. *Journal of Coastal Research*, 23(2), pp. 298-309.

TSUJIMOTO, H. 1987. Dynamic conditions for shore platform initiation. *Science Report, Institute of Geoscience, University of Tsukuba, Sec. A*, 8, pp. 45-93.

UMILI, G., FERRERO, A. AND EINSTEIN, H. 2013. A new method for automatic discontinuity traces sampling on rock mass 3D model. *Computers and Geosciences,* 51, pp. 182–192.

VALVO, L.M., MURRAY, A.B. AND ASHTON, A. 2006. How does underlying geology affect coastline change? An initial modeling investigation. *Journal of Geophysical Research: Earth Surface*, 111(F2).

VAN VEEN, M., HUTCHINSON, D.J., KROMER, R., LATO, M. AND EDWARDS, T. 2017. Effects of sampling interval on the frequency-magnitude relationship of rockfalls detected from terrestrial laser scanning using semi-automated methods. *Landslides*, 14(5), pp. 1-14.

Vann Jones, E.C., Rosser, N.J., Brain M.J. and Petley, D.N. 2015. Quantifying the environmental controls on erosion of a hard rock cliff. *Marine Geology,* 363, pp. 230-242.

Vehling, L., Rohn, J. and Moser, M. 2016. Quantification of rock fall processes in a proglacial high mountain site, Gepatsch glacier (Tyrol, Austria). *Zeitschrift für Geomorphologie, Supplementary Issues*, 60(1), pp. 93-108.

Viero, A., Teza, G., Massironi, M., Jaboyedoff, M. and Galgaro, A. 2010. Laser scanning-based recognition of rotational movements on a deep seated gravitational instability: The Cinque Torri case (North-Eastern Italian Alps). *Geomorphology*, 122(1), pp. 191-204.

Viles, H.A. 2013. Linking weathering and rock slope instability: non-linear perspectives. *Earth Surface Processes and Landforms*, 38(1), pp. 62-70.

Villaescusa, E. and Brown, E. T. 1990. Characterizing joint spatial correlation using geostatistical methods. In Barton, N. and Stephansson, O. (Eds.) *Rock Joints*. Rotterdam: Balkema, pp. 115-122.

Vöge, M., Lato, M.J. and Diederichs, M.S. 2013. Automated rockmass discontinuity mapping from 3-dimensional surface data. *Engineering Geology*, 164, 155-162.

Vousdoukas, M.I., Voukouvalas, E., Annunziato, A., Giardino, A. and Feyen, L. 2016. Projections of extreme storm surge levels along Europe. *Climate Dynamics*, 47(9-10), pp. 3171-3190.

Vosselman, G., Kessels, P. and Gorte, B. 2005. The utilisation of airborne laser scanning for mapping. *International Journal of Applied Earth Observation and Geoinformation*, 6(3-4), pp. 177-186.

Walkden, M.J.A. and Hall, J.W. 2005. A predictive Mesoscale model of the erosion and profile development of soft rock shores. *Coastal Engineering*, 52(6), pp. 535-563.

Walkden, M.J.A and Dickson, M.E 2008. Equilibrium erosion of soft rock shores with a shallow or absent beach under increased sea level rise. *Marine Geology*, 251(1-2), pp. 75-84.

Walkden, M.J.A. and Hall, J.W. 2011. A Mesoscale predictive model of the evolution and management of a soft-rock coast. *Journal of Coastal Research*, 27(3), pp. 529-543.

Wang, X., Frattini, P., Crosta, G.B., Zhang, L., Agliardi, F., Lari, S. and Yang, Z. 2014. Uncertainty assessment in quantitative rockfall risk assessment. *Landslides*, 11(4), pp. 711-722.

Warrick, J.A., Ritchie, A.C., Adelman, G., Adelman, K. and Limber, P.W. 2017. New Techniques to Measure Cliff Change from Historical Oblique Aerial Photographs and Structure-from-Motion Photogrammetry. *Journal of Coastal Research*, 33(1), pp. 39-55.

Westoby, M.J., Dunning, S.A., Hein, A.S., Marrero, S.M. and Sugden, D.E. 2016. Interannual surface evolution of an Antarctic blue-ice moraine using multi-temporal DEMs. *Earth Surface Dynamics*, 4(2), pp. 515-529.

Whadcoat, S.K. 2017. *Numerical modelling of rockfall evolution in hard rock slopes.* Ph.D. thesis. Durham University, UK.

Wieczorek, G.F., Morrissey, M.M., Iovine, G. and Godt, J. 1998. Rockfall hazards in the Yosemite Valley. *US Geol. Survey Open-File Report*, 98(467), 14 p.

Wieczorek, G.F., Stock, G.M., Reichenbach, P., Snyder, J.B., Borchers, J.W. and Godt, J.W. 2008. Investigation and hazard assessment of the 2003 and 2007 Staircase Falls rock falls, Yosemite National Park, California, USA. *Natural Hazards and Earth System Sciences*, 8(3), pp. 421-432.

WILLIAMS, B.M., LU, C.C. AND QIN, W. 2004. Coastal bluff erosion – numerical model using Monte Carlo simulation technique and Sunamura's equation. *Shore and Beach*, 72(3), pp. 3-9.

WILLIAMS, J.G. 2017. *Insights into Rockfall from Constant 4D Monitoring.* Ph.D. thesis. Durham University, UK.

WILLIAMS, J.G., ROSSER, N.J., HARDY, R.J., BRAIN, M.J. AND AFANA, A.A. 2018. Optimising 4D Approaches to Surface Change Detection: Improving Understanding of Rockfall Magnitude-Frequency. *Earth Surface Dynamics*, 6, pp. 101-119.

WOLTERS, G. AND MÜLLER, G. 2008. Effect of Cliff Shape on Internal Stresses and Rock Slope Stability. *Journal of Coastal Research*, 24(1), pp. 43-50.

WOOLF, D.K., CHALLENOR, P.G. AND COTTON, P.D. 2002. Variability and predictability of the North Atlantic wave climate. *Journal of Geophysical Research*, 107(C10), 14 p.

WOTH, K., WEISSE, R. AND VON STORCH, H. 2006. Climate change and North Sea storm surge extremes: an ensemble study of storm surge extremes expected in a changed climate projected by four different regional climate models. *Ocean Dynamics*, 56(1), pp. 3-15.

WYLLIE, D.C. AND MAH, C. 2004. Rock slope engineering. 4th edition. New York: Spon Press, 456 p.

XHARDÉ, R., LONG, B.F. AND FORBES, D.L. 2006. Accuracy and Limitations of Airborne LiDAR Surveys in Coastal Environments. In *Proceedings of the International Geoscience and Remote Sensing Symposium*, pp. 2412-2415.

YOUNG, A.P. 2015. Recent deep-seated coastal landsliding at San Onofre State Beach, California. *Geomorphology,* 228, pp. 200-212.

YOUNG, A.P. 2018. Decadal-scale coastal cliff retreat in southern and central California. *Geomorphology*, 300, pp. 164-175.

YOUNG, A.P. AND ASHFORD, S.A. 2008. Instability investigation of cantilevered sea cliffs. *Earth Surface Processes and Landforms*, 33(11), pp. 1661–1677.

YOUNG, A.P., GUZA, R.T., FLICK, R.E., O'REILLY, W.C. AND GUTIERREZ, R. 2009. Rain, waves, and short-term evolution of composite seacliffs in southern California. *Marine Geology*, 267(1-2), pp. 1-7.

YOUNG, A.P., ADAMS, P.N., O'REILLY, W.C., FLICK, R.E. AND GUZA, R.T. 2011. Coastal cliff ground motions from local ocean swell and infragravity waves in southern California. *Journal of Geophysical Research: Oceans*, 116(C9), 11 p.

YOUNG, A.P., GUZA, R.T., ADAMS, P.N., O'REILLY, W.C. AND FLICK, R.E. 2012. Cross-shore decay of cliff top ground motions driven by local ocean swell and infragravity waves. *Journal of Geophysical Research: Oceans*, 117(C6), 12 p.

YOUNG, A.P., GUZA, R.T., DICKSON, M.E., O'REILLY, W.C. AND FLICK, R.E. 2013. Ground motions on rocky, cliffed, and sandy shorelines generated by ocean waves. *Journal of Geophysical Research: Oceans*, 118(12), pp. 6590-6602.

YOUNG, A.P., GUZA, R.T., O'REILLY, W.C., BURVINGT, O. AND FLICK, R.E. 2016. Observations of coastal cliff base waves, sand levels, and cliff top shaking. *Earth Surface Processes and Landforms*, 41(11), pp. 1564-1573.

YOUNG, A.P., GUZA, R.T., O'REILLY, W.C., FLICK, R.E. AND GUTIERREZ, R. 2011. Short-term retreat statistics of a slowly eroding coastal cliff. *Natural Hazards and Earth System Sciences*, 11(1), pp. 205-217.

Yuan, X., Kind, R. and Pedersen, H.A. 2005. Seismic monitoring of the Indian Ocean tsunami. *Geophysical Research Letters*, 32(15), 4 p.

Zhang, L. and Einstein, H.H. 2000. Estimating the intensity of rock discontinuities. *International Journal of Rock Mechanics and Mining Sciences*, 37(5), pp. 819-837.

Zhang, X. and Sanderson, D.J. 2001. Evaluation of instability in fractured rock masses using numerical analysis methods: Effects of fracture geometry and loading direction. *Journal of Geophysical Research: Solid Earth*, 106(B11), pp. 26671-26687.

Zimmer, V.L., Collins, B.D., Stock, G.M. and Sitar, N. 2012. Rock fall dynamics and deposition: an integrated analysis of the 2009 Ahwiyah Point rock fall, Yosemite National Park, USA. *Earth Surface Processes and Landforms*, 37(6), pp. 680-691.

This page is intentionally left blank

Appendices

Appendix A

Benjamin, J., Rosser, N.J. and Brain, M.J. 2016. Rockfall detection and volumetric characterisation using LiDAR. In Aversa, S., Cascini, L., Picarelli, L. & Scavia, C. (Eds.) *Landslides and Engineered Slopes. Experience, Theory and Practice: Proceedings of the 12th International Symposium on Landslides.* The Netherlands: CRC Press, pp. 389-395.

Landslides and Engineered Slopes. Experience, Theory and Practice – Aversa et al. (Eds)

Rockfall detection and volumetric characterisation using LiDAR

J. Benjamin, N.J. Rosser & M.J. Brain
Department of Geography, Durham University, UK

ABSTRACT: The most commonly used methods for detecting and characterising regional-scale changes in cliff morphology involve differencing high resolution Digital Elevation Models. An inherent assumption of this 2D method is that the cliff can be reduced to a planar surface, which becomes invalid where cliffs change aspect. In this paper we examine the relative benefits of 2D and 3D methods of change detection, the latter of which draw on raw point cloud data, for deriving inventories of change. In our analysis we test both methods of change detection on two high resolution point clouds derived from Terrestrial Laser Scanning of the coastal cliffs at Staithes, North Yorkshire (UK). The analysis highlights the importance of the chosen method for accurately constraining the size distributions of rockslope failures, as well as the geometry of the failures themselves. We conclude by considering the implications of 3D techniques for defining rockfall geometry and inferring different processes of change.

1. INTRODUCTION

The most significant advances in our ability to detect rock slope deformation and to quantify change across a range of spatial and temporal scales have come from the application of terrestrial, airborne and spaceborne remote sensing techniques (Metternicht *et al.*, 2005). Among these, the use of Terrestrial Laser Scanning (TLS) technology has become increasingly widespread due to its ability to rapidly acquire dense 3D point clouds that can be used to derive 3D slope geometry on steep to vertical rock faces (Royán *et al.*, 2013). Sequential TLS can be used to efficiently monitor rockfall activity, providing a more accurate representation of the distribution of types and rates of cliff erosion and failure than measurements of cliff top recession (Lee & Clark, 2002; Rosser *et al.*, 2013).

The ability to precisely quantify and therefore understand rockfall behaviour is critical for a number of reasons, including (1) that rockfalls are an important factor in defining rates of rock wall retreat in cliff and high-mountain geosystems (Moore *et al.*, 2009), (2) that rockfall shapes, volumes, source area locations and cliff surface geometry are known to influence rockfall trajectories (Leine *et al.*, 2014), (3) for successfully modelling the present and future dynamics of failing rock slopes, and (4) that the reliability and efficiency of rockfall hazard protection measures depends on the outcome of these modelling practices (Crosta *et al.*, 2015). However, quantifying rockfall activity has proven problematic, with a range of approaches currently used to measure the retreat, area or volume of changes in rock-slopes (Abellán *et al.*, 2014).

In this paper we examine the relative benefits of 2D and 3D methods of change detection for quantifying rockfall volume. The paper begins by introducing both methods of change detection before discussing the influence of the chosen method on rockfall volume estimates, which is demonstrated using data obtained from an inventory of rockfalls recorded at Staithes, North Yorkshire (UK). We conclude by considering the implications of 3D techniques for defining rockfall geometry and for inferring different processes of change on near-vertical rock slopes.

2. 2D CHANGE DETECTION

Quantification of volumetric change between TLS surveys is most commonly achieved by rasterising successive point clouds and differencing the resultant Digital Elevation Models (DEMs; James *et al.*, 2012). Many of these approaches resort to gridding the data into erosional cells in order to reduce processing time and complexity. This technique has been used to monitor rock-slope deformation (Bauer *et al.*, 2005) and precursors to slope failure (Abellán *et al.*, 2009); debris flows (Scheidl *et al.*, 2008; McCoy *et al.*, 2010; Blasone *et al.*, 2014); landslide dynamics (Corsini *et al.*, 2009; Burns *et al.*, 2010; Kasperski *et al.*, 2010); rock glaciers (Avian & Kellerer-Pirklbauer, 2009); and for monitoring slope failures in rapidly eroding, soft rock sea cliffs (Adams & Chandler, 2002; Kidner *et al.*, 2004; Xhardé *et al.*, 2006; Kuhn & Prüfer, 2014; Young, 2015). Quantifying change by differencing DEMs is relatively simple, fast and permits the explicit calculation of uncertainties related to point cloud quality, co-registration and surface roughness.

However, representing a surface as a regular 2D grid imposes a limit on the level of detail that can be obtained when using that surface in subsequent change detection analyses. This is particularly important when considering surfaces that are prone to changes such as rockfall activity, which occurs over different length scales (Lim *et al.*, 2010). Differencing these surfaces derives a one-dimensional measurement of change in the z direction only, typically aligned towards the sensor (see Avian & Kellerer-Pirklbauer, 2009). Rough surfaces therefore generate patterns of occlusion that are view-dependent and convolute volume estimation. Deviation away from the normal viewing angle (0 degrees) can have a profound influence on the magnitude of change detected. The case in Fig. 1 illustrates the influence of viewing angle on the amount of occlusion generated by roughness and pre-/post-failure micro-topography across the rockfall surface, and the consequences of this for volume estimation. Where rock slopes have more a complex, non-planar aspect, for example in a headland-embayment sequence, this type of approach requires the scan data to be rasterised and differenced in separate sections in order to maintain a cliff-normal viewing angle. Given that the pattern in the range of volume estimates is not consistent, the degree of under- or over-estimation of change cannot necessarily be compensated for if the view-angle from the sensor to the slope is known.

Reducing 3D point cloud data to a pseudo-3D surface in this manner therefore hinders accurate quantification of rock wall adjustment and retreat (Abellán *et al.*, 2014). This has the effect of losing detail and the true 3D character of the data, with the development of new algorithms for 3D deformation tracking and change detection thus representing a priority for monitoring rock slope dynamics (Carrea *et al.*, 2012). The use of these methods will allow the precision of 2D techniques to be assessed, and to thereby place more realistic error margins on previous estimates of rockfall volume or rates of rockwall retreat.

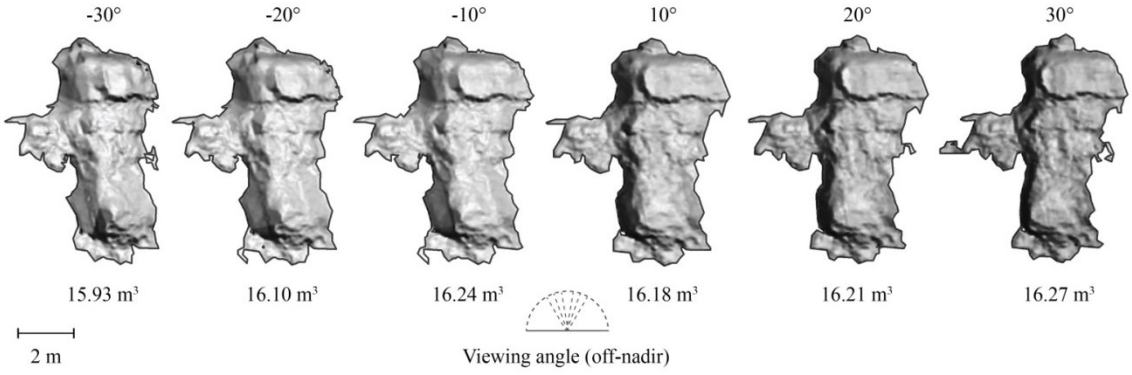

Figure 1. Influence of viewing angle on the magnitude of change detected. The rockfall (volume = 16.20 m³) was recorded at Staithes, North Yorkshire (UK) over a 10 month monitoring period between August 2014 and June 2015.

3. 3D CHANGE DETECTION

A number of 3D methods have been developed to measure the distance between two successive point clouds (Girardeau-Montaut *et al.*, 2005). These techniques include cloud-to-mesh (C2M) and direct cloud-to-cloud (C2C) comparison methods. C2M methods create a surface model from the reference point cloud via meshing or triangulation and measure the distance between this and subsequently gathered point clouds (e.g. Abellán *et al.*, 2009; 2010; Olsen *et al.*, 2010). Such methods have been successfully used to investigate cases of structural or surface deformation, including structural monitoring of a large dam (Alba *et al.*, 2006); detecting land surface changes in the Grand Canyon, Arizona (Collins *et al.*, 2012); and quantifying erosion in the coastal bluffs of the Le Sueur River, southern Minnesota (Day *et al.*, 2013). However, in order to accurately determine volumetric change, triangulated surfaces must be free of topological holes and intersecting triangles. The surface normal for each triangle, which is calculated using the orientation of its three edges, must also point towards the same side of the mesh. The majority of surface reconstruction techniques have been developed and tested using regular shapes and/or denoised point clouds (see Lim & Haron, 2014 for a review), meaning that they are difficult to employ on rough, complex surfaces defined by marked topographic variability (Olsen *et al.*, 2015).

C2C techniques instead estimate surface changes directly from the distance between point neighbours in successive point clouds, eliminating the need for mesh construction and the smoothing of any noisy data (Lague *et al.*, 2013). These distances can be measured automatically using the Hausdorff metric, which computes the unsigned distance for each point in the reference cloud to its nearest neighbor in the second cloud. If and where point clouds are sparse, their quality can be improved by using a local model of the reference surface obtained by using a least square fit, a quadratic height function, or a Delaunay

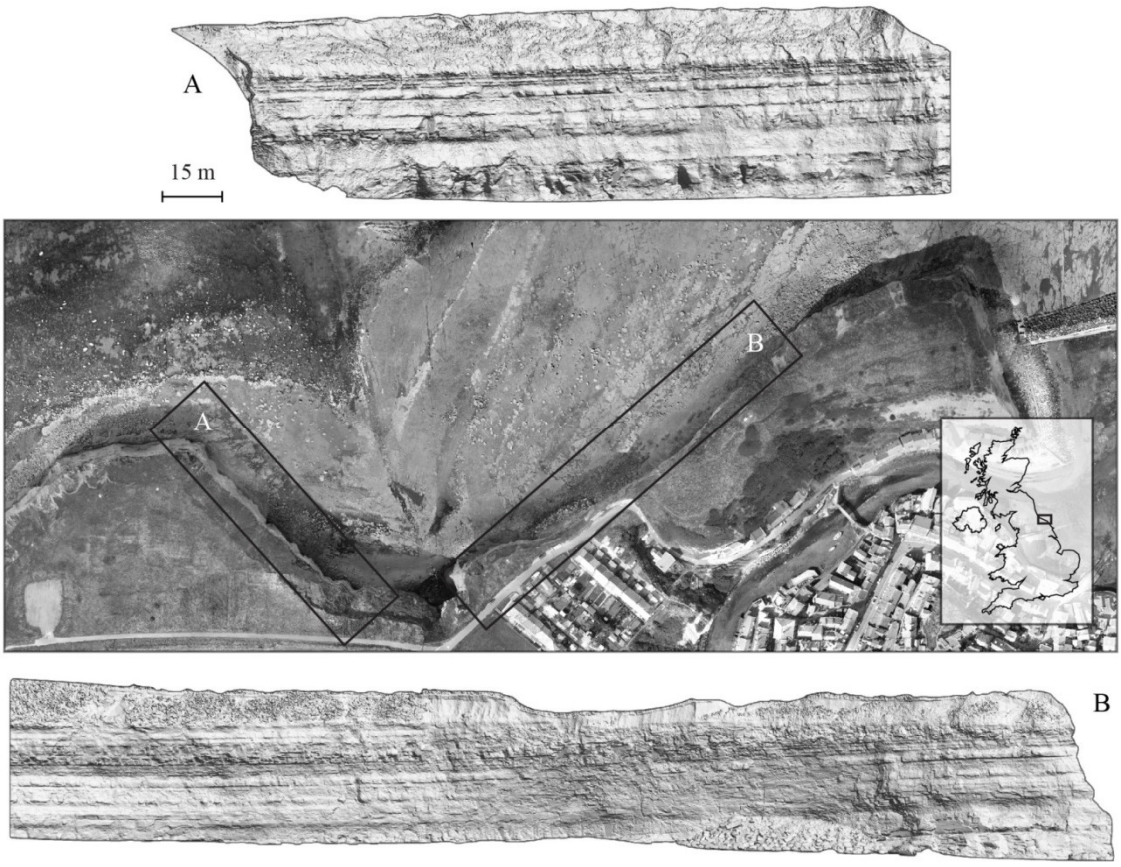

Figure 2. Aerial photo of the coastal rock slopes at Staithes, North Yorkshire. The cliffs are divided into Sites A and B to account for the changing aspect of the coastline.

triangulation of the closest point neighbours (Gruen & Akca, 2005). These provide a better approximation of the true position of the surface and are better able to deal with outliers and variations in surface roughness than Hausdorff distances. These techniques have recently been extended by the Multiscale Model-to-Model Cloud Comparison approach (M3C2; Lague *et al.*, 2013). M3C2 estimates surface normals in 3D and measures the signed mean surface change along the normal direction, with the explicit calculation of a spatially variable confidence interval (SVCI). The algorithm incorporates a local measure of cloud roughness and point density for estimating the SVCI, which can be used to test the statistical significance of any measured changes (Barnhart & Crosby, 2013; Earlie *et al.*, 2013; Stumpf *et al.*, 2015).

4. APPLICATION TO ROCKFALL DATA

We now explore the implications of different methods of change detection using rockfall data derived from a near-vertical coastal rock slope at Staithes, North Yorkshire (UK; Fig. 2). The cliffs along the North Yorkshire coast have been extensively monitored using TLS for over a decade, providing a baseline dataset on erosion rates, rockfall inventories, nearshore wave conditions and patterns of energy delivery to the cliffs (e.g. Lim *et al.*, 2005, 2010; Rosser *et al.*, 2005, 2013; Barlow *et al.*, 2012). Our analysis is divided into two parts: a comparison between inventories derived using both a 2D and a 3D method of change detection, and secondly, a comparison between these and a number of other 3D methods discussed in Section 3. Two inventories were first produced using data that was captured over a 10 month monitoring period between August 2014 and June 2015. A 2D inventory was obtained by rasterising the two point clouds at 0.05 m grid spacing and differencing the resultant DEMs. A 3D inventory was then obtained using M3C2 to identify areas of significant volumetric change. Four additional 3D inventories were also obtained for the same dataset using C2C comparison methods (Hausdorff distance; height function; least squares plane; Delaunay triangulation). These areas were then isolated and meshed to generate a 3D rockfall inventory. In all cases, a minimum detectable change of 0.10 m was used in order to allow for registration errors and to ensure comparability between the datasets.

The differences between the outputs of 2D and 3D methods of change detection are first illustrated using two rockfalls captured by both inventories, which are shown in Fig. 3. Volumetric meshing clearly presents a significant advantage over traditional 2D approaches to change

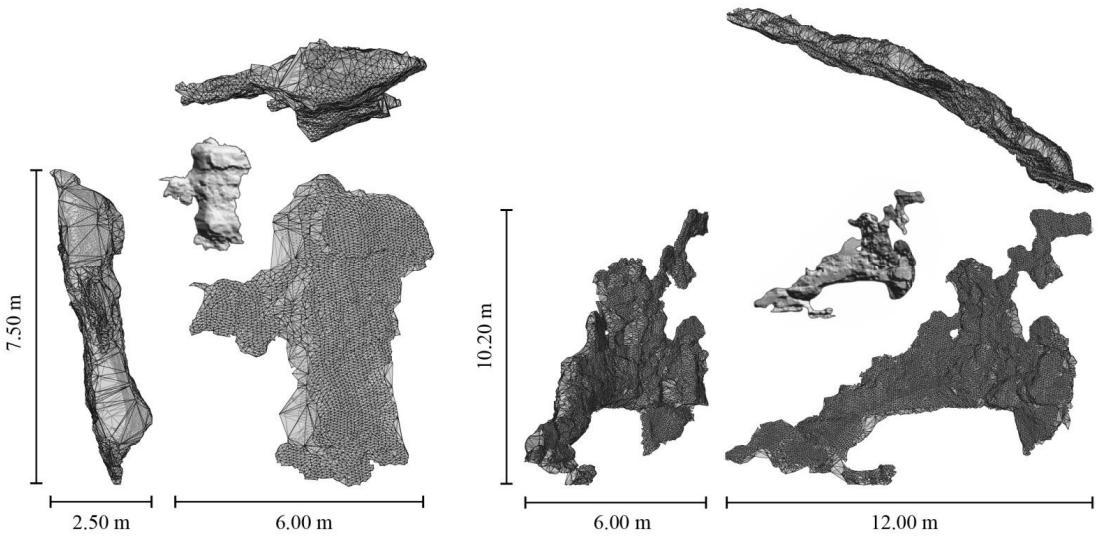

Figure 3. Two large rockfalls captured by both inventories. The volumetric meshes are viewed in the Y-Z (left), X-Z (right) and X-Y (top) directions for both rockfalls. The 2D polygon and hillshade image is displayed for each rockfall alongside its volumetric mesh.

detection by virtue of its ability to retain the 3D shape of the failure. The resultant meshes are not view-dependent, unlike the rasterising process used to generate rockfall polygons. This allows for more accurate characterisation of the failure geometry and surface roughness as well as derivation of the centre of mass and/or gravity. In the future, measures of surface texture and roughness derived from 3D meshes could be developed and used to determine rock slope failure mode, such as fracturing, sliding, circular failure or toppling. Inventories that are obtained in 3D therefore have the potential to considerably improve rockfall runout modelling and the design of structural mitigation measures. It is also worth noting that an important area for future research will be to extend these procedures in order to efficiently evaluate rockfalls occurring over greater areas than are presented in this paper.

Over 460 rockfalls were captured in both inventories, with volumes ranging between < 0.0001 m^3 and *c.* 27 m^3. The volume-area scaling relationship for both inventories is shown in Fig. 4A. Both relate to a power law scaling relationship of the form $V = \alpha A^{\gamma}$, where α = -0.588 (2D) and -1.391 (3D), and γ = 1.202 (2D) and 1.491 (3D). The large difference in α between the two datasets is likely to be due in part to differences in the way that each method calculates the surface area: 2D methods generate a polygonal rockfall scar area while 3D methods calculate the surface area of the rockfall mesh. However, the difference between rockfall volumes estimated by 2D and 3D methods also suggests that the scale and manner in which they differ varies with rockfall magnitude (Fig. 4B). This reflects the fact that 2D and 3D approaches behave differently when considering small depth changes on the periphery of a rockfall. For example, changes in point density, surface roughness and normal direction are known to lead to considerable under- or over-estimation of calculated volumes (e.g. Earlie *et al.*, 2013). For smaller rockfalls (< 0.01 m^3) the volumetric differences introduced by these edge effects constitute a greater proportion of the overall rockfall volume than larger rockfalls, such as those shown

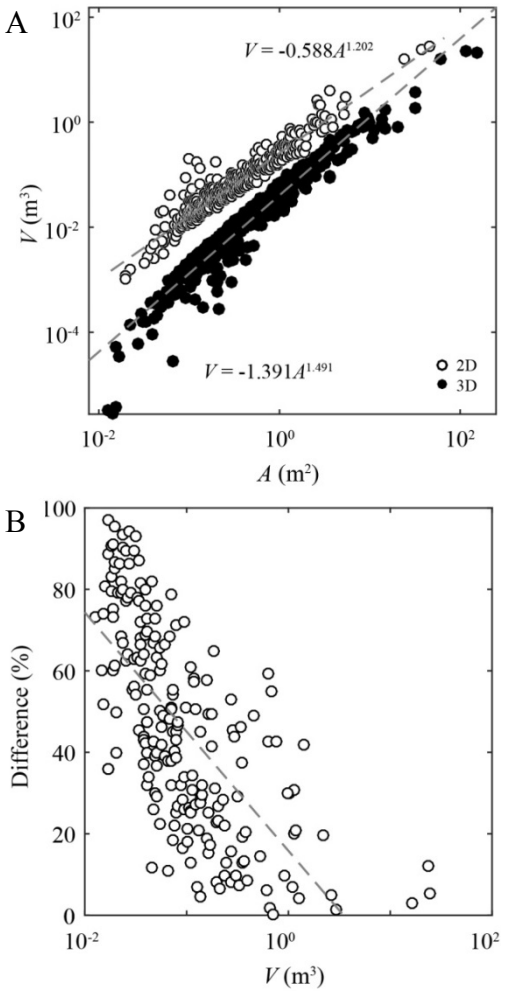

Figure 4. A. Volume-area scaling for the rockfall inventories obtained in Section 4. B. Difference between 2D and 3D volumes expressed as a percentage of 2D volume.

in Fig. 3. In 2D volume estimates these effects are compounded by the influence of viewing angle on the amount of occlusion generated by roughness and micro-topography across the rockfall surface.

We now consider the differences between magnitude-frequency distributions derived using 2D and 3D volume estimates. Considerable research has been published on magnitude-frequency distributions and their ability to quantify the erosive impact of geomorphic processes, such as landslides and rockfalls, over large areas (Malamud *et al.*, 2004). It is well-established that rockfall magnitude-frequency distributions exhibit a negative power law scaling that can be modelled using:

$$f(V) = sV^{-\beta} \qquad (1)$$

Table 1. Volume estimates and corresponding scaling relationships

	V	Erosion rate	Scaling
	m^3	$m\ yr^{-1}$	-
2D	139.86	0.0095	$1.219\,V^{-0.861}$
3D (M3C2)	101.09	0.0069	$1.025\,V^{-0.699}$
3D (C2C)	96.29	0.0066	$1.031\,V^{-0.688}$
3D (C2C HF)	97.47	0.0066	$1.013\,V^{-0.673}$
3D (C2C LSP)	100.03	0.0068	$0.997\,V^{-0.649}$
3D (C2C DT)	96.31	0.0066	$1.016\,V^{-0.676}$

where *f(V)* represents the frequency density, V is the event magnitude, and s and β are constants (Brunetti *et al.*, 2009).

Both the 2D and 3D inventories can be represented using power law scaling relationships, where the exponent β falls inside the 0.60 – 1.50 range for rockfalls suggested by Hergarten (2003; Fig. 5A). The inventories also exhibit a clear rollover in the distribution at low event magnitudes (< 0.01 m^3). This can be attributed to censoring by under-sampling and other biases, such as the relatively high threshold that was set for the minimum detectable change (0.10 m) during data processing, as well as differences in the way that direct cloud-to-cloud comparison methods identify and treat 'insignificant' change.

Our most notable finding is that the forms of the magnitude-frequency distributions obtained using 2D and 3D methods of change detection are profoundly different: this is reflected by the pronounced differences between the values for s (1.219 and 1.025) and β (-0.861 and -0.699) for both datasets, respectively (Table 1). While there is some variation in the magnitude-frequency distributions obtained by other methods of 3D change detection (Fig. 5B; Table 1), this is to be expected given that the various approaches behave differently when considering different types of surface. For example, distance computation using a local model with a Delaunay triangulation is more adapted to representing sharp edges, while a quadratic height function best represents smooth surfaces. These differences have important ramifications for our ability to accurately quantify and predict the volumetric erosional fluxes associated with rockfalls. Here, the total erosion estimated using a 2D method of change detection (139.86 m^3) exceeds that obtained by volumetric meshing (101.09 m^3) by over 25%. Assuming a similar performance across

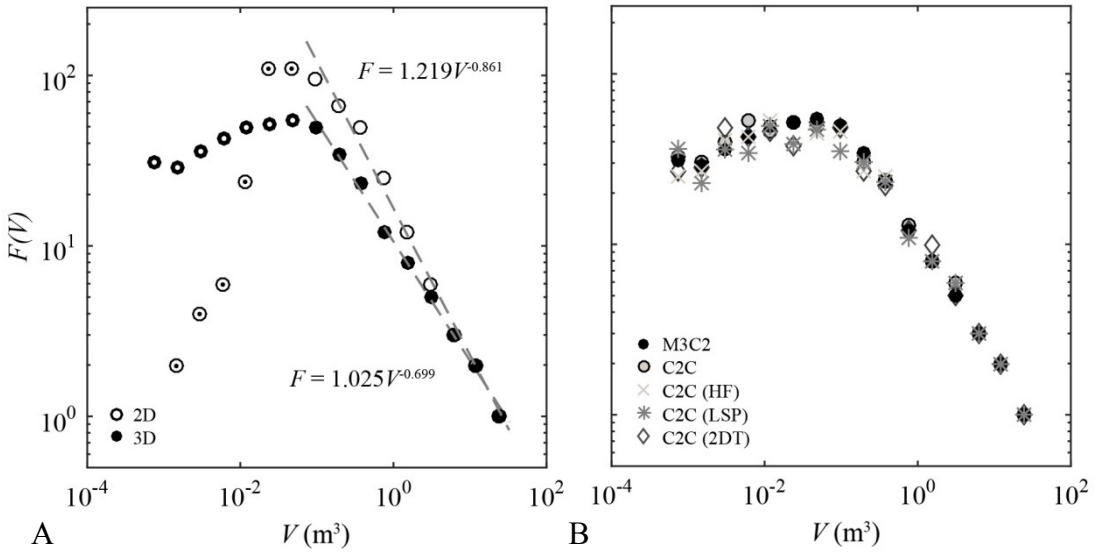

Figure 5. A. Magnitude-frequency distributions for the 2D and 3D rockfall inventories. B. Magnitude-frequency distributions for the five methods of 3D change detection tested (M3C2; C2C; C2C with a quadratic height function (HF); with a least squares plane (LSP) and with a Delaunay triangulation (2DT).

other datasets, the results obtained suggest that existing inventories may considerably overestimate rockfall volumes.

4. CONCLUSIONS

Using observed rockfall data we have explored the implications of different methods of change detection for rockfall volume estimation. The results indicate that rockfall geometry has a profound influence on the ability of any given method to accurately quantify rockfall volume. This is attributed to the combined effects of viewing angle and surface texture, whereby the most appropriate change detection method for any given rock slope can be defined as a function of point density, surface roughness and the overall shape or geometry of the rockfalls being generated. The pronounced variability between these methods clearly demonstrates a need for specific and consistent processing of TLS data in order to maximize analytical accuracy. Our analysis demonstrates that reducing 3D data to a pseudo-3D surface can exert a profound effect on rockfall volume estimation, and we therefore encourage a thorough appraisal of the influence of the change detection method used during the creation of rockfall volume inventories.

5. REFERENCES

Abellán, A., Jaboyedoff, M., Oppikofer, T. & Vilaplana, J. 2009. Detection of millimetric deformation using a terrestrial laser scanner: Experiment and application to a rockfall event. *Natural Hazards and Earth System Sciences*, 9:365-372.

Abellán, A., Calvet, J., Vilaplana, J. & Blanchard, J. 2010. Detection and spatial prediction of rockfalls by means of terrestrial laser scanner monitoring. *Geomorphology*, 119:162-171.

Abellán, A., Oppikofer, T., Jaboyedoff, M., Rosser, N.J., Lim M. & Lato, M.J. 2014. Terrestrial laser scanning of rock slope instabilities. *Earth Surface Processes and Landforms,* 39(1):80-97.

Adams, J. & Chandler, J. 2002. Evaluation of Lidar and Medium Scale Photogrammetry for Detecting Soft-Cliff Coastal Change. *The Photogrammetric Record,* 17(99):405-418.

Alba, M., Fregonese, L., Prandi, F., Scaioni, M. & Valgoi, P. 2006. Structural monitoring of a large dam by terrestrial laser scanning. In Maas, H.-G. & Schneider, D. (Eds.) *Proceedings of the ISPRS Commission V Symposium: Image Engineering and Vision Metrology*, 36(5):6 p.

Avian, M. & Kellerer-Pirklbauer, A. 2009. LiDAR for monitoring mass movements in permafrost environments at the cirque Hinteres Langtal, Austria, between 2000 and 2008. *Natural Hazards and Earth System Sciences*, 9:1087-1094.

Barlow, J., Lim, M., Rosser, N.J., Petley, D.N., Brain, M.J., Norman, E.C. & Geer, M. 2012. Modeling cliff erosion using negative power law scaling of rockfalls. *Geomorphology*, 139-140:416-424.

Barnhart, T.B. & Crosby, B.T. 2013. Comparing Two Methods of Surface Change Detection on an Evolving Thermokarst Using High-Temporal-Frequency Terrestrial Laser Scanning, Selawik River, Alaska. *Remote Sensing,* 5:2813-2837.

Blasone, G., Cavalli, M., Marchi, L. & Cazorzi, F. 2014. Monitoring sediment source areas in a debris-flow catchment using terrestrial laser scanning. *Catena*, 123:23-36.

Burns, W.J., Coe, J.A., Kaya, B.S. & Ma, L. 2010. Analysis of Elevation Changes Detected from Multi-Temporal LiDAR Surveys in Forested Landslide Terrain in Western Oregon. *Environmental and Engineering Geoscience*, 16(4):315-341.

Brunetti, M.T., Guzzetti, F. & Rossi, M. 2009. Probability distributions of landslide volumes. *Nonlinear Processes in Geophysics*, 16:179-188.

Carrea, D., Abellán, A., Derron, M.-H., Gauvin, N., Jaboyedoff, M., Eberhardt, E., Froese, C., Turner, K. & Leroueil, S. 2012. Using 3D surface datasets to understand landslide evolution: From analogue models to real case study. In Eberhardt, E., Froese, C. & Turner, K. (Eds.) *Landslides and Engineered Slopes: Protecting Society Through Improved Understanding*. London: Taylor & Francis, pp. 575-579.

Collins, B., Corbett, S., Fairly, H., Minasian, D., Kayen, R., Dealy, T. & Bedford, D. 2012. Topographic Change Detection at Select Archaeological Sites in Grand Canyon National Park, Arizona, 2007–2010. *US Geologic Survey Scientific Investigation Report 2012-5133*. Reston, VA: US Geological Survey, 77 p.

Corsini, A., Borgatti, L., Cervi, F., Dahne, A., Ronchetti, F. & Sterzai, P. 2009. Estimating mass-wasting processes in active earth slides – earth flows with time-series of High-Resolution DEMs from photogrammetry and airborne LiDAR. *Natural Hazards and Earth System Science,* 9(2):433-439.

Crosta, G.B., Agliardi, F., Frattini, P. &

Lari, S. 2015. Key Issues in Rock Fall Modeling, Hazard and Risk Assessment for Rockfall Protection. In Lollino, G., Giordan, D., Crosta, G., Corominas, J., Azzam, R., Wasowski, J. & Sciarra, N. (Eds.) *Engineering Geology for Society and Territory – Volume 2: Landslide Processes*, pp.43-58.

Day, S.S., Gran, K.B., Belmont, P. & Wawrzyniec, T. 2013. Measuring bluff erosion part 1: terrestrial laser scanning methods for change detection. *Earth Surface Processes and Landforms,* 38(10): 1055-1067.

Earlie, C.S., Masselink, G., Russell, P., Shail, R. & Kingston, K. 2013. Accurate 3D point cloud comparison and volumetric change analysis of Terrestrial Laser Scan data in a hard rock coastal cliff environment. *American Geophysical Union, Fall* Meeting 2013, Abstract EP13A-0868.

Girardeau-Montaut, D., Roux, M., Marc, R. & Thibault, G. 2005. Change detection on point cloud data acquired with a ground laser scanner. International Archives of Photogrammetry, Remote Sensing and Spatial Information Sciences, 36(3):6 p.

Hergarten, S. 2003. Landslides, sandpiles and self-organized criticality. *Natural Hazards and Earth System Sciences*, 3:505-514.

James, L.A., Hodgson, M.E., Ghoshal, S. & Latiolais, M.M. 2012. Geomorphic change detection using historic maps and DEM differencing: The temporal dimension of geospatial analysis. *Geomorphology*, 137(1):181-198.

Kasperski, J., Delacourt, C., Allemand, P., Potherat, P., Jaud, M. & Varrel, E. 2010. Application of a Terrestrial Laser Scanner (TLS) to the Study of the Séchilienne Landslide (Isère, France). *Remote Sensing*, 2:2785-2802.

Kidner, D.B., Thomas, M.C, Leigh, C., Robert, O.J. & Morgan, C.G. 2004. Coastal monitoring with LiDAR: challenges, problems, and pitfalls. *Proceedings of SPIE,* 5574:80-89.

Kuhn, D. & Prüfer, S. 2014. Coastal cliff monitoring and analysis of mass wasting processes with the application of terrestrial laser scanning: A case study of Rügen, Germany. *Geomorphology,* 213:153-165.

Lague, D., Brodu, N. & Leroux, J. 2013. Accurate 3D comparison of complex topography with terrestrial laser scanner: Application to the Rangitikei canyon (N-Z). *ISPRS Journal of Photogrammetry and Remote Sensing,* 82:1026-1054.

Leine, R.I., Schweizer, A., Christen, M., Glover, J., Bartelt, P. & Gerber, W. 2014. Simulation of rockfall trajectories with consideration of rock shape. *Multibody System Dynamics*, 32:241-271.

Lim, M., Petley, D.N., Rosser, N.J., Allison, R.J., Long, A.J. & Pybus, D. 2005. Combined Digital Photogrammetry and Time-of-Flight Laser Scanning for Monitoring Cliff Evolution. *The Photogrammetric Record,* 20(110):109-129.

Lim, M., Rosser, N.J., Allison, R.J. & Petley, D.N. 2010. Erosional processes in the hard rock coastal cliffs at Staithes, North Yorkshire. *Geomorphology,* 114(1-2):1221.

Lim, S.P. & Haron, H. 2014. Surface reconstruction techniques: a review. *Artificial Intelligence Review*, 42:59-78.

Moore, J.R., Sanders, J.W., Dietrich, W.E. & Glaser, S.D. 2009. Influence of rock mass strength on the erosion rate of alpine cliffs. *Earth Surface Processes and Landforms*, 34: 1339-1352.

Olsen, M.J., Kuester, F., Chang, B.J. & Hutchinson, T.C. 2010. Terrestrial laser scanning-based structural damage assessment. *Journal of Computing in Civil Engineering*, 24:264-272.

Rosser, N.J., Petley, D.N., Lim, M., Dunning, S.A. & Allison, R.J. 2005. Terrestrial laser scanning for monitoring the process of hard rock coastal cliff erosion. *Quarterly Journal of Engineering Geology and Hydrogeology,* 38(4):363-375.

Rosser, N.J., Brain, M.J., Petley, D.N., Lim, M. & Norman, E.C. 2013. Coastline retreat via progressive failure of rocky coastal cliffs. *Geology,* 41(8):939-942.

Scheidl, C., Rickenmann, D. & Chiari, M. 2008. The use of airborne LiDAR data for the analysis of debris flow events in Switzerland. *Natural Hazards and Earth System Sciences*, 8:1113-1127.

Sneed, E.D. & Folk, R.L. 1958. Pebbles in the lower Colorado River, Texas, a study of particle morphogenesis. *Journal of Geology*, 66(2):114-150.

Stumpf, A., Malet, J.P., Allemand, P., Pierrot-Deseilligny, M. & Skupinski, G. 2015. Ground-based multi-view photogrammetry for the monitoring of landslide deformation and erosion. *Geomorphology,* 231:130-145.

McCoy, S.W., Kean, J.W., Coe, J.A., Staley, D.M., Wasklewicz, T.A. & Tucker, G.E. 2010. Evolution of a natural debris flow: In situ measurements of flow dynamics, video imagery, and terrestrial laser scanning. *Geology*, 38(8):735-738.

Xhardé, R., Long, B.F. & Forbes, D.L. 2006. Accuracy and Limitations of Airborne LiDAR Surveys in Coastal Environments. *Proceedings of the International Geoscience and Remote Sensing Symposium*, 2412-2415.

Young, A.P. 2015. Recent deep-seated coastal landsliding at San Onofre State Beach, California. *Geomorphology,* 228:200-212.

This page is intentionally left blank

Appendices

Appendix B

Ground control data for airborne LiDAR surveys

Below is a map showing the ground control points used in the four airborne LiDAR surveys undertaken. The locations of each of the repeated sites (CBAR, GOLF, KETT, RUNS, and SKIN) differ only slightly between surveys, and so are represented by the same point.

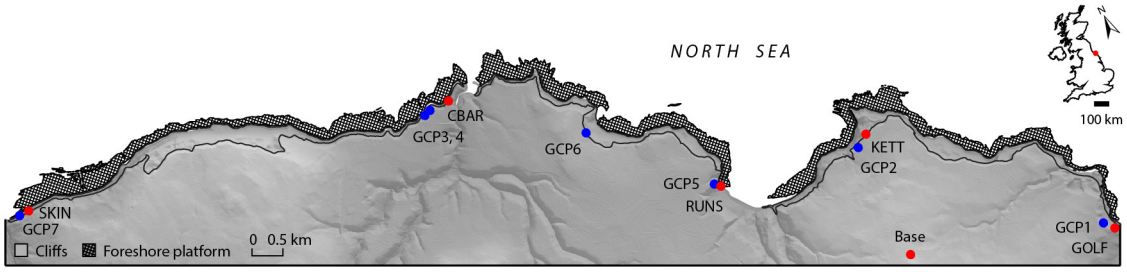

Ground control points and measured data for the first airborne LiDAR survey (15/08/2014). 'Outside' denotes that the point was beyond the laser range.

Site	*Easting*	*Northing*	*Known Z*	*Laser Z*	*DZ*
	-	-	*m*	*m*	*m*
GCP1	486212.91	512722.60	7.13	7.16	+0.03
GCP2	483041.05	515631.56	88.99	89.02	+0.03
GCP3	477655.35	518824.29	50.13	50.16	+0.03
GCP4	477652.29	518884.98	49.50	49.51	+0.01
GCP5	480895.89	516001.91	24.23	24.22	-0.01
GCP6	479581.41	517653.39	92.66	92.61	-0.05
GCP7	471440.21	520102.31	6.34	Outside	-
Base	482857.46	513475.47	198.23	Outside	-
CBAR	477952.36	518874.76	40.37	40.42	+0.03
GOLF	487742.31	511977.04	36.03	36.03	0.00
KETT	483188.69	515750.95	96.14	96.12	-0.02
RUNS	481001.77	515993.46	7.17	7.12	-0.01

Ground control points and measured data for the second airborne LiDAR survey (04/06/2015).

Site	*Easting*	*Northing*	*Known Z*	*Laser Z*	*DZ*
	-	-	*m*	*m*	*m*
CBAR	477657.55	518843.71	50.12	50.10	-0.02
GOLF	488240.44	511967.09	5.59	5.65	+0.06
KETT	483188.70	515749.60	95.99	96.09	+0.10
RUNS	481008.19	515990.98	7.37	7.40	+0.03
SKIN	472577.04	519814.29	75.91	75.95	+0.04

Ground control points and measured data for the third airborne LiDAR survey (08/04/2016).

Site	*Easting*	*Northing*	*Known Z*	*Laser Z*	*DZ*
	-	-	*m*	*m*	*m*
CBAR	477655.09	518844.78	50.09	50.05	-0.04
GOLF	488236.92	511966.69	5.57	5.62	+0.05
KETT	483188.16	515750.10	96.09	96.09	0.00
RUNS	481005.92	515991.91	7.34	7.35	+0.01

Ground control points and measured data for the fourth airborne LiDAR survey (29/03/2017).

Site	*Easting*	*Northing*	*Known Z*	*Laser Z*	*DZ*
	-	-	*m*	*m*	*m*
CBAR	477659.64	518844.08	50.08	50.08	0.00
GOLF	488243.69	511965.36	5.56	5.56	0.00
KETT	483188.96	515751.77	96.53	96.55	+0.02
RUNS	480979.79	516006.53	13.26	13.25	-0.01

Summary statistics for each of the four airborne LiDAR surveys undertaken.

Survey	*Min DZ*	*Max DZ*	*Average DZ*	*RMSE*	*SD*
	m	*m*	*m*	*m*	*m*
15/08/2014	-0.05	+0.03	+0.004	± 0.03	0.03
04/06/2015	-0.02	+0.10	+0.040	± 0.05	0.04
08/04/2016	-0.04	+0.05	+0.005	± 0.03	0.04
29/03/2017	-0.010	+0.02	+0.002	± 0.01	0.01

Appendix C

Calculating the volume of objects represented by triangular surface meshes

The volume and centroid of a rigid body represented by a triangular surface mesh can be calculated using the divergence theorem. All rigid bodies, and therefore their parameters, can be expressed in terms of 3D moments. Closed-form expressions for the 3D moments of objects represented by triangular surface meshes are derived here. The workings are summarised from Semechko (2014), whose `RigidBodyParams` function was used in this work. The function can be downloaded from the MATLAB® file exchange, at: https://uk.mathworks.com/matlabcentral/fileexchange/48913-compute-exact-rigid-body-parameters-of-objects-represented-by-triangular-surface-meshes.

If a region of space $\Omega \in \mathbb{R}^3$ is occupied by a rigid body, the material density of which is described by the scalar function:

$$p(x,y,z): \Omega \to \mathbb{R}^+, \qquad \text{[C1]}$$

for a particular point in space, then the 3D moment of order $p+q+r$ is defined as:

$$\widetilde{m}_{p,q,r}(\Omega) = \int_{\Omega} p(x,y,z) x^p y^q z^r d\Omega, \qquad \text{[C2]}$$

For an object with uniform density, $p(x,y,z)$ is constant, so Equation 2 can be simplified to:

$$\widetilde{m}_{p,q,r}(\Omega) = \int_{\Omega} x^p y^q z^r d\Omega\,. \qquad \text{[C3]}$$

The 3D moments defined in Equation C4 can also be evaluated by changing the domain of integration from the volume occupied by the region, Ω, to the surface enclosing that region, S, such that $\widetilde{m}_{p,q,r}(\Omega) = \widetilde{m}_{p,q,r}(S)$. This equivalence is enabled by the divergence theorem, which states that the outward flux of a vector field through a closed surface is equal to the volume integral of the divergence over the region inside the surface:

$$\int_{\Omega} \left(\vec{\nabla} \cdot \vec{F}\right) d\Omega = \oint \vec{F} \cdot \vec{n}\, dS, \qquad \text{[C4]}$$

where $\vec{\nabla} = \frac{\delta}{\delta_x}\hat{\mathrm{i}} + \frac{\delta}{\delta_y}\hat{\mathrm{j}} + \frac{\delta}{\delta_z}\hat{\mathrm{k}}$, and $\vec{F} = {}^1F(x,y,z)\hat{\mathrm{i}} + {}^2F(x,y,z)\hat{\mathrm{j}} + {}^3F(x,y,z)\hat{\mathrm{k}}$.

Let $\vec{F} = \vec{F}_{p,q,r}$, so that, by combining Equation C3 and Equation C4:

$$\vec{\nabla} \cdot \vec{F} = \vec{\nabla} \cdot \vec{F}_{p,q,r} = x^p y^q z^r. \quad [C5]$$

Therefore:

$$x^p y^q z^r = \frac{\delta\{{}^1F_{p,q,r}\}}{\delta x} + \frac{\delta\{{}^2F_{p,q,r}\}}{\delta y} + \frac{\delta\{{}^3F_{p,q,r}\}}{\delta z}. \quad [C6]$$

One of the solutions of this partial differential equation is:

$$\begin{aligned} {}^1F_{p,q,r} &= \frac{1}{3(p+1)} x^{p+1} y^q z^r, \\ {}^2F_{p,q,r} &= \frac{1}{3(q+1)} x^p y^{q+1} z^r, \\ {}^3F_{p,q,r} &= \frac{1}{3(r+1)} x^p y^q z^{r+1}. \end{aligned} \quad [C7]$$

Since a triangular surface mesh is composed from a union on N triangles ($S = \bigcup Ti$), the moment of the region enclosed by the mesh surface can be written as the sum of the moments of the individual triangles:

$$\widetilde{m}_{p,q,r}(\mathrm{S}) = \oint_{\Omega} \vec{F}_{p,q,r} \cdot \vec{n} dS = \sum_{i=1}^{N} \int_{T_i} \vec{F}_{p,q,r} \cdot \vec{n} dS = \sum_{i=1}^{N} m_{p,q,r}(T_i). \quad [C8]$$

By combining Equation C7 with Equation C8:

$$m_{p,q,r}(T_i) = \sum_{j=1}^{3} n_{ij} \int_{T_i} {}^jF_{p,q,r} dS. \quad [C9]$$

This can be rewritten in terms of barycentric coordinates (see Figure C1), such that:

$$\int_{T_i} {}^jF_{p,q,r} dS = 2A_i \int_0^1 \int_0^{1-u} {}^j_iF_{p,q,r}(u,v) dv du, \quad [C10]$$

where A_i is the area of the triangle T_i, and the integrand ${}^j_iF_{p,q,r}(u,v)$ is defined as:

$$ {}_{i}^{j}F_{p,q,r}(u,v) = \frac{1}{3}\begin{cases} \frac{1}{(p+1)}x_i^{p+1}(u,v)y_i^{q}(u,v)z_i^{r}(u,v), j=1 \\ \frac{1}{(q+1)}x_i^{p}(u,v)y_i^{q+1}(u,v)z_i^{r}(u,v), j=2 \\ \frac{1}{(r+1)}x_i^{p}(u,v)y_i^{q}(u,v)z_i^{r+1}(u,v), j=3 \end{cases} \quad [C11] $$

where:

$$ \begin{aligned} x_i(u,v) &= (x_{i2}-x_{i1})u + (x_{i3}-x_{i2})v + x_{i1}, \\ y_i(u,v) &= (y_{i2}-y_{i1})u + (y_{i3}-y_{i2})v + y_{i1}, \\ z_i(u,v) &= (z_{i2}-z_{i1})u + (z_{i3}-z_{i2})v + z_{i1}, \end{aligned} \quad [C12] $$

To summarise:

$$ m_{p,q,r}(T_i) = 2A_i \sum_{j=1}^{3} n_{ij} \int_0^1 \int_0^{1-u} {}_{i}^{j}F_{p,q,r}(u,v)\,dv\,du. \quad [C13] $$

The total volume, V, of the region Ω occupied by the rigid body is:

$$ V = \int_{\Omega} d\Omega\,, \quad [C14] $$

which, by comparison with Equation 3, is equal to the zeroth moment:

$$ V = m_{0,0,0}. \quad [C15] $$

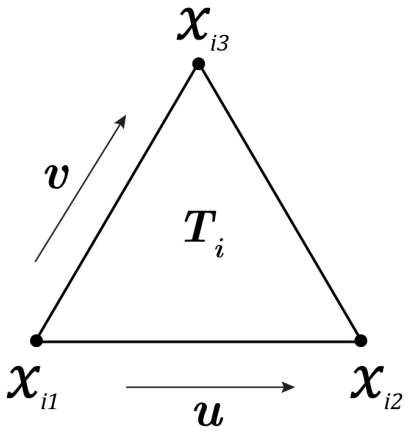

Figure C1 *Barycentric coordinates (u,v) can be used to specify the location of a point inside a planar triangle. Note that* $0 \le u, v \le 1$ *and* $0 \le u + v \le 1$.

Centroids of the rigid body with respect to the x-, y-, and z-axes are defined as:

$$\bar{x} = \frac{\int_\Omega x d\Omega}{\int_\Omega d\Omega}, \qquad \bar{y} = \frac{\int_\Omega y d\Omega}{\int_\Omega d\Omega}, \qquad \bar{z} = \frac{\int_\Omega z d\Omega}{\int_\Omega d\Omega}, \qquad \text{[C16]}$$

where comparison with Equation 3 gives:

$$\bar{x} = \frac{m_{1,0,0}}{m_{0,0,0}}, \qquad \bar{y} = \frac{m_{0,1,0}}{m_{0,0,0}}, \qquad \bar{z} = \frac{m_{0,0,1}}{m_{0,0,0}}. \qquad \text{[C17]}$$

For reference, a figure showing the trianglular surface mesh of a rockfall is shown below. In order to accurately calculate rigid body parameters, the face normals of the mesh must be consistent in their orientation and point outwards, away from the region enclosed by the surface (Figure C2).

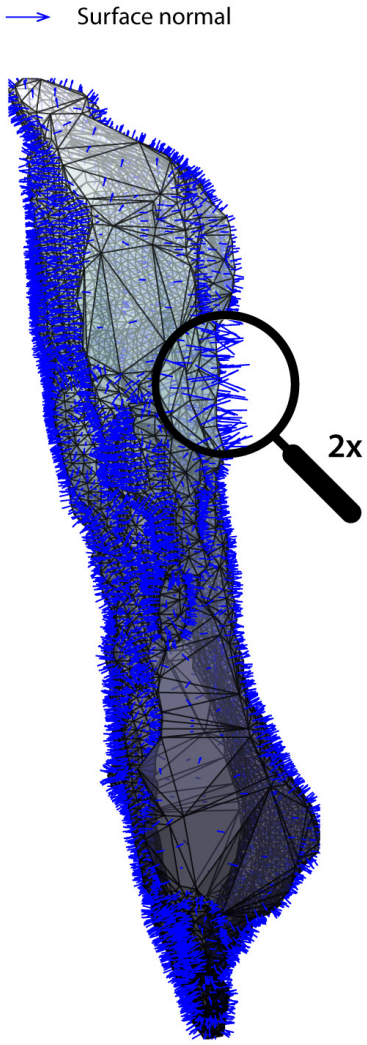

Figure C2 *Triangular surface mesh of a rockfall recorded at Staithes over a 10-month monitoring period between August 2014 and June 2015. The mesh is viewed from the side. The surface normals for each triangle are pointing outwards, away from the region enclosed by the surface.*

Appendix D

Power law scaling parameters derived from terrestrial monitoring of rockfalls

Absolute β/ϱ values derived from previous terrestrial monitoring of rockfalls, sorted by β. Values in bold are those reported.

Location	*Rockfalls*	*Length scale*[b]	*Interval*[c]	*Volume*	*Threshold*[d]	*Distribution*[e]	*PDF*[f]	*CCDF*	*Reference*
	-	*m*	*hr/d/m/yr*	m^3	m^3	-	*Slope,* β	*Slope,* ϱ	-
North Yorkshire, UK	14,460	20,459	294 d	$10^{-4} - 10^{3}$	1×10^{-3}		**1.69**	0.69	This work
	18,729	20,459	310 d	$10^{-4} - 10^{3}$	1×10^{-3}	*NC F*(V_R)	**1.64**	0.64	
	24,843	20,459	356 d	$10^{-4} - 10^{4}$	1×10^{-3}		**1.54**	0.54	
Sharon Escarpment, Israel	101	730	V	$10^{0} - 10^{3}$	1×10^{0}	NC_F	**1.02**	0.02	Katz and Mushkin (2013)
Grenoble, France	87	120,000	60 yr	$10^{-2} - 10^{6}$	5×10^{1}	C_F	1.41	**0.41**	Dussauge-Peisser *et al.* (2002)
British Columbia, Canada	390	-	30 yr	$10^{-2} - 10^{4}$	1×10^{0}	C_F	1.43	**0.43**	Hungr *et al.* (1999)
Upper Arly Gorges, France	59	2,200	22 yr	$10^{0} - 10^{4}$	2×10^{1}	C_F	1.45	**0.45**	Dussauge-Peisser *et al.* (2002)
Yosemite Valley, California	101	100,000	78 yr	$10^{0} - 10^{6}$	5×10^{1}	C_F	1.46	**0.46**	Dussauge-Peisser *et al.* (2002)
Mesnil-Val, France	8,582	750	6 m	$10^{-4} - 10^{4}$	1×10^{-3}	C_F	1.54	**0.54**	Dewez *et al.* (2013)
Balza Tagliata, Italy	1,696	2,200	E	$10^{-5} - 10^{1}$	2.4×10^{-5}	*NC F*(V_R)	**1.60**	0.60	Guzzetti *et al.* (2004)
British Columbia, Canada	918	n/a	22 yr	$10^{-2} - 10^{4}$	1×10^{0}	C_F	1.65	**0.65**	Hungr *et al.* (1999)
Illgraben, Switzerland	2,170	1,250	19 yr	$10^{1} - 10^{6}$	1×10^{2}	*NC F*(V_R)	**1.65**	0.65	Bennett *et al.* (2012)
Feifeng, China	27	150	200 yr	$10^{-1} - 10^{2}$	1×10^{0}	C_F	1.65	**0.65**	Wang *et al.* (2014)

La Cornalle, Switzerland	118	115	6 m	10^{-2} – 10^{1}	1×10^{-1}	C_F	1.68	**0.68**	Carrea *et al.* (2015)
Lauterbrunnen, Switzerland	122	6,000	2 m	10^{-2} – 10^{2}	1×10^{-2}	$NC\ F(V_R)$	**1.71**	0.71	Strunden *et al.* (2015)
Illgraben, Switzerland	1,475	1,250	19 yr	10^{1} – 10^{6}	1×10^{3}	$NC\ F(V_R)$	**1.76**	0.76	Bennett *et al.* (2012)
Boulby – Staithes, UK	114,505	482	30 d	10^{-6} – 10^{3}	1.25×10^{-4}	C_F	1.80	**0.80**	Lim *et al.* (2010)
Whitby, UK	> 180,000	215	30 d	10^{-3} – 10^{1}	1×10^{-3}	$NC\ F(V_R)$	**1.81**	1.81	Williams *et al.* (2018)
Hong Kong	201	n/a	5 yr	10^{-1} – 10^{3}	1×10^{0}	C_F	1.89	**0.89**	Chau *et al.* (2003)
British Columbia, Canada	1,982	1,000	38 – 114 d	10^{-2} – 10^{1}	3×10^{-2}	C_F	2.01	**1.01**	van Veen *et al.* (2017)
Boulby, UK	31,987	88	30 d	10^{-3} – 10^{1}	1×10^{-3}	$NC\ F(V_R)$	**2.17**	1.17	Norman (2012)
Whitby, UK	> 180,000	215	< 1 hr	10^{-3} – 10^{1}	1×10^{-3}	$NC\ F(V_R)$	**2.27**	1.27	Williams *et al.* (2018)
Boulby – Staithes, UK	61,529	482	30 d	10^{-6} – 10^{4}	3×10^{-4}	$NC\ F(V_R)$	**1.12 – 2.12**	0.12 – 1.12	Barlow *et al.* (2012)*
Boulby – Staithes, UK	513,576	604	30 d	10^{-6} – 10^{3}	5×10^{-4}	NC_F	**1.12 – 2.37**	0.12 – 1.37	Rosser *et al.* (2007)*

[a] *Specifies whether the inventory was collected in 2D (rockfall polygons) or 3D (rockfall meshes).*
[b] *Horizontal length scale over which the inventory was collected. For example, along 100 m of cliffs, or in a 2,000 m long valley.*
[c] *Monitoring interval in hours, days, months or years. Note that this is not the same as the monitoring period, which might either be the same or longer. E, event-based; V, variable.*
[d] *Threshold volume below which the power law scaling relationship can no longer be applied.*
[e] *Type of power law distribution: C_F, cumulative number or frequency per year; NC_F, non-cumulative number or frequency per year; $F(V_R)$ frequency density.*
[f] *Slope of the power law distribution. This varies depending on whether the power law distribution is modelled using a probability density function (PDF, slope = β) or a complementary cumulative distribution function (CCDF, slope = ϱ). The slope of the CCDF is related to β by $\varrho = \beta$ - 1.*
* *Denotes papers that provide monthly variations in β, which is given here as a range.*

Appendix E

Regional-scale examples of facet analysis

Included in this appendix are three figures that demonstrate the facet analysis undertaken in *Chapter 4* on a broader scale ($> 10^2$ m). Point clouds and the facets derived during the analysis, which are coloured by density, facet dip, and facet aspect, are shown for the cliffs at Kettleness, Staithes, and Boulby.

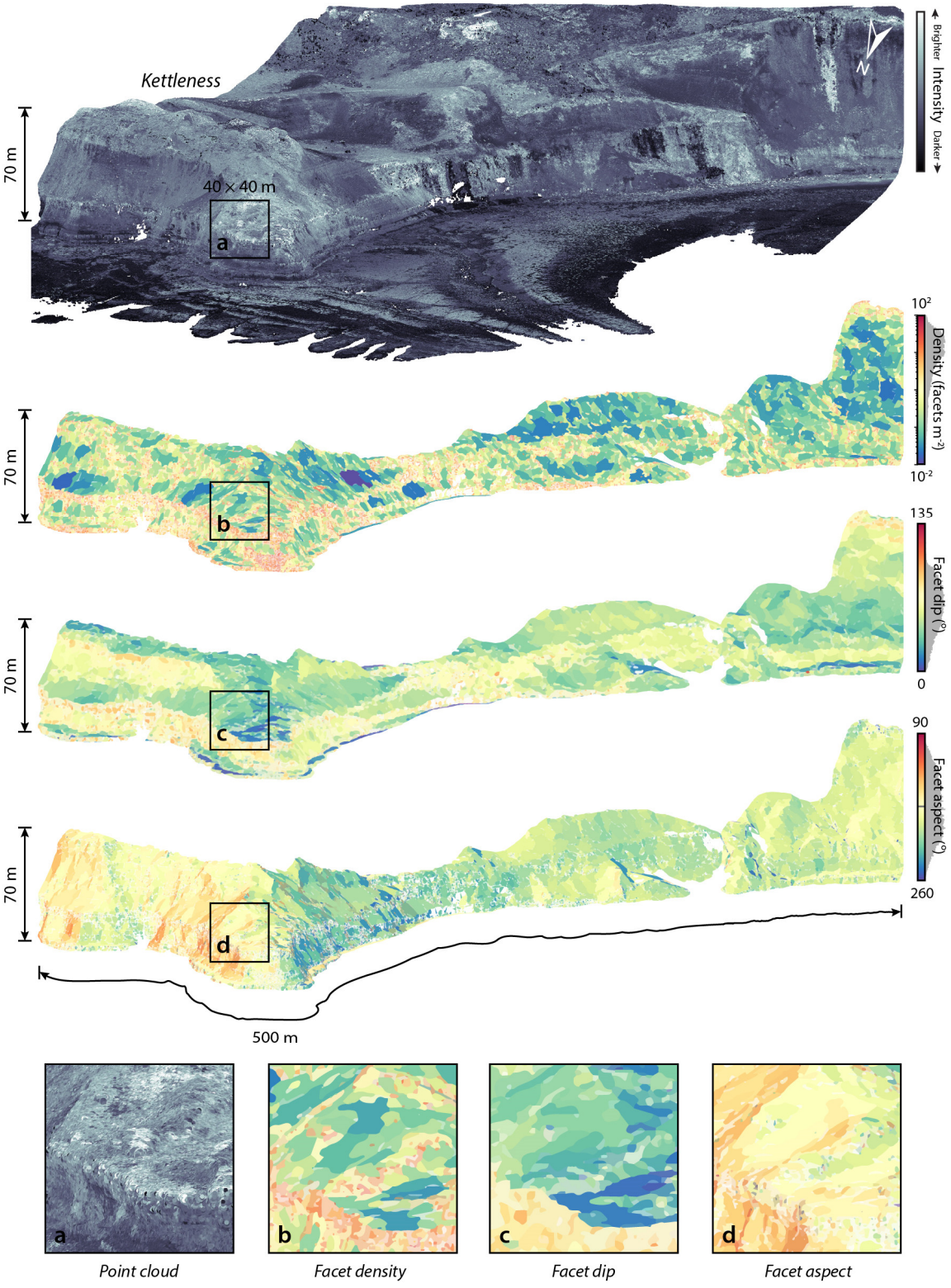

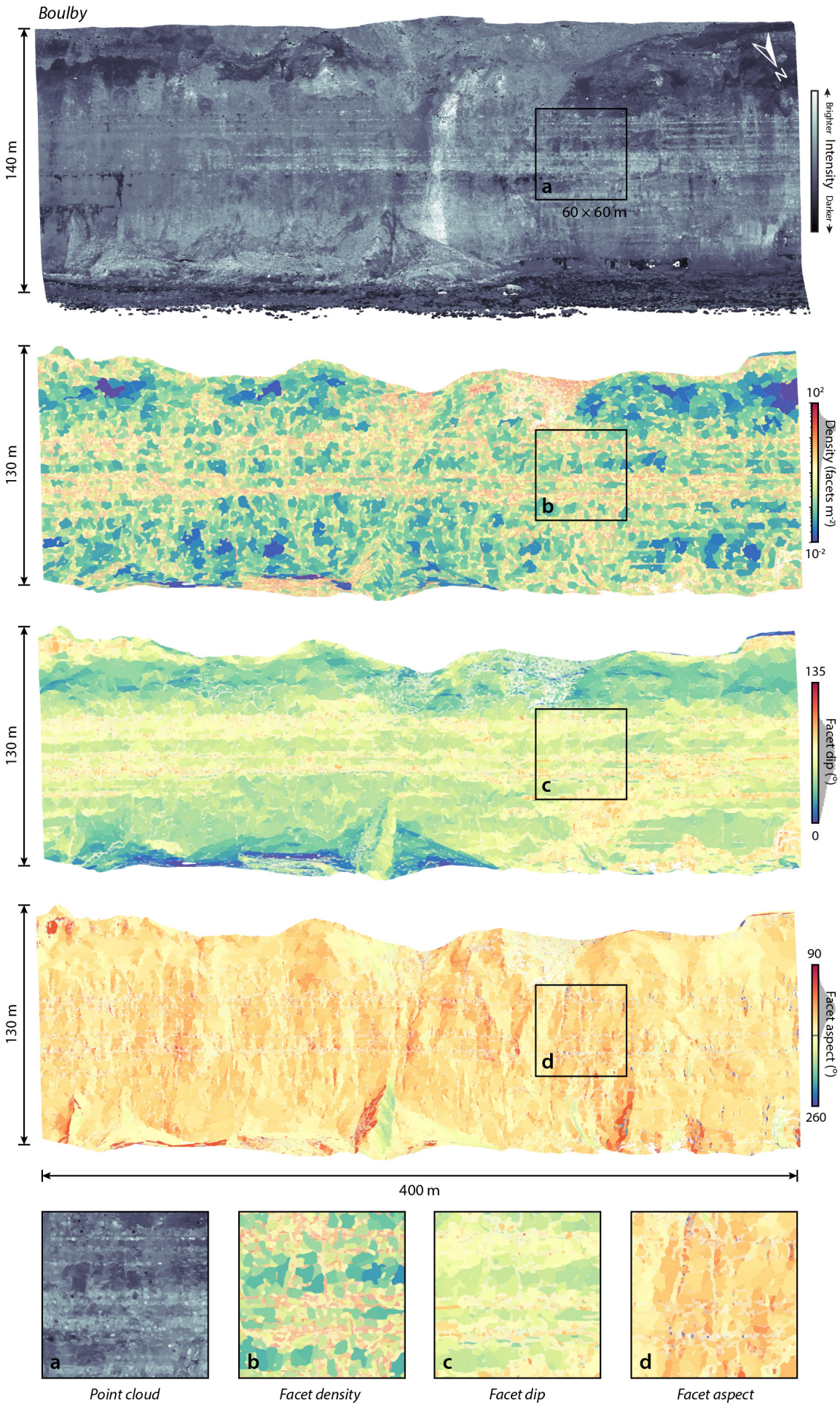
Boulby
140 m
N
Brighter
Intensity
Darker
a
60 × 60 m
130 m
10^2
Density (facets m^{-2})
10^{-2}
b
130 m
135
Facet dip (°)
0
c
130 m
90
Facet aspect (°)
260
d
400 m
a
b
c
d
Point cloud
Facet density
Facet dip
Facet aspect


Brighter Intensity Darker
Density (facets m-2)
10²
10⁴
Facet dip (°)
135
0
Facet aspect (°)
90
270
N
Staithes
50 m
50 m
50 m
50 m
Total cliff length = 500 m

Appendix F

Spatial variations in rockfall volume distributions

The two figures presented in this appendix complement the analyses shown in Figures 4.17 (*p.* 76) and 4.18 (*p.* 78), which consider variations in rockfall shape along the North Yorkshire coast, and variations in how rockfall shape is correlated through time. Accompanying information is included below.

The first figure (*p.* 193) complements Figure 4.17 (*p.* 76) and shows rockfall volume distributions monitored along the North Yorkshire coast, UK, from (*a*) 2014 – 2015, (*b*) 2015 – 2016, and (*c*) 2016 – 2017. Rockfall volume is plotted as a stacked bar graph, with distance along the coastline divided into 100 m bins. Colours correspond to volumes that were plotted using logarithmically binned data, as in the magnitude-frequency analysis undertaken in *Section 3.2.6*. The inset in (*d*) shows in detail the previously monitored sites (Table 2.01, *p.* 19) as well as the sites monitored in *Chapter 5*. White bands denote harbours, beachy embayments, and other gaps in the point cloud data where cliffs are absent or densely vegetated.

The second figure (*p.* 194) complements Figure 4.18 (*p.* 78) and shows spatial variations in the correlations between rockfall volumes. Correlations are windowed (± 200 m) and only shown in (*a*) if there is a positive correlation between volumes observed in both 2014 – 2015 and 2015 – 2016, *and* 2015 – 2016 and 2016 – 2017. The total number of positively correlated volume classes (out of a possible 24) for each 100 m bin is shown in (*b*). The percentage of 100 m bins (total = 237) in each volume class that exhibit positive correlations is shown in (*c*). The inset in (*d*) shows in detail the previously monitored sites (Table 2.01, *p.* 19) as well as the sites monitored in *Chapter 5*.

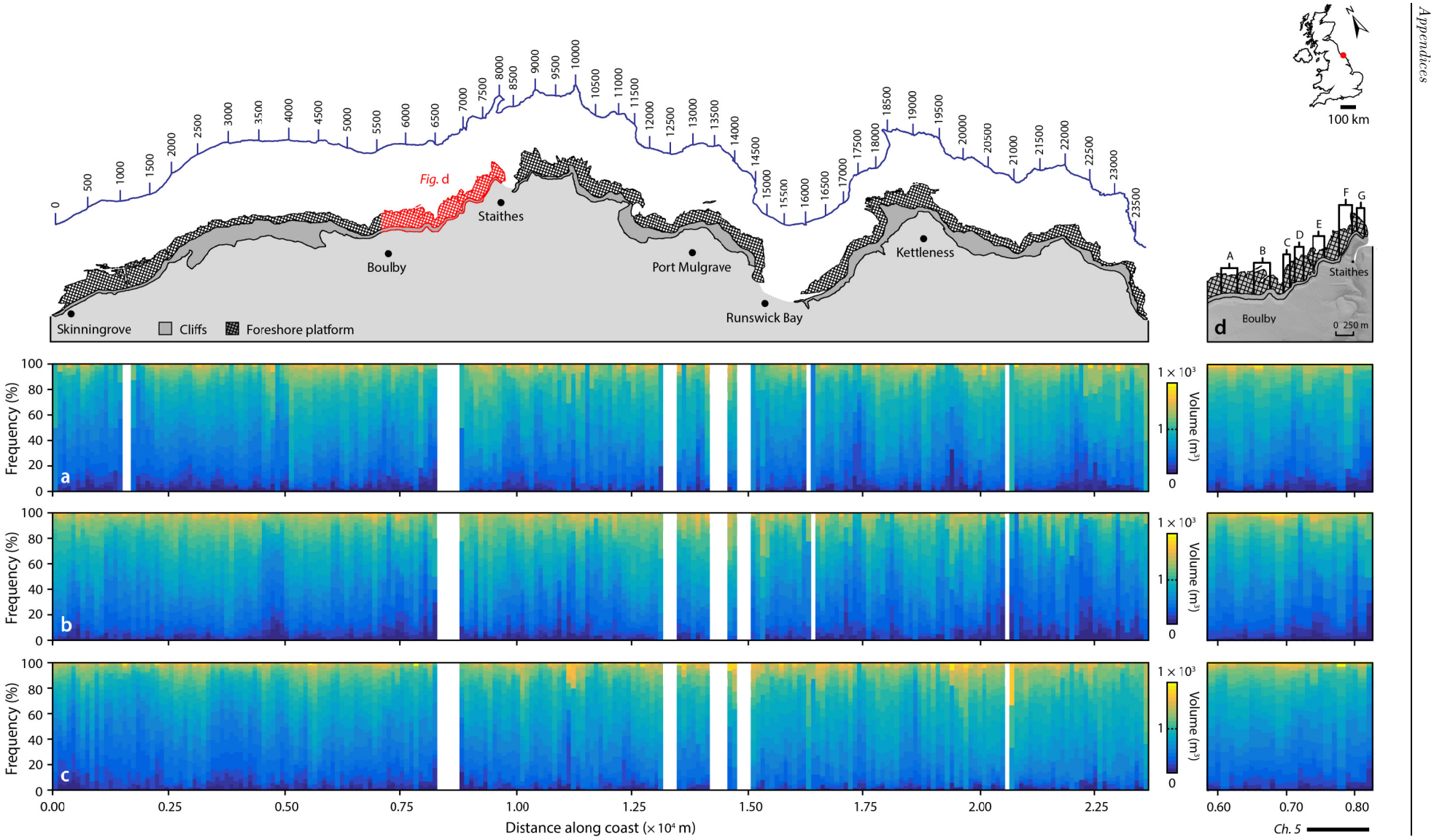
100 km
Fig. d
Staithes
Boulby
Port Mulgrave
Kettleness
Runswick Bay
Skinningrove
Cliffs
Foreshore platform
A
B
C
D
E
F
G
Staithes
Boulby
0 250 m
d
Frequency (%)
Volume (m³)
1 × 10³
a
b
c
Distance along coast (× 10⁴ m)
Ch. 5

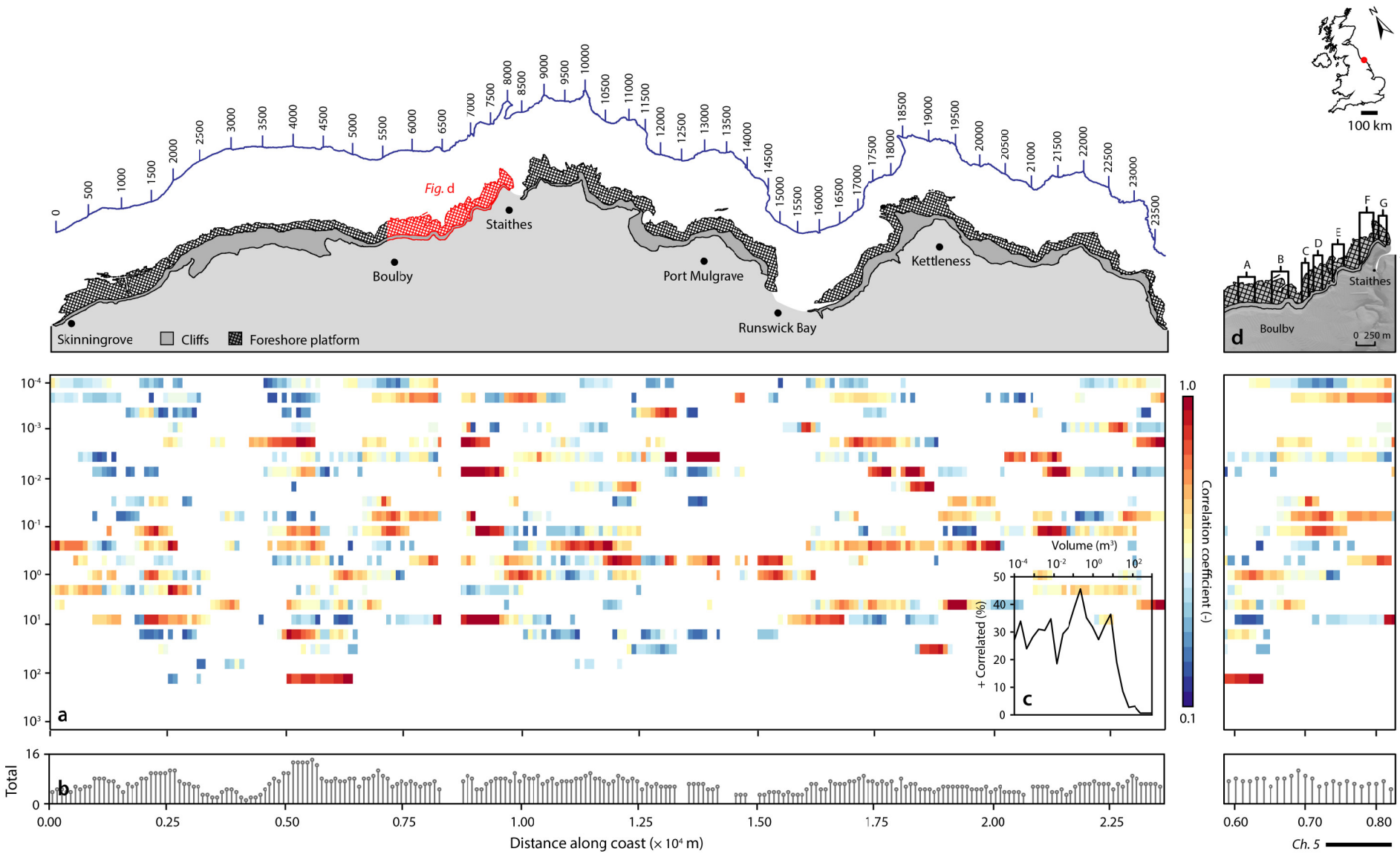
Fig. d
Staithes
Boulby
Port Mulgrave
Kettleness
Runswick Bay
Skinningrove
Cliffs
Foreshore platform
100 km
A
B
C
D
E
F
G
Staithes
Boulby
0 250 m
d
a
b
c
Volume (m³)
+ Correlated (%)
Correlation coefficient (-)
1.0
0.1
Total
Distance along coast (× 10⁴ m)
Ch. 5

Appendix G

Wave transformation modelling

To approximate conditions across the cliffs, monitored distal waves and tidal data were modelled using a transformation based on Battjes and Stive (1985) derived by Norman *et al.* (2013). The information presented here is summarised from Norman *et al.* (2013). The model uses two types of inputs, including (1) those calculated at each timestep and at each location in the profiles given in Figure G1, and (2) those that were given initial values at the offshore location. An initial distance of 1,000 m was used as the water depth at this distance, and therefore wave conditions, are approximately equal to those offshore according to linear wave theory.

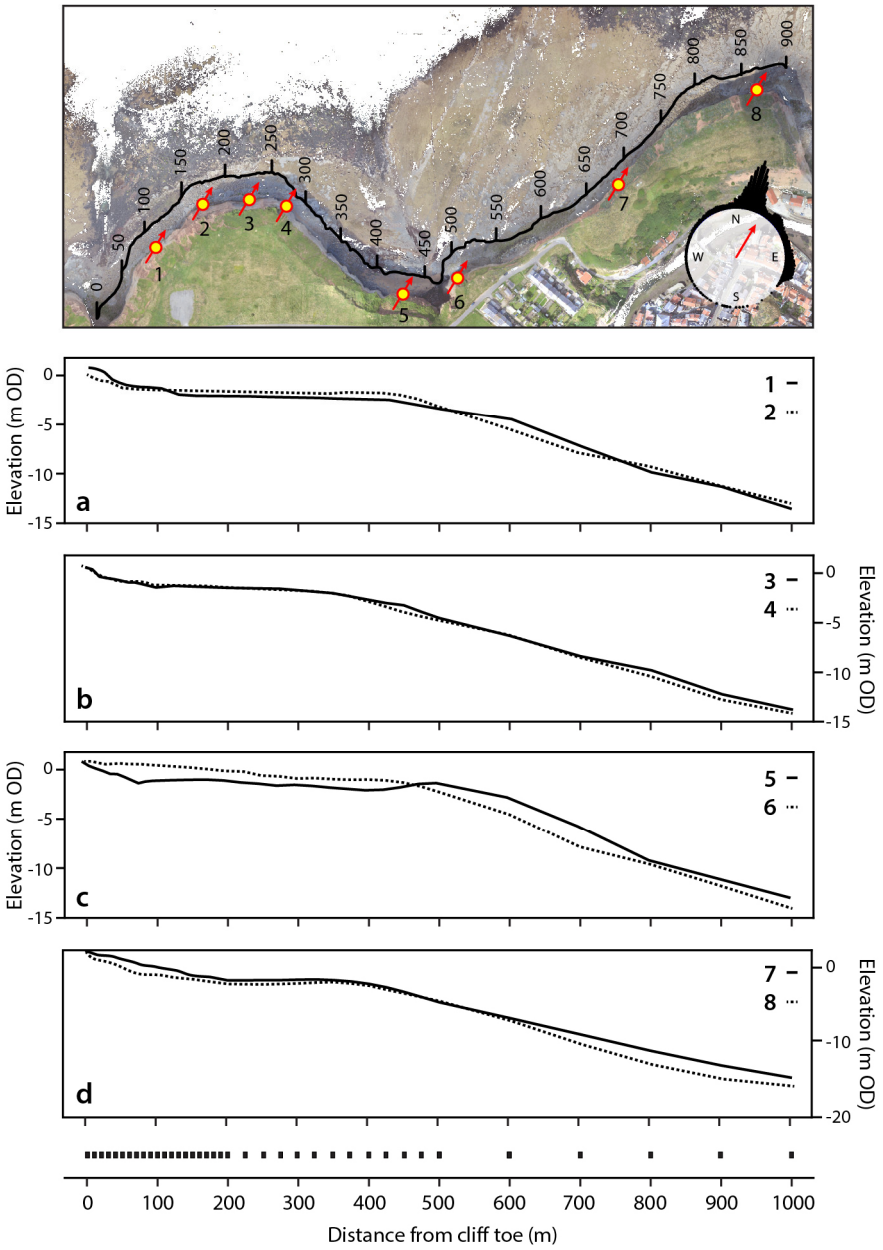

Figure G1 *Bathymetric profiles at each monitoring site. Red arrows show the profile direction, which was chosen using the prevailing wave direction observed over the monitoring period (inset). Black squares represent where wave characteristics were estimated by the model.*

Still water depths were calculated at each timestep and at each location in the profiles based on the tidal elevation relative to the bathymetry at that location. The wave number, k, was then calculated as follows:

$$k = \frac{2\pi}{L}, \qquad \text{[G1]}$$

where the dependence of k on the wavelength, L, means that k varies with depth. The wave period, T, for each timestep was recorded by the wave buoy and assumed constant throughout the depth profile for each timestep. Initial values of the wave height at 1,000 m offshore were obtained by shoaling the offshore significant wave heights, H_s, measured at the wave buoy. This was converted to the root mean square wave height, H_{rms}, using:

$$H_{rms} = 1.42 \cdot H_s. \qquad \text{[G2]}$$

These values were then provided as initial wave height values as follows:

$$H_2 = H_1 \sqrt{\frac{c_1 n_1}{c_2 n_2}}, \qquad \text{[G3]}$$

where c_1 and c_2 are the wave celerity at the wave buoy and 1,000 m offshore (Equation G4), and n_1 and n_2 are equal to n at the wave buoy and 1,000 m offshore (Equation G5). According to Airy linear theory, the calculation of wave celerity varies depending on the ratio of the water depth below the still water tide level, d, to offshore wavelength, L_o, such that:

$$\begin{aligned} &\textit{Shallow depths } \left(\frac{d}{L_o} \leq 0.05\right), \qquad c = \sqrt{gd}, \\ &\textit{Intermediate depths } \left(0.05 < \frac{d}{L_o} \leq 0.50\right), \qquad c = \frac{L}{T}, \\ &\textit{Deep waters } \left(\frac{d}{L_o} > 0.50\right), \qquad c = \frac{gT}{2\pi}, \end{aligned} \qquad \text{[G4]}$$

$$n = \frac{1}{2}\left[1 + \frac{2kd}{\sinh(2kd)}\right], \qquad \text{[G5]}$$

where g is the gravitational acceleration (9.81 m s^{-2}). The level of energy dissipation in a breaking wave, α, and the fraction of breaking waves, γ, are used as coefficients in the model. Battjes and Stive (1985) obtained values for these coefficients by comparing modelled results with laboratory and field experiments, with α equal to 1 and γ variable relative to the offshore wave steepness, s_o

(H_{rms}/L_o). Given that the input wave and bathymetric conditions are similar to those monitored along the North Yorkshire coast, these values are also used here. The breaker height coefficient, γ, which is used to predict breaking wave heights, is calculated as follows:

$$\gamma = 0.5 + 0.4 \cdot \tanh(33 \cdot s_o). \quad [G6]$$

This is then used to calculate the breaking wave height, H_m, which is determined by the offshore wave steepness, the local water depth, and wave number:

$$H_m = 0.88 \cdot k^{-1} \cdot \tanh\left(\frac{\gamma kd}{0.88}\right). \quad [G7]$$

The model calculates energy dissipation, D, based on the fraction of waves, Q, that are breaking. The breaking wave height is used as a threshold to identify the proportion of breaking waves in the cumulative probability distribution of wave heights. Q is calculated iteratively based on the ratio of H_{rms} to H_m. When $H_{rms} \geq H_m$, the water depth approaches 0 and Q is equal to 1, signalling that the majority of waves have broken. When $H_{rms} \geq H_m$, H_{rms} is set equal to H_m so that the wave energy decreases once the majority of waves have broken:

$$\frac{1 - Q}{-\ln Q} = \left(\frac{H_{rms}}{H_m}\right)^2. \quad [G8]$$

The variables and coefficients derived above are then used to calculate the rate of energy dissipation per unit of horizontal area, D, that occurs as waves are breaking:

$$D = \frac{1}{4} \cdot \alpha \cdot Q \cdot f \cdot \rho \cdot g \cdot {H_m}^2, \quad [G9]$$

where f is equal to the peak wave frequency, which is obtained from the offshore wave buoy, and ρ is the density of sea water (1,030 kg m^{-3}). The energy dissipation is used in the integration of the energy flux through the depth profile. This accounts for the energy dissipation due to the fraction of waves that are breaking as they progress towards the coast. The energy flux, P, is integrated from 1,000 m to the water's edge and varies according to the rate of energy dissipation, D, as follows:

$$P_x = E \cdot cg, \quad [G10]$$

where E is the wave energy density, and cg is the wave group celerity, which is the speed at which the energy density is transported. These are derived as follows:

$$E = \frac{1}{8}\rho \cdot g \cdot H^2, \quad \text{[G11]}$$

$$cg = c \cdot n. \quad \text{[G12]}$$

The energy flux, P, is integrated over the wave profile at each location, x, accounting for the energy dissipation due to wave breaking that occurs between x and the previous location (x - 1), such that:

$$\frac{\delta P_x}{\delta_x} + D = 0. \quad \text{[G13]}$$

Following Battjes and Stive (1985), this is solved as follows:

$$P_x = \delta x_x(-D_x) + P_{x-1}. \quad \text{[G14]}$$

The predicted H_{rms} is then calculated as follows:

$$H_{rms_x} = \sqrt{\frac{8 \cdot P_x}{\rho \cdot g \cdot c_x}}. \quad \text{[G15]}$$

The momentum flux, S_{xx}, of waves on sloping beaches/foreshores causes changes in the mean water level as waves break (Komar, 1998). These changes are commonly referred to as set-up or set-down, and are calculated at each location along the depth profile by integrating the momentum flux. As waves approach a sloping beach or foreshore, there is a shoreward increase in momentum that exerts stresses that act in a number of directions (Davidson-Arnott, 2010). This stress, known as the shoreward radiation stress, represents the shoreward momentum flux, S_{xx}. This increases as the wave height increases towards the breakpoint. Wave set-up or set-down is therefore the response to the changes in momentum flux as the wave approaches, and eventually passes, the breakpoint. The momentum flux is derived as follows:

$$S_{xx} = \left[\frac{1}{2} + \frac{2kh}{\sinh(2kh)}\right] E, \quad \text{[G16]}$$

where h is the sum of the water depth at still tide level, d, at location x and the wave set-up height, η, calculated at the previous location (x-1). Initial values of wave set-up height 1,000 m offshore were therefore calculated as follows:

$$\eta = \frac{kH^2}{8 \cdot \sinh(2kd)}. \quad \text{[G17]}$$

The wave set-up that occurs across the rest of the profile is then calculated via the integration of the momentum balance:

$$\frac{\delta S_{xx}}{\delta_x} + \rho \cdot g \cdot (d + \eta)\frac{\delta_\eta}{\delta_x} = 0, \quad \text{[G18]}$$

which is solved using the following:

$$\eta_x = \left[-\frac{\delta S_{xx}}{\delta_x}\right] \cdot \left[\frac{1}{\rho \cdot g \cdot (d_x + n_{x-1})}\right] \delta_x + \eta_{x-1}. \quad \text{[G19]}$$

The model loops through the depth profiles shown in Figure G1, integrating both the energy flux and momentum flux to produce a number of key outputs. These include the root mean square wave height (H_{rms}), wave set-up (η), energy flux (P), and energy flux dissipation (D) at each location. After the waves break, H_{rms} is set to H_m for the other positions in the depth profile up to the water's edge. This acts to simulate surf zones, where broken waves travel through the surf zone and dissipate energy to the foreshore via bed friction and turbulence, which results in a decrease in wave height (Komar, 1998).

Appendix H

Validation of the wave transformation model

Outputs from the wave transformation model detailed in *Appendix G* and used in *Chapter 5* were validated using nearshore wave information derived from an RBR*solo* depth channel logger, which was deployed *ca.* 5 m seaward of the cliff toe at S8 (Figure H1). Over a two-week period from 6 February 2017 to 21 February 2017, during which time significant wave heights were observed to exceed 5 m at the offshore wave buoy, a comparison of modelled and measured water depths yielded a correlation coefficient of 0.93, with a mean absolute error of 0.09 m.

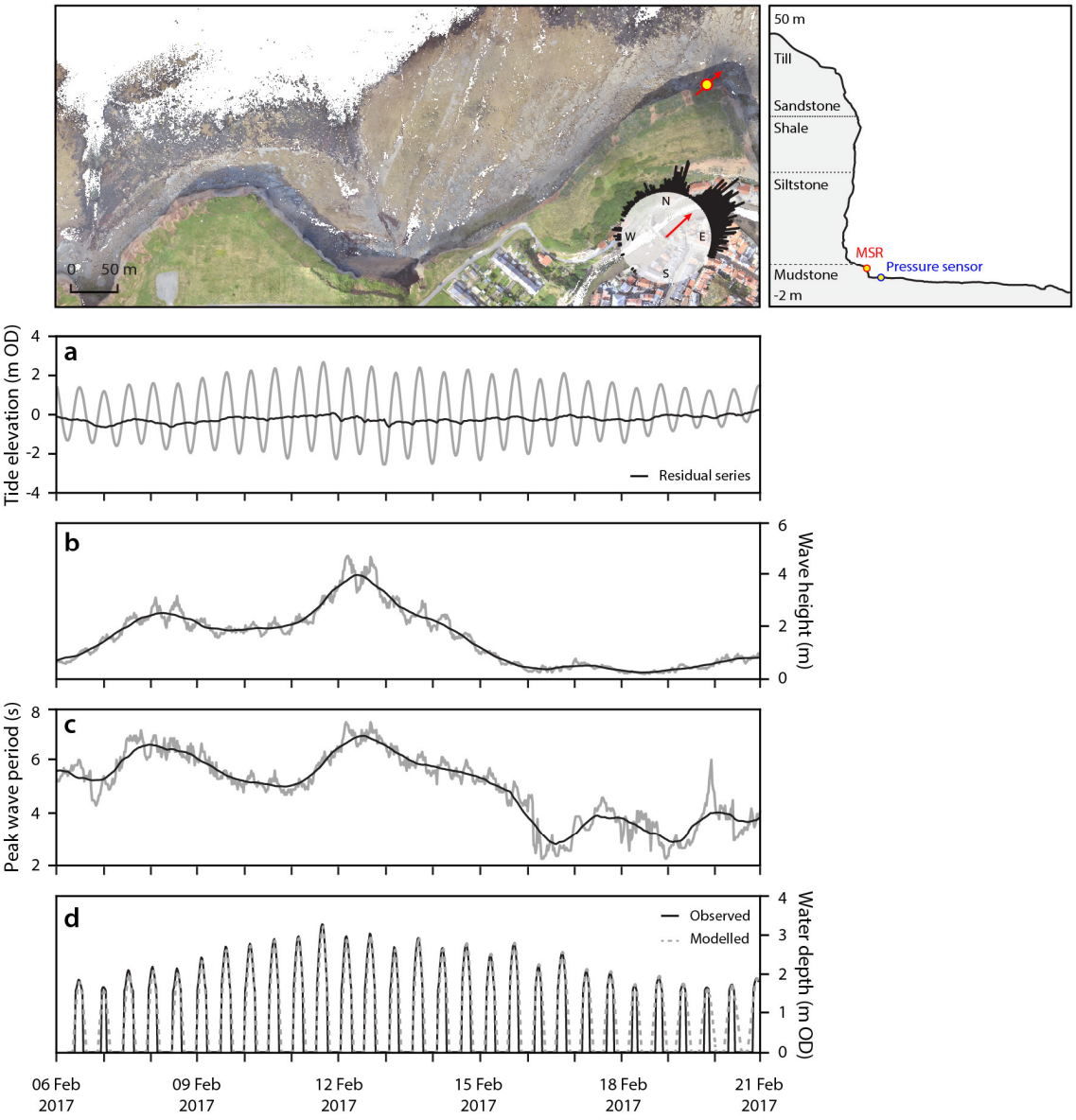

Figure H1 *Model validation water depths observed at S8. Model inputs include (a) tide elevation, (b) significant wave height, and (c) peak wave period, which were obtained from the nearest available tide gauge (UK National Tide Gauge Network, Whitby, ca. 25 km south) and an offshore wave buoy (CEFAS Wave Net, Whitby). Observed and modelled water depths are shown in (d). Modelled depths include the combined effects of the tide, wave, and set-up elevations.*

Appendix I

Harmonic tidal constituents

Harmonic tidal constituents of the Whitby tide gauge data presented in Figure 5.14 (*p.* 106), derived using the MATLAB® toolbox `T_TIDE`, developed by Pawlowicz *et al.* (2002).

*Harmonic tidal constituents. *Denotes significant constituents.*

		Frequency	*Amplitude*	*Error*	*SNR*
Long period		*cycles hr^{-1}*	*m*	*m*	-
S_{sa}	Solar semiannual	0.00023	0.0316	0.037	0.8
M_{sm}	Solar monthly	0.00131	0.0146	0.032	0.2
M_m	Lunar monthly	0.00151	0.0312	0.042	0.5
M_{sf}	Lunisolar synodic fortnightly	0.00282	0.0043	0.030	0.02
M_f	Lunisolar fortnightly	0.00305	0.0196	0.038	0.3
Diurnal					
ALP_1		0.0344	0.0099	0.014	0.5
$2Q_1$	Larger elliptic diurnal	0.0357	0.0033	0.009	0.1
σ_1	Lunar variation	0.0359	0.0050	0.012	0.2
$\mathbf{*Q_1}$	Larger lunar elliptic diurnal	0.0372	0.0284	0.014	4.2
$\rho 1$	Larger lunar evectional diurnal	0.0374	0.0099	0.012	0.7
$\mathbf{*O_1}$	Lunar diurnal	0.0387	0.0937	0.016	36.0
$\mathbf{*\tau_1}$		0.0390	0.0198	0.015	1.8
χ_1	Smaller evectional	0.0405	0.0036	0.011	0.1
$\mathbf{*P_1}$	Solar diurnal	0.0416	0.0597	0.014	17.0
$\mathbf{*K_1}$	Lunar diurnal	0.0418	0.0944	0.014	44.0
φ_1	Second-order solar	0.0420	0.0165	0.015	1.1
ϑ_1	Evectional	0.0431	0.0080	0.011	0.5
J_1	Smaller lunar elliptic diurnal	0.0433	0.0053	0.010	0.3
OO_1	Lunar diurnal	0.0448	0.0042	0.011	0.2
Semi-diurnal					
OQ_2		0.0760	0.0115	0.061	0.04
$2N_2$	Lunar elliptical semidiurnal	0.0775	0.0391	0.061	0.4
MU_2	Variational	0.0777	0.0165	0.062	0.1

***N_2**	Larger lunar elliptic semidiurnal	0.0790	0.3244	0.077	18.0
NU_2	Larger lunar evectional	0.0792	0.0728	0.078	0.9
***M_2**	Principal lunar semidiurnal	0.0805	1.5834	0.083	370.0
***MKS_2**		0.0810	0.1203	0.072	2.8
L_2	Smaller lunar elliptic semidiurnal	0.0820	0.0768	0.075	1.1
***S_2**	Principal solar semidiurnal	0.0833	0.5268	0.087	37.0
***K_2**	Lunisolar semidiurnal	0.0836	0.1429	0.082	3.0
MSN_2		0.0848	0.0248	0.057	0.2

Higher harmonics

***MO_3**		0.1192	0.0074	0.004	3.9
***M_3**	Lunar terdiurnal	0.1208	0.0090	0.004	5.2
SO_3		0.1221	0.0040	0.003	1.4
MK_3	Shallow water terdiurnal	0.1223	0.0043	0.004	1.3
SK_3		0.1251	0.0014	0.003	0.2
***MN_4**	Shallow water quarter diurnal	0.1595	0.0105	0.004	6.5
***M_4**	Shallow water overtides of the principal lunar	0.1610	0.0246	0.004	33.0
SN_4		0.1623	0.0045	0.004	1.1
***MS_4**	Shallow water quarter diurnal	0.1638	0.0229	0.005	19.0
***MK_4**		0.1641	0.0104	0.004	5.4
S_4	Shallow water overtides of the principal solar	0.1667	0.0038	0.004	0.8
SK_4		0.1669	0.0048	0.005	1.0
$2MK_5$		0.2028	0.0020	0.002	1.3
$2SK_5$		0.2084	0.0010	0.002	0.4
$2MN_6$		0.2400	0.0031	0.002	1.5
$*M_6$	Shallow water overtides of the principal lunar	0.2415	0.0058	0.002	6.0
***$2MS_6$**		0.2444	0.0074	0.003	7.3
$2MK_6$		0.2446	0.0032	0.003	1.6
$2SM_6$		0.2472	0.0010	0.002	0.3
MSK_6		0.2474	0.0006	0.002	0.1
***M_8**	Shallow water eighth diurnal	0.3220	0.0014	0.001	2.5
M_{10}		0.4026	0.0007	0.001	0.9

Appendix J

Cliff toe ground motions and relationships with drivers

Summary of the data presented in Figures 5.18, 5.21, and 5.22.

Site	*Displacement magnitude*[a]			*Frequency*[b]		*Drivers*				*Rockfalls*
	Mean	*Median*	*Maximum*	*Impacts*	*Rate*	*Aspect*	*Platform length*[c]	*Platform slope*[d]	*Inundation*[e]	*Volume*[f]
	μm	*μm*	*× 10³ μm*	-	*min⁻¹*	°	*m*	*%*	*dd:hh:mm*	*m³*
1	56.9	60.1	1.66	2,677,956	14.1	320	202 ± 18	1.3 ± 0.1	132:21:10	37.32 ± 3.95
2	94.5	94.2	6.21	3,213,238	17.0	346	92 ± 26	2.7 ± 0.2	131:21:40	84.71 ± 2.31
3	99.6	100.7	6.63	4,160,598	20.6	357	80 ± 20	3.1 ± 0.3	140:13:45	21.05 ± 5.17
4	71.2	70.2	4.80	3,120,380	15.6	45	87 ± 25	2.9 ± 0.3	148:02:14	76.17 ± 7.46
5*	85.4	86.7	5.43	441,860	19.2	16	155 ± 13	2.5 ± 0.3	16:14:52	58.67 ± 12.39
6	66.9	70.6	3.66	2,825,580	14.2	335	216 ± 26	1.5 ± 0.3	140:01:48	44.78 ± 2.82
7	54.8	58.4	0.95	1,310,992	10.9	318	245 ± 25	1.3 ± 0.1	83:22:44	24.16 ± 0.88
8	85.8	90.8	2.17	1,000,892	16.4	13	226 ± 17	2.4 ± 0.3	41:20:27	17.57 ± 3.71

[a] *Metrics derived using the vector magnitude of the particle motion ellipsoid for each impact.*
[b] *Metrics derived using the number of impacts recorded at each site.*
[c] *Platform length measured in the predominant wave direction (30.9°). Measurements of platform length in other probable directions (based on cliff aspect and incoming wave direction) are included by calculating the standard deviation of these measurements (± 1σ).*
[d] *Platform slope and standard deviations calculated as in* [c].
[e] *Time elapsed where the total water level exceeded the cliff toe.*
[f] *Total volume of the rockfalls that occurred over the 50 m of cliffs (± 25 m) surrounding each instrument, between August 2014 and March 2017.*
* *Observations at this site were recorded over 102 days (as opposed to 306) due to a rockfall that occurred on 12/01/2017.*

Appendix K

Structural and morphological controls on cliff erosion

Scatterplots demonstrate the relationships between cliff erosion and structural controls (derived in *Chapter 4*), in Figure K1, and cliff erosion and morphological controls (derived in *Chapter 5*), in Figure K2. For each 100 m bin along the North Yorkshire coast, shown in Figure 3.12 (*p.* 43), the total number of rockfalls (frequency), the total volume eroded, and the mean erosion rate over the monitoring period (August 2014 – March 2017) was calculated. These estimates of erosion were then related to the mean of each control.

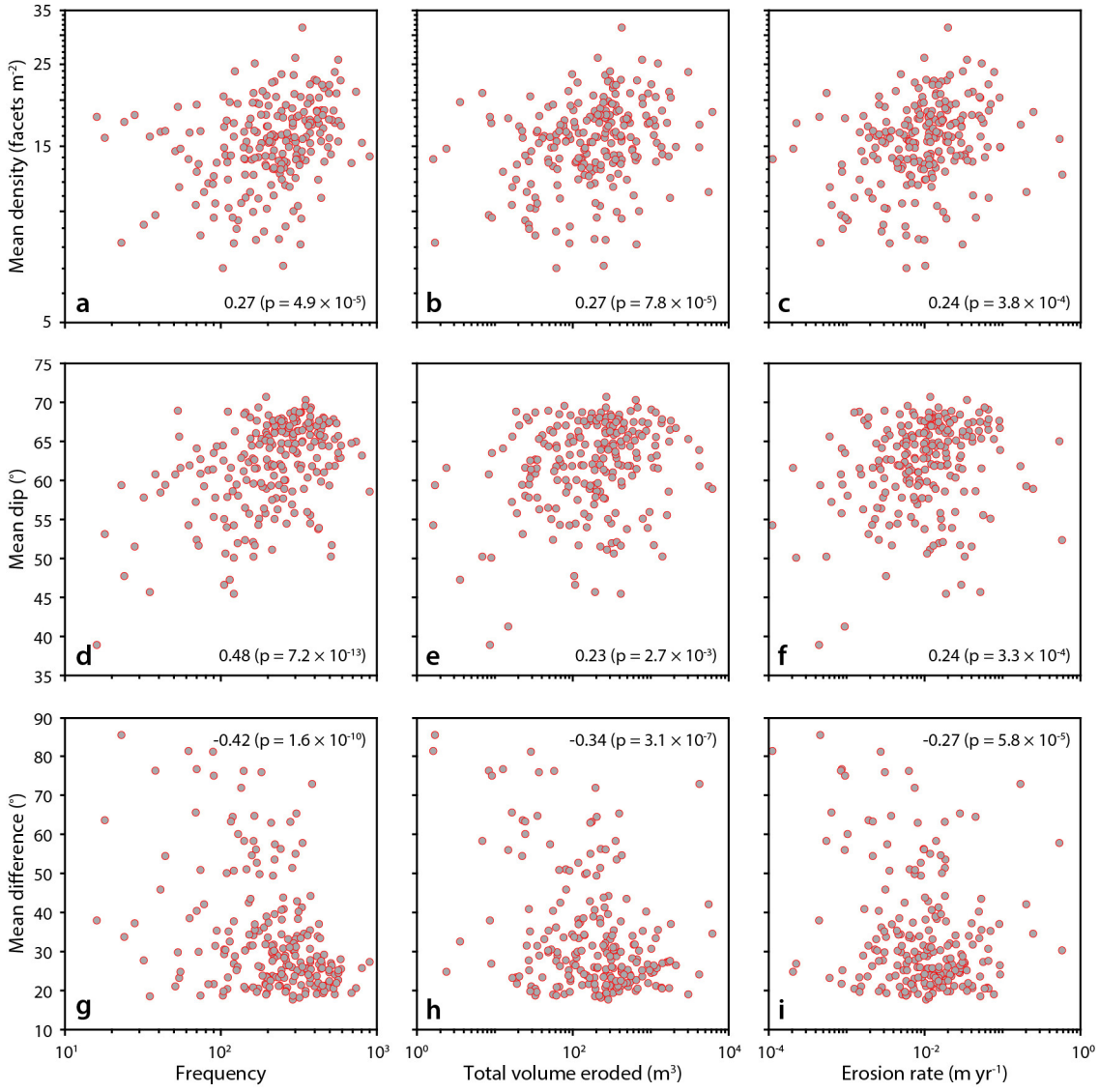

Figure K1 *Relationships between cliff erosion and structural controls, identified in Chapter 4. Correlations are shown for several indicators of cliff erosion, which were derived in Chapter 4, and include the frequency of rockfalls, the total volume eroded, and the erosion rate in each 100 m bin along the North Yorkshire coast. Panels (a) – (c) show correlations between cliff erosion and the mean facet density, panels (d) – (f) the mean dip, and panels (g) – (i) the mean difference between facet and cliff aspects. Correlation coefficients and their p-values are shown where relationships are statistically significant (red).*

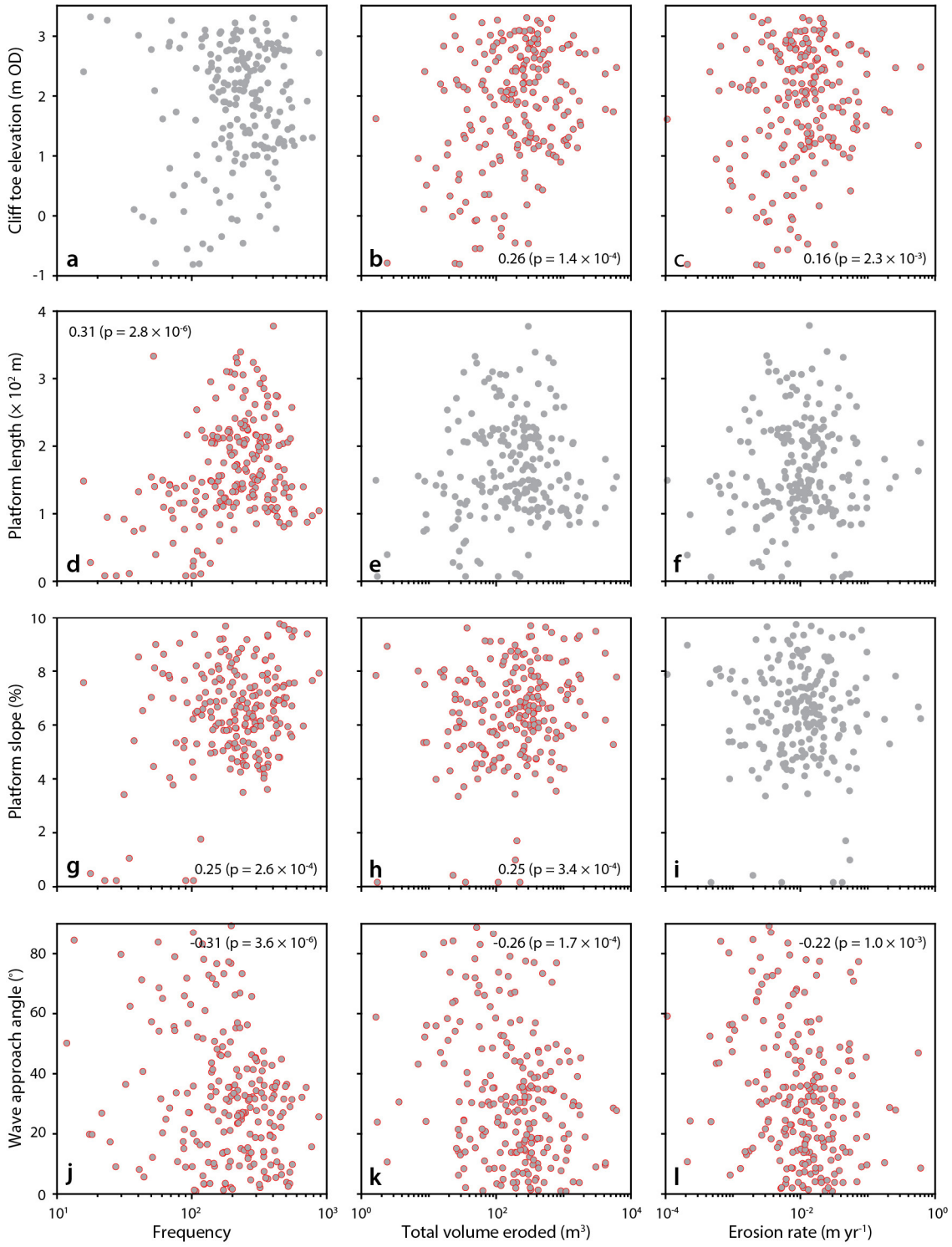

Figure K2 *Relationships between cliff erosion and morphological controls, identified in Chapter 5. Correlations are shown for several indicators of cliff erosion, which were derived in Chapter 4, and include the frequency of rockfalls, the total volume eroded, and the erosion rate in each 100 m bin along the North Yorkshire coast. Panels (a) – (c) show correlations between cliff erosion and the mean cliff toe elevation, panels (d) – (f) the mean platform length, panels (g) – (i) the mean platform slope, and panels (j) – (l) the mean wave approach angle. All morphological controls were measured at 10 m intervals within each 100 m bin and then averaged. Correlation coefficients and their p-values are shown where relationships are statistically significant (red).*